Vector Solitons and Different Scenarios of Universal Dynamics in a Spin-1 Bose-Einstein Condensate

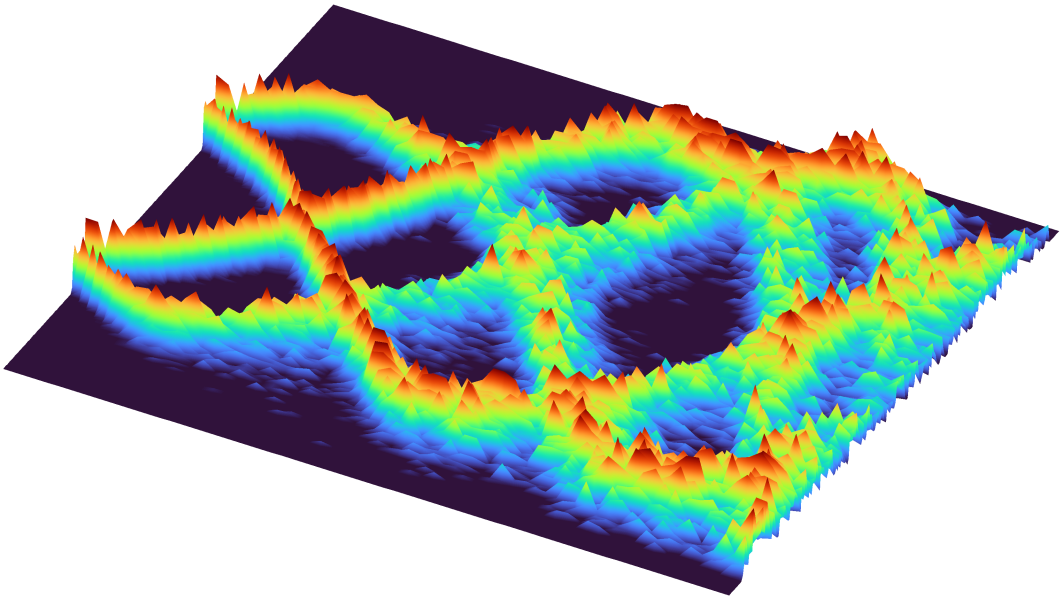

Stefan Lannig

2022

Dissertation

submitted to the

Combined Faculty of Mathematics, Engineering and Natural Sciences

of Heidelberg University, Germany

for the degree of

Doctor of Natural Sciences

Put forward by

Stefan Lannig

born in Würzburg, Germany

Oral examination: 26.07.2022

Vector Solitons and Different Scenarios of Universal Dynamics in a Spin-1 Bose-Einstein Condensate

Referees: Prof. Dr. Markus K. Oberthaler

Prof. Dr. Selim Jochim

Abstract

Solitons are fascinating non-dispersive solutions to non-linear systems, which appear in various scenarios across nature. Because of their stability and longevity these excitations are of great interest in non-equilibrium scenarios. In multi-component systems, the solitons acquire an internal degree of freedom, contributing to a rich variety of interaction effects, which make these excitations particularly interesting.

In this work we experimentally realize the deterministic generation of coherent three-component vector solitons in a quasi one-dimensional Bose-Einstein condensate of ^{87}Rb. For this, a local spin rotation is generated with a single laser beam. We investigate the spatial profiles and propagation of the solitons in a trap as well as their dynamics during soliton-soliton collisions. These are found to be well-described by the analytical Manakov model. In particular, we realize the striking phenomenon of ploarization scattering during soliton collisions, known from the attractive multi-component Manakov system, in a repulsively interacting condensate. The polarization dynamics of the vector solitons is further applied in an application to precisely determine magnetic field gradients.

In a second set of experiments, the non-equilibrium dynamics following an interaction quench is investigated. For this, the excitations in the transverse spin which are spontaneously generated by spin-changing collisions are characterized. Utilizing multiple solitons as initial condition, two regimes are realized, in which localized excitations either decay or strong fluctuations persist over long times. In these scenarios, two distinct dynamical scaling evolutions are identified. These indicate the presence of two different non-thermal fixed points in the spin-1 Bose gas.

Zusammenfassung

Solitonen sind faszinierende nichtdispersive Lösungen nichtlinearer Systeme, die in verschiedenen Szenarien in der Natur vorkommen. Aufgrund ihrer Stabilität und Langlebigkeit sind diese Anregungen in Nichtgleichgewichtsszenarien von großem Interesse. In mehrkomponentigen Systemen besitzen Solitonen einen internen Freiheitsgrad, welcher zu einer Vielzahl von Wechselwirkungseffekten beiträgt, die diese Anregungen besonders interessant machen.

In dieser Arbeit realisieren wir experimentell eine deterministische Erzeugung von kohärenten dreikomponentigen Vektorsolitonen in einem quasieindimensionalen ^{87}Rb Bose-Einstein-Kondensat. Dazu wird eine lokale Spinrotation mithilfe eines einzelnen Laserstrahls erzeugt. Wir untersuchen die räumlichen Profile und die Bewegung der Solitonen in einer Falle, sowie deren Dynamik bei Soliton-Soliton-Kollisionen. Diese werden durch das analytische Mankov-Modell gut beschrieben. Insbesondere realisieren wir das bemerkenswerte Phänomen der Polarisationsstreuung während Solitonenkollisionen, welches für das mehrkomponentige attraktive Mankov-System wohlbekannt ist, in einem Kondensat mit repulsiven Wechselwirkungen. Die Polarisationsdynamik der Vektorsolitonen wird ferner angewandt um Magnetfeldgradienten präzise zu vermessen.

In einer zweiten Reihe von Experimenten wird die Nichtgleichgewichtsdynamik infolge eines Wechselwirkungsquenches untersucht. Dazu werden die spontan erzeugten Anregungen, welche von spinverändernden Stößen verursacht werden, charakterisiert. Durch Verwendung mehrerer Solitonen als Anfangsbedingung werden zwei Regime realisiert, in welchen lokalisierte Anregungen entweder zerfallen oder Fluktuationen über lange Zeit bestehen bleiben. In diesen Szenarien wird unterschiedliches dynamisches Skalieren in der Zeitentwicklung beobachtet. Dies weist auf die Existenz von zwei unterschiedlichen nichtthermischen Fixpunkten im Spin-1 Bosegas hin.

Contents

1. Introduction

Non-linear phenomena are ubiquitous in nature and lead, for instance, to chaos [1], turbulence [2] and the generation of entanglement [3]. These mechanisms affect every-day life through the intricate dynamics of weather and climate [4], but are relevant also in more abstract scenarios as diverse as chemical reactions [5], population dynamics in biology [6], or the application of squeezed light [7–9] for the detection of gravitational waves [10–13]. In particular, in interacting many-body systems these non-linear interactions give rise to complex non-equilibrium physics. It is exactly such a non-linearly interacting many-body system which has been studied in the famous work of Fermi, Pasta, Ulam and Tsingou [14]. They numerically investigated the equilibration of a chain of coupled particles with close to cubic interactions. Initially, the displacement of the particles from their rest position was excited with a superposition of sinusoidal modes. Much to their surprise, the system did not show ergodicity but instead they observed recurrences of the initially excited modes. A decade later, Zabusky and Kruskal explained the appearance of recurrences by scattering of certain non-linear and non-dispersive wave excitations, which retain their shape during collisions [15]. These excitations are called solitons. Their actual discovery dates back to the famous account of the pursuit of a non-dispersive water wave by John Scott Russell. He followed such a wave on horseback over a few thousand meters down a narrow channel in the summer of 1834 [16]. Nevertheless, the study by Zabusky and Kruskal marks the central rediscovery of these non-linear excitations, which have since been studied in many different systems. Especially in optics solitons are applied to reduce dispersion and soliton interactions have even been proposed to realize logic gates [17, 18] and even quantum gates [19].

In Bose-Einstein condensates (BECs), where the s-wave interaction gives rise to the non-linear interactions, such excitations can be realized as well [20, 21]. Here, solitons correspond to a localized and collective excitations which propagate without dispersion [22]. In multi-component systems solitons may also consist of a coupled excitation between multiple of these components. These are so-called vector solitons, which incorporate internal degrees of freedom that are completely separated from their free spatial propagation. Analogous to scattering of particles, these vector solitons change their internal state during collisions [23], showing a particularly intriguing example of dynamics between stable collective excitations.

In this thesis, and experimental implementation for the deterministic generation of three-component vector solitons in a spin-1 BEC is presented. The properties of these solitons are characterized during their propagation and in collisions. The experimental results are found to be in good agreement with the analytical Manakov model. Strikingly, their interactions during collisions provide the means to directly obtain an interferometric contrast, which probes their phase evolution. This

phase evolution is further applied to determine the magnetic field gradient along the condensate. The vector solitons promise to be a powerful tool for precise phase measurements, which do not require additional potentials to realize an interferometer [24–26], and are not limited by density-dependent mean-field shifts.

These controlled scenarios with only a few excitations, like a pair of colliding solitons, are captured well by the microscopic theory. However, far from equilibrium the description of an interacting many-body system on the microscopic level becomes intractable. In a second set of experiments we investigate the influence of non-linear excitation in the system to the non-equilibrium dynamics of the spin-1 BEC. In order to highly excite the system, typically a quench (rapid change) of a control parameter is applied [27]. The following dynamics may then be expected to depend on the details of the system. However, over the last years numerical studies suggested that in such scenarios the dynamics of certain observables becomes independent of microscopic details [28–30]. The notion of non-thermal fixed points (NTFPs) emerged as candidate for a unifying concept to capture these phenomena in physically vastly different systems [31]. However, in general it is not yet clear, which of the system properties determine these scaling parameters. Experimentally, universal dynamics associated to the presence of a NTFP has already been measured in different systems [32–34] and there is some evidence for the insensitivity of this phenomenon on the initial state of the system [32]. Nevertheless, a general experimental classification of the dependence of the non-equilibrium dynamics close to a NTFP on the initial condition has not yet been achieved.

In a first step towards this goal we apply the same techniques previously used to generate vector solitons to obtain an initial condition containing non-linear excitations. We then proceed to classify the spin defects following an interaction quench to obtain two qualitatively different dynamical scenarios in the evolution. One is characterized by a well-defined spin length and phase excitation, while the other exhibits strong fluctuations in both observables. Both scenarios show non-equilibrium scaling, albeit with different parameters. This indicates the presence of distinct NTFPs in a spinor Bose gas.

Structure of this Thesis

In **Chapter 2** general theoretical concepts for treating BECs are discussed and the properties of the spin-1 gas employed in experiment are introduced. Additionally, an overview over the experiment and the control techniques for manipulating and extracting the internal spin states is provided. Particularly emphasis is put on the implementation and characterization of the local control setup.

In **Chapter 3** a general overview of solitons is provided and the properties of the vector solitons generated in experiment are discussed in detail. This is complemented by a description of the experimental technique for the deterministic soliton preparation and a characterization of the measured soliton properties. In particular, the collisional dynamics are investigated. Further, the coherent nature of the vector solitons is employed to precisely characterization of magnetic field gradients in the system.

In **Chapter 4** the spin dynamics after an interaction quench is investigated. Here a homogeneous system is compared to an initial condition leading to multiple vector soliton pairs (of the type discussed in the previous chapter). In both cases the generated spin excitations are characterized and compared to expectation derived from different approximate models.

In **Chapter 5** the non-equilibrium dynamics characteristic for systems close to a NTFP is investigated experimentally. Distinct scaling properties are extracted for the two scenarios discussed in chapter 4.

In **Chapter 6** a short summary of the results obtained in this thesis is provided.

In **Chapter 7** a range of proposals for future experiments and investigations of the various topics touched over the previous chapters is provided. These include both, technical improvements of the setup and new experiments to investigate different physical phenomena.

List of Publications

M. Prüfer, P. Kunkel, H. Strobel, S. Lannig, D. Linnemann, C.-M. Schmied, J. Berges, T. Gasenzer, M. K. Oberthaler, *Observation of universal dynamics in a spinor Bose gas far from equilibrium*, Nature **563**, 217-220 (2018)

P. Kunkel, M. Prüfer, S. Lannig, R. Rosa-Medina, A. Bonnin, M. Gärttner, H. Strobel, M. K. Oberthaler, *Simultaneous Readout of Noncommuting Collective Spin Observables beyond the Standard Quantum Limit*, Phys. Rev. Lett. **123**, 063603 (2019)

M. Prüfer, T. V. Zache, P. Kunkel, S. Lannig, A. Bonnin, H. Strobel, J. Berges, M. K. Oberthaler, *Experimental extraction of the quantum effective action for a non-equilibrium many-body system*, Nature Physics **16**, 1012–1016 (2020)

S. Lannig, C.-M. Schmied, M. Prüfer, P. Kunkel, R. Strohmaier, H. Strobel, T. Gasenzer, P. G. Kevrekidis, M. K. Oberthaler, *Collisions of three-component vector solitons in Bose-Einstein condensates*, Phys. Rev. Lett. **125**, 170401 (2020)

P. Kunkel, M. Prüfer, S. Lannig, R. Strohmaier, M. Gärttner, H. Strobel, M. K. Oberthaler, *Detecting entanglement structure in continuous many-body quantum systems*, Phys. Rev. Lett. **128**, 020402 (2022)

M. Prüfer, D. Spitz, S. Lannig, H. Strobel, J. Berges, M. K. Oberthaler, *Condensation and thermalization of an easy-plane ferromagnet in a spinor Bose gas*, arXiv:2205.06188

2. Experimental System

This chapter will introduce the experimental concepts relevant for the measurements presented in this thesis. First, a brief overview over the experimental setup is presented. The apparatus employed in this thesis already has a long history and therefore most of its setup is already presented in other works [35–41], which will also be referenced at the appropriate points. Further, a short overview of the full experimental cycle will be given here. Additionally, as basis for the discussion of dynamics and the experimental control, the spin-1 system will be introduced in some detail. This is complemented with an overview of various techniques to control the atoms and their internal states. In particular, these are relevant for the preparation and readout of the system. Since a substantial part of this work is centered around the local control of the spin degree of freedom, this chapter will provide a detailed description of the local control setup. At first, however, some quite general basic theoretical concepts will be introduced, which are of importance at different points throughout the whole thesis.

2.1. The Gross-Pitaevskii Equation – A Mean-Field Model for BECs

The fascination sparked by the process of Bose-Einstein condensation lies in the generation of a macroscopic coherent system, i.e. a system consisting of many particles in which all constituents are in the same state. This system consequently allows for the fascinating quantum phenomena like superfluidity [42–44] or interference of BECs [45].

In order to capture these phenomena, it is sufficient to consider the system on the mean-field level, which is valid for large populations. In this limit of large occupations, the small (quantum-)fluctuations can be neglected. Thus, instead of treating the system in terms of quantum fields $\hat{\psi}(\boldsymbol{x}, t)$ described by operators, the fields are replaced by complex-valued functions $\psi(\boldsymbol{x}, t)$. In this scenario the equation of motion of these "classical" fields takes the form of the Gross-Pitaevskii equation (GPE) [44]

$$i\hbar\partial_t\psi = \left(-\frac{\hbar^2\nabla^2}{2m} + V_{\text{ext}} + g\left|\psi\right|^2\right)\psi, \tag{2.1}$$

where V_{ext} denotes the trapping potential and the constant g describes the interactions between the atoms. In ultracold gases where only low-energy s-wave scattering is relevant it is parameterized solely by the s-wave scattering length a via $g = 4\pi\hbar^2 a/m$ [44]. For stable BECs the interactions are usually repulsive ($g > 0$). The GPE provides a simple but extremely useful model for the condensate.

As we will also see in the next chapter, this equation will also form the basis for the vector solitons discussed in this thesis.

An important quantity, which will appear at various points, is the healing length

$$\xi = \frac{\hbar}{\sqrt{2mng}}. \tag{2.2}$$

It specifies the length scale on which condensate density $n = |\psi|^2$ adjusts to sharp features like a potential barrier in the external potential V_{ext} in the steady-state limit. Considering for example a constant potential with an infinitely large wall, then also the condensate density would be constant far away from the wall, while becoming zero at the wall. The healing length specifies the length scale over which the transition between these two regimes takes place. Alternatively, it can be interpreted as the wavelength scale (though not precisely the wavelength λ but rather $\lambda/(2\pi)$) for which the kinetic energy of plane waves with momentum $p = \hbar k = \hbar/\xi$ becomes equal to the chemical potential $\mu = ng$ fixed by the interactions. [44]

Thomas-Fermi Approximation

Particularly for analyzing the static density distribution of condensates in a static potential $V_{\text{ext}}(\boldsymbol{x})$ it is useful to introduce the Thomas-Fermi (TF) approximation to eq. (2.1). For the GPE the wavefunction can be written in the form $\psi(\boldsymbol{x}, t) = \sqrt{n(\boldsymbol{x}, t)}e^{i\varphi(\boldsymbol{x},t)}$ of a superfluid order parameter with density $n(\boldsymbol{x}, t)$ and phase $\varphi(\boldsymbol{x}, t)$. The TF approximation neglects the so called quantum pressure term $\sim \nabla^2\sqrt{n}$, which is part of the kinetic term related to gradients in the density. It is valid if the density varies on scales large compared to the healing length ξ. For a static state where the phase φ is flat, also the contributions of the superfluid velocity $v_s \sim \nabla\varphi$ can be dropped. This corresponds to fully neglecting the kinetic term in eq. (2.1). By introducing the chemical potential μ as energy scale for the evolution of the condensate phase φ we obtain the TF density profile

$$n(\boldsymbol{x}) = \frac{\mu - V_{\text{ext}}(\boldsymbol{x})}{g} \tag{2.3}$$

of the condensate groundstate in a trap. This result is only valid in the limit of vanishing temperature and dilute gases where $na^3 \ll 1$. By setting the minimum of V_{ext} to zero we also obtain the chemical potential from the peak condensate density n_0 as $\mu = n_0 g$.

Many of the experimentally employed potentials are approximately harmonic with $V_{\text{ext}} = m\omega^2 x^2/2$, where for simplicity we consider the 1-dimensional (1d) case. The density therefore also assumes a parabolic shape with TF radius

$$r_{\text{TF}} = \frac{1}{\omega}\sqrt{\frac{2\mu}{m}} = \frac{a_{\text{ho}}^2}{\xi_0} \tag{2.4}$$

between the center at maximal density and the edge where the condensate density drops to zero. It is given by the harmonic oscillator length $a_{\text{ho}} = \sqrt{\hbar/(m\omega)}$ scaled

by the ratio between a_{ho} and the healing length ξ_0 with respect to the peak density n_0.

Experimentally, the measurement of the full 3D density distribution is not directly possible. Therefore, it is helpful to estimate the chemical potential from 1d density distributions. For this, the chemical potential is fixed to the (local) 1d density $n_{1\mathrm{d}}$ by integrating eq. (2.3) over the transverse directions. Assuming a cylindrically symmetric harmonic potential, which is flat in the longitudinal direction, we obtain

$$\mu = \omega_\perp \sqrt{\frac{m g n_{1\mathrm{d}}}{\pi}}, \tag{2.5}$$

where $\omega_\perp$ is the transverse harmonic trap frequency. Further, when all dynamics in the transverse direction is suppressed, a 1d version of the GPE (2.1) can be derived by integration over the normalized transverse wavefunction. When only the transverse harmonic oscillator groundstate is occupied the effective 1d interaction constant takes the convenient form of [44, 46]

$$g_{1\mathrm{d}} = \frac{g}{2\pi a_\perp^2}. \tag{2.6}$$

By replacing g in eq. (2.1) by $g_{1\mathrm{d}}$ an effective description for the 1d wavefunction is obtained. Note that, unless noted otherwise, everywhere except in this section an effective 1d description is applied implicitly, i.e. densities n are usually referring to the 1d density $n_{1\mathrm{d}}$ (see section 2.2.3 for more details).

A more comprehensive overview over the mean-field description of BECs (and beyond) may be found in [44, 47].

2.2. Preparation of the BEC

In our experiments we are working with elongated quasi 1-dimensional condensates of ^{87}Rb which contain up to $\sim 150\,\mathrm{k}$ atoms. In the electronic groundstate the electron spin $S = 1/2$ and nuclear spin $I = 3/2$ couple to two values of the total hyperfine spin $F = 1, 2$. Therefore, multiple internal magnetic substates $m_{\mathrm{F}} = -F, \ldots, F$ are available.

The experiment is run continuously in cycles. During the first 37 s the atoms are cooled and finally condensed into a BEC [35, 36]. Then the desired experimental sequence is run, consisting of the initial state preparation, evolution and, finally, the readout of the atomic density distributions. Here, the evolution period may last up to $\sim 50\,\mathrm{s}$ while all remaining steps are completed within a few milliseconds [40].

2.2.1. Stabilization and Monitoring

To accumulate a sufficient number of single realizations during measurements, the repeatability of the experiment with the same parameters is of central importance. Because some measurements last for up to a week, the experimental conditions need to remain stable over extended periods of time. For this, experimental quantities are either actively stabilized or measured periodically to detect drifts. Here, an

active temperature regulation of the complete room to $\sim \pm 0.2\,°\mathrm{C}$ combined with a passive stabilization of all optical components near the atoms by a full enclosure sets the baseline for the required stability. Further, special care has to be taken to regulate the magnetic field and microwave dressing (see section 2.4.2 for details on the microwave setup). The magnetic field is actively stabilized to a flux gate sensor positioned close to the atoms and the microwave power is monitored with a power diode [41]. This ensures a sufficient short-time stability which is complemented by periodic control measurements to account for long-term drifts.[1] The magnetic offset field strength is calibrated hourly (see section 2.7 for details) while every $(12-25)\,\mathrm{h}$ the magnetic field gradient is monitored (see also section 2.7) and the microwave dressing is calibrated using a spectroscopy measurement (see section 2.3.5 for details).

2.2.2. Cooling and Trapping

The preparation of the condensate starts by cooling ^{87}Rb atoms of the background gas in the "high" pressure region of the vacuum setup in a 2D magneto-optical trap (MOT). These atoms are transferred through a differential pumping stage into a 3D MOT in the low pressure region of the vacuum chamber. After continuously loading the 3D MOT for approx. 4 s and a short sequence of sub-doppler cooling the atoms are transferred into a magnetic time-orbiting potential (TOP) trap for evaporative cooling. Before loading the TOP trap, the atoms are pumped into the trapped low-field seeking state $|F = 1, m_\mathrm{F} = -1\rangle$ and remaining $F = 2$ atoms are removed via MOT light. The basic setup and principle of these first stages are described in [35, 36] but a short overview is also given in [37, 38].

After approx. 25 s of evaporation, the atom cloud is transferred into a far red-detuned crossed-beam dipole trap (also called crossed dipole trap (XDT)) at a wavelength of 1030 nm (see fig. 2.1 for an overview of the optical trapping beams). Here, the power of the beams is ramped down for further evaporation. The endpoint of this evaporation ramp is also used to change the final atom number. After this step we obtain a spin-polarized condensate of up to $\sim 150\,\mathrm{k}$ atoms in the state $|1, -1\rangle$. One of the crossed beams is then ramped down, such that the cloud expands in the potential of the remaining beam. This beam is rotationally symmetric and only weakly focused and hence provides a cigar-shaped harmonic trap with longitudinal and transverse trap frequencies of $(\omega_\parallel, \omega_\perp) = 2\pi \times (1.6\,\mathrm{Hz}, 170\,\mathrm{Hz})$. As it provides a quasi-1d propagation channel for matterwaves we will call this dipole trap waveguide (WG). A general overview over the laser setup is provided in [37] although some components like the dipole laser and the imaging system have been replaced (see [39–41]).

Additionally, blue-detuned laser beams can be superimposed with the WG such that the expansion of the atoms is limited to the central part of the harmonic WG potential (see fig. 2.1). This approximately realizes a box-potential for the atoms along the WG axis, which will be utilized in chapters 4 and 5. More details on the

[1] For the magnetic field a significant portion of the drifts originate from a temperature-induced change of the output value of the fluxgate sensor due to its temperature coefficient [41]. Therefore, changes in the cycle period need to be limited to suppress magnetic field drifts.

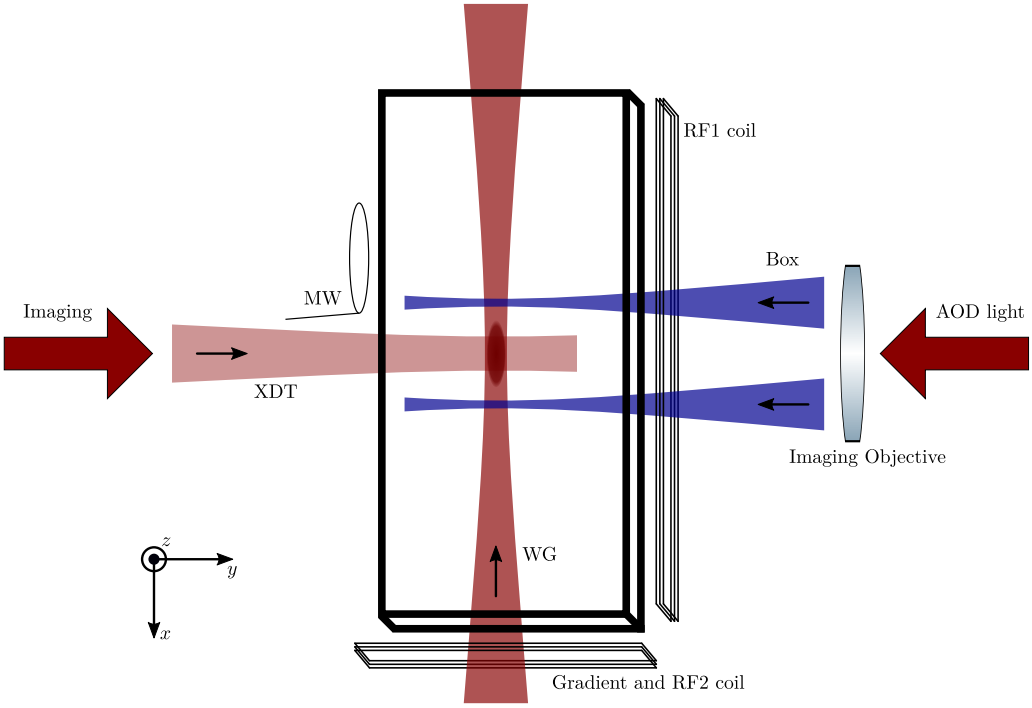

Figure 2.1.: Setup of the optical traps and arrangement of magnetic coils for the control of internal hyperfine levels. The WG and XDT beams are red-detuned (1060 nm) dipole traps and the box beams are blue-detuned (760 nm) repulsive end caps which restrict the expansion of atoms in the WG beam. This approximately generates a 1d box trap for the atoms.

laser setup and the implementation of this trap will be given in section 2.6.

One crucial ingredient for achieving access to long-time spin dynamics in our system was the reduction of the WG trap power. When tuning the system into a parameter regime where the groundstate features a non-zero spin length we observed that large WG powers lead to a decay of spin coherence, signaled by a decay of both the average values as well as the fluctuations of the spin observables. In contrast, for low powers, both the mean spin length and fluctuations show a decay only on the time scale of the atom number lifetime or even slower than that. For a more detailed study on this see [48]. For the experiments discussed here we reduced the WG power slightly above the limit at which the atom number lifetime starts to reduce. With this configuration we are able to achieve atom number and spin lifetimes larger than 40 s.

2.2.3. Quasi-1d Limit of the Condensate

Although the WG trap provides a strong transverse confinement, our experiments are usually performed at typical densities of $n_{1\mathrm{d}} \sim 400\,\mathrm{atoms/\mu m}$ where $a_{\mathrm{ho}}/\xi \sim 3$. This implies that the condensate wavefunction may change on scales smaller than the extent of the Gaussian groundstate of the transverse harmonic confinement. Thus, the effective 1d description of the system via eq. (2.6) is not strictly correct. However, in this situation the system is also not well described by the TF approximation, which would require the variation of the transverse density profile to be slow ($r_{\mathrm{TF}}/\xi = (a_{\mathrm{ho}}/\xi)^2 \gg 1$). Nevertheless, calculating the effective 1d interaction constant $g_{1\mathrm{d}}$ in the transverse TF approximation yields values which deviate by less than 20 % from the harmonic oscillator groundstate value of eq. (2.6). Therefore, to obtain an approximate but simple description of our system we combine both limits by using the Gaussian effective interactions given in eq. (2.6) together with a TF estimation of the chemical potential in eq. (2.5). Thus, unless noted otherwise, from now on all quantities are related to this effective 1d description (i.e. densities n denote the transversely integrated 1d density n_{1d} from now on).

Independent from the extraction of the exact parameters of the system we can clearly distinguish the directions which will participate in the dynamics. In transverse direction the system size is on the order of a few density healing lengths $\xi_{\mathrm{d}} \sim 0.3\,\mu\mathrm{m}$ (this denotes the healing length with respect to the density-density interactions; see section 2.3.2 for more details). Thus, excitations in the density degree of freedom (d.o.f.) are possible in transverse direction. However, in the longitudinal WG direction larger-scale excitations are possible, which therefore have considerably smaller kinetic energy. Thus, mainly longitudinal excitations are expected. Here, however, we are mainly interested in structures with an extension corresponding to the spin healing length $\xi_{\mathrm{s}} \sim 5\,\mu\mathrm{m}$ with respect to the much smaller spin interaction in our system.[2] Therefore, the dynamics relevant for these excitations should be well described by the 1d approximation introduced before.

[2] Not for all structures we are considering here their typical size is associated to the spin interaction. One example of this are the vector solitons discussed in chapter 3. Nevertheless, their size, determined by the method of their generation, is also on the order of ξ_{s}.

2.2.4. Manipulation and Readout

After expanding the atoms in the final trapping potential (WG or with additional box walls) the initial state for investigating the desired dynamics is prepared. For this, we manipulate the atoms by driving transitions within or between the $F = 1$ and $F = 2$ hyperfine manifolds. An overview of these techniques are given in sections 2.4 and 2.6, where also the internal structure of ^{87}Rb is discussed in more detail.

After preparation and a certain period of dynamical evolution we read out the in-situ density distribution of the system using absorption imaging. Because we additionally require internal state resolution this step is regularly preceded by another set of internal state rotations and population transfers.

Further we apply a magnetic field gradient to facilitate a Stern-Gerlach (SG) force on the atoms. After a short (2 ms) period of time-of-flight to separate the different m_F levels, the atoms are illuminated. A first pulse of light is only resonant to atoms in the $F = 2$ state. This is used to read out the $F = 2$ density distribution and remove this species of atoms from the focal plane of the imaging setup. A second pulse contains light with frequencies resonant to both $F = 1$ and $F = 2$, which is used to measure the $F = 1$ density. Relevant details for understanding the measurement of the observables relevant for this thesis are given later in section 2.5. A more comprehensive overview of the imaging setup and its calibration is described in [40, 49].

2.3. The Spin-1 System

In our experiments all levels of the $F = 1$ and $F = 2$ hyperfine levels are relevant. To individually control couplings we apply a homogeneous magnetic bias field of $B = 0.894\,\mathrm{G}$ such that all levels split energetically (see fig. 2.2 and fig. 2.7 for quantitative details on the splitting). While especially for the readout also the $F = 2$ levels are relevant, all dynamics takes place in the $F = 1$ system. In the following we will discuss the theoretical model for spinor gases and a classification of their dynamics.

2.3.1. Symmetries and Operators

The $F = 1$ hyperfine manifold consists of three magnetic sublevels $m_\mathrm{F} = 0, \pm 1$. The state vector of each atom may be characterized by a complex function for each of these levels. Therefore, the space of possible transformations of the system is given by the special unitary group SU(3). For our purposes, a suitable representation of the generators of this group is the spin-quadrupole basis [50, 51]. It conveniently captures the symmetries of the interactions in spinor gases and allows an efficient description of the system dynamics.

The beauty of describing the spinor system in such a basis lies in the realization that SU(3) contains several SU(2) subspaces. This means that there exist triples of spin and quadrupole operators whose commutation relations induce a behavior analogous to the spin operators in a spin-1/2 system. Thus, the time evolution of

expectation values under a Hamiltonian given in terms of these spin or quadrupole operators can directly be understood as rotations around the coordinate axes. The most prominent example of this are, of course, the 3 spin operators which we will denote $\hat{F}_j$ with $j \in \{x, y, z\}$.

However, instead of describing each single atom, a more efficient description is possible in terms of a quantum fields [52]

$$\hat{\psi}_j^{(\dagger)}(x) = \sum_k \hat{a}_{k,j}^{(\dagger)} \zeta_{k,j}(x), \tag{2.7}$$

where $\hat{a}_{k,j}^\dagger$ and $\hat{a}_{k,j}$ are the bosonic creation and annihilation operators and $\zeta_{k,j}(x)$ are the spatial mode functions for atoms with momentum $\hbar k$ in the magnetic substate $m_\mathrm{F} = j$. In contrast to the mean-field description given in section 2.1, these operators capture the full quantum mechanical nature of the system, including quantum fluctuations. Since the atoms are bosons, the operators fulfill the commutation relations

$$\begin{aligned} [\hat{a}_{k,j}, \hat{a}_{k',j'}^\dagger] &= \delta_{kk'}\delta_{jj'}, \\ [\hat{a}_{k,j}, \hat{a}_{k',j'}] &= 0, \end{aligned} \tag{2.8}$$

and therefore

$$\begin{aligned} [\hat{\psi}_j(x), \hat{\psi}_{j'}^\dagger(x')] &= \delta_{jj'}\delta(x - x'), \\ [\hat{\psi}_j(x), \hat{\psi}_{j'}(x')] &= 0. \end{aligned} \tag{2.9}$$

In this language the density operators of the magnetic substates are given by $\hat{n}_j(x) = \hat{\psi}_j^\dagger(x)\hat{\psi}_j(x)$ and the spin operators are expressed as $\hat{F}_j = \hat{\mathbf{\Psi}}^\dagger f_j \hat{\mathbf{\Psi}}$. Here, the vector $\hat{\mathbf{\Psi}} = (\hat{\psi}_{+1}, \hat{\psi}_0, \hat{\psi}_{-1})^T$ describes the full spinor field and the spin-1 matrices are given by

$$f_x = \frac{1}{\sqrt{2}} \begin{pmatrix} 0 & 1 & 0 \\ 1 & 0 & 1 \\ 0 & 1 & 0 \end{pmatrix}, \quad f_y = \frac{i}{\sqrt{2}} \begin{pmatrix} 0 & -1 & 0 \\ 1 & 0 & -1 \\ 0 & 1 & 0 \end{pmatrix}, \quad f_z = \begin{pmatrix} 1 & 0 & 0 \\ 0 & 0 & 0 \\ 0 & 0 & -1 \end{pmatrix}. \tag{2.10}$$

Because in some cases the explicit form of the observables is useful we will also give it here:

$$\begin{aligned} \hat{F}_x &= \frac{1}{\sqrt{2}} \left(\hat{\psi}_0^\dagger \left(\hat{\psi}_{+1} + \hat{\psi}_{-1} \right) + \hat{\psi}_0 \left(\hat{\psi}_{+1}^\dagger + \hat{\psi}_{-1}^\dagger \right) \right), \\ \hat{F}_y &= \frac{i}{\sqrt{2}} \left(\hat{\psi}_0^\dagger \left(\hat{\psi}_{+1} - \hat{\psi}_{-1} \right) + \hat{\psi}_0 \left(\hat{\psi}_{-1}^\dagger - \hat{\psi}_{+1}^\dagger \right) \right), \\ \hat{F}_z &= \hat{\psi}_{+1}^\dagger \hat{\psi}_{+1} - \hat{\psi}_{-1}^\dagger \hat{\psi}_{-1}. \end{aligned} \tag{2.11}$$

As will be described in the following, the inter-atomic interactions and the external magnetic field break the full SU(3) symmetry. For certain parameter regimes we find that the dynamics is predominantly confined to the F_x-F_y plane.

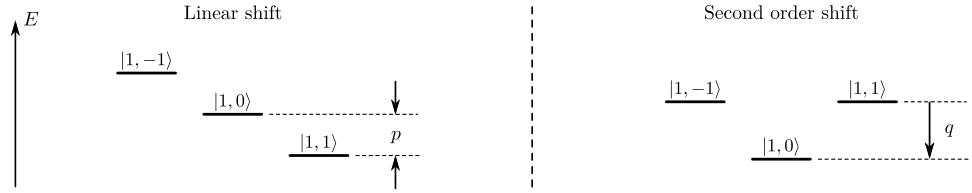

Figure 2.2.: Splitting of the spin-1 hyperfine levels $|F, m_\mathrm{F}\rangle$. p labels the splitting linear in m_F and q denotes the quadratic shift.

2.3.2. Hamiltonian

The microscopic model of spinor gases is well understood and an in-depth description of the models can be found in the reviews [52, 53]. Here, we give a short summary of the description relevant for the experiment.

The energy contributions to the system Hamiltonian $\mathcal{H} = \mathcal{H}_0 + \mathcal{H}_\mathrm{int}$ can be divided into a single-particle term $\mathcal{H}_0$ and inter-particle interactions $\mathcal{H}_\mathrm{int}$. The single-particle terms

$$\mathcal{H}_0 = \int d^3x \; \hat{\mathbf{\Psi}}^\dagger \left(-\frac{\hbar^2 \nabla^2}{2m} + V_\mathrm{ext} + p f_z + q f_z^2 \right) \hat{\mathbf{\Psi}} \tag{2.12}$$

stem from the kinetic energy, the trapping potential V_ext, and shifts of the magnetic hyperfine sublevels. The linear and quadratic contributions p and q (see fig. 2.2) mainly originate from the linear and second order Zeeman shift induced by the homogeneous magnetic offset field, respectively. However, as will be discussed in section 2.4, there are additional contributions to these shifts which are not associated to the magnetic field. Except in a few scenarios where it is explicitly discussed, the linear shift does not influence the dynamics of the system and can be removed by transforming to the co-rotating frame.

As introduced in section 2.1 the low energy interactions in BECs are characterized by s-wave scattering lengths. In spinor BECs, where multiple internal levels couple with different strengths, these scattering lengths $a_\mathcal{F}$ describe the interaction of an atom pair which couples their individual hyperfine spins F to a total spin $\mathcal{F} = -2F, \ldots, 2F$. Due to the bosonic exchange symmetry for the low-energy s-wave scattering only even pair spins interact. Therefore, all interactions in the $F = 1$ manifold are characterized by the scattering lengths a_0 and a_2. From these one obtains the interaction constants

$$c_0 = \frac{4\pi\hbar^2}{m} \frac{a_0 + 2a_2}{3} \qquad \text{and} \qquad c_1 = \frac{4\pi\hbar^2}{m} \frac{a_2 - a_0}{3}, \tag{2.13}$$

where m denotes the atomic mass. Using this representation allows conveniently writing the interaction Hamiltonian of spin-1 gases as

$$\mathcal{H}_\mathrm{int} = \int d^3x \; \frac{c_0}{2} :\hat{n}^2: + \frac{c_1}{2} :\hat{\boldsymbol{F}}^2: \tag{2.14}$$

Here, : : denotes normal ordering of the field operators, the spin operator $\hat{\boldsymbol{F}}$ has already been introduced in section 2.3.1 and $\hat{n} = \hat{n}_{+1} + \hat{n}_0 + \hat{n}_{-1}$ is the total

density operator, where $\hat{n}_j = \hat{\psi}_j^\dagger \hat{\psi}_j$. From this Hamiltonian it becomes clear that c_0 describes the density-density interaction strength and c_1 is only relevant for the spin-spin interactions. As for all stable BECs the density interactions are repulsive ($c_0 > 0$), while the spin interactions are ferromagnetic ($c_1 < 0$).

For ^{87}Rb the ratio between density and spin interaction strength is $|c_0/c_1| \sim 220$ [53]. This implies that also the timescales $t_\mathrm{d} = h/(nc_0) \sim 2\,\mathrm{ms}$ and $t_\mathrm{s} = h/|nc_1| \sim 400\,\mathrm{ms}$ of the density and spin interactions are separated by more than 2 orders of magnitude. This implies that for an adequate description of the total energy, which is precise on the $\sim 1\,\%$ level, the spin interaction term can be neglected. In certain scenarios also the contributions from the external magnetic field can be dropped. Then, on the mean-field level the system may be described by a GPE similar to eq. (2.1). We will explicitly make this connection and discuss the applicability of these approximations in section 3.4.2.

As discussed in section 2.1, an effective 1d description of the system can be derived and as presented in section 2.2 the WG trap provides a sufficiently strong transverse confinement that all spin excitations only appear in axial direction. Thus, it is sufficient to only consider the spatial extension in x-direction along the weakly confined WG axis.

Spin-Changing Collisions

Nevertheless, although the energy scale of the spin interactions is small, under certain conditions their dynamics dominates the system. The most important process connected to this are the spin-changing collisions introduced here. When expanding the spin interaction term $:\hat{\boldsymbol{F}}^2:$ in terms of the fields $\hat{\psi}_j$ it decomposes into two contributions. One can solely be written in terms of the hyperfine densities $\hat{n}_j$, giving rise to energy shifts, which only depend on the population of the different hyperfine levels. More interestingly, the second contribution is $\hat{\psi}_{+1}^\dagger \hat{\psi}_{-1}^\dagger \hat{\psi}_0 \hat{\psi}_0 + \mathrm{h.c.}$, which gives rise to a redistribution of populations between the hyperfine levels. This spin-changing collision (SCC) process redistributes two atoms in level $m_\mathrm{F} = 0$ to $m_\mathrm{F} = \pm 1$ and vice versa (cf. fig. 2.7). Since this redistribution is symmetric in m_F, the SCCs are not influenced by the linear Zeeman shift of the external field. However, the second-order shift detunes this process such that a redistribution of population violates energy conservation. Therefore, to tune the energy offset q of this process into resonance, we apply off-resonant microwave (MW) dressing to control the SCCs (see section 2.4.2 for more details).

2.3.3. Bogoliubov Theory and Instabilities

In order to analyze dynamical properties of the system it is desirable to diagonalize the full Hamiltonian. For the full spinor Hamiltonian this is not possible but in certain limits a Bogoliubov transformation can be derived to achieve this goal. A comprehensive set of Bogoliubov transformations and results for the mean-field groundstates of spinor gases are presented in [52, 54]. Throughout this thesis only a few properties of the Bogoliubov solutions are required so this section will only cover the basic idea of the method and the reader is referred to the previously listed references for more details.

The starting point of the diagonalization procedure is the Bogoliubov approximation. It is centered around the assumption that only small fluctuations around a mean-field state of the system are relevant for its dynamics. For the spin-polarized initial conditions in the experiment this assumption is certainly valid because the large populations of these states ensure the validity of the mean-field limit. Therefore, the field operators can be written in terms of a (classical) complex mean field ψ_j and a fluctuating field $\delta\hat{\psi}_j$ as

$$\hat{\psi}_j(x) = \psi_j(x) + \delta\hat{\psi}_j(x). \tag{2.15}$$

Because these fluctuations are small, only terms up to second order in $\delta\hat{\psi}_j$ are kept in the Hamiltonian. As the kinetic term only is diagonal in momentum space, the fields (in a homogeneous system with flat potential) are usually represented in momentum modes

$$\hat{\psi}_j = \frac{1}{\sqrt{V}} \sum_k \hat{a}_{k,j} e^{ikx} \tag{2.16}$$

with system volume V. Here, we assume that the $k = 0$ mode is highly occupied and that therefore the $k = 0$ contribution is given by $\psi_j(x)$. The Bogoliubov transformation then provides a generic method to construct a transformation which diagonalizes the Hamiltonian. This leads to a set of quasi-particle operators $\hat{b}^{(\dagger)}_{k,m}$, where the index m describes the quasi-particle modes instead of the hyperfine levels m_F. For each of these modes an accompanying dispersion relation $\omega_m(k)$ is obtained. The structure of these quasi-particles and dispersion will be used at different points.

For this work the most relevant Bogoliubov dispersion is the one of the polar state (all atoms occupy the $m_\mathrm{F} = 0$ level), which will be used as initial state for most of the measurements discussed here. The Bogoliubov modes relevant for this thesis[3] are related to transverse spin excitations and are given by [52]

$$\hat{b}_{k,\pm1} = -\sqrt{\frac{\varepsilon(k) + q + nc_1 + \hbar\omega(k)}{2\hbar\omega(k)}}\hat{a}_{k,\pm1} + \sqrt{\frac{\varepsilon(k) + q + nc_1 - \hbar\omega(k)}{2\hbar\omega(k)}}\hat{a}^\dagger_{-k,\mp1}, \tag{2.17}$$

where $\varepsilon(k) = \hbar^2k^2/(2m)$ denotes the kinetic energy. These modes are related to excitations in the hyperfine levels $m_\mathrm{F} = \pm1$. Both modes are degenerate and have the dispersion relation

$$\hbar\omega(k) = \sqrt{(\varepsilon(k) + q)\,(\varepsilon(k) + q + 2nc_1)}. \tag{2.18}$$

While these modes give a valuable insight into the dynamics of the system, the most prominent feature is the existence of instabilities. For $q < 2n\,|c_1|$ the dispersion ω becomes imaginary, which gives rise to an exponential growth of these spin modes in time $\propto \exp(-i\omega t) = \exp(\gamma t)$ with $\gamma > 0$. Figure 2.3 shows the dispersion for a range of q values from the stable to the unstable regime. It is visible that for $n\,|c_1| \leq q \leq 2n\,|c_1|$ the most unstable momentum k with the largest growth rate γ is $k_\mathrm{mu} = 0$ while for $q < n\,|c_1|$ the instability range shifts to larger k and below

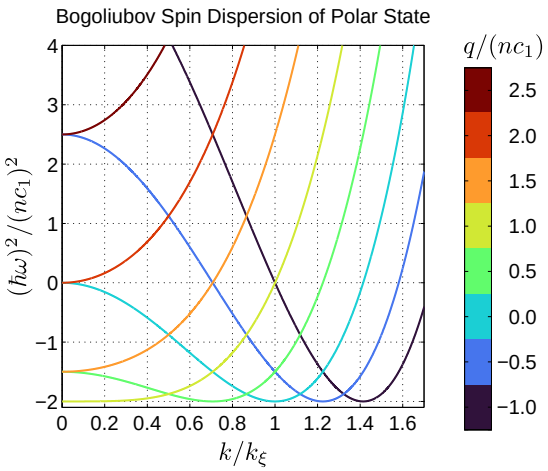

Figure 2.3.: Bogoliubov dispersion relation of the transverse spin modes for the polar state. For $q \leq 2n|c_1|$ this mode becomes unstable where $\omega^2 < 0$. For $n|c_1| \leq q \leq 2n|c_1|$ $k = 0$ has the larges growth rate while the most unstable momentum grows with decreasing $q < n|c_1|$. Below $q = 0$ the $k = 0$ momentum becomes stable again. The k-axis is normalized by the healing momentum $k_{\xi_s} = 1/\xi_s$ with respect to the spin interaction c_1.

$q = n|c_1|/2$ $k = 0$ even becomes stable again.

In the experiments carried out for this thesis this Bogoliubov instability serves as a process to drive the system far from equilibrium by generating a momentum mode occupation which is very distinct from the (thermal) equilibrium distribution. For q in the unstable region the SCC process is resonant and redistributes population between $m_\mathrm{F} = 0$ and $m_\mathrm{F} = \pm 1$. The picture of the Bogoliubov instability is strictly only valid for small excitations around the polar state where the Bogoliubov approximation is still valid. However, in section 4.4 we will see that the Bogoliubov description seemingly provides a good qualitative guide for the generation of even large excitations.

2.3.4. Mean-Field Ground State Phase Diagram

A further central step in understanding the dynamics of spinor BECs is their phase diagram as a function of the parameter q. To derive a basic picture, some simplifying approximations are made. These are assuming the condensate to be "zero-dimensional", i.e. without spatial dynamics (also known as single-mode approximation where only the $k = 0$ mode is considered), and to be well in the mean field limit of large occupation numbers. This allows dropping terms of the interaction Hamiltonian (2.14) which are linear in the density n compared to n^2. We are therefore left with the single-mode mean-field energy per particle

$$\epsilon = V_\mathrm{ext} + p(\rho_{+1} - \rho_{-1}) + q(\rho_{+1} + \rho_{-1}) + \frac{1}{2}nc_0 + \frac{1}{2}nc_1\boldsymbol{F}^2, \tag{2.19}$$

[3] In total there are 3 modes. Additional to the two transverse spin modes there also exist density excitations of the condensate in $m_\mathrm{F} = 0$, which have the usual properties of single-component Bogoliubov modes (see [52]).

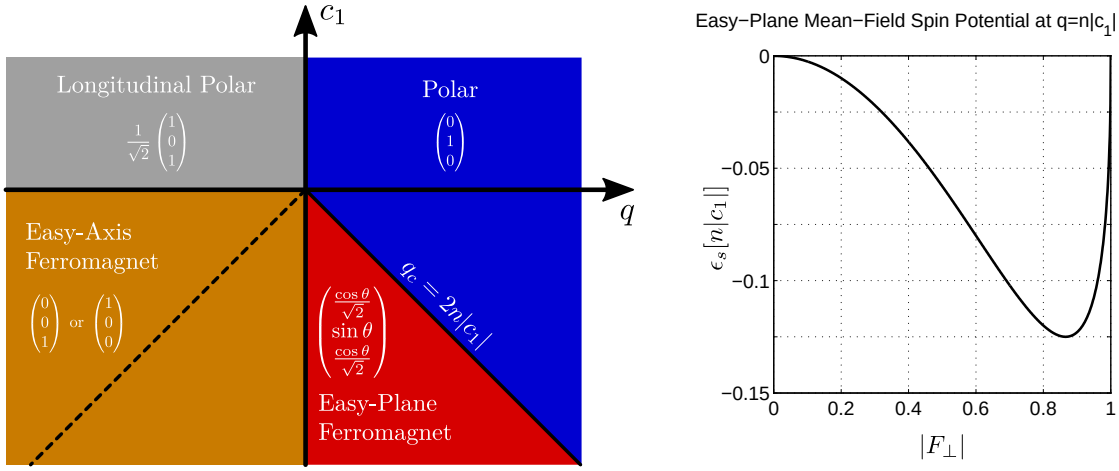

Figure 2.4.: Spin-1 phase diagram (left) and easy-plane phase spin potential (right) in the mean-field single-mode approximation. The vectors in the phase diagram denote the normalized mean-field groundstate spinor wavefunctions. For the experimentally relevant case of ferromagnetic spin interactions ($c_1 < 0$) the spin features 3 different phases. In the EP ferromagnetic phase and for $F_z = 0$ the groundstate has transverse spin according to eq. (2.22). Here, the groundstate populations follow given via eq. (2.21) as $\sin\theta = \sqrt{(1 - q/(2nc_1))/2}$. The dashed line marks the $-q_c$ line; between $-q_c$ and $+q_c$ the minimal energy states for $F_z = 0$ have transverse spin (see discussion of eq. (2.22) for details). Within the EP phase the spin part ϵ_s of the mean-field energy assumes a Mexican-hat shape in the transverse spin plane according to eq. (2.20). An example for a radial cut of this potential is given in the right-hand plot for $q = n\,|c_1|$.

where the mean densities $\rho_j = n_j/N$ are normalized by the total atom number N. Deviating from the introduction of the spin operators but for ease of notation we also interpret the spin expectation values connected to the vector $\boldsymbol{F}$ to be normalized by N to a maximum of 1 in the analogous fashion.

Since we are only considering the case $F_z = 0$ in this thesis and the Hamiltonian conserves the z-projection of the spin, we will drop the linear Zeeman term here. Further, because we are considering a system with stationary density profile, the V_{ext} and nc_0 terms only contribute as constant offset and will therefore also be neglected for the following discussion. Minimizing the resulting energy function with respect to the mean fields results in the groundstate phase diagram shown in fig. 2.4. For the antiferromagnetic interactions $c_1 < 0$ of the $F = 1$ manifold of ^{87}Rb three phases with different spin order are relevant. At large positive q the polar state with all population in $m_{\text{F}} = 0$ has least energy while at large negative q either $m_{\text{F}} = +1$ or $m_{\text{F}} = -1$ are the degenerate groundstates. In between the easy-plane (EP) ferromagnetic phase emerges, where the competition between q and c_1 forces the spin into the F_x-F_y-plane transverse to the external magnetic field. In all cases the ferromagnetic spin interaction always favors the spin length $|\boldsymbol{F}|$ to be as large as possible for the given populations. Within the EP phase the transverse length continuously grows from the continuous quantum phase transition to the polar phase at $q_c = 2n|c_1|$ towards unity at $q = 0$.

To gain some intuition about the system properties in the experimentally relevant EP phase it is useful to reformulate the mean-field energy of eq. (2.19) in terms of the transverse spin. Because we choose $F_z = 0$ in our experiments, the spin contribution may be expressed as[4]

$$\begin{aligned}\epsilon_s &= q\left(\rho_{+1} + \rho_{-1}\right) + \frac{1}{2}nc_1\boldsymbol{F}^2 \\ &= \frac{1}{2}nc_1\left(F_x^2 + F_y^2\right) + \frac{q}{2}\left(1 - \sqrt{1 - \left(F_x^2 + F_y^2\right)}\right).\end{aligned} \tag{2.20}$$

This mean-field energy, which may be pictured as a Mexican-hat-like potential in the transverse spin plane, favors a certain transverse spin length as function of q (see right plot in fig. 2.4) as given by eq. (2.22). This potential has a steep gradient in the radial direction of the transverse spin $F_\perp = F_x + iF_y = |F_\perp|\, e^{i\varphi_\mathrm{L}}$ while the energy along the bottom of the spin potential ϵ_s is flat. This scenario gives rise to two excitation modes: one "massive" (i.e. with quadratic dispersion) Higgs mode and a gappless (i.e. $\omega(k = 0) = 0$) linear Goldstone mode. These correspond approximately to excitations in the transverse length $|F_\perp|$ and the Larmor phase φ_L, respectively (see [52, 54] for more details on the quasi-particle excitations in the EP phase). In the non-equilibrium dynamics following a quench to a q value in the EP phase, the low-energy Goldstone excitations have been identified to drive dynamics [32, 55] close to a NTFP. In chapter 5 we will revisit this scenario and compare it to a case where also the spin length excitations are relevant. For these different cases we will find two distinct NTFPs.

2.3.5. Spin-Changing Collision Spectroscopy Measurements

Due to the second-order Zeeman shift induced by the magnetic offset field, the q parameter of the experiment starts deep in the polar phase at $q \approx 30\, n\, |c_1|$. In typical non-equilibrium experiments the system is suddenly quenched close to $q = 0$ by applying off-resonant MW dressing (for details see section 2.4.2). For the polar state there exist transverse spin modes which become unstable at the phase transition to the EP phase (cf. fig. 2.3). SCCs populate the $m_\mathrm{F} = \pm 1$ levels and the spin interactions lead to a build-up of coherence in the transverse plane if q is in the range of the EP phase (see peak in $|F_\perp|$ in the upper plot of fig. 2.6). A few seconds ($\sim 8t_s$) after the quench we observe that in a certain range of q values SCCs have populated the $m_\mathrm{F} = \pm 1$ levels. Figure 2.5 shows a strong increase of the instability region with density. This can be understood because the critical value $q_c = 2n|c_1|$ for the existence of the Bogoliubov instabilities at $q < q_c$ increases linearly with the density n. From this density shift we can extract an effective value for the spin interactions c_1^eff in our system. To determine q_c for each measured atom number, we fit a linear function to the right edge of the $m_\mathrm{F} = \pm 1$ population and set q_c to the

[4] Let us denote the normalized mean-field spin wavefunctions as ζ_j, such that $\psi_j = \sqrt{n}\zeta_j$. By setting $F_z = 0$ we have $|\zeta_{+1}| = |\zeta_{-1}|$. Because the global phase of the state may be chosen arbitrarily, we set the wavefunction ζ_0 to be real. Thus, we obtain the spin expectation values $F_x = 2\sqrt{2}\zeta_0|\zeta_{+1}|\cos\varphi_\mathrm{L}$ and $F_y = 2\sqrt{2}\zeta_0|\zeta_{+1}|\sin\varphi_\mathrm{L}$ with the Larmor phase φ_L (angle of the transverse spin vector in the F_x-F_y-plane). This also allows expressing the $m_\mathrm{F} = \pm 1$ densities in terms of the transverse spins.

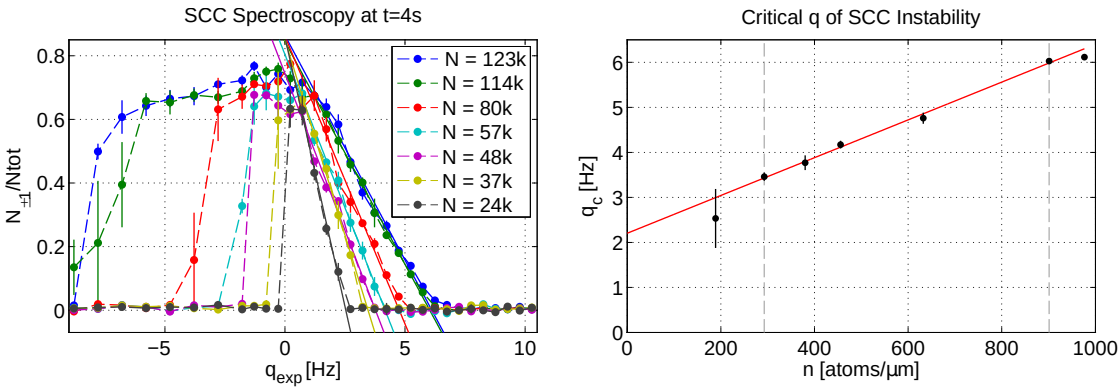

Figure 2.5.: Density dependence of the SCC instability after a quench of the polar state. After preparation of the polar state (all atoms in $m_F = 0$) off-resonant MW dressing is used to instantaneously change the energy detuning q to the experimentally adjusted value q_{exp} (see section 2.4.2 for details on the difference between q and q_{exp}). The left plot shows the relative population of the $m_F = \pm 1$ levels after 4 s of evolution after the quench over the full range of densities applied in the experiments presented in this thesis. From the crossing point of linear fits with the zero line we determine the critical value q_c for the instability for each atom number. The 1d box trap employed in this measurement with a size of approx. 130 µm ensures an approximately flat density over the whole system and thus enables the direct conversion between atom number N and 1d density n. From the linear density dependence of q_c for the Bogoliubov spin dispersion we extract the effective spin interaction strength $c_1^{\text{eff}} = -h \times (2.10 \pm 0.09)\,\text{Hz nm}$. The error bars indicate 1 standard deviation (s.d.) intervals of the mean.

value where the fit crosses the zero line. The values of q_c determined in this fashion increase linearly with the density of the system over most of the experimentally relevant range of densities (see right plot of fig. 2.5). From the gradient of q_c we obtain the effective spin interaction $c_1^{\text{eff}} = -h \times (2.10 \pm 0.09)\,\text{Hz nm}$.

This value is not only effective in the sense that it is a value valid only in our specific quasi-1d trap geometry but it also contains effects from temperature and depletion effects not captured by the Bogoliubov approximation [56, 57]. On the one hand, with increasing temperature q_c is expected to decrease but on the other hand it also grows with increasing depletion at larger densities. Comparing to literature values of the spin interaction [53, 58], the effective value c_1^{eff} for our system lies in the range of (25 – 35) % of the 1d literature values $c_1/(2\pi a_\perp^2)$. Nevertheless, for the application in our experiments this value serves as useful quantity as it contains all effects stemming from the exact trap geometry, temperature and interactions, which are notoriously hard to describe theoretically.

For long times after the quench, when the initial excitations generated by the instabilities have been redistributed, average spin observables show a behavior compatible with the mean-field expectations. In the vicinity of q values expected for the EP phase we find a large transverse spin length. When averaging F_z over the whole cloud we also obtain values close to zero, as expected from the global F_z conservation of the Hamiltonian. For deriving the properties of the minimal energy

state which can be reached by the system, we explicitly impose $F_z = 0$ and stay in the single-mode approximation.[5] To obtain the minimal energy with respect to all sublevels we require the variation of the energy to vanish independent from the m_F level, i.e. $\partial\epsilon_s/\partial\zeta_j = 0$ (ζ_j being the single-mode mean-field spinor wavefunctions of the hyperfine levels).[6] From this the level population and transverse spin length can directly be obtained as

$$\rho_0 = \frac{1}{2} - \frac{q}{4nc_1} \quad \text{and} \tag{2.21}$$

$$|F_\perp| = \sqrt{1 - \left(\frac{q}{2nc_1}\right)^2}. \tag{2.22}$$

Due to the F_z constraint the remaining populations are given by $\rho_{\pm1} = (1-\rho_0)/2$. These equations are valid for $2nc_1 \leq q \leq -2nc_1$ and thus also cover the EP phase (see solid and dashed lines marking $\pm q_c$ in fig. 2.4). Interestingly, the $F_z = 0$ constraint leads to the same EP like structure for $q < 0$ mirrored at the c_1 axis. Note, however, that these equations are only applicable to ferromagnetic systems with $c_1 < 0$.

In order to compare the experimental results with these predictions, we measure the transverse spin length for different q a long time of $t = 30\,\mathrm{s}$ (corresponding to $\geq 45t_s$) after the quench. As initial condition we again apply the polar state. Here, we observe that for experimental values q_exp around zero the transverse spin, averaged over the whole system, follows eq. (2.22) (see the upper plot of fig. 2.6). For comparison between data and the theoretical model we allow for an offset in q and introduce a coherence prefactor which reduces the maximal transverse length from unity (as in eq. (2.22)) to approx. 0.6. The amplitude reduction may be associated to excitations of higher spatial (spin-)modes, finite temperature effects and possibly also due to technical fluctuations of q_exp. Additionally, a small residual F_z magnetization builds up to a level of approx. 0.1, which is associated to a small uncompensated magnetic field gradient. In section 4.3 data will be shown which shows a higher mean spin length, possibly resulting from improvements of some of the previously mentioned points.

Fitting the measured $|F_\perp|$ values in between the blue dashed lines with eq. (2.22) (including the heuristic coherence factor) results in the black line. The points where it becomes zero mark the critical value $\pm q_c = \pm 2n|c_1|$ of the easy plane phase transition. These results are consistent with the value of $n|c_1^\mathrm{eff}| \approx h \times 0.97\,\mathrm{Hz}$

[5] The experimentally investigated system is a quasi-1d box with a size of approx. 130 µm. This corresponds to $\sim 20\xi_s$ such that imposing the single-mode approximation in this scenario does not make sense. Nevertheless, fig. 2.6 shows that the experimentally obtained results for observables averaged over the whole system show quite good agreement with eqs. (2.21) and (2.22) obtained in the single-mode approximation.

[6] For ease of calculation the rotational symmetry of the energy around the z-axis also allows choosing $F_y = 0$. This fixes $\zeta_{+1} = \zeta_{-1}$. When again setting $\zeta_0 \in \mathbb{R}$ the remaining free complex phase φ_S is the one between $\zeta_{\pm1}$ and ζ_0. This phase is called spinor phase and rotates the spin coherences between the transverse spins $F_{x/y}$ and the quadrupoles $Q_{yz/xz}$ (see [51] or [59] for more details on this). For minimizing ϵ_s with $c_1 < 0$ it is thus clear that $\varphi_\mathrm{S} = 0$. This can also be shown explicitly by introducing $\zeta_{\pm1} = \zeta_\mathrm{S} e^{-i\varphi_\mathrm{S}}$ with $\zeta_\mathrm{S} \in \mathbb{R}$ and varying the energy with respect to φ_S.

extracted from the value of c_1^{eff} obtained in fig. 2.5 together with the density of $n \approx 460\,\text{atoms}/\mu\text{m}$ at the time of the measurement (see blue lines). The plot below also shows that the population of the $m_F = 0$ level roughly follows the mean-field expectation of eq. (2.21).

Additional to the averaged observables, the histograms of the transverse spin observables F_x and F_y shown at the bottom of fig. 2.6 give additional insights into the state of the system long after the quench. At large $q_{\text{exp}} \approx h \times 5.2\,\text{Hz}$ where the EP phase transition has not been crossed, no instabilities are present and therefore the system remains in the polar state, as signaled by the large probability to find the state at vanishing spin length. For smaller q_{exp} the Bogoliubov instabilities generate transverse spin through SCCs. With decreasing q_{exp} the spin length grows and in the range $q_{\text{exp}} \approx h \times (1.7 - 2.7)\,\text{Hz}$ a ring builds up. This distribution is consistent with the mean-field Mexican-hat type potential of the transverse spin shown in fig. 2.4. This transition also happens over the range of $2n|c_1|$ expected for the width of the EP phase in the ground state phase diagram (cf. fig. 2.4). Decreasing q_{exp} further, the histograms first fill up in the center and then their width decreases until at large negative q_{exp} the histograms tend towards the one of the polar state, albeit the $m_F = 0$ level is almost unoccupied.

While the evaluation of averaged observables shows quite good agreement with the single-mode mean-field picture of the minimal energy state of the spin-1 system, there are more excitations present in the experiment. The trap in which this measurement has been performed is a 1d box potential with a size of approx. 130 µm, corresponding to ~ 20 spin healing lengths ξ_s.[7] Therefore, the system is far away from the single-mode approximation and indeed, there are also higher spatial modes excited in the spin degree of freedom while the density remains flat.

When comparing the value q_{exp} calculated from the magnetic field and microwave dressing to the q values expected from the mean-field phase diagram for the spin dynamics observed here, the values differ by an offset of $\Delta q_{\text{exp}} \approx h \times 1.7\,\text{Hz}$. This shift may originate from a calibration offset of the microwave dressing (cf. section 2.4.2). The offset Δq_{exp} is also roughly consistent with the offset of q_c at zero density in the right-hand plot of fig. 2.5, further supporting the consistency between the mean-field picture and the spin observables for long times after the quench form the polar state. Note, however, that this behavior does seem to depend on the initial state before the quench. For example, a homogeneous initial condition which is spin-polarized along the x-direction everywhere (i.e. $F_x = 1$) and quenching to values around $q_{\text{exp}} \sim h \times 5\,\text{Hz}$ retains some of its initial spin coherence in the transverse plane even after 30 s of evolution. Thus, the question of the equilibration process after a quench and the eventual final state do seem to depend on the initial state in some way.

2.4. Spin Control

In order to prepare initial states, control the dynamics and read out the desired observables, population transfers and the control of hyperfine sublevel energies are

[7] ξ_s is the healing length according to eq. (2.2) associated to the spin interaction constant c_1.

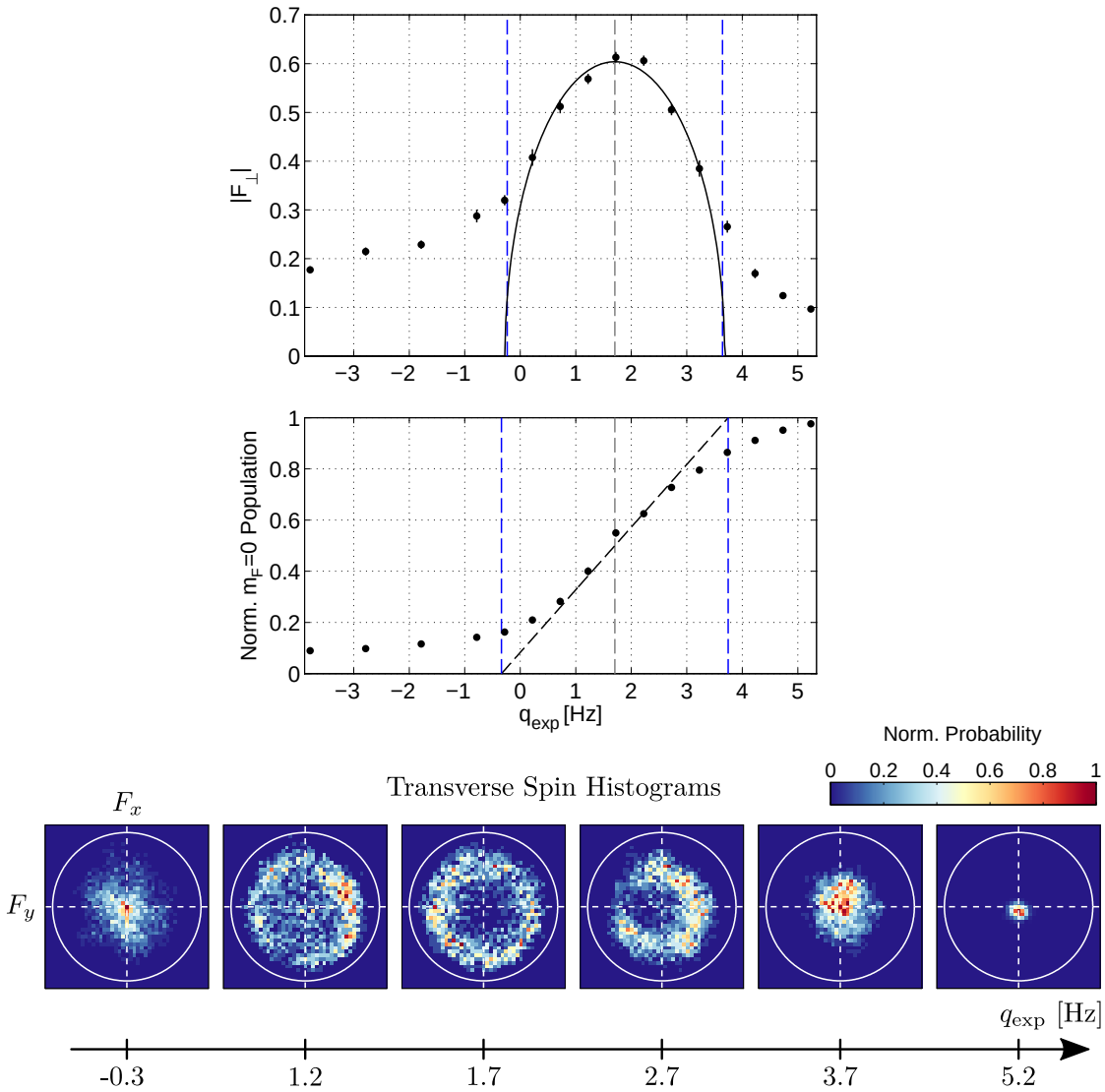

Figure 2.6.: Measurement of the transverse spin and $m_\mathrm{F} = 0$ population after long evolution times of 30 s after a quench in q, starting from the polar state as initial condition. The data points in the upper plot show the transverse spin length $|F_\perp|$ averaged over the size of the 1d box trap with a size of approx. 130 µm. At the time of the measurement the average density is approx. 460 atoms/µm. The black line is a fit of eq. (2.22) with an additional coherence prefactor for the amplitude and an offset Δq_exp along q_exp to the data points between the dashed blue lines. The blue lines indicate the $\pm 2n|c_1^\mathrm{eff}|$ interval around the center $\Delta q_\mathrm{exp} = h \times (1.70 \pm 0.04)$ Hz of the fit, where we use the values c_1^eff extracted from fig. 2.5. The error bars indicate the 1 s.d. interval of the mean. The plot below shows the normalized population N_0/N of the $m_\mathrm{F} = 0$ level. The black line indicates the mean-field values expected from eq. (2.21) with the same parameters as the fit to $|F_\perp|$. The lower plots show histograms of the spin in the F_x-F_y-plane for all positions and (approx. 20) realizations for different values of q_exp of the same measurement. The color indicates the relative probability to find results in the corresponding 2D bin, normalized to unity for comparability between different q_exp.

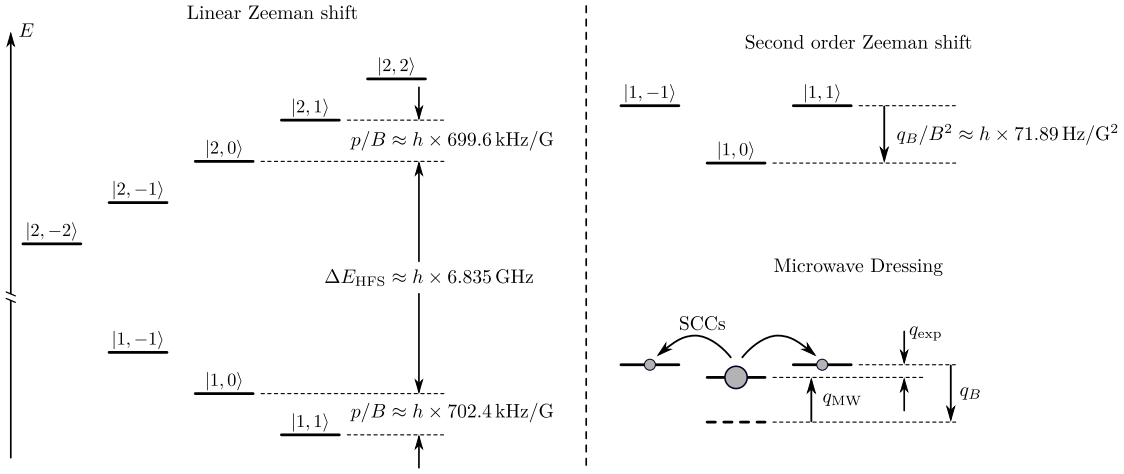

Figure 2.7.: Energy splitting of internal hyperfine levels of ^{87}Rb in a magnetic field. The left-hand side shows the linear splitting of the levels while the right-hand side shows the energy shifts in the co-rotating frame of the Larmor precession. For controlling the parameter q we apply off-resonant microwave dressing (see section 2.4.2 for details) and obtain $q_{\mathrm{exp}} = q_B - q_{\mathrm{MW}}$. For q in the range of the EP phase or smaller SCCs become resonant and redistribute population to $m_{\mathrm{F}} = \pm 1$ when initializing the polar state with all atoms in $m_{\mathrm{F}} = 0$. The energies are obtained from formulas provided in [60].

required. All these techniques can be understood in the standard formulation of coupled 2-level systems. Here, we first give a short overview of the system structure and the basic techniques needed. Building on these, we then assemble the readout schemes required for performing the experiments.

2.4.1. Level Structure

The electronic groundstate of ^{87}Rb features two hyperfine manifolds with total spin $F = 1$ and $F = 2$ (see left-hand side of fig. 2.7). All the dyanmics investigated in this thesis takes place in $F = 1$ but for the preparation, control and readout also the $F = 2$ states need to be accessed.

In the external homogeneous offset field of $B \approx 0.894\,\mathrm{G}$ the magnetic sublevels separate energetically. The linear splitting of the hyperfine levels is the largest energy scale in the system and is determined to good approximation by the linear Zeeman shift $p = g_F \mu_{\mathrm{B}} B$ with Landé g-factor ($g_F = -1/2$ for $F = 1$ and $g_F = 1/2$ for $F = 2$) and Bohr magneton μ_{B}. For the spin dynamic only the much smaller quadratic shift q is relevant (see right-hand side of fig. 2.7). The contribution due to the external magnetic field is $q_B = (g_J - g_I)^2 \mu_{\mathrm{B}}^2 / (16 \Delta E_{\mathrm{HFS}}) B^2$, where ΔE_{HFS} denotes the hyperfine splitting and g_J and g_I are the electronic and nuclear g-factors, respectively. For more details on the calculation of these quantities, see [60].

2.4.2. Microwave Pulses and Dressing

For the initial state preparation and readout, transfers of the atomic populations between sublevels are required. Due to the hyperfine coupling, the $F = 1$ and $F = 2$ states are separated energetically by ΔE_{HFS}, which corresponds to frequencies in the MW range. The corresponding signal at a frequency of around 6.8 GHz required for the coupling between levels these two hyperfine manifolds are generated with two commercial MW generators HP 8673D and HP 83620A. Their signals are combined, amplified and radiated from an antenna close to the atoms. The basic microwave setup is presented in [41]; the few additional modifications relevant for the presented measurements are described in the following.[8] The MW source HP 8673D is used in combination with an external power diode for actively power-stabilized off-resonant dressing. The MW signal of the other source is mixed with an arbitrary waveform generator (AWG) signal (33612A from Keysight Technologies) at around 30 MHz to quickly switch between the different transitions and is the specifically used for short pulses to induce population transfers. For the multiplication of the two signals the IQ-Mixer AD HMC 8193 is used, where both, the in-phase and quadrature inputs are supplied by the two AWG channels. This signal is then fed through an electronic switch (HP 11720A) and an amplifier before it is combined with the MW source for the dressing signal.

In the experiments we apply resonant microwave-frequency pulses which couple two levels $|F = 1, m_{\mathrm{F}}\rangle \leftrightarrow |F = 2, m_{\mathrm{F}} + \Delta m_{\mathrm{F}}\rangle$ with $\Delta m_{\mathrm{F}} = 0, \pm 1$. Using a single-loop antenna (see fig. 2.1) separated by a few centimeters from the atoms we achieve Rabi frequencies on the order of $\Omega \sim 2\pi \times (2-10)$ kHz. The MW radiation contains all polarizations and therefore simultaneously couples all levels but tuning the frequency resonant to a specific linear Zeeman splitting allows selecting the desired transitions. To minimize spatial gradients for the control of the spin dynamics via off-resonant MW dressing, the position of the antenna is adjusted for minimal Rabi frequency gradients. By driving a Rabi oscillation in the WG trap for up to 400 ms we determine our Rabi frequency gradients $\Delta\Omega/\Delta x$ along the cloud to be smaller than

$$
\begin{aligned}
5 \times 10^{-4} \frac{\Omega}{100\,\mu\mathrm{m}} \quad & \text{for } \pi \text{ polarization} \\
1 \times 10^{-2} \frac{\Omega}{100\,\mu\mathrm{m}} \quad & \text{for } \sigma^{+} \text{ polarization} \\
7 \times 10^{-4} \frac{\Omega}{100\,\mu\mathrm{m}} \quad & \text{for } \sigma^{-} \text{ polarization.}
\end{aligned}
$$

Due to lower Rabi frequencies of the σ^{+} the absolute gradient for this polarization is only $\sim 5\times$ larger than for the other polarizations. Nevertheless, for all polarizations the Rabi period is well below the fastest dynamical timescale of the density interaction. Therefore, all manipulation pulses may be regarded as instantaneous with respect to the dynamics.

[8] As described in [61] the MW stabilization setup has also been further modified to allow for a more versatile control of the power. The concept of the stabilization is similar to the previous approach and these changes impact only a few of the measurements presented here.

For controlling the energy detuning q in the experiment we apply off-resonant microwave radiation which is blue-detuned by about $\delta_{\mathrm{mw}} \sim 2\pi \times 300\,\mathrm{kHz}$ to the $|1,0\rangle \leftrightarrow |2,0\rangle$ transition. This shifts the energies of the magnetic sublevels and can be described in the dressed-atom picture by taking into account the dressing contributions from all transitions between the $F = 1$ and $F = 2$ manifolds [62]. In the effective rotating frame of the Larmor precession (see right-hand side of fig. 2.7) the total experimental shift due to the magnetic offset field and microwave dressing can be expressed as

$$q_{\mathrm{exp}} = q_B - q_{\mathrm{mw}}, \tag{2.23}$$

where, in first approximation, the dressing contribution takes a form similar to $q_{\mathrm{mw}} = \hbar\Omega^2/(4\delta_{\mathrm{mw}})$. By adjusting the detuning δ_{mw}, the energy mismatch q can be adjusted conveniently, giving control over the SCC processes particularly relevant in parameter regime of the EP phase (see section 2.3.2). However, due to off-resonant coupling between all pairs of levels between the hyperfine manifolds, all their contributions have to be taken into account for the calculation of q_{mw}, similar to the approach presented in [62]. Drifts of the MW Rabi frequencies on any of these transitions may lead to an offset in q_{exp}, which may explain the discrepancy of q_{exp} observed in fig. 2.6.

2.4.3. Spin Rotations

To rotate the spin vector we utilize oscillating magnetic fields close to the Larmor frequency ω_{L} given by the linear Zeeman splitting ($\omega_{\mathrm{L}} \sim 2\pi \times 630\,\mathrm{kHz}$). For the short coupling pulses $\lesssim 100\,\mu\mathrm{s}$ relevant here, the detuning induced by the second order shift are neglected.[9] In the experiment two magnetic coils are used to generate small oscillating magnetic fields transverse to the offset field. Each of these fields can be vector-decomposed into two counter-rotating fields. One of these co-rotates with the Larmor precession of the transverse spin components while the other one counter-rotates at almost twice this frequency. Therefore, the co-rotating component induces a precession of the spin in the rotating frame while the influence of the other component is negligible due to the large relative oscillation frequency. It is precisely this precession around the co-rotating magnetic field component which drives the spin rotations.

To rigorously derive the spin rotation Hamiltonian, the same approach is followed as is given in [49]. Since the timescale of the spin rotations is much shorter than that of the previously discussed interactions, they can be neglected. Here, we only need to consider the Hamiltonian for the linear Zeeman shift

$$\hat{\mathcal{H}}_B = \hbar\omega_{\mathrm{L}}\hat{F}_z \tag{2.24}$$

and for the transverse oscillating field

$$\hat{\mathcal{H}}_{\mathrm{rf}} = 2\hbar\Omega_{\mathrm{rf}}\cos\left(\omega_{\mathrm{rf}}t + \phi_{\mathrm{rf}}\right)\hat{F}_y, \tag{2.25}$$

[9] These can, however, be treated rigorously and have also been measured in our system. See [49] for details.

which we choose to point in y-direction.[10] Here, the oscillation frequency ω_{rf} of the magnetic field will usually be chosen close to ω_{L} in the experiment and ϕ_{rf} is the phase of the oscillation. Ω_{rf} is the Rabi frequency of the spin rotation, which is equal to the precession rate around the co-rotating field component on resonance ($\omega_{\mathrm{rf}} = \omega_{\mathrm{L}}$). Transforming the total Hamiltonian $\hat{\mathcal{H}} = \hat{\mathcal{H}}_B + \hat{\mathcal{H}}_{\mathrm{rf}}$ into the frame of the transverse field component co-rotating with the Larmor precession we obtain

$$\begin{aligned}\hat{\mathcal{H}}^{\mathrm{rot}} &= \hbar(\omega_{\mathrm{rf}} - \omega_{\mathrm{L}})\hat{F}_z + e^{-i\omega_{\mathrm{rf}}t\hat{F}_z}\hat{\mathcal{H}}_{\mathrm{rf}}e^{i\omega_{\mathrm{rf}}t\hat{F}_z} \\ &= \hbar\delta\hat{F}_z + 2\hbar\Omega_{\mathrm{rf}}\cos\left(\omega_{\mathrm{rf}}t + \phi_{\mathrm{rf}}\right)\left(\cos(\omega_{\mathrm{rf}}t)\hat{F}_y - \sin(\omega_{\mathrm{rf}}t)\hat{F}_x\right) \\ &= \hbar\delta\hat{F}_z + \hbar\Omega_{\mathrm{rf}}\left(\cos(\phi_{\mathrm{rf}})\hat{F}_y + \sin(\phi_{\mathrm{rf}})\hat{F}_x\right),\end{aligned} \tag{2.26}$$

where we have applied the rotating wave approximation [63] in the last line and dropped the quickly oscillating terms with frequency $2\omega_{\mathrm{rf}}$. In the experiment the radio frequency (RF) field is always driven on resonance such that the detuning $\delta = \omega_{\mathrm{rf}} - \omega_{\mathrm{L}} = 0$. Therefore, the magnetic coupling induces spin rotations around a transverse axis controlled by the phase ϕ_{rf}. Typically, the Rabi frequency of this rotation is $\Omega_{\mathrm{rf}} \sim 2\pi \times 7\,\mathrm{kHz}$.

By applying two coils, oriented roughly along both transverse directions (see RF coils 1 and 2 in fig. 2.1), rotating fields can be generated when choosing the driving phases of both coils appropriately. One of these coils is also used to compensate magnetic field gradients along the axis of the cloud. Here, a bias tee consisting of an inductor and a capacitor is used to combine the direct and alternating signal components for the gradient compensation and the RF pulses, respectively.

For rotating magnetic fields the counter-rotating field component present for linearly oscillating coupling can be suppressed. This is relevant in scenarios where both hyperfine manifolds are occupied. Due to the opposite signs of the g-factors, the counter-rotating field for a spin in $F = 1$ is co-rotating in $F = 2$ and vice versa. Because of the small difference in the Larmor frequencies between the two hyperfine levels (see fig. 2.7) compared to the Rabi frequency Ω_{rf} a linearly polarized transverse coupling field leads to simultaneous spin rotations in $F = 1$ and $F = 2$. For our readout scheme hyperfine-selective spin rotations are required, which are generated by circularly polarized coupling fields from the application of two field coils. The treatment of these rotations in the rotating frame is analogous to eq. (2.26) and the orientation of the rotation axis can similarly be adjusted with the phase ϕ_{rf}. A full treatment of the spin rotations in our setup and a characterization of the setup with both RF coils can be found in [49].

2.5. Simultaneous Detection of Multiple Spin Components

For our measurements the transverse spin two sets of observables are of central interest: the hyperfine level occupations and the transverse spin. Both can be

[10] As shown in eq. (2.26) the axis of the spin rotation can be controlled by the phase ϕ_{rf}. Therefore, the actual oscillation direction of the magnetic field in the transverse plane is not crucial.

accessed by standard absorption readout techniques combined with spin rotations. However, to determine the transverse spin also correlations between the length $|F_\perp|$ and the Larmor phase φ_L of the spin need to be measured within the same realization. For this a simultaneous readout of multiple observables is required. A detailed description of this method may be found in [49, 64] and also a short overview of the transverse spin readout is contained in the method section of [65]. Although the simultaneous readout of multiple observables introduces quantum noise, such types of measurements can still be utilized to directly certify entanglement [66].

One of the central benefits of this simultaneous readout is the independence from phase coherence with respect to the preparation. When preparing a transverse spin, for example, the fluctuations of the magnetic offset field will dephase the Larmor phase with respect to the initial direction after $\sim 10\,\mathrm{ms}$. Because the readout effectively utilizes one of the spin directions at the time of the readout as reference for the other observables, correlation can be obtained at arbitrarily long evolution times. Therefore, when observing the system in the parameter regime of the EP ferromagnetic phase we are able to observe transverse spin coherence in excess of 50 s of evolution time with spin coherence times larger than the BEC lifetime.

2.5.1. Imaging

In general, the readout consists of three steps:

i) Spin rotations to map the desired observables on the measurable occupation numbers of the hyperfine levels

ii) Application of a Stern-Gerlach magnetic field gradient to separate the m_F levels by a short ($\sim 2\,\mathrm{ms}$) time-of-flight

iii) High-intensity absorption imaging of the $F = 2$ and $F = 1$ levels with short $15\,\mu\mathrm{s}$ pulses of resonant light spaced by $\sim 1\,\mathrm{ms}$

Details on the imaging method are described in [40] and the calibration procedure of the involved imaging parameters based on the readout of atom shot noise fluctuations is given in [49].

This method allows the extraction of the 1d densities of all 8 hyperfine levels in both manifolds. By summing over the vertical (z-) direction we obtain the averaged density over the size of one pixel along axial (x-) direction of the atom cloud (see fig. 2.1 for the definition of the coordinate system). Because the optical resolution of the imaging system is approx. $1.2\,\mu\mathrm{m}$, for the analysis of density profiles we usually bin 3 pixels along the x-direction. Since the time-of-flight period is kept short enough to only separate the atomic clouds to detect them independently, the technique effectively constitutes an in-situ imaging of the densities. Therefore, our readout effectively extracts coarse-grained values of the observables (averaged over a volume containing ~ 600 atoms, which is given by the width of the binned pixels). This directly resembles the interpretation of fields applied in effective quantum field theories relevant for the description of the non-equilibrium evolution discussed in chapter 5.

2.5.2. General Idea for the Readout of Spin Observables

For the spin observables given in the basis of the external magnetic offset field aligned along z-direction (see section 2.3.1), the F_z value can directly be read out from the level populations. Using again the normalized form of the spin observables, the local z-projection is calculated from the atom numbers N_{m_F} measured in the vertical bin via

$$F_z = \frac{N_{+1} - N_{-1}}{N} \tag{2.27}$$

with the total atom number $N = N_{+1} + N_0 + N_{-1}$. In contrast, the transverse components are additionally encoded in the phase relations (in analogy to quantum optics also called coherences) between the levels. Therefore, a simple $\pi/2$ spin rotation around the F_x or F_y axis prior to imaging maps the observables to the detectable atom numbers.

For the simultaneous detection of multiple spin observables an extension of the Hilbert space is required to encode all necessary information of the observables in level populations.[11] This is facilitated by splitting populations between the $F = 1$ and initially empty $F = 2$ manifold by the application of MW $\pi/2$-pulses. The exact schemes for the relevant sets of observables are detailed in the following.

2.5.3. Transverse Spin

To obtain full information about the length $|F_\perp|$ and Larmor phase φ_L of the spin in the transverse plane it is necessary to read out both transverse projections F_x and F_y. This, in turn, allows constructing the full order-parameter field $F_\perp = F_x + iF_y$ of the EP ferromagnetic phase. This is also the central quantity for the investigation of far-from equilibrium dynamics following quenches of q (cf. chapters 4 and 5).

The readout sequence is given in fig. 2.8. It starts with a $\pi/2$ spin rotation around F_y to map the F_x projection to the population imbalance between $m_\mathrm{F} = \pm 1$. Then all three level populations are split with MW $\pi/2$-pulses, which shelve half of the populations in the $F = 2$ manifold. Afterwards, another $\pi/2$ spin rotation around the F_x-axis maps the F_y projection of the state to the population imbalance (this is the last pulse shown in the figure). For this RF pulse it is crucial that only the $F = 1$ manifold is addressed to preserve the observable shelved in $F = 2$. Thus, by measuring the imbalances in $F = 1$ and $F = 2$ the projections F_y and F_x are extracted, respectively:

$$\begin{aligned} F_x &= \frac{N_{2,+1} - N_{2,-1}}{N_{2,+1} + N_{2,0} + N_{2,-1}}, \\ F_y &= \frac{N_{1,+1} - N_{1,-1}}{N_{1,+1} + N_{1,0} + N_{1,-1}}, \end{aligned} \tag{2.28}$$

where N_{F,m_F} denotes the occupation of the magnetic sublevel $|F, m_\mathrm{F}\rangle$. In order to minimize errors in the projection angle of the extracted observables, which stem from small drifts of the magnetic field or gradients, a spin echo sequence is

[11] The basic idea of this scheme is more generally connected to the concept of positive operator-valued measures (POVMs). See [49, 64] for more details.

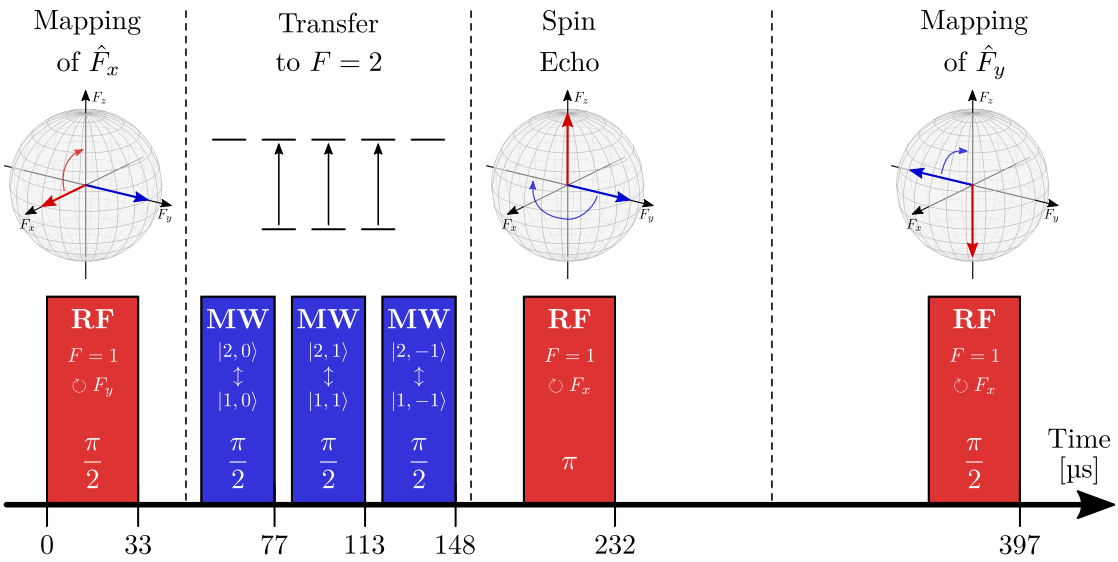

Figure 2.8.: Pulse sequence for the simulataneous readout of both transverse spin-1 observables F_x and F_y. The observables are extracted from the populations via eq. (2.28)

performed. For this, a π spin rotation is inserted in the middle of the time interval between the $\pi/2$-pulses, which cancels the effect of the Larmor phase evolution between these $\pi/2$-pulses.

2.5.4. All 3 Spin-Dipole Operators

The transverse spin readout can straightforwardly be extended to also include the z-projection. Prior to the first spin rotation a quarter of the population of the $|1, \pm 1\rangle$ levels is shelved in $|2, \pm 1\rangle$, followed by a similar readout scheme as described in the previous section (see fig. 2.9 for the full pulse sequence). However, because the populations before the spin rotations have been altered, now the transverse spin observables are not simply given by the population imbalances anymore. To determine the proper combination of the populations required to extract the desired observables, the readout transformations applied to the combined 8-level system of both hyperfine manifolds needs to be considered. This way the explicit encoding of the final state populations after the readout pulse sequence in terms of the spin observables of the system prior to readout can be derived. The resulting spin

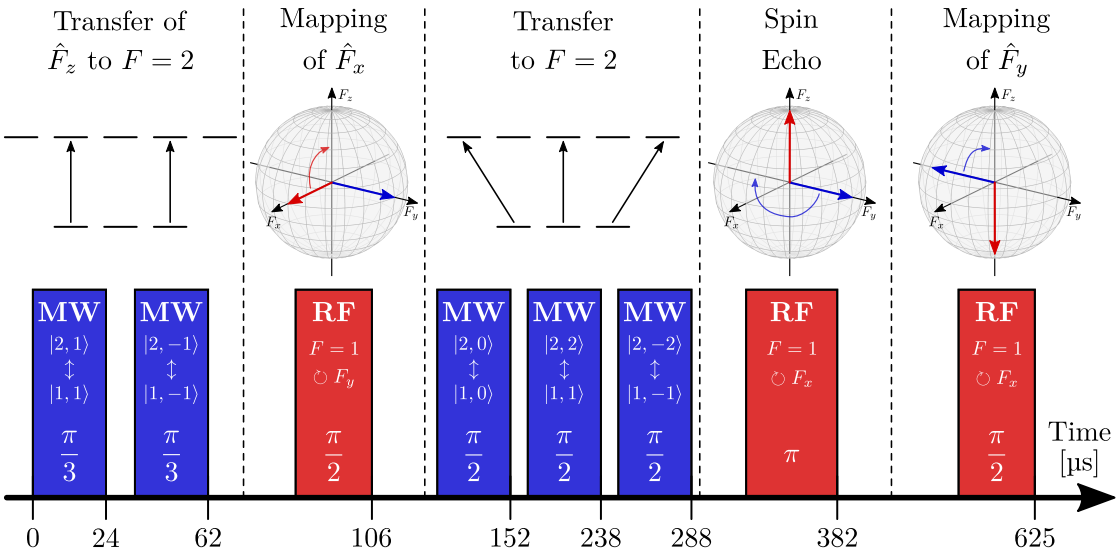

Figure 2.9.: Pulse sequence for the simultaneous readout of all three spin-1 observables F_x, F_y, and F_z. The observables are extracted from the populations via eq. (2.29)

observables are then given by (see [49] for the actual form of the mapping[12])

$$\begin{aligned} F_x &= \frac{4}{\sqrt{3}} \frac{N_{2,-2} - N_{2,+2}}{N}, \\ F_y &= \frac{4}{\sqrt{3}} \frac{N_{1,-1} - N_{1,+1}}{N}, \\ F_z &= \frac{1}{4} \frac{N_{2,+1} - N_{2,-1}}{N}. \end{aligned} \tag{2.29}$$

Here, N_{F,m_F} denotes the occupation of the magnetic sublevel $|F, m_\mathrm{F}\rangle$ and $N = \sum_{F,m_\mathrm{F}} N_{F,m_\mathrm{F}}$ is the total atom number (in the corresponding evaluation interval).

2.5.5. 2-Level Spin

For characterizing the vector solitons discussed in chapter 3 it will be relevant to access the coherences between the two states $|1, \pm 1\rangle$. Interpreting these levels as pseudo-spin-1/2 system, the corresponding spin operators can be written in the form

$$\begin{aligned} \hat{S}_x &= \hat{\psi}_{+1}^\dagger \hat{\psi}_{-1} + \hat{\psi}_{-1}^\dagger \hat{\psi}_{+1}, \\ \hat{S}_y &= i \left(\hat{\psi}_{-1}^\dagger \hat{\psi}_{+1} - \hat{\psi}_{+1}^\dagger \hat{\psi}_{-1} \right), \\ \hat{S}_z &= \hat{\psi}_{+1}^\dagger \hat{\psi}_{+1} - \hat{\psi}_{-1}^\dagger \hat{\psi}_{-1}, \end{aligned} \tag{2.30}$$

[12] The mapping between populations (or POVM elements) and spin observables is given in appendix B.1 of [49]. The splitting ratio of the first two MW $\pi/3$-pulses is $\eta = 1/4$. Note that in [49] the $F = 1$ spin operators are denoted by $\hat{S}_j$ instead of $\hat{F}_j$. Due to the additional RF π-pulse of the spin echo the sign of the S_y terms is flipped for the $F = 1$ observables.

with the field operators $\hat{\psi}_j^{(\dagger)}$ of the magnetic substates introduced in section 2.3.1. Similarly to the spin-1 variables, in the following we will consider the quantities which are normalized by the population $N_{+1} + N_{-1}$ of the two levels.

While the previously extracted spin-1 observables $\hat{F}_x$ and $\hat{F}_y$ also contain information about these 2-level coherences, the phase relation between $m_\mathrm{F} = \pm 1$ and $m_\mathrm{F} = 0$ also enters in $\hat{F}_{x/y}$ (cf. eq. (2.11)). Therefore, it is necessary to directly couple the $m_\mathrm{F} = \pm 1$ levels for mapping the coherences to the detectable populations. The most straight-forward method to facilitate this coupling would involve an initial removal of all $m_\mathrm{F} = 0$ atoms followed by an RF pulse to implement a pseudo-spin-1/2 rotation. However, we observed that in that case the sharp density structures of the solitons undergo spatial dynamics on time scales of the readout ($\sim 3\,\mathrm{ms}$). This happens because of the loss of repulsive interaction with the background provided by the $m_\mathrm{F} = 0$ component. To suppress such deformation of the $m_\mathrm{F} = \pm 1$ densities as much as possible the readout scheme needs to keep the $m_\mathrm{F} = 0$ component trapped along with the $m_\mathrm{F} = \pm 1$ components, although no information is extracted from the $m_\mathrm{F} = 0$ density. Therefore, these atoms are shelved in $F = 2$ at the start of the readout. Because for the following readout the populations of all three $F = 1$ levels need to be split between the two hyperfine manifolds the initial shelving of the $m_\mathrm{F} = 0$ atoms must take place in $|2, -1\rangle$ (or $|2, +1\rangle$). The frequency of the transition $|1, 0\rangle \leftrightarrow |2, -1\rangle$ is almost equal to $|1, -1\rangle \leftrightarrow |2, 0\rangle$ (cf. fig. 2.7). Therefore, such MW coupling would also affect the $m_\mathrm{F} = -1$ atoms. To prevent this, the first MW π-pulse temporarily transfers the $|1, -1\rangle$ population to $|2, -2\rangle$. After shelving the $m_\mathrm{F} = 0$ atoms, another MW π-pulse brings the $|2, -2\rangle$ population back to $|1, -1\rangle$.[13] At this point the actual mapping of the 2-level spins to the populations begins.

The central idea of the readout is based on the realization that the 2-level observables $\hat{S}_x$ and $\hat{S}_y$ can be written as an observable

$$\hat{\Lambda} = 2\hat{n}_0 - \hat{1} = \hat{\psi}_0^\dagger \hat{\psi}_0 - \left(\hat{\psi}_{+1}^\dagger \hat{\psi}_{+1} + \hat{\psi}_{-1}^\dagger \hat{\psi}_{-1}\right), \tag{2.31}$$

which only depends on populations in the m_F levels, transformed by spin rotations around the transverse spin axis $\hat{F}_{xy}(\alpha) = \cos(\alpha)\hat{F}_x + \sin(\alpha)\hat{F}_y$ as

$$\cos(2\alpha)\hat{S}_x + \sin(2\alpha)\hat{S}_y = \hat{\mathcal{P}}_{\pm 1} \exp\left(i\frac{\pi}{2}\hat{F}_{xy}(\alpha)\right) \hat{\Lambda} \exp\left(-i\frac{\pi}{2}\hat{F}_{xy}(\alpha)\right) \hat{\mathcal{P}}_{\pm 1}. \tag{2.32}$$

Here, $\hat{\mathcal{P}}_{\pm 1}$ denotes the projector on the $m_\mathrm{F} = \pm 1$ states. The action of this operator corresponds to the removal of the $m_\mathrm{F} = 0$ population from the $F = 1$ manifold, as described in the previous paragraph. For $\alpha = 0$ and $\alpha = \pi/4$ we therefore obtain exactly the pseudo-spin observables $\hat{S}_x$ and $\hat{S}_y$ encoded in the detectable densities after a $\pi/2$ spin rotation of the system without the $m_\mathrm{F} = 0$ component. This also shows that the simultaneous extraction of the observables with consecutive RF pulses around different rotations axes is possible analogous to the readout schemes discussed previously.

[13] The two MW π-pulses on $|1, -1\rangle \leftrightarrow |2, -1\rangle$ can introduce a phase offset between the $m_\mathrm{F} = \pm 1$ states, which effectively rotates the state in the S_x-S_y-plane. However, such a rotation can easily be calibrated by changing the phase of the MW pulses or the following RF pulses.

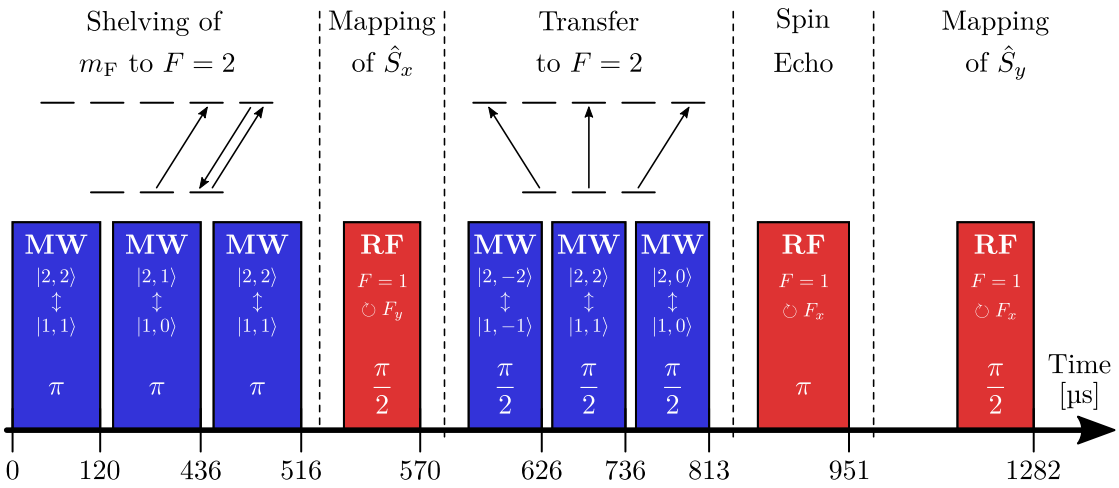

Figure 2.10.: Pulse sequence for the simultaneous readout of the 2-level observables S_x and S_y as defined in eq. (2.30). The observables are extracted from the populations via eq. (2.33)

Here, however, because the rotation axis only needs to be rotated by $\pi/4$ to obtain the conjugate pseudo-spin operator, the amplitude of the rotation angles in the simultaneous readout will be different. For the first spin rotation a $\pi/2$-pulse is performed as given in eq. (2.32) (see fig. 2.10). After shelving half of the $F = 1$ population in $F = 2$ the state in the $F = 1$ manifold is rotated again. Since the readout axes are only separated by $\pi/4$ in the azimuthal angle of the spin-1 operators, also only a $\pi/4$-pulse is required when rotating around a spin axis orthogonal to the first rotation. To cancel any phase evolution induced by the magnetic field between the two RF pulses, again a spin-echo π-pulse is inserted in the readout. After performing this pulse scheme the 2-level spin observables can therefore be extracted from the densities associated to the operator $\hat{\Lambda}$ as

$$\begin{aligned} S_x &= \frac{N_{2,0} - (N_{2,+2} + N_{2,-2})}{N_{2,+2} + N_{2,0} + N_{2,-2}}, \\ S_y &= -\frac{N_{1,0} - (N_{1,+1} + N_{1,-1})}{N_{1,+1} + N_{1,0} + N_{1,-1}}. \end{aligned} \tag{2.33}$$

2.6. Local Control

For the purpose of local control of the spin as well as the total density with spatially arbitrary patterns steerable laser beams at different wavelengths are applied. These act in the form of ac-Stark shifts by modifying the energy of the atomic levels. For circularly polarized light the vector-Stark shift allows the generation of effective magnetic fields which vary spatially on distances corresponding to the size of the laser beam. Additionally, far red- or blue-detuned light facilitates dipole potentials.

The position of these beams are controlled by an acousto-optic deflector (AOD) which is controlled by applying a combination of RF signals. The basic concept of the AOD is similar to that of the more common acousto-optic modulator (AOM):

A piezo transducer driven at $\sim 100\,\mathrm{MHz}$ generates a sound wave in an optically transparent crystal. This can effectively be interpreted as a modulation of the refractive index, which induces effects similar to a grating. In detail, however, the photon-phonon scattering processes relevant for an AOD differ, which lead to a larger bandwidth of frequencies and therefore a larger range of possible deflection angles. This allows controlling the position of the beams via the frequency of the RF tone applied to the piezo transducer. By combining multiple frequency components, also multiple beams are generated in the first scattered order.

In the following a summary of the physical effects relevant for this setup are given, complemented by a detailed description of the optical setup and the required signal generation for controlling the laser beams.

2.6.1. Linear and Vector Stark Shift for Dipole Traps and Magnetic Fields

Although close-to-resonance application of the light is sometimes useful (see section 2.6.4), in this section we want to consider cases in which the light is at least a few nm away from resonance. Therefore, only atom-light interactions described by ac-Stark shifts are relevant.[14] For the groundstate of alkali-metal atoms where the total electron angular momentum quantum number $J = 1/2$ and only the electric dipole contributions are considered, the Stark shift Hamiltonian may be written in the form [67, 68]

$$\hat{\mathcal{H}}_{\mathrm{Stark}} = -\frac{1}{4}\left(\alpha^{\mathrm{s}}(\boldsymbol{E}_1^* \cdot \boldsymbol{E}_2)\hat{1} - \frac{i\alpha^{\mathrm{v}}}{2F}\left(\boldsymbol{E}_1^* \times \boldsymbol{E}_2\right)\hat{\boldsymbol{F}}\right) \tag{2.34}$$

with "classical" electric field components $\boldsymbol{E}_j = E_j \boldsymbol{\mathcal{E}}_j e^{i(\omega_j t + \phi_j)}$ of the light,[15] scalar and vector polarizabilities α^{s} and α^{v} of the atoms, and spin operator $\hat{\boldsymbol{F}} = \hat{\boldsymbol{J}} + \hat{\boldsymbol{I}}$. The polarizabilities include a sum over the transition matrix elements $\left|\langle \mathrm{g}\,|\,\hat{\boldsymbol{d}}\,|\,\mathrm{e}\rangle\right|^2$ with respect to the atomic dipole $\hat{\boldsymbol{d}} = -e\hat{\boldsymbol{r}}$ between the ground and excited states $|\mathrm{g}\rangle$ and $|\mathrm{e}\rangle$, weighed with the distance from the corresponding transition energy (see [67] for details). This form of eq. (2.34), however, is only valid in the limit of small Zeeman shifts and light intensities such that $\langle \mathcal{H}_{\mathrm{Stark}} \rangle \ll \hbar\omega_{\mathrm{L}} \ll E_{\mathrm{HFS}}$. This is well satisfied in the experiment.

There, we apply a single laser beam (i.e. all field components are co-propagating) with the same polarization for all frequency components. While for equally polarized field components the first term of eq. (2.34) only depends on the power and phase of the fields, the second term also involves their polarization. In the experiment the local control laser beams propagate to good approximation along the y-direction. Therefore, the general form of the unit polarization vector for all field components

[14] Obviously, for dipole potentials also off-resonant scattering rates are important. However, in our case these rates are much lower than that of the WG beam trapping the condensate or the atoms are only illuminated for short durations $< 1\,\mathrm{ms}$.

[15] These electric fields may be same ($\boldsymbol{E}_1 = \boldsymbol{E}_2$) or different frequency components of the same or of different laser beams (possibly even propagating in different directions).

takes the form (see e.g. [69])

$$\boldsymbol{\mathcal{E}} = \begin{pmatrix} \cos(\theta) \\ 0 \\ \sin(\theta)\, e^{i\phi} \end{pmatrix}, \tag{2.35}$$

where ϕ determines the phase shift between vertical and horizontal field components and θ specifies the plane of the polarization for purely linearly polarized light.

The scalar ac-Stark shift described by the first term of eq. (2.34) gives rise to the dipole force of far off-resonant radiation employed in dipole traps. In the dressed atom picture [70], for a light field far-detuned by the frequency $\delta = \omega - \omega_\mathrm{r}$ from the transition at ω_r this term can analogously be obtained as

$$\Delta^\mathrm{s} = \frac{\Omega^2}{4\delta} \tag{2.36}$$

with Rabi frequency Ω in the limit $\delta \gg \Omega$. Thus, for red-detuned light ($\delta < 0$) an attractive and for blue-detuned light ($\delta > 0$) a repulsive dipole force is obtained.

The second term of eq. (2.34) describes the vector-Stark shift. Its energy contribution is proportional to the magnetic quantum number m_F and can be cast into the form of a Zeeman shift

$$\hbar\Delta^\mathrm{v} = g_F \mu_\mathrm{B} \boldsymbol{F} \boldsymbol{B}^\mathrm{fict} \tag{2.37}$$

with the light-induced fictitious magnetic field

$$\boldsymbol{B}^\mathrm{fict} = \frac{\alpha^\mathrm{v}}{8 g_F \mu_\mathrm{B} F}\, i\boldsymbol{E}_1^* \times \boldsymbol{E}_2. \tag{2.38}$$

Note that this field is not connected to the magnetic field of the light but stems from the interaction between the electric atomic dipole and the electric field of the light. The fictitious field is parallel to the propagation direction of the light and, in case of equally polarized and co-propagating field components, it is maximal for circularly polarized light (i.e. $\phi = \pm\pi/2$ and $\theta = \pi/4$). This becomes obvious when calculating

$$i\boldsymbol{\mathcal{E}}^* \times \boldsymbol{\mathcal{E}} = \sin(2\theta)\sin(\phi) \begin{pmatrix} 0 \\ 1 \\ 0 \end{pmatrix}. \tag{2.39}$$

For linearly polarized light, i.e. $\sin(2\theta)\sin(\phi) = 0$, the magnetic field completely vanishes.[16]

To obtain purely magnetic fields it is necessary to choose the wavelength of the light such that the scalar shift vanishes. This occurs at a wavelength where the red- and blue-detuned Stark shifts of the neighboring lines (here the D_1 and D_2-line) cancel each other. The specific point is called tune-out wavelength and for the $F = 1$ manifold of ^{87}Rb this occurs at approx. 790.018 nm [71–74].[17] Thus, for

[16] Therefore, to prevent relative shifts of the m_F levels dipole traps for spinor gases should not contain circular polarization components.

[17] Measurements indicate that the value of the scalar tune-out wavelength for the $F = 2$ manifold occurs at a slightly larger value of 790.032 nm [71–73]. For the purpose of generating fictitious magnetic fields in the experiment however, such small differences are not relevant.

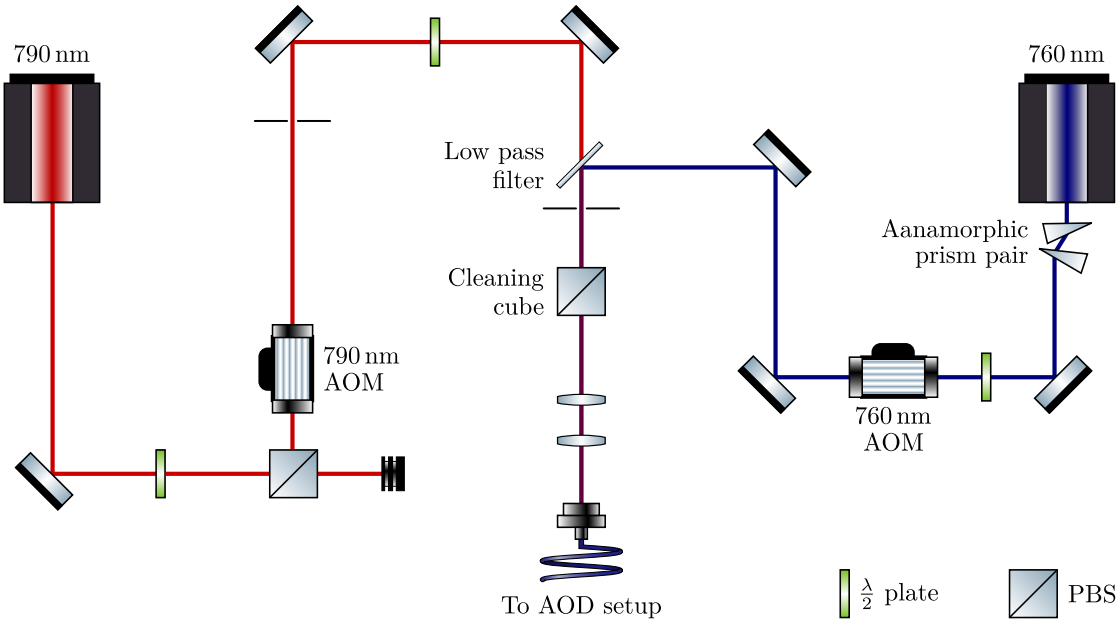

Figure 2.11.: Laser setup for the generating local spin rotations (790 nm light) and blue-detuned potentials (760 nm light). Both beams are combined and delivered to the AOD setup (see fig. 2.14) via fiber, where the laser is steered over the condensate. This figure uses symbols from [75].

optically generating fictitious magnetic fields in our experiment we set the laser close to the tune-out wavelength to prevent density excitations associated to the scalar Stark shifts. This will be used to induce local spin rotations (see section 2.6.6 for details).

2.6.2. Laser Setup

In order to utilize both, the scalar ac-Stark shift for optical traps as well as the vector-Stark shift for generating local spin rotations, two lasers at different frequencies are required. The full optical setup for the generation of the laser utilized for the local control setup is shown in fig. 2.11. For the tune-ability in a wavelength range of $\sim \pm 10\,\mathrm{nm}$ around the Rb D_2-line while maintaining stability of the wavelength, extended cavity diode lasers (DL pro from Toptica Photonics AG) were chosen. The laser for generating the fictitious magnetic field is tuned to the scalar tune-out wavelength close to 790 nm. The other laser, which is intended for generating blue-detuned repulsive potentials, is lasing at 760 nm. This wavelength is chosen to be sufficiently far outside the pass-band of the filters in front of the camera in our system, to block the light during imaging.

Both lasers are passed through AOMs for fast switching and stabilization of their optical power. For the 790 nm light the AOM is additionally used for modulating the beam amplitude at the Larmor frequency ω_L of the spins, which is required for implementing local spin rotations (see fig. 2.12). To ensure the full modulation of the laser a square-wave modulation of the RF signal of the AOM is chosen. Compared to a sinusoidal modulation this induces side-bands at higher harmonic frequencies.

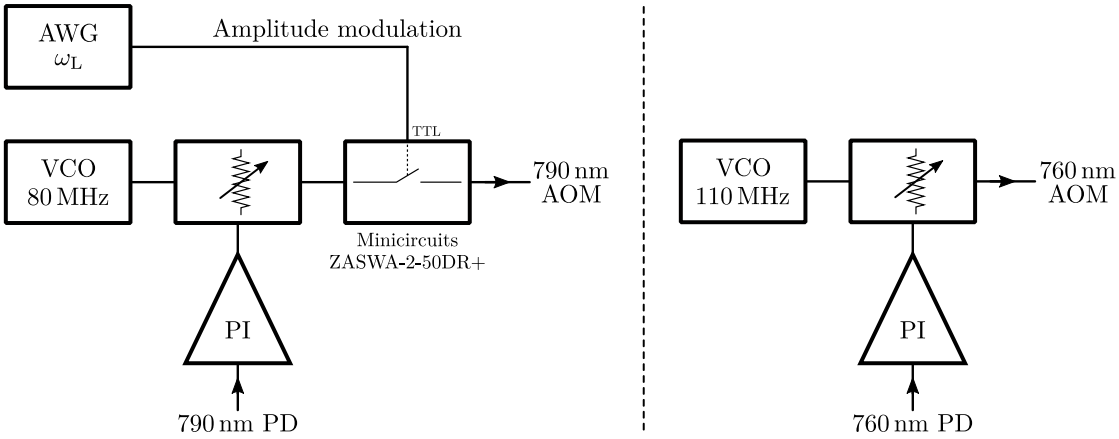

Figure 2.12.: Signal generation for the AOMs of the local control setup shown in fig. 2.11. Feedback from the photodiodes (PDs) in the AOD setup (fig. 2.14) close to the BEC are used to independently stabilize the laser power.

However, these also contribute to the local spin rotations (see appendix A). Since both lasers are driven far from resonance, the shifts of the laser frequencies induced by the AOMs (and also later by the AODs) are irrelevant.

Afterwards both beams are coupled in to the same fiber. To efficiently combine both beams a long pass interference filter (type T 770 LPXR from AHF analysentechnik AG) is utilized. At a certain angle of incidence the 790 nm light is transmitted while most of the 760 nm light is reflected. Here, the filter acts a dichroic mirror, which is used to overlap the beams. This combined beam is then passed through a polarizing beam splitter (PBS) to ensure that both frequency components are linearly polarized along the same axis. Finally, the beam is coupled into a single-mode fiber. The two lenses in front of the fiber implement a reduction telescope which improves this coupling. The fiber transports the light to the AOD setup which is assembled close to the vacuum chamber containing the BEC.

An overview of the setup for the AOM signal generation is shown in fig. 2.12. It includes PI-loops for independently power stabilizing both lasers to photo diodes mounted after the fiber. Additionally, the application of an AWG (model 33612A from Keysight Technologies) allows full control over the phase, amplitude and duration of the 790 nm light modulation.

2.6.3. AOD Setup

For steering the local control laser beam over the condensate a pair of crossed acousto-optic deflectors (AODs) is used. Deflectors are devices which are optimized to modulate the deflection angle of collimated beams. Similar to modulators this is achieved by scattering the light off an acoustic wave of frequency $\omega_a = ck_a$ and wavevector $\boldsymbol{k}_a$ traveling through a crystal, where c denotes the relevant speed of sound (cf. left part of fig. 2.13). To increase the acoustic bandwidth, and therefore also the range of achievable deflection angles, AODs utilize birefringent crystals instead of isotropic media applied in acousto-optic modulators (AOMs). During the scattering of an incident beam with wavevector $\boldsymbol{k}_i$ the light changes

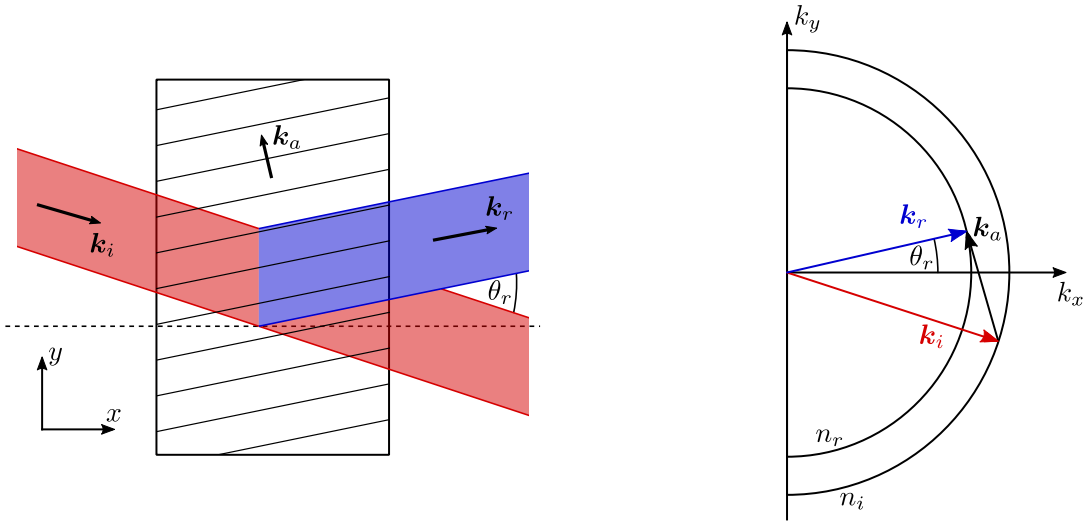

Figure 2.13.: Principle of operation of acousto-optic deflectors (AODs). A linearly polarized light beam with wavevector $\boldsymbol{k}_i$ passes through a birefringent crystal. There, it refracts off the modulation of the index of refraction n_i induced by a sound wave (wave fronts of the sound wave are indicated by black lines). The scattered light has a different polarization, which is associated to a different index of refraction $n_r < n_i$. Due to the corresponding change in the wavelength the refracted wavevector $\boldsymbol{k}_r$ lies on a smaller sphere in the Ewald construction (right). In the scenario where the direction of the acoustic wave with $\boldsymbol{k}_a$ is almost orthogonal to $\boldsymbol{k}_r$ a broad range of acoustic frequencies $\omega_a = ck_a$ fulfills momentum conservation.

its polarization direction. Therefore, the index of refraction n_i experienced by the incoming wave is different from the index $n_r < n_i$ relevant for the outgoing light. Hence, the refracted wavevector $\boldsymbol{k}_r$ is significantly shorter than the inicident one. In the Ewald construction this implies that the vecotrs end on spheres with different radii. If the acoustic wave propagates almost perpendicular to the refracted beam momentum conservation is still approximately fulfilled over a broad range of the acoustic frequencies ω_a. In contrast to AOMs built from isotropic media, the birefringent momentum matching is significantly relaxed in AODs. This broader range of acoustic momenta permissible for scattering processes results in an increased bandwidth and is associated to an extended range of deflection angles θ_r. More details may be found in [69, 76].

The optical setup incorporating the AODs in the experiment has initially been built up and characterized in the scope of a Master's thesis [77]. Since then it has been modified slightly and the full layout is shown in fig. 2.14. The deflectors applied in the experiment are a pair consisting of horizontal and vertical deflector, pre-aligned and mounted onto a metal holder (model DTSXY-400-780 from AA Opto-Electronic). They each consist of TeO_2 crystals in which a shear-mode wave with a speed of sound of $c = 650\,\mathrm{m/s}$ is excited. The usual driving frequency lies in a range of $\sim 100\,\mathrm{MHz} \pm 2\,\mathrm{MHz}$ which is well inside the total bandwidth of $\sim \pm 18\,\mathrm{MHz}$. This range is sufficient to address the whole condensate (extent of approx. $2r_{\mathrm{TF}} \approx 400\,\mu\mathrm{m}$) with a horizontal resolution of $(39.3 \pm 0.2)\,\mu\mathrm{m/MHz}$ on the atoms. While this value has been measured in horizontal direction, from direct

deflection measurements of the AODs we expect the vertical direction to have the same resolution value [77].

Before the local control beam passes through the AODs its polarization is first cleaned by passing through a PBS. Afterwards, a small fraction of its power is diverted onto photodiodes (PDs) (the wavelengths are separated with the same low pass filter as used in the laser setup) by a wedged pick-up quartz plate. Finally, a half-wave plate adjusts the beam polarization to the axis required for the operation of the AODs. At this point the waist radius[18] of the collimated Gaussian beam is 3.8 mm [77]. After deflection by the AODs it passes through a quarter-wave plate to transform the polarization from linear to circular, which is required to utilize fictitious magnetic fields induced by the vector-Stark shift. For focusing the beam on the condensate down to a waist radius of $(7.0 \pm 0.3)\,\mu\text{m}$ (cf. section 2.6.6) we use the imaging objective in reverse direction. To couple the light into the imaging path we apply a pellicle (model BP208 from Thorlabs). This is a membrane with a thickness of 2 µm which has been chosen to prevent a significant offset of the imaging beam, which passes through the pellicle from left to right in fig. 2.14. According to the manufacturer's specifications it reflects approx. 3 % of the light polarized parallel to the plane of incidence and approx. 26 % of the light with perpendicular polarization at 760 nm and 790 nm. Therefore we expect only $\sim 3\,\%$ of the total deflected light to contribute to the vector stark shift. Nevertheless, $\sim 5\,\text{mW}$ in either of the wavelength components at the output of the fiber are sufficient to fully confine the atoms with the dipole force exerted by the 760 nm light or implement spin rotations with a Rabi frequency of $\sim 10\,\text{kHz}$ for the 790 nm component.

To control the deflection angles of the AODs we utilize AWGs (model 33622A[19] from Keysight Technologies) to directly generate the required RF signals at $\sim$ 100 MHz. The advantage of utilizing AWGs lies in the possibility to generate short local rotation pulses by switching on the AOD signals without the requirement of external RF switches, arbitrarily combining frequency components for generating multiple beams, and the possibility to sweep frequencies or amplitudes.[20] In our experiments the local control beams serve two distinct purposes: generating blue-detuned end-caps for a box-like confinement in the center of the WG trap (760 nm light) and performing local spin rotations (790 nm light). Both of these require signals which pose different requirements to the AWG programming. To optimize the signal handling we divide the generation of the signals onto two AWGs which are subsequently combined and amplified before being fed into the AODs.

[18] The waist radius is the distance from the center of a Gaussian beam where the intensity drops to $1/e^2$ of the peak value.

[19] This AWG has two independent output channels capable of replaying 120 MHz signals at a maximal sample rate of 1 GHz with a waveform memory of 64 MSa per channel (device option MEM).

[20] For sweeps over extended periods of time, however, the sample memory of the devices is not sufficient. For this, the integrated frequency or amplitude modulation of the function generator mode may be used in combination with an external AWG which provides the modulation waveform (at significantly lower sample rate).

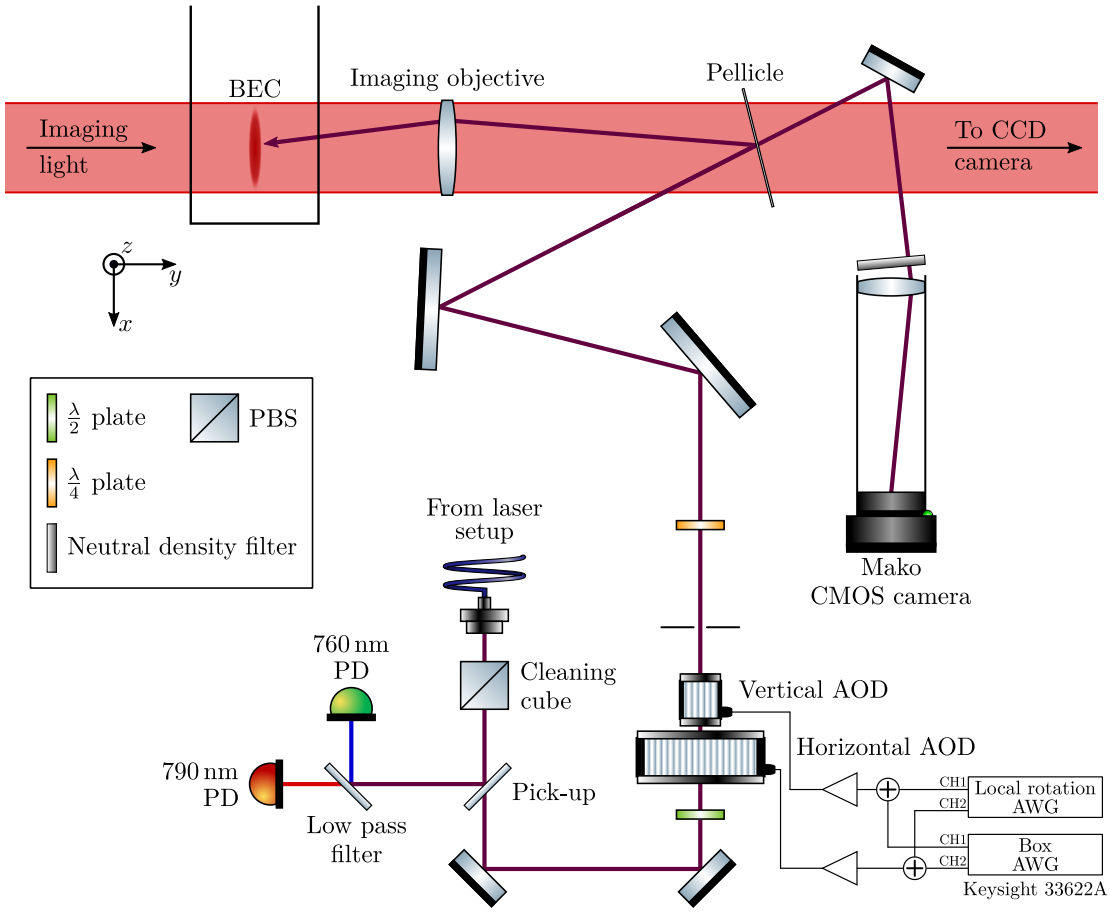

Figure 2.14.: Setup for steering the local control beams over the condensate with the application of two crossed AODs. Two wavelength components at 760 nm and 790 nm are used for blue-detuned potentials (e.g. for confinement in a box-like potential) and local spin rotations, respectively. They are generated in the laser setup shown in fig. 2.11 and delivered to this part by fiber. A small portion of the optical power is directed towards photodiodes (PDs) for power stabilization. The optical low-pass filter acts as dichroic mirror, as described in section 2.6.2. The collimated beam with a waist radius of 3.8 mm is deflected in horizontal and vertical direction by the AODs and is focused on the condensate by the imaging objective with focal length of 31.23 mm [40]. This results in a waist radius of (7.0 ± 0.3) µm on the atoms with a spatial sensitivity of (39.3 ± 0.2) µm/MHz to the frequency of the RF signal delivered to the AODs. This figure uses symbols from [75].

2.6.4. Alignment and Characterization

Due to the small size of the condensate compared to the full accessible scan range of the AODs the initial alignment of the local control beams to the atoms is difficult. The most convenient method of "finding" the correct AOD frequencies tuned out to be locally detuning a MW π-pulse. For this the 790 nm laser is tuned to the resonance of the D_2-line close to 780.24 nm for the $F = 2 \rightarrow F' = 3$ transition. Here, even small beam powers induce a splitting of the $F = 2$ states sufficiently large to prevent MW transitions with usual Rabi frequencies of ~ 10 kHz. This provides a clear signal when the local control laser overlaps with the cloud, owing to the short interaction time and low power requirements.

The resonance of the scattering with the acoustic waves in the AOD crystal is governed by a modified Bragg condition (see fig. 2.13 for the optimal working condition $\boldsymbol{k}_r \perp \boldsymbol{k}_a$)

$$\sin\theta_r = \frac{\lambda_i}{n_i \lambda_a} \tag{2.40}$$

with acoustic wavelength $\lambda_a = 2\pi/k_a$. Therefore, the deflection angle θ_r has a wavelength dependence similar to a grating. Therefore, different RF frequencies are required to deflect beams with different wavelengths to the same position. This seemingly inconvenient property has two crucial benefits: even lasers with a broad spectrum may be used for the generation of close-resonant potentials[21] (with potentially long hold times) and the local spin rotations can be applied at positions which are, to a certain degree, independent from the box beams.

Figure 2.15 shows the local control beam deflection in an exemplary scenario where two 760 nm beams are required to confine the atoms in a box-like trap (see section 2.6.5 for details) and simultaneously a local rotation is performed with 790 nm light. Due to the dispersive deflection of the AODs this requires two vertical frequency components $f_{\text{AOD-V}}$ to deflect both wavelengths to the plane of the atoms. In horizontal direction two frequencies $f_{\text{AOD-H}}$ are required to generate the two end-caps of the box and a third one to independently place the local rotation in the trap. All these frequency components lead to a deflection of both wavelengths, resulting in a total of 12 deflected beams.[22] As indicated in the figure, only three of these are actually focused onto the condensate. However, due to the horizontal frequency components of the box beams, it is possible that also an additional local rotation beam is deflected to the position of the atoms. For the particular combination of frequencies shown in the picture, the frequency $f_{\text{AOD-H}}$ of the right box wall results in a deflection of a local rotation beam (790 nm) to the position of the left box wall. This means that for a larger box a second local rotation would appear at the left edge of the box. This can of course be suppressed by switching off the box for the short duration (~ 100 µs) of a local rotation without significantly affecting the condensate density.

[21] Using two 780.16 nm beams as end-cap potentials, which are blue-detuned to the D_2-line by only 0.08 nm, we were able to fully contain the atoms in a box trap with atom number lifetimes of more than 40 s. This lifetime is comparable to box-like traps with beams which are blue-detuned by more than 10 nm.

[22] We are only considering the first deflection order of each of the AODs here. In total there are more beams exiting the AODs which are, however, blocked by an iris.

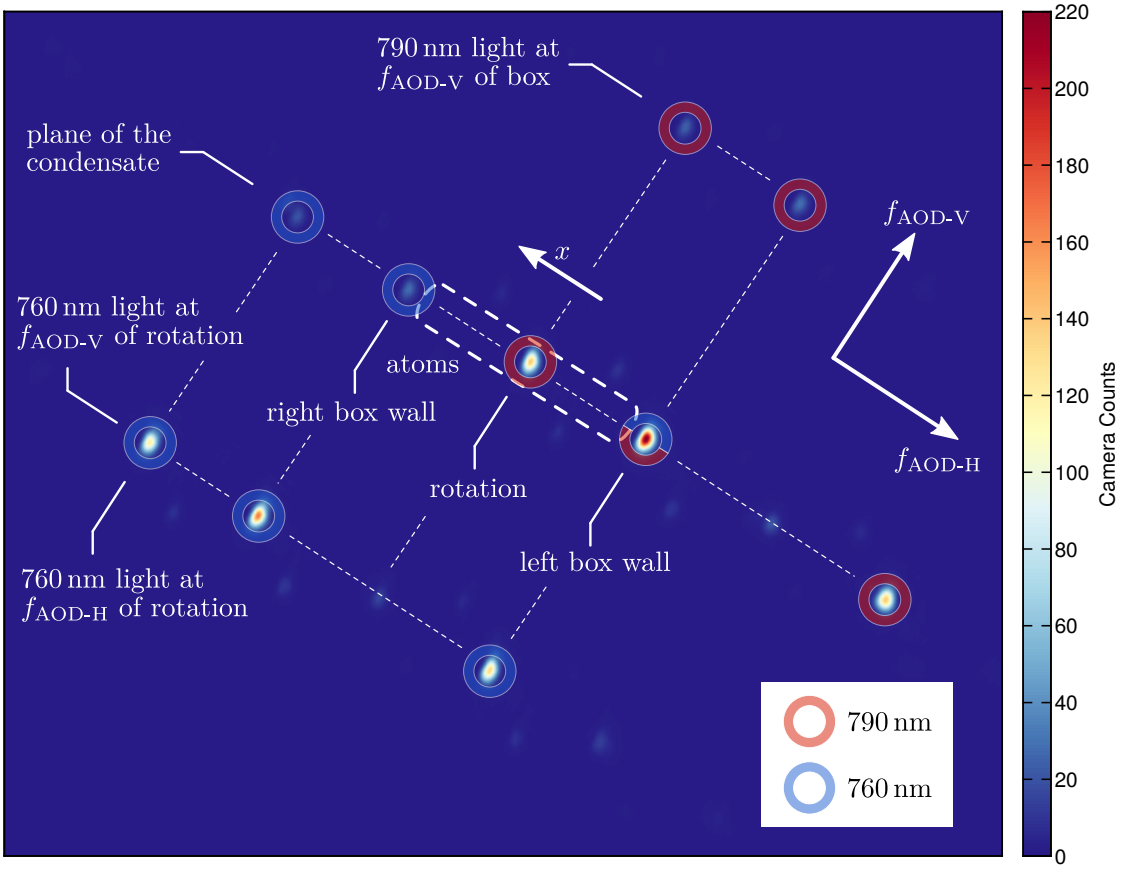

Figure 2.15.: Picture of the local control beams for a scenario with box beams (760 nm) and a local rotation (790 nm) with color-coded intensity. Two frequency components $f_{\text{AOD-V}}$ deflect both wavelengths to the plane of the atoms. For generating the two walls of box-like trap and a local rotation in its center, three horizontal components $f_{\text{AOD-H}}$ are applied. Each wavelength is therefore split into six single beams marked by colored circles (one of the 790 nm beams is not visible in the picture). Note that the camera is mounted at an angle of approx. 33° with respect to the horizontal plane; cf. the coordinate axes, which indicate the direction of the deflection with respect to the applied AOD frequencies f_{AOD} and the physical position x on pictures or the setup. In the depicted scenario one of the 790 nm beams overlaps with the left wall (760 nm) of the box, marked by a split blue and red circle. Additionally, the region which would be occupied by the atoms in the focal plane of the imaging objective is indicated by a dashed contour. The picture is taken by focusing the deflected beams onto the camara (Mako G234B from Allied Vision) shown in fig. 2.14. Note, that the focal position of the lens is not optimized and the measured intensities do not correspond to the distribution at the position of the condensate.

Due to excessive polarization drifts in the fiber between laser and AOD setups the intensity fluctuations of the local control beams initially were on the order of $\sim 10\,\%$. By implementing a power regulation with photodiodes in front of the AODs these fluctuations have been significantly reduced. For the short local spin rotations pulses a sample-and-hold circuit (see fig. 2.12) is applied, which updates the regulation values after imaging and applies the stored values during the next experimental cycle approx. 40 s later. This approach leads to residual relative fluctuations of 0.004 in the 790 nm beam power. The fluctuations of single deflection orders imaged by the observation CMOS camera (Mako from Allied Vision) are of similar size, implying that the beam power at the condensate should be stabilized to the same level. The stabilization may be further improved by sampling the regulation signal shortly before the experiment. To prevent illuminating the atoms during the short regulation period of ~ 10 ms the RF signals to the AODs should be switched off. This may be implemented by an RF switch in front of the AOD signal amplifiers.

Additionally to amplitude fluctuations, also position noise may be induced by mechanical vibrations in the system. In the setup shown in fig. 2.14 this may become problematic because the distance of ~ 1 m between the AODs and the imaging objective may strongly amplify any vibrations of the optical components. For short coupling pulses (see section 2.6.6) with a typical time scale of $< 100\,\mu$s this would manifest as position fluctuations of the coupling region between realizations because mechanical oscillations of massive objects would be expected to occur in the frequency range $<$ kHz. However, the setup shows excellent positional stability with typical standard deviations of only about 0.4 µm, less than 10 % of the waist radius of the local control beam. Nevertheless, temperature drifts lead to significant deviations in the beam position, such that appropriately spaced control scans should be executed to account for such drifts in both, horizontal and vertical direction.

2.6.5. Box Trap

In the experimental setup the atoms are usually confined in the attractive dipole-potential of the WG beam, which provides an elongated cigar-shaped trap. By combining it with two blue-detuned local control beams, which serve as repulsive end-caps, the atoms can be confined in the approximately flat center of the WG potential. This effectively implements a box trap [78].

For loading this box we slowly ramp down the XDT beam and let the atoms expand in the WG potential until they fill out the whole box. The time evolution of the density profiles during this process are shown in fig. 2.16. Here, $t = 0$ indicates the usual time at which the initial state preparation starts; this coincides with the point when the density profile settles to the final shape. For $t > 0$ the density is approximately flat and only shows small short-range deviations around this profile. Because these short-wavelength deviations persist over many times t is can be excluded that they resemble propagating sound waves but rather originate from slight modulations in the WG potential along its beam axis.

While the right edge of the box shows a sharp gradient in the density profile,

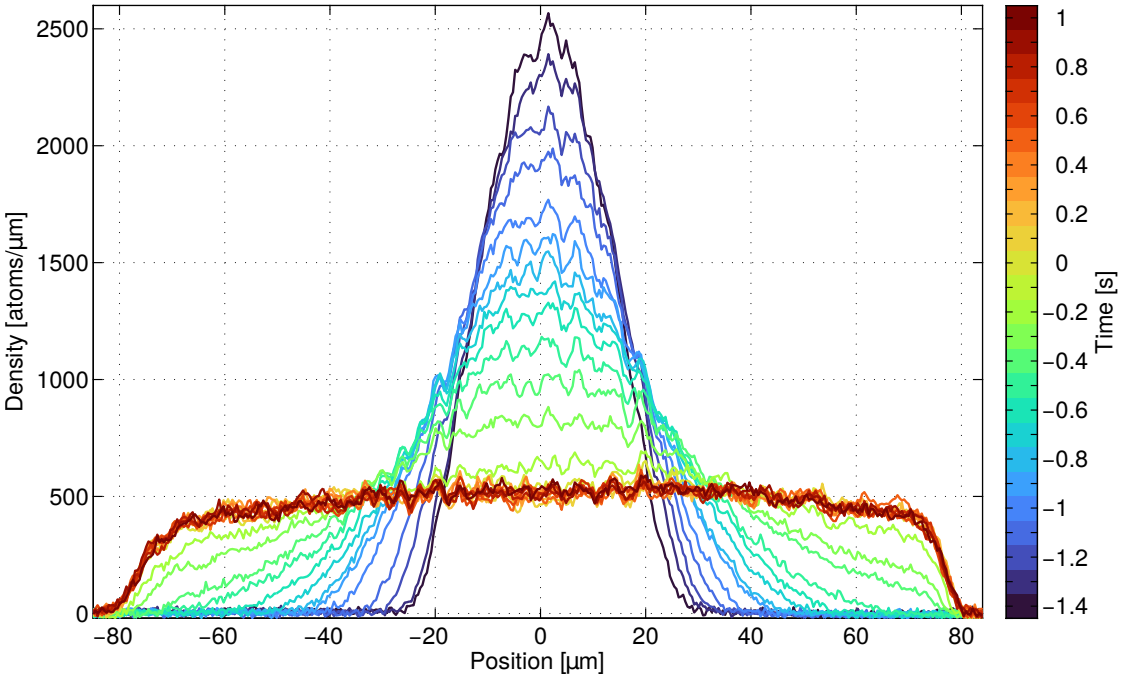

Figure 2.16.: Density profiles (averaged over 1 – 3 realizations) during the loading process of the box trap for an atom number of $\sim 70\,\mathrm{k}$. While slowly ramping down the XDT potential the atoms expand in the WG until the full region between the blue-detuned local control beams are occupied by the atoms. The time $t = 0$ indicates the point when experiments usually start. No spatial dynamics is visible after loading the box-like trap. The profile for $t = -0.1\,\mathrm{s}$ is missing.

the left edge is much broader. This results from an imbalance in the optical power of both box walls; in the particular case shown in fig. 2.16, the right beam is less intense than the left one. The condensate density expands in the confining trap to the point where the external potential corresponds to the chemical potential: $V_{\mathrm{ext}}(x) = \mu$. This implies that only the spatial region of the potential where $V_{\mathrm{ext}}(x) < \mu$ determines the density profile. According to eq. (2.34) the potential of the blue-detuned box walls has the Gaussian shape of the laser beam intensity. Therefore, at large beam powers the density only occupies the region of small gradient farther away from the center. Contrary, for small power the region of large gradients closer to the maximum dominate and lead to a sharper density drop-off at the edges. These gradients become largest when choosing the peak power I_p such that the chemical potential crosses the dipole potential of the beam around the inflection points of the intensity profile. This implies $I_p = \sqrt{e}\mu \approx 1.6\mu$. Choosing these parameters also ensures that despite small intensity fluctuations of the beam or variations of the atom number tunneling out of the box-like trap is still sufficiently suppressed.

Because a part of the experiments presented in chapters 4 and 5 take place over vastly different durations (0 – 40) s it is crucial to take the heating of the AOD crystal due to the dissipation of the applied RF power into consideration. This leads to a slight change in the refractive index and therefore to a change of the deflection angle over time. Especially in vertical direction this effect is important because the beam needs to be aligned to the position of the condensate with a radius of $\sim 2\,\mu\mathrm{m}$ (estimated in TF approximation for $n = 400\,\mathrm{atoms}/\mu\mathrm{m}$). The main heating contribution to the AOD is provided by the deflection signal for the box beams (760 nm) because these are active for the full duration of the experiment after loading the dipole traps. In contrast, the short spin rotation pulses are usually active for a duration shorter than 1 ms and therefore only dissipate a vanishing amount of energy in the AODs. To avoid drifts associated to changes in heating we continuously apply the box frequencies to the AODs, even during the cooling cycle and when no 760 nm light is applied to the atoms.

2.6.6. Spin Rotations

Analogous to the treatment of spin rotations in section 2.4.3 the fictitious magnetic field induced by the vector-Stark shift can be applied to generate spin rotations locally. For this, oscillating magnetic fields are required. These are generated by an amplitude modulation of the local control laser at frequency ω_{rf}.[23] This leads to the generation of different frequency components in the electric field of the local control beam. For simplicity, the electric field $\boldsymbol{E} = \boldsymbol{E}_1 + \boldsymbol{E}_2$ of the light is considered

[23] The modulation is performed by digitally switching the RF signal applied to the 790 nm AOM (cf. figs. 2.11 and 2.12). This leads to a square-wave modulation of the laser amplitude, giving rise to multiple frequency components separated by ω_{rf}. According to eq. (2.41) the closest Fourier components of this spectrum therefore contribute to the oscillating fictitious field $\boldsymbol{B}_{\mathrm{rf}}^{\mathrm{fict}}$ at frequency $\Delta\omega = \omega_{\mathrm{rf}}$. This coincides with the sine modulation assumed in eq. (2.25). All higher frequency differences are sufficiently far detuned from the resonance at ω_{L} to be neglected within the scope of the rotating wave approximation. See appendix A for more details.

to consist only of two equally polarized frequency components $\boldsymbol{E}_1 = E_1\boldsymbol{\mathcal{E}}e^{i(\omega t+\phi)}$ and $\boldsymbol{E}_2 = E_2\boldsymbol{\mathcal{E}}e^{i((\omega+\Delta\omega)t+\phi+\Delta\phi)}$ with real amplitudes E_j and frequency separation $\Delta\omega = \omega_{\mathrm{rf}}$. According to eq. (2.38) the fictitious magnetic field is given by

$$\boldsymbol{B}^{\mathrm{fict}} \propto i\boldsymbol{E}^* \times \boldsymbol{E} = \left(E_1^2 + E_2^2 + 2E_1E_2\cos\left(\Delta\omega + \Delta\phi\right)\right)\boldsymbol{e}_y, \tag{2.41}$$

with unit vector $\boldsymbol{e}_y$ pointing in y-direction and where we assumed circularly polarized light and applied eq. (2.39). The cross products with the same frequency components give rise to a static fictitious field $\boldsymbol{B}_0^{\mathrm{fict}}$ while all pairs of different frequency components contribute fields $\boldsymbol{B}_{\mathrm{rf}}^{\mathrm{fict}}$, oscillating at the difference frequency $\Delta\omega$. The fictitious field components oscillating close to resonance (i.e. the Larmor frequency ω_{L}) thus result in a coupling described by the Hamiltonian (2.25). Analogous to before, by changing the phase of the laser amplitude modulation the spin rotation axis is adjusted to an arbitrary angle in the transverse plane in the rotating frame. Note that, contrary to direct optical dipole couplings, for the fictitious magnetic field the Rabi frequency Ω_{RF} is proportional to the optical power of the cross terms $P \propto E_1E_2$.

Alternatively to the picture of oscillating fictitious magnetic fields, this coupling between the magnetic substates may also be interpreted as Raman transitions between the different magnetic substates [68]. The amplitude modulation of the laser beam at frequency ω_{rf} leads to the generation of pairs of side-bands at frequency offset $\pm n\omega_{\mathrm{rf}}$ ($n \in \mathbb{N}$) around the original laser beam frequency (see appendix A for more details on the modulation spectrum). At resonance (i.e. $\omega_{\mathrm{rf}} = \omega_{\mathrm{L}}$) neighboring components with a frequency difference of $\Delta\omega = \omega_{\mathrm{L}}$ thus drive Raman transitions between two states with $\Delta m_{\mathrm{F}} = \pm 1$. This is equivalent to a coupling with the spin operators as given in the spin rotation Hamiltonian (2.26).

This method of coupling the magnetic substates of spinor condensates with off-resonant light has also been applied in different experiments. Similarly to the application presented here, this coupling has been implemented to generate magnon excitations and map out their dispersion [79]. By detuning this coupling from the Raman resonance, these vector-Stark shifts have also been applied to implement an artificial vector potential [80]. Inducing spatial gradients in the vector potential, artificial magnetic fields which couple to neutral atoms have been engineered [81]. These techniques are relevant in the broader context of spin-orbit coupling and artificial gauge fields.

To characterize this local coupling, all atoms are prepared in $m_{\mathrm{F}} = -1$, i.e. in a state with $F_z = -1$. Then a local spin rotation pulse of varying duration t is applied. This coupling leads to a redistribution which transfers atoms to $m_{\mathrm{F}} = 0$ and for larger coupling times to $m_{\mathrm{F}} = +1$. The Rabi frequency profile of this transfer results from the intensity profile of the laser beam. The resulting spatial variation of the population transfer is shown in the absorption pictures in fig. 2.17.

Assuming a Gaussian beam with transverse intensity profile $I \propto \exp(-2x^2/w^2)$ with waist radius w (in the focal plane) the rotation around a transverse spin rotation leads to a spatially varying z-projection

$$F_z(x,t) = -\cos\left(\alpha(t)e^{-2\frac{x^2}{w^2}}\right) \tag{2.42}$$

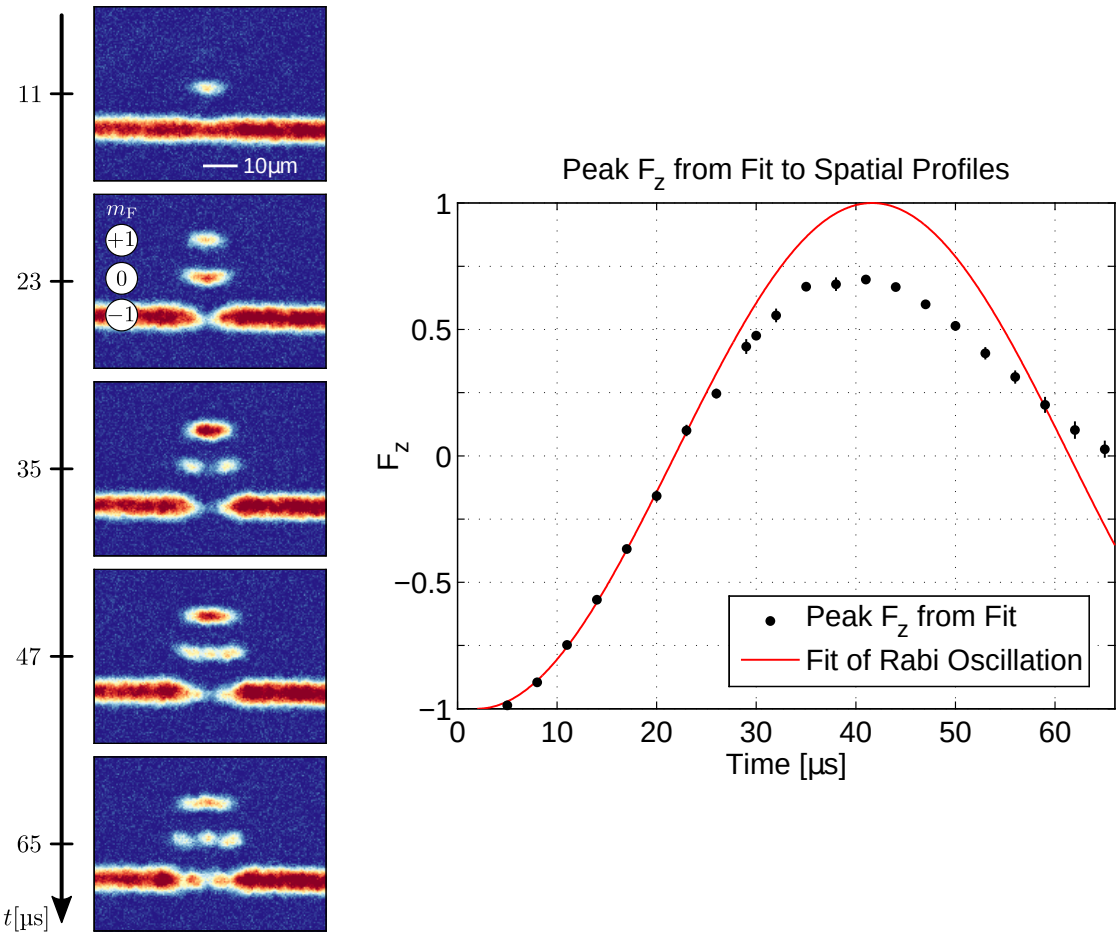

Figure 2.17.: Local spin rotation around a transverse spin direction starting with all atoms in $m_F = -1$. This leads to oscillations of the z-projection of the spin ($F_z \propto N_{+1} - N_{-1}$) according to eq. (2.42) in space and time. On the left-hand side absorption pictures of the three m_F densities are shown to illustrate the spatial dynamics. Free evolution during the short time-of-flight period ($\sim (2-3)$ ms) prior to imaging leads to a deformation of the density profiles. Fitting each of the spatial profiles with eq. (2.42) allows the extraction of local rotation angle amplitude α_0. Due to the deformation of the spatial profiles the fit always converges towards $\alpha_0 < 2\pi$. From these fit parameters the F_z projection amplitudes in the center of the local rotation are calculated as $F_z = -\arccos(\alpha_0)$ and displayed in the right-hand plot. The red line is a sinusoidal fit, corresponding to a Rabi frequency of $\Omega_{rot} = 2\pi \times (12.6 \pm 0.2)$ kHz, to the data up to 23 µs with a time-offset of the pulse duration of 2 µs. For large pulse durations the most likely reason for the deviation of the data points from the curve is spatial dynamics of the density profiles prior to imaging.

with rotation angle $\alpha_{\mathrm{rot}} = \Omega_{\mathrm{rot}} t$ and local rotation Rabi frequency amplitude Ω_{rot} in the center of the beam. For rotation angles up to $\alpha \approx \pi$, which occurs at around $t = 35\,\mu\mathrm{s}$, the spatial modulation, visible in the absorption pictures, roughly fits to the oscillation predicted by this formula. Afterwards, however, no clear transfer back to the $m_{\mathrm{F}} = -1$ level is visible in the center of the beam. Nevertheless, for larger times spatial structure appears, especially in the $m_{\mathrm{F}} = 0$ component at $t = 65\,\mu\mathrm{s}$. This trend is also visible when comparing the oscillation of the extracted F_z amplitude with the expected oscillation (right-hand plot). From a fit to short coupling times $t \leq 23\,\mu\mathrm{s}$ a local Rabi frequency of $\Omega_{\mathrm{rot}} = 2\pi \times (12.6 \pm 0.2)\,\mathrm{kHz}$ is extracted.

While fluctuations of the beam position or noise of the amplitude modulation could, in principle, lead to a vanishing of the spatial structure and thus a damping of the extracted oscillations, these are most likely not the causes for the deviations from the expected behavior. Position fluctuations, which originate from mechanical fluctuations of massive objects, are expected to occur at small frequencies $<$ kHz, which is slow compared to the relevant coupling times here. Additionally, a measurement of the beam modulation confirms a stable control beam amplitude modulation. Insead, in this scenario the exact imaging sequence becomes important because it gives rise to spatial dynamics. For spin excitations, usually the spin interaction time scale $t_{\mathrm{s}} \sim 400\,\mathrm{ms}$ (cf. section 2.3.2), governed by the difference in interactions between the m_{F} levels, is the relevant scale for dynamics. Before imaging, the m_{F} components are separated by a SG pulse followed by a $(2-3)\,\mathrm{ms}$ time-of-flight period. During this period, after the clouds have separated, the only remaining interaction scale is that of the density interactions with $t_{\mathrm{d}} \sim 2\,\mathrm{ms}$, which may thus lead to significant dynamics. Here, the dispersion of the density wavepackets generated by the local rotation in the single m_{F} components is expected.

As shown in eq. (2.41), the local control laser does not only generate an oscillating fictitious field $\boldsymbol{B}_{\mathrm{rf}}^{\mathrm{fict}}$ but also a static offset field $\boldsymbol{B}_{0}^{\mathrm{fict}}$. This results from the presence of static, i.e. zero-frequency components in the spectrum of the fictitious field (cf. eq. (2.41)). The fictitious magnetic field is oriented parallel to the laser beam axis. It adds vectorially to the global magnetic offset field as $\boldsymbol{B}(x) = \boldsymbol{B}_0 + \boldsymbol{B}_0^{\mathrm{fict}}$. Because $B_0 \gg B_0^{\mathrm{fict}}$ it rotates the quantization axis only slightly but simultaneously generates a magnetic potential $V_{\mathrm{mag}}^{\mathrm{fict}}(x) = \hbar\Omega(x) F_z$ for the atoms occupying the states $m_{\mathrm{F}} = \pm 1$. Here, $\hbar\Omega(x) = g_F \mu_{\mathrm{B}} (|\boldsymbol{B}(x)| - |\boldsymbol{B}_0|)$ originates from the change of the total magnetic field amplitude.

This can be measured directly by observing the local density depletion of a single-component condensate after adiabatically ramping up the local control beam. To prevent spin rotations, the amplitude modulation frequency $\omega_{\mathrm{rf}} = 2\omega_{\mathrm{L}}$ is detuned far from resonance. Here, care has to be taken to image the condensate without switching off the laser beams or time-of-flight to prevent spatial dynamics.[24] We achieve this by imaging without SG separation and before switching off the local rotation beam or the WG potential.[25] Repeating this experiment for single-

[24] This leads to a splitting of the single density depletion into two traveling wavepackets, even for time-of-flight periods as short as 2 ms.

[25] Note, that the ac-Stark shift due to the WG beam may lead to a shift of the resonance of the imaging transition away from the frequency of the imaging light. This may affect the

component condensates prepared in each of the three m_F levels leads to the density curves shown in fig. 2.18. For the $m_F = \pm 1$ densities the local rotation beam acts as repulsive/attractive potential while not affecting the $m_F = 0$ component, in accordance to the action of a magnetic field. This shows that the local rotation beam generates a magnetic potential with an amplitude of $\hbar\Omega_0 \sim 0.4\hbar\Omega_{\mathrm{rot}}$.

Thus, phase gradients imprinted to the $m_F = \pm 1$ components during local spin rotations will also affect the subsequent spatial dynamics. While the local magnetic potential attracts the $m_F = +1$ atoms, the $m_F = -1$ component is expelled from the region of the local rotation. This further prevents the faithful measurement of the local rotations in the absorption pictures. Nevertheless, this may explain why spatial structures in $m_F = 0$ resemble the expectations more closely than the $m_F = \pm 1$ densities. The presence of this magnetic potential implies only a small reduction in the amplitude of the local rotation (see appendix A). This is consistent with the observed amplitude of the spin rotation, which seems to be almost unity (cf. absorption picture at 35 µs in fig. 2.17).

The fits to the spatial profiles of figs. 2.17 and 2.18 also allow for an estimation of the beam diameter. By applying the function given in eq. (2.42) to the case of the local rotation a beam waist radius of $w \approx 9.7\,\mu\mathrm{m}$ is obtained. In comparison, fitting a Gaussian profile to the density deviations due to the magnetic potential results in a radius of $w = (7.0 \pm 0.3)\,\mu\mathrm{m}$.[26] It is conceivable that the radius extracted from the spin rotation profiles is larger due to the additional dispersive broadening during time-of-flight. Here, the sharp density gradients at the edge of the rotation profile reduce, which leads to broader structures. Thus, the radius extracted from the density imprinting method is likely to resemble the actual waist radius more closely. This value is in accordance with a previous measurement [77] but is still above the expected beam waist radius of approx. 4 µm in the focus of the imaging objective.

Fluctuations

Another important characteristic of the local rotations are the technical fluctuations associated to this coupling method. For a rough estimation of these we record the fluctuations of F_z for a spin Rabi as shown in fig. 2.17. The coupling time is chosen such that the rotation angle in the center is $\alpha_{\mathrm{rot}} \approx \pi/2$. In this case F_z is calculated by first summing all atoms within ± 1 RMS radius of the local rotation profile before inserting the atom numbers of the different m_F levels into the formula for F_z. This leads to relative fluctuations of $\Delta F_z/F_z \sim 0.05$. These are a mangitude larger than the power fluctuations of the local control beams (cf. section 2.6.4), which would contribute to noise in this quantity through rotation amplitude fluctuations. Furthermore, these fluctuations are also more than twice the fluctuations expected after rotation of the initial coherent spin state.[27]

extracted atom number. Here, however, the determination of the amplitude of the magnetic potential is presumably limited by the estimation of the chemical potential.

[26] This waist radius corresponds to an root mean square (RMS) radius of $\sigma = w/2 = (3.5 \pm 0.2)\,\mu\mathrm{m}$.

[27] In a typical measurement (e.g. fig. 2.19) the central $\sim 4\,\mu\mathrm{m}$ of the local rotation region, which mainly fixes the rotation amplitude, are occupied by $N \sim 1300$ atoms. Considering a local coupling which rotates the spin to the equator in the center (e.g. $F_x = 1$) the expected coherent

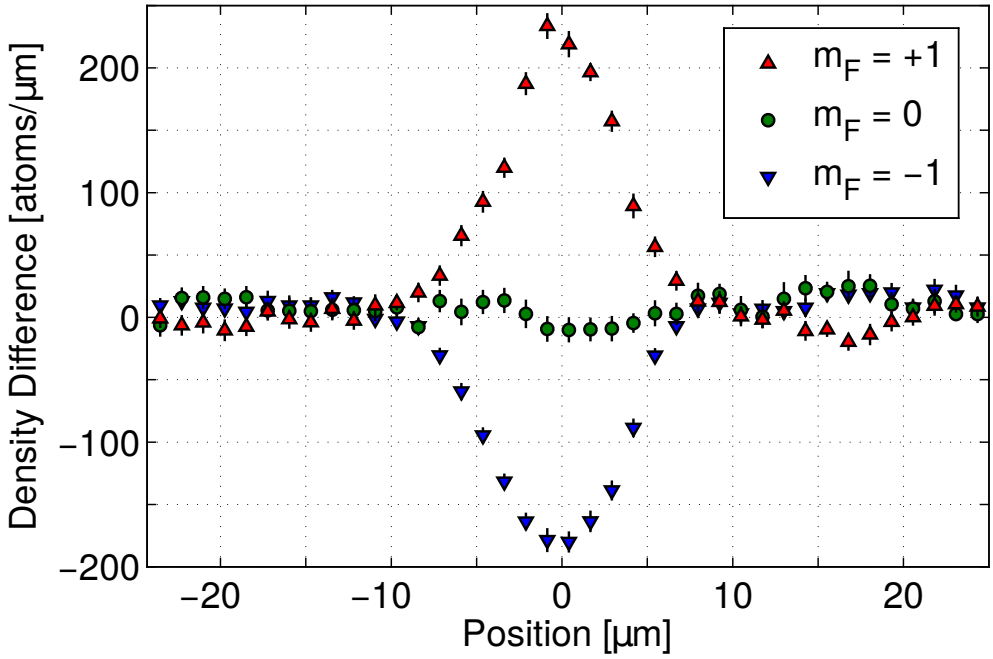

Figure 2.18.: Single-component density response to the local rotation baser beam (790 nm) with far off-resonant amplitude modulation at frequency $\omega_{\mathrm{rf}} = 2\omega_{\mathrm{L}}$ to prevent spin rotations. The beam intensity is ramped up linearly over a period of 500 ms and the density is imaged without turning off neither the 790 nm beam nor the WG potential to prevent spatial dynamics before imaging. In different experiments the atoms are prepared in either of the three m_{F} levels and the density difference to the unperturbed case without local rotation beam is plotted as an average over multiple realizations (error bars indicate the 1 s.d. error interval of the mean). The static fictitious field component $\boldsymbol{B}_0^{\mathrm{fict}}$ leads to a depletion (attraction) of the $m_{\mathrm{F}} = -1$ ($m_{\mathrm{F}} = +1$) component while not affecting the density distribution of $m_{\mathrm{F}} = 0$, as expected for a magnetic potential. For the density of approx. 400 atoms/µm the maximal depletion/attraction of atoms corresponds to a potential amplitude of $\hbar\Omega_0 \sim h \times 380\,\mathrm{Hz}$ (estimated by assuming the 1d coupling constant given by eq. (2.6)). For this measurement the local spin rotation Rabi frequency has been reduced to $\Omega_{\mathrm{rot}} \approx 2\pi \times 890\,\mathrm{Hz}$. From Gaussian fits to the density profiles a beam waist radius of $w = (7.0 \pm 0.3)\,\mu\mathrm{m}$ is estimated as the average over $m_{\mathrm{F}} = \pm 1$.

For the stability of the rotation amplitude of local spin rotations the position fluctuations of the beam are important. This is especially relevant for poor vertical overlap of the local control beam with the condensate. To illustrate this, the F_z projections and standard deviations ΔF_z are plotted as a function of the vertical beam position in fig. 2.19 (blue line). Here, ΔF_z is extracted from the local rotation center (analogously to the treatment in fig. 2.17). The fluctuation profiles in the figure show that in the vertical beam center the amplitude fluctuations of the measured spin reduce when the beam is centered on the condensate. In contrast, they increase when the flanks of the beam lie in the center of the atom cloud.

For the fraction of atoms transferred to other levels by the local spin rotation at some position x the full 3d overlap between the local rotation laser beam and the atomic cloud needs to be considered. In scenarios where slight shifts of the laser beam or cloud do not significantly change the overlap between these quantities the local rotation is relatively robust against noise induced by position fluctuations (i.e. when the beam and cloud are centered). However, because the condensate (radius of $\sim 2\,\mu$m in the TF approximation) is smaller than the laser beam, the largest gradient in the overlap occurs when the steepest gradient of the beam intensity lies in the center of the condensate.

Therefore, the fluctuations show a shape similar to the derivative of the vertical intensity profile of the local rotation beam. The application of this fluctuation model to our system is studied in [82]. Assuming that the typical horizontal beam position fluctuations of approx. 0.4 µm also apply to the vertical direction is not sufficient to explain the magnitude of the observed fluctuations. However, evaluating the position fluctuations on the atom cloud on the picture, a typical standard deviation of approx. 1 µm is observed. This additional noise may account for the full noise excess when the local rotation beam is not centered on the condensate.

Inversely, this noise model may be applied to the experiment to reduce the fluctuations of the local coupling by increasing the beam size in vertical direction. This may be accomplished by optical components, e.g. cylindrical lenses or prisms, or with an appropriate RF signal applied to the vertical AOD. The additional lines in fig. 2.19 correspond to a slow frequency modulation of the diffraction signal during the local spin rotation pulse period of 80 µs. For this, the vertical frequency $f_{\text{AOD-V}}$ is swept once by the value of the modulation width Δf from $-\Delta f/2$ to $+\Delta f/2$ around the frequency indicated on the vertical axis. The resulting effective vertical profiles show, as expected, an increasing width. Simultaneously, the sharp noise peaks start to decrease due to the decreased effective vertical gradient of the beam intensity. This helps to significantly reduce the fluctuation sensitivity to drifts in the vertical beam position, as induced by e.g. temperature changes. Nevertheless, no reduction below the fluctuation level in the center of the unmodulated beam is achieved. This hints towards another remaining fluctuations source, like e.g. imaging noise which has not been properly calibrated in this measurement.

state fluctuations are $\Delta F_z = \sqrt{(\langle \hat{F}_z^2 \rangle - \langle \hat{F}_z \rangle^2)/N} = \sqrt{(0.5-0)/N} \approx 0.02$. These arguments can be performed rigorously by considering the total amount of atoms to be distributed over the m_{F} levels according to a binomial distribution with probabilities determined by the integrated rotation profile. In this example, this results in approximately the same standard deviation.

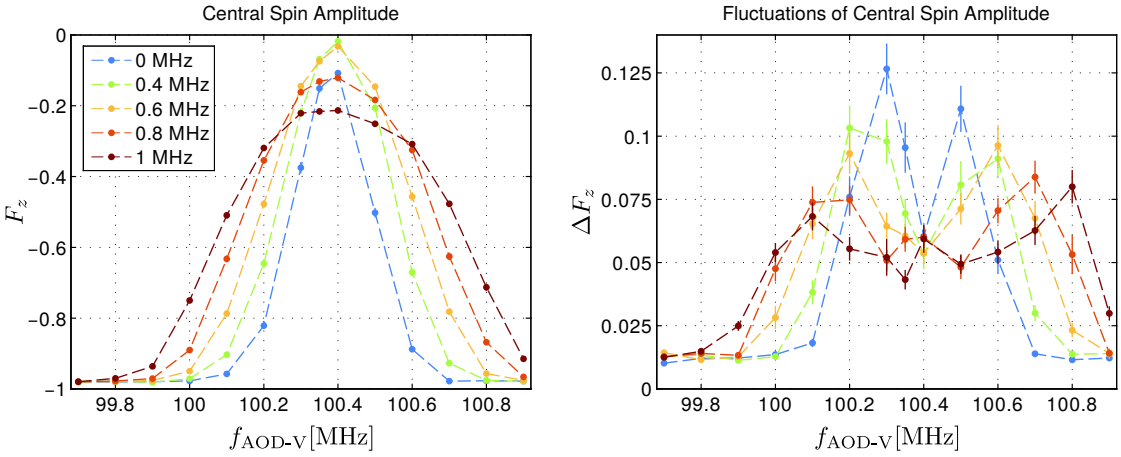

Figure 2.19.: Vertical F_z profile and fluctuations of a local spin rotation starting for all atoms initialized in $m_{\text{F}} = -1$ for different vertical beam widths. The left-hand plot shows the peak F_z projection extracted analogously to the procedure in fig. 2.17 and the right-hand plot shows the corresponding standard deviation of this observable. The different colors encode the frequency modulation widths Δf over which the vertical AOD frequency $f_{\text{AOD-V}}$ is swept during the local rotation duration of $\tau = 80\,\mu\text{s}$ to effectively obtain a larger beam width in vertical direction. The fluctuations obtain a profile similar to the derivative of the vertical intensity profile, consistent with rotation amplitude fluctuations originating from variations of the overlap between the local control beam and the condensate induced by vertical position noise (see text). Assuming the same vertical AOD resolution as in horizontal direction (in accordance to the calibration of the deflection angles in both directions [77]), the unmodulated ($\Delta f = 0\,\text{MHz}$) Gaussian beam radius in vertical direction is approx. $7.9\,\mu\text{m}$.

2.7. Control of the Magnetic Offset Field

For the observation and manipulation of spin dynamics in our experiment the control of the magnetic fields is of central importance. Employing two vertical pairs of coils (one for a static offset and the other for regulation), the magnetic field amplitude is actively stabilized to the value measured by a flux-gate sensor mounted close to the glass cell of the vacuum chamber. The details of this stabilization can be found in [41] and reaches a stability of $\sim 50\,\mu\mathrm{G}$.[28] To account for slow drifts of the regulation we calibrate the magnetic field to the detuning measured in a Ramsey spectroscopy in approximately hourly intervals. As frequency reference the clock signal of the global position system is used to ensure a sufficient long-time stability.

Magnetic field gradients along the axial direction of the condensate are controlled daily. When observing the spin dynamics after a quench (especially relevant for the measurements in chapters 4 and 5) usually large evolution times need to be accessed. Therefore, it is sensible to apply control measurements with similar interrogation times of $\sim 30\,\mathrm{s}$ to obtain a sufficiently large resolution. By tuning q_{exp} approx. $h \times 1\,\mathrm{Hz}$ to the left of the center of the resonance feature in $|F_\perp|$ (gray vertical line in fig. 2.6) the presence of population in all m_F levels is ensured. Because $q < 0$ in this range, short-ranged excitations prevent long-range order and the $m_\mathrm{F} = \pm 1$ densities redistribute according to the magnetic gradients along the cloud. This technique has also been applied in [55] and allows for precise cancellation of the gradient.

For the experiments presented in chapter 3 usually the soliton collisions themselves are applied as Larmor phase sensitive detectors (see section 3.5.3 for details). Here, a Ramsey spectroscopy with long interrogation time is used to calibrate this method and we find the phase sensitivity of the solitons to exceed that of the Ramsey sequence at small gradients.

[28] This value is obtained from fluctuations between single realizations of Ramsey spectroscopies on the $|1,-1\rangle \leftrightarrow |2,0\rangle$ transition with an interrogation time of $625\,\mu\mathrm{s}$ at a fixed detuning of $400\,\mathrm{Hz}$.

3. Vector Solitons

In this section we will discuss the theoretical concepts required to describe solitons and the experimental generation of vector solitons and the observation and characterization of their dynamics. Some of the results discussed here have been published in [83]. After a short general introduction to solitons the basic theoretical concepts for solitons in BECs will be introduced. Here, a focus will be placed on the Manakov limit of equal interactions between all atoms, which is the relevant model for the experiments performed in this work. This is complemented by a short summary of soliton experiments performed with BECs.

In the remainder of the chapter, the experimental implementation of 3-component vector solitons will be discussed. Interleaved, the required theoretical concepts will be worked out, where appropriate. First, the general preparation and characterization of these solitons will be explained. Here, the discussion of the static profiles is complemented by the propagation in a harmonic trap. Further the collision dynamics of the vector solitons is investigated and compared to an analytical Manakov description, which shows good agreement with the experiments. Finally, an application of these collisions as interferometer is given, which allows the precise measurement of magnetic field gradients.

3.1. A (Short) Introduction to Solitons

In general, solitons are non-dispersive waves which can exist in systems where a non-linearity cancels the dispersion in such a way that excitations with stationary shape can exist (see fig. 3.1). Their names stem from solitary waves, which were first reported in the 19th century as water waves propagating over long distances without significant change of their shape [16, 84]. The great interest the topic of solitons has attracted over the last decades has been sparked by the puzzling lack of equilibration in the simulations of a non-linearly coupled chain performed by Fermi, Pasta, Ulam and Tsingou [14]. This phenomenon has then been explained through the analysis of soliton scattering [15], which found almost exact recurrences of the initial in simulations. This shows another fascinating property of solitons: their particle-like behavior. After collisions they continue the propagation with preserved shape but offset in their positions. Since these initial works, solitons have been studied in many fields of science. Especially in optics, where the power-dependent change of the refractive index introduces non-linearities, solitons have been studied in great detail [85, 86]. Further examples are their application to describe domain walls in lattices [87], excitations in conducting polymers [88], blood pressure waves in arteries [89, 90] and protein movement in muscle contraction [91, 92] and more applications in e.g. biology [93]. For a short and historic overview on the topic of solitons in various systems see [94]. Finally, shortly after the generation of the

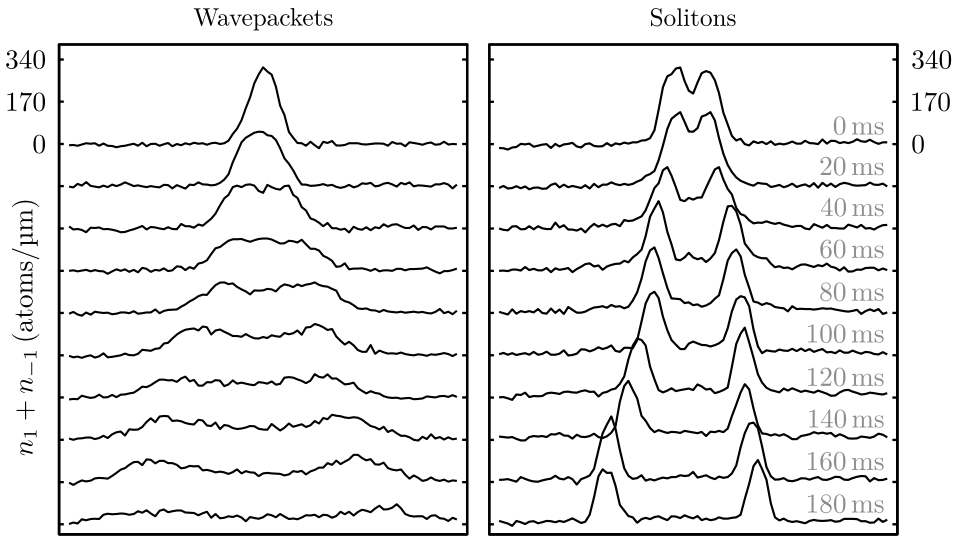

Figure 3.1.: Comparison between Gaussian wavepackets and solitons in a BEC. On the left-hand side a pair of wavepackets are generated, which disperse over time (each line corresponds to the time given in gray). On the right, non-dispersive solitons propagate without significant change in their shape. The plots show density profiles of the $m_F = \pm 1$ components of the condensate after the generation of a local excitation (see section 3.4.1 for details). The duration of the local rotation is $\tau = 33\,\mu s$ on the left and $\tau = 65\,\mu s$ on the right. The figure is adapted from [83].

first BECs [95, 96] solitons have also been generated and studied in ultracold gases [20, 21]. Here, the interactions between the atoms provides the crucial non-linearity which supports the existence of solitons.

Although in the recent years more flavors have been discussed in literature, solitons come in two distinct basic categories: bright and dark solitons. This classification originates from optics where the soliton structure describes the electric field amplitude. Correspondingly, a bright soliton describes an object consisting of large radiation power on a dark background and a dark soliton is a localized depletion of a bright background. As such, bright solitons bear a certain kind of resemblance with wavepackets, albeit not being a superposition of linear waves and completely lacking their dispersion, of course. Dark solitons, sometimes also called "kinks", bear an additional feature compared to bright solitons. While their amplitude envelopes, apart for obvious inversion, are described by the same function, are similar the underlying field supporting dark solitons possess a phase change localized around the position of greatest depletion in its amplitude. [97] The gradient and size of the phase jump correlate with the depletion amplitude of the soliton; for a total depletion of the background the jump becomes instantaneous–a "kink". In optics this phase would correspond to an offset in the phase angle of the electric field and for BECs the complex phase of the macroscopic wavefuntion describing the condensate.

While the preceding classification of solitons is valid only for single component systems, they build the basis for the following. In this chapter, we will concern ourselves with composite solitons, namely vector solitons, which consist of a

superposition of solitons in different degrees of freedom [98, 99]. For optical systems this may be two orthogonal polarization directions or distinct frequency ranges; in BECs different hyperfine states or different superimposed atomic species may provide the required internal states. Here, we will utilize the three substates of the $F = 1$ hyperfine manifold of ^{87}Rb to harbor bright and dark soliton components. Each of these, inherit their basic properties from the single-component excitations discussed above [100]. Therefore, these will be treated in some more detail before introducing the multi-component solitons, which, in a loose sense, contain bright and dark components as "building blocks". Although solitons are possible even if the underlying field is incoherent [101, 102], we will discuss vector solitons in the presence of large coherence within and between the different components.

3.2. Manakov Theory

While the previous section gave a general overview on the topic of solitons we now want to specifically discuss a certain model system relevant for the later discussion. As we are interested in interacting ultracold gases, such a model should appropriately involve the kinetic properties of the atoms as well as their interaction trough point-like s-wave interactions. On the mean-filed level, and neglecting the trapping potential, such a suitable model, which may also describe the electric field in optics [23, 86], is given by the non-linear Schrödinger equation (NLSE) (which is equivalent to the GPE without trapping potential) [22, 103]

$$i\hbar\partial_t\psi = -\frac{\hbar^2\nabla^2}{2m}\psi + g\left|\psi\right|^2\psi. \tag{3.1}$$

In our interpretation of ψ as mean-field macroscopic wavefunction of a (single-component) condensate the first term on the right-hand side describes the contributions from kinetic energy. The second term, involving the interaction constant g arises from the atomic interactions and introduces the non-linearity required to balance the kinetic dispersion to allow for the existence of solitons. This system is integrable [104], therefore allowing for a complete analytic solution of its dynamics. These have initially been derived via the inverse scattering transform (IST) [105–107]. This method has then been adjusted to more generalized systems by Manakov [23] and nowadays systems described by the NLSE discussed in the context of solitons are often referred to under his name. Therefore, we will also call the soliton solutions for these types of equations "Manakov solitons".

In ultracold gases solitons are strictly only stable in 1d systems. The transverse extension breaks the integrability of the NLSE, which leads to dissipation via phonon scattering [108] and decay to vortices or vortex rings via the snake instability [109]. Therefore, we will consider only transversely tightly confined systems. In particular we will assume the experimentally realistic case of a cigar-shaped harmonic trap with large transverse trap frequency $\omega_\perp$ such that only the lowest harmonic oscillator state is occupied in transverse direction. Longitudinally we assume the trap to be sufficiently flat to neglect the trapping potential in this direction in accordance with eq. (3.1). In order to appropriately describe experiments in (or close) to this 1d limit all quantities in this equation must be expressed as functions of only the

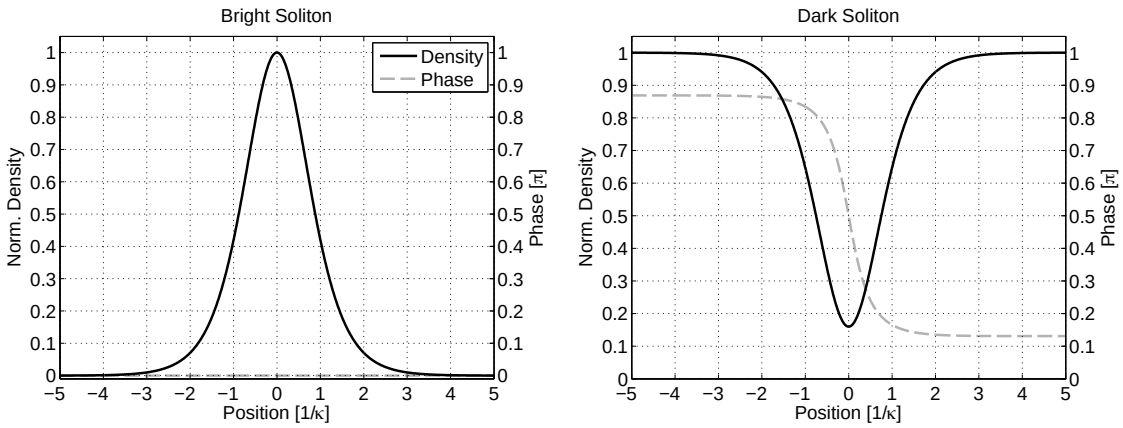

Figure 3.2.: Density and phase profiles of bright and dark solitons of the NLSE (3.1). The density profiles are normalized to the maximum. The bright soliton (left) is displayed for $v = 0$ while the dark soliton is shown vor $v/c = 0.4$. At this velocity the associated phase jump, width and darkness of the dark soliton are $\Delta\varphi \approx -0.74\pi$, $1/\kappa \approx 1.54\xi$, and $D = 0.84$, respectively.

spatial coordinate x along the longitudinal trap direction. To achieve this, an effective 1d interaction constant $g_{1\mathrm{d}} = g/(2\pi a_\perp^2)$ can be obtained by incorporating the transverse energy contributions from applying the system Hamiltonian to the transverse wavefunction; here, this corresponds to an integration $\int dydz\,|\psi_\perp(y,z)|^4$. For the harmonic oscillator groundstate the result naturally incorporates the the transverse harmonic oscillator length $a_\perp = \sqrt{\hbar/(m\omega_\perp)}$. Because this whole chapter focuses on 1d systems we will drop the designation "1d" of the interaction constant in the following and implicitly assume 1d systems from now on.

In general, eq. (3.1) supports both of the two previously introduced distinct types of bright and dark solitons in dependence of the interaction parameter. Subject to a so-called "focusing" nonlinearity with $g < 0$ (a name again transferred from optics), bright solitons are of the form [103]

$$\psi(x,t) = \frac{a_\perp \kappa}{\sqrt{2\,|a|}} \mathrm{sech}\,\{\kappa\,[x - x_0(t)]\}\, e^{i\varphi(x,t)}. \tag{3.2}$$

Here, $a < 0$ is the scattering length associated to the effective 1d interaction constant $g = 2\hbar^2 a/(m a_\perp^2)$, $\kappa = |a|\,N/a_\perp^2$ is the inverse soliton width, $x_0 = \tilde{x}_0 - vt$ the center-of-mass position of the soliton moving at velocity v, and N is the total number of atoms contributing to the soliton. Note that, in order to fulfill the requirement of the effective 1d approximation the atom number N needs to be sufficiently small ($N \ll a_\perp/|a|$), which also implies $1/\kappa \gg a_\perp$ because of the attractive interaction between the atoms. The associated profile of a bright soliton is shown in the left plot of fig. 3.2. The phase $\varphi(x,t)$ of this soliton wavefunction is equivalent to eq. (3.11).

In the opposite scenario for a repulsively interacting system with $g > 0$ the atoms form a BEC with a flat density. This background density n_0 is associated with the chemical potential $\mu = n_0 g$ of the condensate. Often the term $\mu\psi$ is subtracted from eq. (3.1) to remove phase evolution associated to this constant mean-filed

energy contribution. In this case the dark soliton solution is given by [22, 103]

$$\psi(x,t) = \sqrt{n_0}\left(i\frac{v}{c} + \frac{\sqrt{c^2-v^2}}{c}\tanh\left\{\kappa\left[x - x_0(t)\right]\right\}\right), \tag{3.3}$$

where the inverse length is given by $\kappa = \sqrt{1-v^2/c^2}/(\sqrt{2}\xi)$, the center-of-mass is defined as $x_0 = \tilde{x}_0 - vt$ like before and $c = \sqrt{n_0 g/m}$ and $\xi = \hbar/\sqrt{2mn_0 g}$ are the Bogoliubov speed of sound and healing length, respectively. This velocity also represents the largest upper velocity at which a dark soliton can move. An exemplary dark soliton profile is displayed in the right plot of fig. 3.2. As can be seen from the soliton wavefunction the amplitude of the density depletion given by the prefactor of the tanh term scales with the soliton velocity. A useful quantity related to this is the darkness [22]

$$D = \frac{n_0 - |\psi(x=x_0)|^2}{n_0} = 1 - \frac{v^2}{c^2} = 2\xi^2\kappa^2, \tag{3.4}$$

which specifies the density depletion in the center of the soliton. The last characteristic feature of the dark soliton profile is a jump of the wavefunction phase by $\Delta\varphi = -2\alpha$ from negative to positive x. Most of this rapid change is localized in the region around the density depletion. The so called soliton phase angle associated to the phase jump is given by

$$\tan\alpha = \frac{\sqrt{c^2-v^2}}{v}. \tag{3.5}$$

For dark solitons the velocity is the single parameter defining all their properties. At the upper and lower limit of the velocity, these are given by:

Quantity	$v \to 0$	$v \to c$
Width $1/\kappa$	$\sqrt{2}\xi$	∞
Darkness D	1	0
Phase jump $\Delta\varphi$	π	0

For large velocities $v \to c$ the soliton function continuously transforms into a homogeneous density by decreasing both the phase jump as well as the dip in the density depletion while the width diverges. On the other hand, for vanishing velocity the phase jump becomes instantaneous while the width of the density depletion never decreases below the healing length.

3.3. Overview of Solitons in BEC Experiments

In repulsively interacting BEC experiments dark solitons have been prepared deterministically via phase imprinting methods [20, 21, 110, 111]. For this, a detuned laser beam is partially blocked with a razor blade to generate a sharp intensity gradient which is imaged onto the condensate. A short time evolution in

this anisotropic potential generates the phase jump $\Delta\varphi$, such that in the following free evolution the condensate density dynamically adjusts to form a dark soliton. This has also been combined with density engineering to reduce the velocity of the solitons [112]. Other methods involve the counterflow of condensates [113–115], shock waves [109, 116] or the sweep of a potential barrier through the system [117]. IN most of these works, the motion of the solitons in confining potentials, collisions between solitons, or their decay and dissipation have been investigated.

For repulsive interactions,the formation of bright solitons is possible, which form spontaneously when tuning the inter-atomic interactions to be attractive [118–123]. Also forced evaporation may be applied to obtain bright solitons [124]. Alternatively, the dispersion relation of an underlying lattice potential may be utilized to generate gap solitons in repulsively interacting systems [125]. Stabilized by attractive interactions, in 2d also Townes solitons have been realized [126], which may also be obtained via effective interactions in a 2-component system [127].

After the generation of coupled dark-bright solitons in optics [128, 129] such composite structure were also investigated in BECs. Here, even in purely repulsively interacting BECs bright soliton components can be generated by "trapping" them in the effective potential of a dark soliton in 2-component condensates [100, 130]. Also dark-dark solitons are possible [131]. Experimentally, this has been realized by a local state transfer [132, 133], counterflow induced by a a magnetic field gradient in 2-component BECs [134–139] or miscible mixing [140]. Here, the much richer interactions are of great interest [131, 141]. Similarly, also in a 3-component gas the counterflow technique has been used to excite different composite vector solitons [142]. Such 3-component solitons have been shown to exhibit further interesting collision dynamics and interaction effects [130, 143, 144].

Apart from these multi-component vector solitons there are many more soliton solutions. Particularly relevant examples for spinor gases include magnetic solitons [145–147] or spin solitons in spinor gases [148]. These, in contrast to the Manakov-type vector solitons, exhibit no depletion in the total density. Recently, magnetic solitons have also been realized in experiments [149, 150].

In the following we will introduce the experimental implementation of a reproducible generation of 3-component solitons and the characterize the resulting soliton excitations and their dynamics. This allows a systematic study of the dynamics. In particular, this allows an experimental characterization of 3-component soliton interactions for the first time.

3.4. Experimental Realization of Vector Solitons

To generate solitons in the experiment our strategy starts from a local perturbation. This approach, as it leaves the phase of the condensate wavefunction outside the localized regions unchanged, cannot generate a single dark soliton. On the other hand, because all intra- and interspecies interactions in the $F = 1$ manifold of ^{87}Rb are repulsive bright solitons without phase change are not stable in our system. Consequently, we aim for the generation of a pair of solitons.

Simultaneously, applying local spin rotations also allows us to generate populations in other magnetic sublevels. Due to the coherent nature of the local

manipulation these excitations also possess fixed phase relations. This enables access to vector solitons in which the relative phases are well defined by the initial state preparation and the following propagation dynamics. In particular, we want to generate vector solitons with one dark component and two bright components.

3.4.1. Experimental Generation of Excitations

For this, we start with all atoms occupying the state $|1,0\rangle$. Then, a short local spin rotation (see section 2.6.6 for details) with a Gaussian Rabi frequency profile $\Omega(x) = \Omega_0 \exp(-x^2/(2\sigma^2))$ with radius $\sigma = w/2 \approx 3.5\,\mu\text{m}$ is applied.[1] This Rabi pulse of duration τ leads to a localized transfer of atoms to the $m_\text{F} = \pm 1$ levels with position dependent transfer fraction of $(n_{+1} + n_{-1})/n_0 = \sin(\Omega(x)\tau)$.

In the following period of free time evolution of this initial state the wavepackets propagate in the approximately flat background density in the center of the harmonic trap. Figure 3.3 shows the evolution of the $m_\text{F} = \pm 1$ density averaged over 6 – 9 realizations. All atoms occupying these levels have been transferred there from the $m_\text{F} = 0$ state during the preparation of the wavepacket. Due to the interaction with the density background in the $m_\text{F} = 0$ level, their dynamics allows inferring the total amplitude profile of the wavepacket. Correspondingly, the $m_\text{F} = 0$ show the same behavior as shown in fig. 3.3 with depletions in the density. For short coupling times $\tau \leq 33\,\mu\text{s}$ this leads to a dispersive movement in which the excitations broaden and reduce in amplitude. Increasing τ above a certain threshold leads to a strong decrease in the broadening of the excitations, which is a characteristic sign for the excitation of solitons. In fig. 3.3 the apparent broadening arises from averaging over realizations subject to fluctuations of the soliton position between different realizations. Above a further threshold in τ additional localized excitations are generated. In fig. 3.3 some of these are visible as a second lobe of dispersive wavepackets propagating outwards at larger excitations.

To understand this threshold behavior in the generation of the wavepackets we now look at the spatial structure of the initial condition after the local spin rotation depicted in fig. 3.4. Characterized by a Rabi oscillation the local spin rotation couples the hyperfine states with spatially varying coupling strength. In other words, the typical Rabi oscillation between the initially occupied $m_\text{F} = 0$ and $m_\text{F} = \pm 1$ levels advances with spatially changing Rabi frequency $\Omega(x)$. For small rotation angles $\Omega(x)\tau$ the population transfer to the $m_\text{F} = \pm 1$ levels is largest in the center of the Gaussian Rabi frequency profile (see left column of fig. 3.4). The introduction of the phase jumps along with the density depletion in $m_\text{F} = 0$ is the crucial ingredient for the generation of non-dispersive solitons in our system. This property of the initial conditions explains the qualitative difference between the first and second row in fig. 3.3. In presence of phase jumps during the initial phase of the free propagation the wavepackets dynamically adjust by appropriately shedding atoms and adjusting the amplitude of the phase jump to arrive at a stable soliton solution. Once the rotation angle becomes larger than π atoms are transferred back to $m_\text{F} = 0$ and the Rabi coupling introduces a sign change in the

[1] Here, w denotes the usual beam waist radius of a Gaussian beam. It specifies the distance from the center at which the intensity has dropped to $1/e^2$ of the central value.

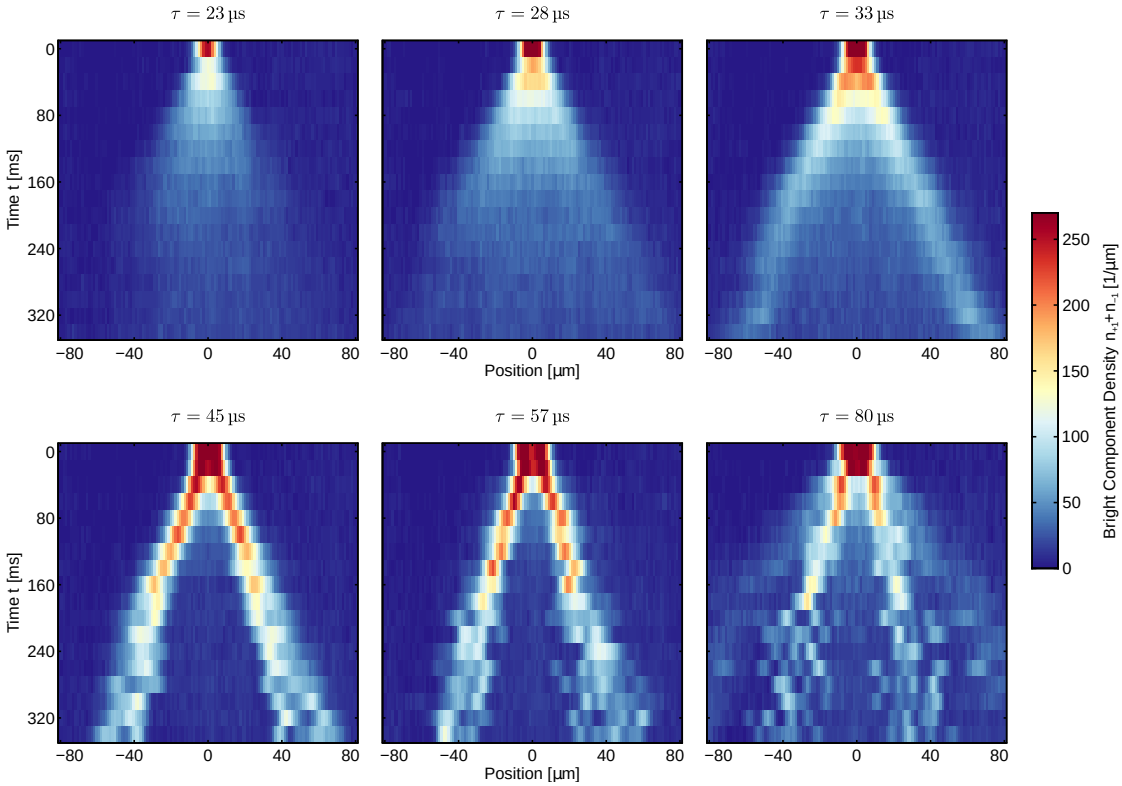

Figure 3.3.: $n_{+1} + n_{-1}$ density during the time evolution of local excitations averaged over $6-9$ realizations. The excitations are generated by different local spin rotation durations τ. Starting from an approximately homogeneous density distribution in only the $|1,0\rangle$ state the local coupling pulse transfers atoms to $m_{\mathrm{F}} = \pm 1$ during the initial state preparation. For $\tau \leq 33\,\mu\mathrm{s}$ (first line) dispersive wavepackets are generated. For longer couplings a phase jump is generated in the center of the local rotation which leads to a stabilization of the exitations as solitons (lower line). The apparent broadening of the solitons over time For very long couplings $\tau \geq 80\,\mu\mathrm{s}$ more than 2 wavepackets are generated due to multiple phase jumps in the initial condition.

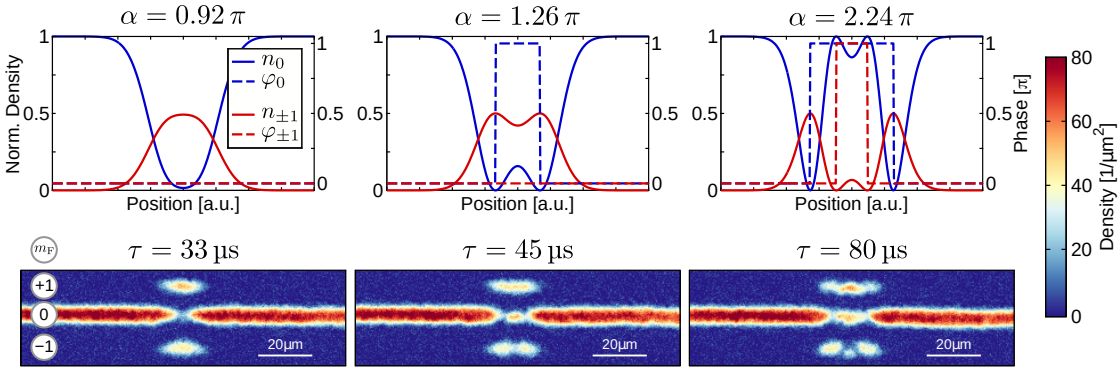

Figure 3.4.: Local Rotation Profiles for different local coupling durations. The upper row shows calculated profiles of the $m_F = 0, +1$ levels (results for $m_F = -1$ are equivalent to $m_F = 1$) rotated for durations τ from a homogeneous density where only the $m_F = 0$ is occupied. The Rabi frequency amplitude $\Omega_0 = 7\,\mathrm{kHz}$ in the center of the Gaussian Rabi frequency profile $\Omega(x)$ is chosen such that the resulting density profiles roughly match the observed distributions. The calculation is performed for a rotation around F_x. This introduces a global phase difference of π between $m_F = 0$ and $m_F = \pm 1$ which is dropped here. In the lower row absorption pictures with SG separation of the hyperfine levels after local rotation are shown for corresponding local coupling durations τ.

$m_F = 0$ wavefunction. Viewed along the condensate axis this corresponds to two phase jumps, first by $+\pi$ and then by $-\pi$ (see central column of fig. 3.4). This qualitatively changes again once the rotation angle crosses 2π where two additional phase jumps are generated in the wavefunction. These, however, are associated with the $m_F = \pm 1$ levels and occur in a region with high $m_F = 0$ density but comparably small $m_F = \pm 1$ density (see right column in fig. 3.4). Therefore, the formation of solitons, which are associated with a strong density depletion in the vicinity of a phase jump, is not strongly affected by the additional phase structure in $m_F = \pm 1$. On the other hand, the presence of this soliton-like structure prevents the $m_F = \pm 1$ atoms from flowing into the solitons created around the density depletions in $m_F = 0$. Consequently, these central atoms form a pair of dispersive wavepackets which propagate independently of the 2 solitons (cf. $\tau = 80\,\mu\mathrm{s}$ in fig. 3.3).

In the absorption pictures shown in fig. 3.4 it is clearly visible that the $m_F = \pm 1$ levels are characterized by different density profiles. However, for the local spin rotation discussed previously both densities should be exactly the same. This results from the implementation of the local rotations. Instead of generating a purely oscillating fictitious magnetic field, according to eq. (2.41) the laser modulation also generates a static fictitious magnetic field. This vectorially adds to the global offset field and locally changes the local magnetic field amplitude, as shown explicitly in section 2.6.6. This generates an effective magnetic potential $V_{\mathrm{mag}}^{\mathrm{fict}}(x) \sim 0.4\hbar\Omega(x)F_z$. Nevertheless, the oscillating fictitious magnetic field still drives the intended spin rotation with coupling Hamiltonian $\hat{\mathcal{H}}_{\mathrm{rot}} = \hbar\Omega(x)\hat{F}_x/2$ in the rotating frame of the Larmor precession. From the Rabi frequency amplitude $\Omega_0 \approx 7\,\mathrm{kHz}$, estimated from fig. 3.4, we can therefore infer the local modulation of the magnetic field

amplitude to be $B^{\text{fict}}_{\text{mag},0} \sim h \times 2.8\,\text{kHz}$. This magnetic potential imposed on the atoms during the local rotation induces a magnetic force which pushes the high-field seeking $m_\text{F} = +1$ atoms into the center of the rotation and expel the low-field seekers in $m_\text{F} = -1$ from this region. This is consistent with the pronounced and almost vanishing gaps between the "blobs" of atoms in $m_\text{F} = -1$ and $m_\text{F} = +1$ in fig. 3.4, respectively.

Experimentally, we observe a mixture of the previously outlined scenarios. The reason for this most likely are fluctuations in the Rabi frequency amplitude between different realizations. Especially for rotation angles close to integer multiples of π in the center of the transfer profile one would expect these fluctuations to lead to increased noise in the evolution dynamics. For example, in a few realizations for $\tau = 80\,\mu\text{s}$ we observed the generation of 4 solitons. This is conceivable if the rotation angle amplitude crossed 1.5π, where 4 phase jumps are generated in the $m_\text{F} = 0$ wavefunction.

3.4.2. Vector Soliton Solutions

For the spin-1 Hamiltonian (2.14), containing density and spin interactions c_0 and c_1, analytical solutions have been derived [151], albeit in the integrable limit of equal spin and density interactions $c_0 = c_1$. Naturally, these solutions are 3-component vector solitons which feature population in all hyperfine levels with specific phase relations fixed by the interactions. Also for c_1 values closer to the case of ^{87}Rb vector solitons in spin-1 BECs have been investigated analytically and numerically [152]. Additionally, in presence of magnetic fields, i.e. under the influence the second-order Zeeman shift q, the stability and soliton phase diagram have been derived [153, 154]. Here, similar to the groundstate of spinor gases, the energy detuning q induces phases which are characterized by different vector solitons consisting of bright and dark components. As function of the second order Zeeman shift different populations are favored in the hyperfine levels. This leads to phase boundaries which are similar to the $F = 1$ mean field phases with different populations and coherences [153]. Our experiments take place inside the ferromagnetic phase which features bright-dark-bright (BDB) solitons, consisting of two bright and one dark component.

To obtain a suitable model for the solitons in our system it is sensible to introduce some approximations to the spinor Hamiltonian given in section 2.3.2.[2] First, as the analytical solutions available for solitons are usually derived on the mean-field level we neglect fluctuations and replace the operators with complex fields. We can therefore introduce macroscopic wavefunctions describing the magnetic substates m_F. In full generality, the equation of motion for these wavefunctions ψ_j for each of the magnetic substates j is given by the 3-component coupled GPE

$$i\hbar\partial_t\psi_j = \left(-\frac{\hbar^2\nabla^2}{2m} + V_\text{ext} + \sum_k g_{jk}\left|\psi_k\right|^2\right)\psi_j \tag{3.6}$$

with suitable external potential V_ext and intra- and interspecies interaction constants

[2] See also [155] for an analytical and numerical investigation of vector solitons in the spin-1 system.

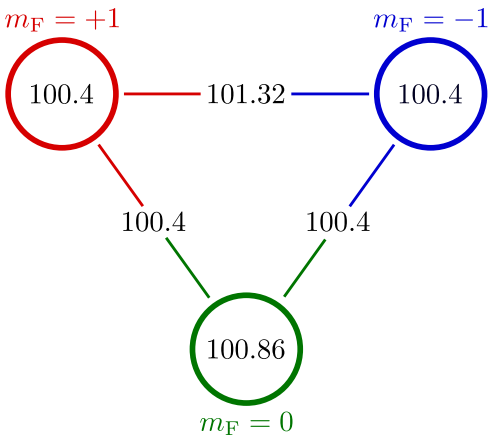

Figure 3.5.: Intra- and interspecies scattering lengths in the $F = 1$ hyperfine manifold of ^{87}Rb in units of the Bohr radius a_B. The values are calculated via eq. (C.3) from the spin pair $\mathcal{F} = 0, 2$ scattering lengths $a_0 = 101.78\,a_B$ and $a_2 = 100.4\,a_B$ [53, 58].

$g_{jk} = 4\pi\hbar^2 a_{jk}/m$ (see fig. 3.5 for the scattering lengths in the $F = 1$ hyperfine manifold). In $\mathcal{H}_{\text{int}}$ given by eq. (2.14) these are expressed as density-density and spin-spin interactions c_0 and c_1, respectively. Here, the spin interactions arise from the differences between the g_{jk} (cf. definition (2.13) of the spin interaction constant c_1). In ^{87}Rb the largest relative deviation between these values is approx. 0.9 % [53, 58], such that the spin interactions can be neglected over the density interactions. See fig. 3.5 and appendix C for the calculation of the scattering lengths between all pairs of $F = 1$ states.

Thus, by neglecting the small differences between the possible collision channels, i.e. dropping the c_1 term in the interaction Hamiltonian $\mathcal{H}_{\text{int}}$, in the condensate we can therefore replace the interaction constants g_{jk} by the weighed average $c_0 = 4\pi\hbar^2(a_0 + 2a_2)/m$ of the density interactions. This is equivalent to neglecting all energy shifts resulting from the mean field spin-spin interactions which are proportional to c_1. Additionally, due to the second order Zeeman shift induced by the magnetic offset field the SCC processes are energetically forbidden and can be ignored.

For the discussion of the spatial structure and time evolution of the solitons we also drop the energy contribution of the homogeneous external magnetic field. In the mean field limit this allows us to formulate a significantly more compact equation of motion for the fields $\mathbf{\Psi} = (\psi_{+1}, \psi_0, \psi_{-1})^T$ in form of the GPE

$$i\hbar\partial_t \mathbf{\Psi} = \left(-\frac{\hbar^2\nabla^2}{2m} + c_0\,|\mathbf{\Psi}|^2 - \mu\right)\mathbf{\Psi}. \tag{3.7}$$

Here, we subtract the phase evolution due to the chemical potential μ of the condensate. Additionally, we also drop the external trapping potential because we can assume the longitudinal axis of the WG to be sufficiently flat to be approximated by a homogeneous potential.

For the BDB type[3] we are experimentally investigating here, analytical soliton

[3] These bright-dark-bright solitons are solitons in a 3-component system, which consist of bright

solutions can be obtained by means of the IST [143] or Hirota's bilinear method [156]. In this scenario the soliton is an excitation in a system where all atoms occuipy the $m_\mathrm{F} = 0$ level with a homogeneous density n_0. Staying close the form of the wavefunctions given in [143], the resulting wavefunctions ψ_{m_F} are given by the expressions (cf. bright and dark soliton solutions given in section 3.2)

$$\begin{aligned} \psi_{\pm 1} &= \sqrt{n_0}\, c_{\pm 1} \eta \sin\alpha \operatorname{sech}\left[\kappa\left(x - x_0 - vt\right)\right] e^{i\varphi_\mathrm{kin}}, \\ \psi_0 &= \sqrt{n_0}\, e^{i\varphi_\mathrm{S}} \left(i\cos\alpha + \sin\alpha \tanh\left[\kappa\left(x - x_0 - vt\right)\right]\right). \end{aligned} \tag{3.8}$$

Here, $c_{\pm 1}$ denotes the components of a normalized complex polarization vector of the bright components in $m_\mathrm{F} = \pm 1$, η the relative amplitude between bright and dark components, α the soliton angle of the dark component, κ the inverse soliton width, x_0 the initial position, v the soliton velocity, φ_kin the kinetic phase of the bright components, and φ_S a phase offset analogous to a spinor phase. The parameters κ and v fully determine the soliton via

$$\eta = \sqrt{1 - \frac{1}{\mu}\left(\frac{\hbar^2\kappa^2}{m} + mv^2\right)}, \tag{3.9}$$

$$\tan\alpha = \frac{\hbar\kappa}{mv}, \tag{3.10}$$

and

$$\varphi_\mathrm{kin} = \frac{mv}{\hbar}\left(x - x_0\right) - \frac{1}{\hbar}\left(\frac{mv^2}{2} - \frac{\hbar^2\kappa^2}{2m}\right)t, \tag{3.11}$$

where $\mu = n_0 c_0$ is the chemical potential and m the mass of ^{87}Rb. The phase φ_kin incorporates the kinetic phase evolution, where the first x-dependent term corresponds to the equivalent of a kx-term of a a linear wave and the second t-dependent term evolves with the energy difference to the stationary background in $m_\mathrm{F} = 0$.

While for single component solitons there exists a relation which fixes κ to v, in multicomponent systems this condition is relaxed and only constrained by the background through the chemical potential by

$$\frac{\hbar^2\kappa^2}{m} + mv^2 \leq \mu. \tag{3.12}$$

This inequality constrains the "localization-induced energy" (by interpreting $\kappa \sim k$ as wave number via the Heisenberg uncertainty relation) and the kinetic energy of the soliton (or rather flow of the background density "under" the soliton) against the condensate energy μ. For equality in eq. (3.12) the soliton becomes a single component dark soliton (cf. eq. (3.9)), where the width is fully constrained by the soliton velocity. In the presence of bright components, which exert a repulsive force against the background, the width of such a filled BDB soliton can support widths larger than a single component dark type. This, in theory, allows the velocities and

solitons in two components and a dark soliton in the remaining component at the same position. Due to the mutual interactions this structure is fully coupled, such that the single components do not behave as individual solitons but as one combined object.

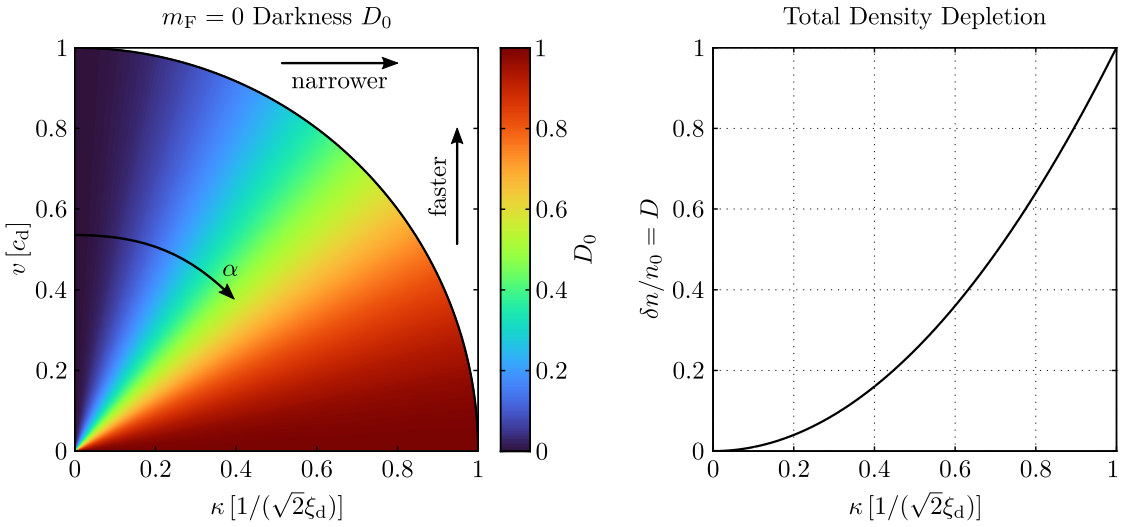

Figure 3.6.: Parameter dependence of darkness D_0 of the $m_F = 0$ component (left-hand plot) and total density depletion $\delta n/n_0$ (right-hand plot). The range of valid inverse soliton widths κ and velocities v is given by the filled area of the left-hand plot. According to eq. (3.12) the soliton width is bounded by the Bogoliubov healing length $\xi_d = \hbar/\sqrt{2mn_0c_0}$ and speed of sound $c_d = \sqrt{n_0c_0/m}$. The black curve given by a circle corresponds to a single component dark soliton solution in $m_F = 0$ without occupation of $m_F = \pm 1$. However, in the presence of bright components, arbitrarily slow and broad soliton solutions are possible. The soliton angle α corresponds to the angle opening from the v-axis. The colormap of the filled area indicates the darkness D_0 given by eq. (3.13). According to eq. (3.14) the total density depletion $\delta n/n_0$ increases quadratically with κ. This is equivalent to the darkness D of a single component soliton given by eq. (3.4).

widths to be changed independently (see fig. 3.6 for permissible parameters). In the experimental preparation utilizing the local rotation a certain average atom number is transferred to $m_\mathrm{F} = \pm 1$. This constrains the possible soliton wavefunctions which can form. Another constraint is imposed by the energy added to the system by the local spin rotation.

Similar to single component dark solitons the darkness (resembling the density depletion in the soliton center; i.e. 1 for a stationary "black" soliton) of the dark component in the BDB soliton is determined by the soliton angle α. Its value for the dark component in $m_\mathrm{F} = 0$ is given by

$$D_0 = \frac{n_0 - |\psi_0\,(x = x_0, t = 0)|^2}{n_0} = \sin^2\alpha = \frac{1}{\left(\frac{mv}{\hbar\kappa}\right)^2 + 1}. \tag{3.13}$$

Additionally, all Manakov vector solitons exhibit a depletion in the total density $n = \sum_{m_\mathrm{F}} n_{m_\mathrm{F}}$ which results from the deviation of η from 1. For the solution in eq. (3.8) this depletion has the form

$$\delta n = n_0 - n = n_0 \frac{\hbar^2\kappa^2}{m\mu}\left(1 - \tanh^2\left[\kappa\,(x - x_0 - vt)\right]\right), \tag{3.14}$$

which, in the center of the soliton, is equivalent to the darkness $D = \delta n/n_0 = 2\xi_\mathrm{d}^2\kappa^2$ of the single-component dark soliton given in eq. (3.4).[4] In that sense the total density depletion is the "true darkness" of the vector soliton. It is also interesting to note that δn only depends on the soliton width while the for the relative amplitudes η or $m_\mathrm{F} = 0$ darkness D_0 also the soliton velocity is important.

In fig. 3.7 the density and wavefunction profiles of a soliton with parameters close to experimental values is shown. The width of the soliton density is related to the parameter κ via

$$\mathrm{FWHM} = \frac{2}{\kappa}\ln\left(1 + \sqrt{2}\right) \approx \frac{1.7627}{\kappa}. \tag{3.15}$$

The gradients of the phases are results of the soliton movement. In the bright component the phase attains a slope similar to linear waves and $m_\mathrm{F} = 0$ exhibits a phase profile typical for dark solitons. This phase profile consists of a smooth change by a value of 2α over the soliton. Compared to the bright component the phase gradient of the dark component is inverted because here the phase is associated with the movement of the background atoms opposite to the soliton velocity.

3.4.3. Systematic Analysis of Soliton Excitations

Due to the filling with bright components the repulsive interactions leads to a broadening of the BDB vector solitons of $\geq 10\times$ the density healing length in our system. This allows a direct observation of the soliton density profiles in each

[4] This depletion of the total density is one crucial difference to magnetic solitons in BECs [145], which only posses a vanishing density depletion in ^{87}Rb or ^{23}Na, based on the small spin interactions c_1/c_0.

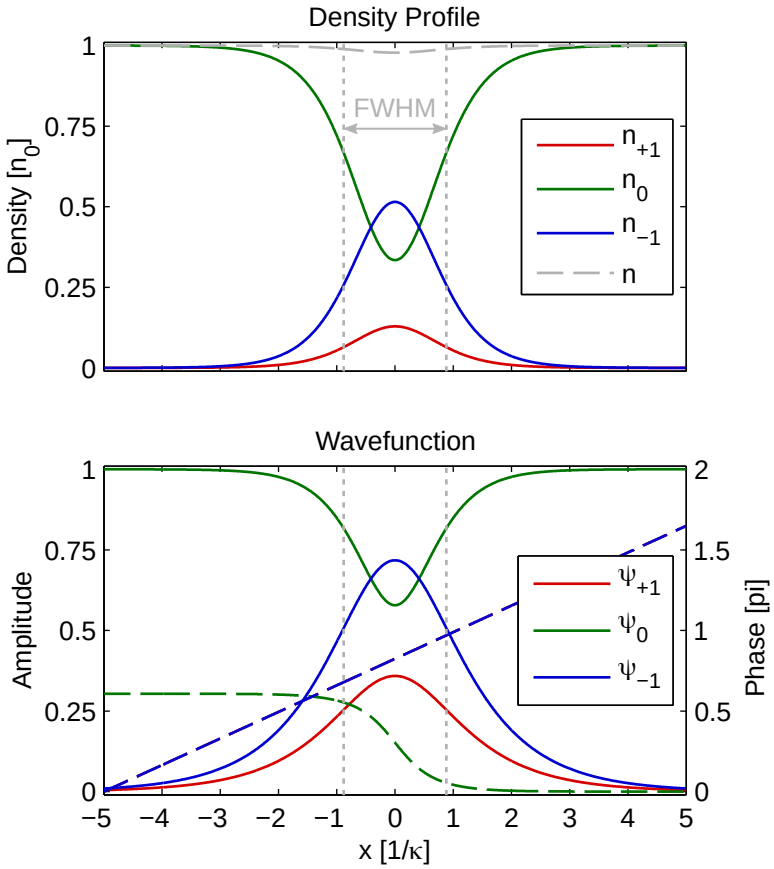

Figure 3.7.: Density and wavefunction profiles of a BDB soliton calculated from eq. (3.8). The background density, chemical potential, inverse width, and velocity are equal to the values extracted in the experiment (see fig. 3.11). These lead to a phase jump of $\alpha \approx 0.30\,\pi$ and a relative total density depletion $\delta n/n_0 \approx 2.2\,\%$ at $x = 0$. As polarization the values $c_{+1} = 1/\sqrt{5}$ and $c_{-1} = 2/\sqrt{5}$ have been chosen. As reference the half amplitude width is marked with vertical dashed lines. For the wavefunctions the absolute values (solid lines) and phases (dashed lines) are plotted. The phases are shifted to cross zero at the plot edges.

experimental realization. To facilitate a systematic evaluation of these excitations we fit the measured density profiles with functions corresponding to eq. (3.8). However, to exclude effects introduced by additional dynamics during time-of-flight before the imaging procedure we optimize the function parameters for each m_F level independently. The origin and effects connected to thsi have been discussed in more detail in sections 2.6.6 and 3.4.1.

Single experimental realizations often are subject of substantial local fluctuations due to e.g. atom number shot noise or fluctuations of the soliton position. For evaluating the experimental data in presence of this noise the following procedure has turned out to provide robust results for finding the solitons generated in the system and extracting their parameters. An exemplary plot with experimental density profiles and corresponding fit results is shown in fig. 3.8. Although not strictly necessary it may be helpful for rejecting noise peaks and extracting solitons with only small amplitudes to constrain the number of solitons to extract in the measurements. For our experiments this is usually possible because we generate a well-defined number of solitons from each local rotation (2 in most cases). For fitting the measured density profiles it is necessary to select a certain region around the soliton (see short vertical colored and dashed lines in fig. 3.8). This ensures that the optimization routine does not converge towards noise peaks on top of the background. Thus, the selection of these fit region requires a rough determination of the most probable soliton positions. This is achieved by a peak-finding algorithm which rejects all local maxima below a certain density threshold (see long vertical colored and dashed lines in fig. 3.8). To increase the signal-to-noise ratio further it turned out to be advantageous to only apply this algorithm to the sum of the bright components $n_{-1} + n_{+1}$ (see black dashed line in the n_{+1} plot of fig. 3.8). The empty density profiles provide a low noise background which allows for the faithful detection of small amplitudes. Fixing the number of solitons allows rejecting all but the largest density peaks. Then, the density profiles around each of the extracted peak positions is fitted over a fixed range; each of the m_F components is fitted independently to ensure optimal flexibility in the following data analysis (see colored and solid lines in fig. 3.8). When two of the peaks are close by or even overlapping it is necessary to define a combined region incorporating both of the peaks (see green fit region in fig. 3.8). In this case also a specialized fit function must be applied with simultaneously optimizes the parameters for two solitons in the fitting region; the previously extracted peak positions can be used as start parameters for the optimization procedure. For $m_\mathrm{F} = 0$ it is necessary to account for the curvature of the background density profile which may vary significantly over the chosen fit range. In our experiment the background profile can be described as a quadratic density distribution in the TF approximation (see dashed black line in the n_0 plot of fig. 3.8). This shape can be fitted at the positions not incorporated in any fit ranges associated to the solitons. Then, during the fit of the soliton density profiles this function can be added to account for the background curvature.

Especially for fitting small amplitudes or decaying wavepackets it is advisable to constrain the fit region by the approximate expected position of the wavepacket. Still, for very small local spin rotation durations $\tau < 33\,\mu\mathrm{s}$ (cf. fig. 3.3) the precise fitting is hindered by the fast dispersion of the wavepackets which leads to a rapid

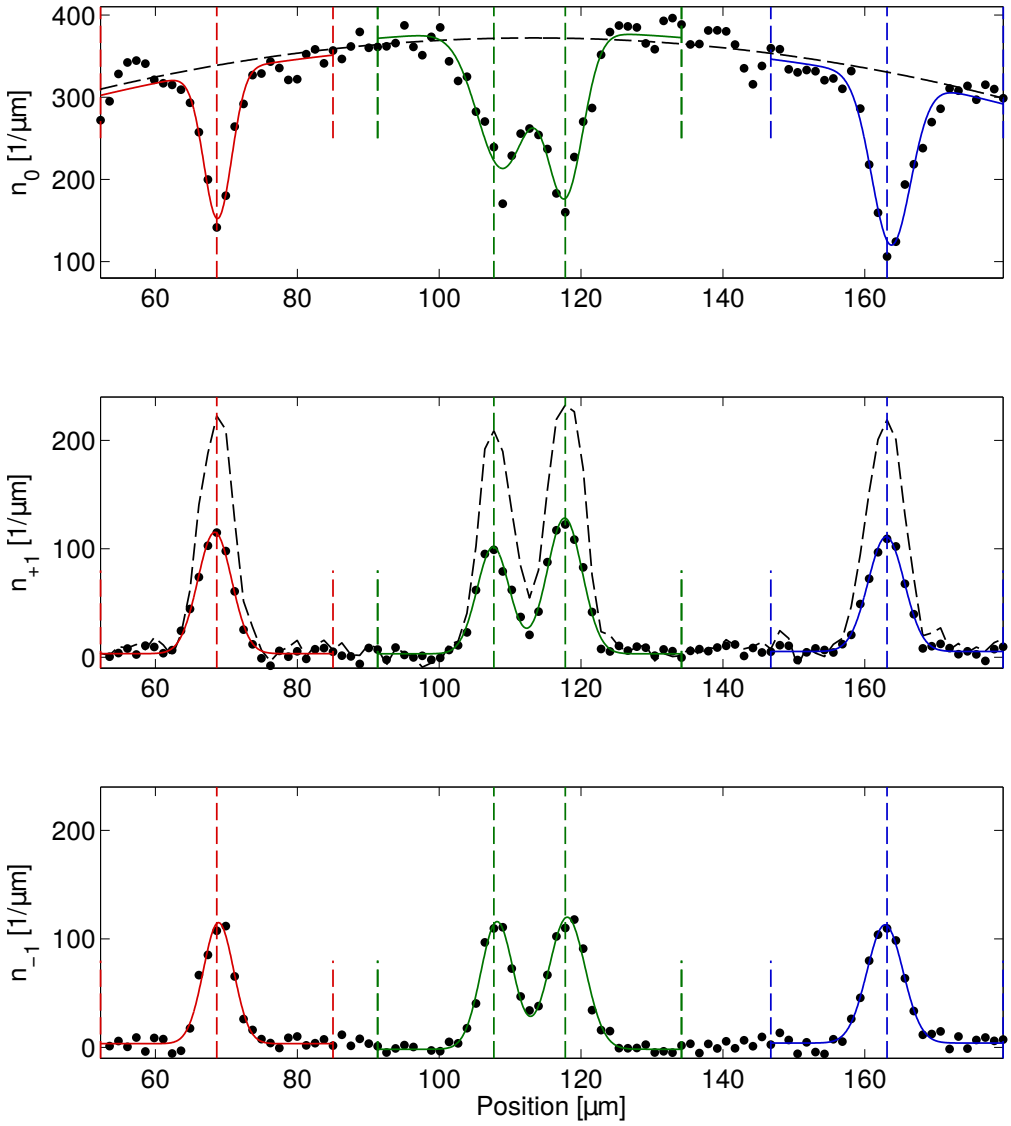

Figure 3.8.: Example for fitting a single experimental realization with 4 solitons after a free evolution of 160 ms. First the rough soliton positions (long vertical dashed lines) are extracted from the peaks in the sum $n_{-1} + n_{+1}$ (dashed black line in n_{+1} plot) of the bright components. Then fit regions are defined around the peaks (short vertical dashed lines). Within each of these region the experimental density (black dots) are fitted with an appropriate model function (solid lines). When the distance between two peaks is below a certain threshold such that independent fitting is not possible a combined fit is used (central fit in green). For $m_\mathrm{F} = 0$ a quadratic fit (black dashed line in n_0 plot) is added to the soliton fit function to account for the background curvature.

decrease of the signal-to-noise ratio in single realizations. In the intermediate regime around $\tau = 33\,\mu s$ this becomes less problematic due to the sufficiently large peak amplitude.

Utilizing these fitting procedures we first analyze the formation process of the solitons more quantitatively. From the evolution shown in fig. 3.3 we already expect a qualitative change in the behaviour of the excitations between $\tau = 33\,\mu s$ and $45\,\mu s$. This change is induced by the generation of phase jumps during the Rabi cycle for sufficiently large rotation angles. As discussed before, in case of a local excitation without introduction of phase jump we would expect the formation of wavepackets. These should be sufficiently close to a Gaussian shape to be able to apply the usual description of the wavepacket as a collective excitation of plane waves with amplitudes following a Gaussian distribution. In real space we therefore model the density distributions as

$$n_{\pm1}(x,t) = A_{\pm1}(t) e^{-\frac{(x-x_0)^2}{2\sigma(t)^2}}. \tag{3.16}$$

Here, we only consider the "bright" components in $m_F = \pm 1$ to reject the noise from total density fluctuations during fitting as outlined earlier. As dispersion relation for these waves we will assume the Bogoliubov dispersion of excitations in the levels $m_F = \pm 1$ for an expansion around the polar phase groundstate $|1,0\rangle$ given by [54]

$$\begin{aligned}\hbar\omega(k) &= \sqrt{(\varepsilon(k)+q)\,(\varepsilon(k)+q+2nc_1)} \\ &= \sqrt{q^2+2qnc_1} + \frac{1+\frac{nc_1}{q}}{\sqrt{1+2\frac{nc_1}{q}}}\,\varepsilon(k) + \mathcal{O}\left(\varepsilon(k)^2\right) \\ &\approx \sqrt{q^2+2qnc_1} + \varepsilon(k) \quad \text{for} \quad q \gg nc_1\end{aligned} \tag{3.17}$$

with $\varepsilon(k) = \hbar^2k^2/(2m)$ describing the kinetic energy, m denoting the mass of ^{87}Rb, q the second order Zeeman shift, and c_1 the spin interaction constant. Our experiment with $q \approx h \times 56\,\text{Hz}$ and $nc_1 \sim h \times 2\,\text{Hz}$ is well in the limit where the dispersion is described by the quadratic dependence of $\varepsilon(k)$. Therefore, we expect a dispersive broadening of the wavepacket with

$$\sigma(t) = \sigma_0 \sqrt{1 + \frac{1}{\sigma_0^4}\left(\frac{\hbar t}{2m}\right)^2} \tag{3.18}$$

with σ_0 denoting the initial RMS width and a decay of the wavepacket amplitude

$$A(t) = A_0 \frac{\sigma_0}{\sigma(t)} \tag{3.19}$$

constrained by the normalization of the wavefunction with initial density amplitude A_0.

Figure 3.9 shows the amplitudes and RMS widths extracted from Gaussian fits to the wavepackets for different rotation amplitudes. The black lines indicate the wavepacket dynamics expected from eqs. (3.18) and (3.19) with σ_0 and A_0 defined

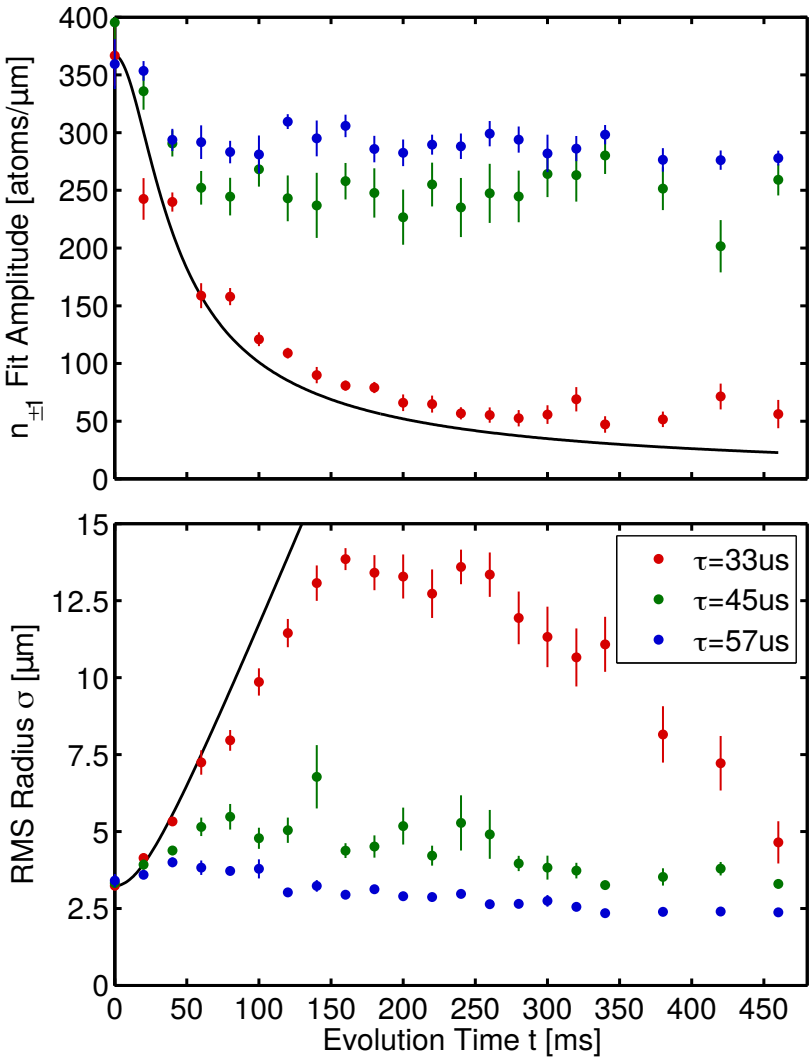

Figure 3.9.: Amplitudes and RMS widths of Gaussian fits to the wavepackets emerging from a local spin rotation for different rotation amplitudes. The rotation amplitudes are controlled by the duration τ of the local rotation (cf. fig. 3.9). The data points are obtained from individual fits to the density profiles of approx. 9 experimental realizations. Here, to each $m_\mathrm{F} = \pm 1$ profile a superposition of two Gaussian functions is fitted. For rejecting total density noise only these two hyperfine levels are evaluated and their results averaged. The black lines are calculated via eqs. (3.18) and (3.19) with A_0 and σ_0 set to the initial values extracted for $\tau = 33\,\mu\mathrm{s}$ at $t = 0$. Only results obtained from the fit to the right one of the two excitations generated by the local rotation is plotted here. The error bars indicate the 1 s.d. interval of the mean over the single realizations and $m_\mathrm{F} = \pm 1$ levels.

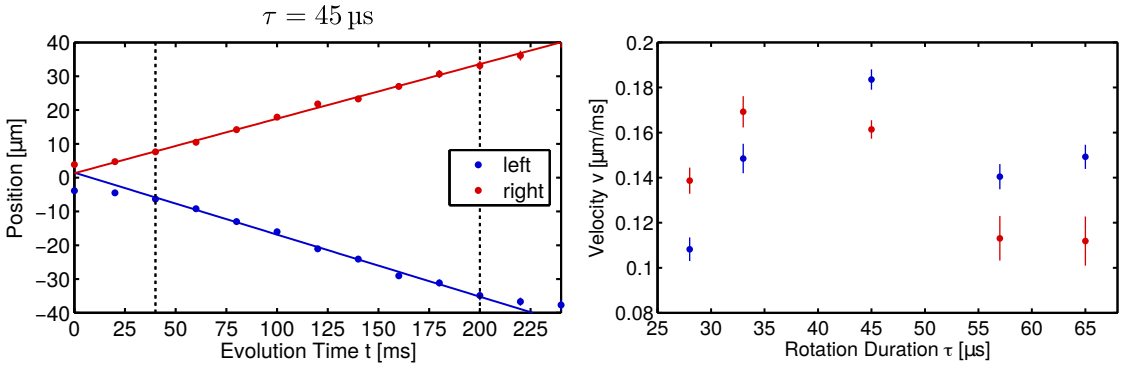

Figure 3.10.: Linear propagation and velocities of solitons and wavepackets generated by a local spin rotation. The left plot shows the propagation of a pair of solitons extracted from fits to the $m_F = \pm 1$ density profiles. By applying linear fits to the positions between $t = 40\,\text{ms}$ and $200\,\text{ms}$ (indicated by vertical dashed lines) the velocities are extracted and plotted in the right graph. The values extracted for wavepackets ($\tau \leq 33\,\mu\text{s}$) increase with the rotation amplitude ($\propto \tau$) and settle back down to a fixed level for solitons ($\tau \geq 45\,\mu\text{s}$). On the left the error bars indicate 1 s.d. interval of the mean and on the right of the statistical fit error.

by the initial values for the duration $\tau = 33\,\mu\text{s}$ of the local rotation. For small rotations with $\tau \leq 33\,\mu\text{s}$ this curve describes the evolution of the wavepackets with reasonable accuracy. As soon as the rotation introduces phase jumps ($\tau \geq 45\,\mu\text{s}$) the amplitude does not decay beyond a certain value and also the width shows no divergence, as expected for the non-dispersive propagation of solitons. In the experiment we observe that the initial formation of the solitons is still dominated by the dispersive behaviour roughly described by the time evolution of Gaussian wavepackets. This is associated to the dynamical formation of the self-consistent solition solution within the first $\sim 40\,\text{ms}$ of the evolution. Here, the reformation of the wavefunction profile seems to transpire via emitting plane waves. Once the wavepacket reaches the shape of the soliton this process stops and the solitonic behavior of the excitation takes over.

For the fitting procedure applied in this evaluation the fit function always consisted of two Gaussian functions, which, for short evolution times t, overlapped. Therefore, the fit amplitude does not correspond to the peak amplitude observed in the density profiles but a smaller value, depending on the overlap of the wavepackets. This procedure is motivated by the experimentally observed movement and spreading of the excitations. This behaviour cannot be described by the purely quadratic dispersion of eq. (3.17) but also requires a linear component. In this scenario the initially stationary wavepacket generated by the local rotation is a superposition of two counterpropagating wavepackets moving at the same speed of sound characteritic for the linear dispersion. Nevertheless, the good agreement between the experimental data and the broadening and associated amplitude decay predicted from eqs. (3.18) and (3.19) implies that the Bogoliubov dispersion accurately models the quadratic part. That this is the case is not clear because the amplitude of excitations generated by the local rotations extend beyond the limit of small excitations, for which the Bogoliubov approximation is derived.

3.4.4. Extraction of the Soliton Density Profile

Due to the experimental resolution of the soliton profile, it is possible to directly compare the measured density profiles with the soliton profiles provided by eq. (3.8). For this, we plot the density profile of a single realization of a soliton after $t = 100\,\mathrm{ms}$ of evolution in fig. 3.11, where we bin[5] 3 adjacent pixels, corresponding to our optical resolution in the image plane. In order to reduce imaging noise we further apply a fringe removal algorithm [157]. To constrain the soliton parameters in eq. (3.8) we extract the required values independently; i.e. we do not rely on a fit to find a closely matching function but extract parameters consistent with the expected motion. For this we determine the velocity to $v = (x(t) - x(t=0))/t$ from the fit positions at the corresponding times. The inverse width κ is extracted as average of sech^2 fits to the $m_\mathrm{F} = \pm 1$ densities. Here, the profiles are convoluted with a Gaussian with RMS width of $1.2\,\mu\mathrm{m}$ to account for the finite resolution of the imaging setup [64]. To fix the background density we set n_0 to the value of the $m_\mathrm{F} = 0$ density around the soliton. To determine the amplitude of the polarization $c_{\pm 1} = \sqrt{(1 \pm S_z)/2}$ we determine the $m_\mathrm{F} = \pm 1$ pseudo-spin imbalance S_z; at this point, the phases of these complex parameters are irrelevant because we are only interested in the densities. The projection $S_z = (N_{+1} - N_{-1})/(N_{+1} + N_{-1})$ in the 2-level pseudo-spin system of the bright components is calculated via the atom numbers $N_j = \int dx\, n_j$ integrated over ± 3 RMS radii of the soliton, where $N_{+1} + N_{-1} \approx 2000\,\mathrm{atoms}$. Finally, to determine the relative amplitude η between bright and dark components and total density depletion δn we also need to estimate the chemical potential. For this, we apply the local density and TF approximations in longitudinal direction and therefore assume a cylindrical symmetric and longitudinally homogeneous trap. By integrating the radial TF profile

$$|\psi_0|^2 (r_\perp) = \frac{1}{c_0}\left(\mu - \frac{1}{2} m \omega_\perp^2 r_\perp^2\right) \tag{3.20}$$

over the transversal plane up to the TF radius $r_\mathrm{TF} = \sqrt{2\mu/m}/\omega_\perp$ we obtain the 1d density n_0 and can then solve for the chemical potential [44]

$$\mu = \omega_\perp \sqrt{\frac{m n c_0}{\pi}}. \tag{3.21}$$

The parameters used for the plotting the model predictions of the soliton profiles shown in fig. 3.11 are:

$$\begin{aligned} v &= -0.16\,\mu\mathrm{m/ms} \\ \kappa &= 0.31\,\mu\mathrm{m}^{-1} \\ n_0 &= 435\,\mathrm{atoms}/\mu\mathrm{m} \\ \boldsymbol{c} &= \begin{pmatrix} 0.73 \\ 0.68 \end{pmatrix} \\ \mu &= h \times 518\,\mathrm{Hz} \end{aligned}$$

[5] Here "binning" means averaging over 3 pixels without overlap with neighboring averaging interavlas.

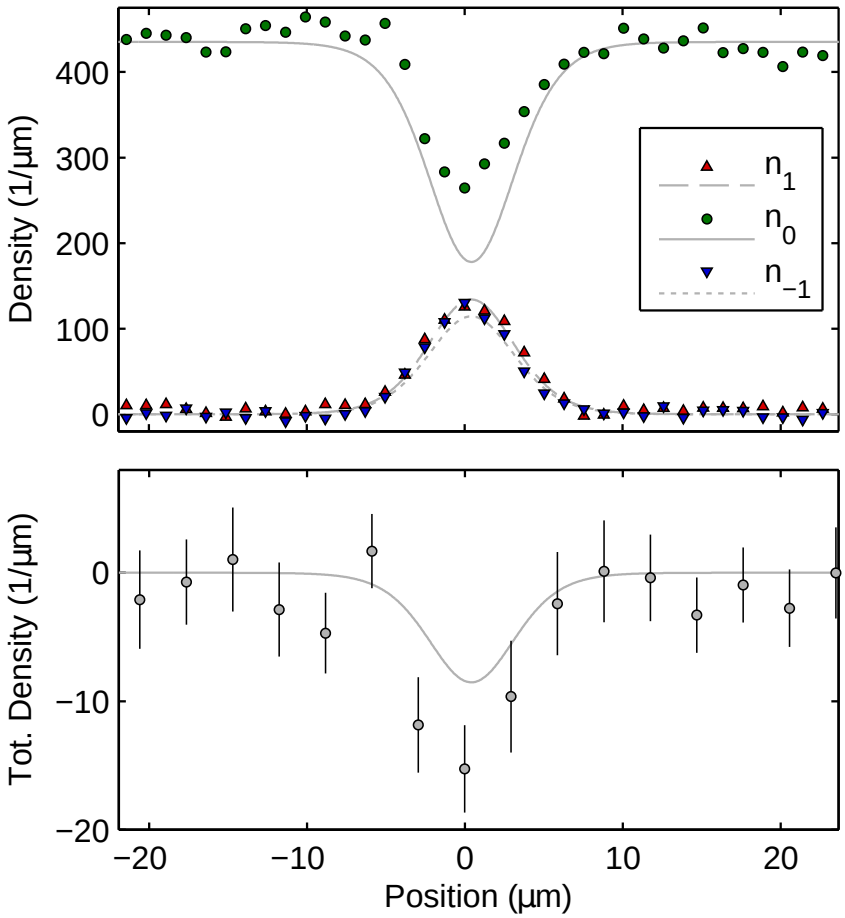

Figure 3.11.: Density profiles of a single vector soliton after 100 ms of free evolution. The markers correspond to the experimentally measured 1d densities binned over 3 pixels (1.26 µm in the image plane of the atoms). In the upper plot values of a single realization are shown. The lines are density profiles calculated from eq. (3.8) convoluted with a Gaussian with 1.2 µm RMS width to simulate the resolution of our imaging setup [64] and a fringe removal algorithm is applied to remove noise from the pictures [157]. The soliton parameters are independently extracted (see text). The bright components in $m_\mathrm{F} = \pm 1$ are occupied by $N_{+1} \approx 1100$ atoms and $N_{-1} \approx 860$ atoms, respectively. The lower plot shows the depletion in the total density associated with the solitons of Manakov type. To obtain the values plotted here we subtract density profiles with and without solitons. The data points are averages over 20 realizations; error bars mark the 1 s.d. interval of the mean. This figure is similar to the one shown in [83].

For the calculation of μ the value $c_0 \approx 5.169 \cdot 10^{-51}\,\mathrm{Jm}^3$ in accordance with the scattering lengths given in [53] has been used.

For the profiles in the upper plot the $m_\mathrm{F} = \pm 1$ model predictions fit the measured data well. For $m_\mathrm{F} = 0$, however, the measured peak depletion shows a significantly larger value than the model. We attribute this deviation to the short time-of-flight period to separate the m_F components during SG imaging (see section 2.5.1). After the SG pulse the m_F components are spatially separated such that no interactions occur between the different components. Thus, the states in these single component condensates does not resemble a self-consistently stabilized soliton solution anymore; in $m_\mathrm{F} = 0$ such a single-component dark soliton should have a width $1/\kappa \sim \sqrt{2}\xi_\mathrm{d} = 0.5\,\mu\mathrm{m}$. Therefore, we would expect the background density to partially fill up the depletion in $m_\mathrm{F} = 0$ during the short time-of-flight. The much lower density of the bright components may be small enough that no significant dynamical expansion occurs during this period.

Due to this dynamical deformation of the density profiles during imaging the measured total density does not correspond to the actual profile during the evolution. Therefore, to resolve the small total density depletion of $\sim 2\,\%$ expected for our soliton parameters we image without SG separation. Additionally, we average over 20 realizations and subtract subtract density profiles without solitons. With this we are able to determine a depletion of 100 atoms in the range of the soliton, corresponding to a peak depletion amplitude of approx. 3 %. Like the single m_F profiles, also this parameter is in good agreement with the Manakov vector soliton model.

3.4.5. Propagation in Harmonic Traps

In homogeneous potentials, i.e. the exact Manakov scenario for which the soliton solutions eq. (3.8) have been derived, the solitons propagate at a fixed velocity between zero and the speed of sound c_s. More complicated external potentials, for which a harmonic trap certainly is a classical example, the motion of solitons is perturbed and even more complex dynamics becomes relevant.

At first, let us consider again the measurement associated to the initial time after soliton formation (cf. figs. 3.3 and 3.9). Tracking the average positions of solitons (and also wavepackets) over time after the initial formation we observe a linear propagation over $\sim 200\,\mathrm{ms}$ (see fig. 3.10). This is expected for both wavepackets and solitons on a homogeneous density background. While for wavepackets the velocity seems to increase with the local rotation duration τ it decreases again in the soliton regime. This effect may be connected to the change of atom number in the initial wavepackets which increases with τ. Additionally, the velocities for the excitations propagating to the left and right of the local rotation exhibit different velocities. The left wavepacket is always slower than the right one while for the solitons the situations is reversed.

For solitons this phenomenon can be understood by taking into account the curved density background provided by the harmonic trap. The rotations are not performed perfectly in the center of the trap but slightly to the right. This means that the right excitation travels in the same direction as the total density gradient

while the left one propagates in a roughly constant trap background. As we will discuss later, the kinetic properties of the BDB solitons seem to be derived from the properties of a single component dark soliton with the same amplitude as the dark component of the vector soliton. For dark solitons propagating in an inhomogeneous density the amplitude of the density depletion stays constant. This means that the darkness, i.e. the amplitude relative to the background, and associated with this quantity also the velocity changes. When propagating towards a lower density the soliton becomes slower. Since the right soliton in our experiments propagate, on average, in a slightly lower background density it is therefore expected for its velocity to be smaller than value extracted for the left soliton.

For single component dark solitons on a stationary background the equation of motion $m\ddot{x} = -\partial_x V/(2m)$ [158] is modified by a factor of 1/2 in comparison to a classical object. In harmonic traps $V = m\omega^2 x^2/2$ with frequency ω this leads to a reduced oscillation frequency of $\omega/\sqrt{2}$. For vector solitons with bright components the situation is similar but modified by the interaction of the bright components with the trapping potential. For 2 component dark-bright vector solitons this leads to [141]

$$\ddot{x} = -\frac{1}{2m}\left(1 - \frac{\bar{N}_\mathrm{B}}{4\sqrt{1+\left(\bar{N}_\mathrm{B}/4\right)^2 - V(x)/\mu}}\right)\partial_x V(x) \tag{3.22}$$

where $\bar{N}_\mathrm{B} = N_\mathrm{B}/(\sqrt{2}\xi_\mathrm{d} n_0)$ denotes the atom number in the bright component relative to the atom number per healing length ξ_d of the background. Since the left term in eq. (3.22) is always $\leq 1/2$ for vector solitons we would therefore qualitatively expect a behavior similar to that of the single component dark solitons. However, the filling of the soliton due to the bright component will reduce the effective force $-\partial_x V(x)$ on the soliton such that the oscillation frequency will be smaller compared to the single component scenario.

For an experimental analysis of the motion of the BDB vector solitons we generate two pairs in the WG trap (see section 3.5.2 for details of the preparation), which has a roughly harmonic trapping potential in longitudinal direction with trap frequency $\omega_\parallel = 2\pi \times 1.6\,\mathrm{Hz}$. Figure 3.12 shows the ensuing oscillation in the trap. For such a harmonic potential V eq. (3.22) implies a soliton frequency of

$$\omega^2 \approx \frac{\omega_\parallel^2}{2}\left(1 - \frac{\bar{N}_\mathrm{B}}{4\sqrt{1+\left(\bar{N}_\mathrm{B}/4\right)^2}}\right) \tag{3.23}$$

for an oscillation where $\bar{N}_\mathrm{B} \gg V(x)/\mu$. As expected from this, we observe a soliton oscillation frequency of $\omega \approx 0.6\,\mathrm{Hz}$ which is smaller than the single component soliton frequency $\omega_\parallel/\sqrt{2} \approx 2\pi \times 1.1\,\mathrm{Hz}$ [158]. However, applying eq. (3.23) with a bright atom number[6] of $N_\mathrm{B} = N_{+1} + N_{-1} \approx 2000$ atoms (cf. fig. 3.14), and with the other parameters similar to the ones given in section 3.4.4 (leading to

[6]The summation of the bright atom numbers is justified because the symmetry of the Manakov NLSE allows the rotation of the complete bright component population to a single hyperfine state. Thus, after rotation the system is a two-component dark-bright system, for which eq. (3.22) is valid [142].

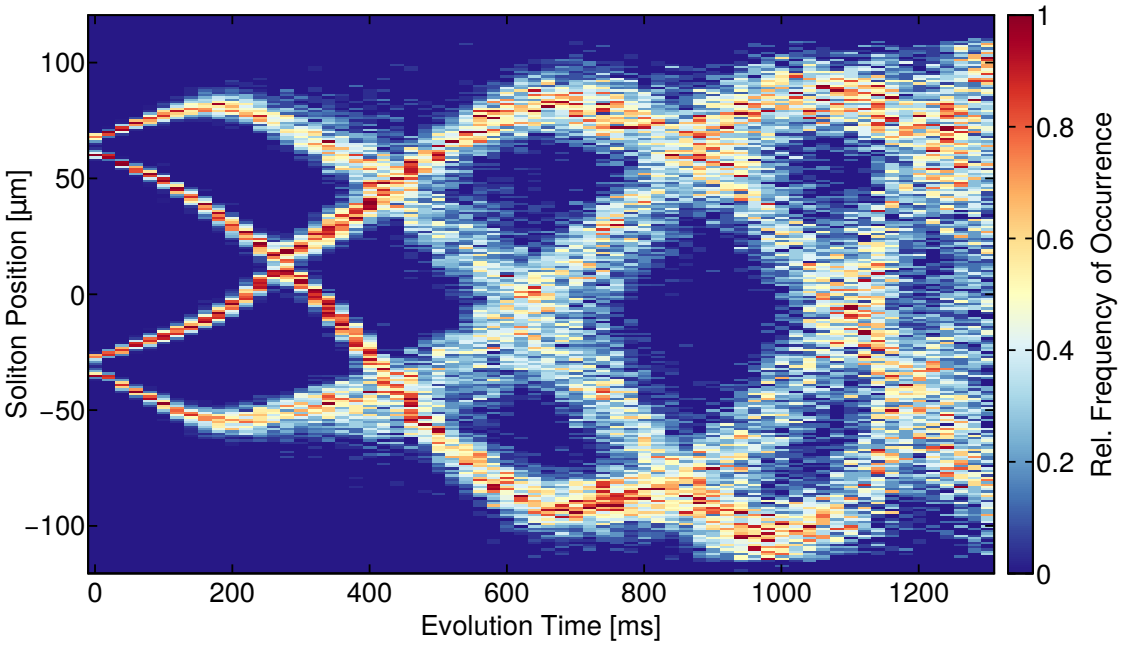

Figure 3.12.: Histogram of soliton positions for an oscillation in a harmonic trap over an extended period of time. Two soliton pairs are generated as initial condition and then freely propagate in the harmonic oscillation potential with trap frequency $\omega = 2\pi \times 1.6\,\mathrm{Hz}$ centered around the zero position. The positions are extracted from Gaussian fits to the $m_\mathrm{F} = \pm 1$ components. Every 20 ms the evolution is sampled and histograms of the positions are calculated. For each time the histogram is independently normalized to the same value independently to enhance the visibility of the spread of positions at late times. The oscillation frequency of the solitons is roughly $1/800\,\mathrm{ms} \approx 0.6\,\mathrm{Hz}$. Over time the soliton amplitude decays (see fig. 3.14) such that the turning points, where the dark component becomes black, move outward. The bending of soliton trajectories towards the trap center around $t = 160\,\mathrm{ms}$ may be caused by a decrease of the trap density due to a slight breathing of the density in the harmonic potential.

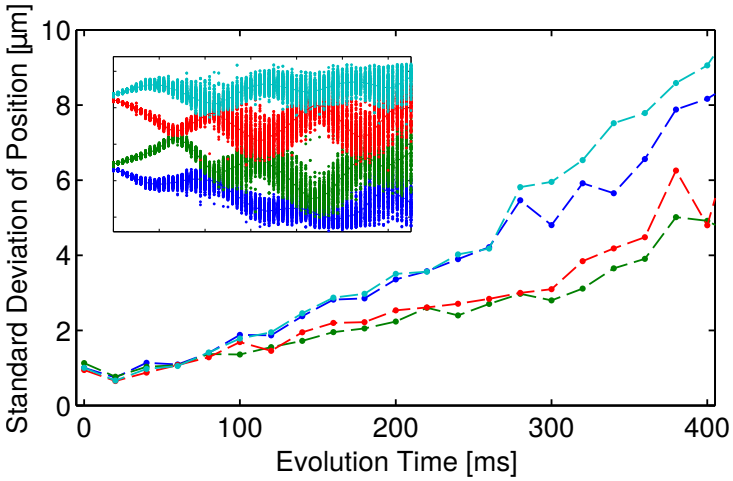

Figure 3.13.: Fluctuations of the soliton position around the extracted average position. In each single realization the fitted solitons are ordered according to their position. The inset shows this ordering into 4 different groups marked by the colors for the result of each single realization (the axes of the inset are the same as in fig. 3.12). The plot shows the standard deviation of the fit positions within each of these groups for evolution times prior to the second collisions at around 450 ms. The solitons which are located farther from the trap center (blue and cyan) consistently show larger position fluctuations than the "inner" solitons (red and green).

$\bar{N}_\mathrm{B} \approx 12$), results in an oscillation frequency $\omega \approx 0.3\,\mathrm{Hz}$, which is much slower than the observed value. This is the case because eq. (3.23) does not account for the soliton-soliton interactions, which modify their oscillation frequency [113, 137, 159].

Additional to the oscillation fig. 3.12 clearly shows that the spread of the soliton position strongly increases over time. This effect may originate from systematic fluctuations of the initial soliton stemming from fluctuations of the local Rabi frequency amplitude. On the other hand, also scattering with thermal excitations of the background affect the soliton motion [108, 160]. While the former should be equal for all solitons around 200 ms a clear increase of the position spread is visible for the solitons at their turning point at the trap edges (see fig. 3.13). Because the non-condensed part of the background predominantly occupies the trap edges in a harmonic trap [47] it is conceivable that mostly thermal scattering is responsible for the increase of fluctuations in the position and therefore also in the velocity.

Experimentally we also observe a decay of the soliton amplitude. To quantify this evolution we consider two observables which should behave similarly: the sum of the atom number N_B in both the bright components, summed over a range of ± 3 RMS radii, and the fit amplitude to the $m_\mathrm{F} = \pm 1$ density profiles. Both show an exponential decay (see left plot of fig. 3.14) with $1/e$ lifetime of $(1.40 \pm 0.02)\,\mathrm{s}$ and $(1.49 \pm 0.02)\,\mathrm{s}$, respectively.

N_B shows two jumps around 250 ms and 450 ms, which correspond to the times of collision between the solitons in fig. 3.12. On the mean field level, soliton collisions should conserve the atom number N_B [141, 143]. Therefore, these jumps may be a sign of a non-elasticity in the soliton collisions in our system, associated with the

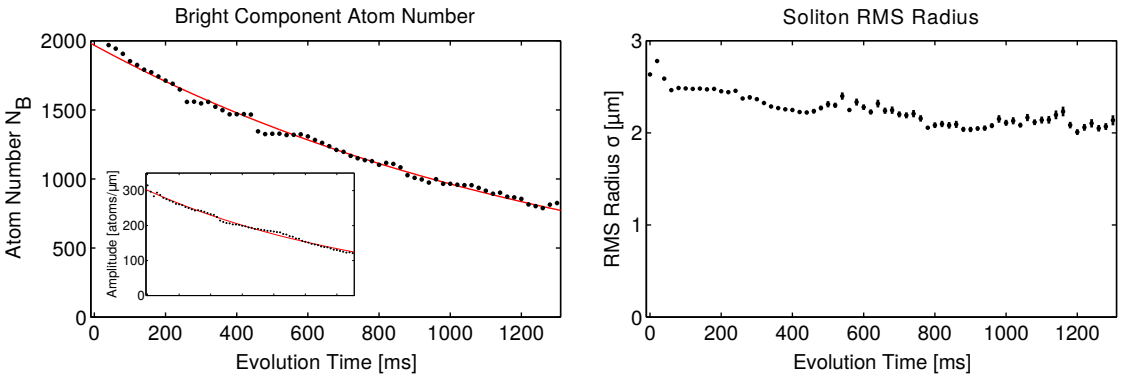

Figure 3.14.: Bright component atom numbers and RMS radius extracted for the oscillations shown in fig. 3.12. The left plot (and inset) show the decay of the atom number $N_\mathrm{B} = N_{+1} + N_{-1}$ (fit amplitude) of the bright components averaged over all solitons and realizations. The red line is a fit of an exponential function $f(t) = a\exp(-t/t_0)$ with $t_0 = (1.40 \pm 0.02)\,\mathrm{s}$ ($t_0 = (1.49 \pm 0.02)\,\mathrm{s}$). On the right the corresponding average values of the RMS with of the fits to the solitons are shown. While the soliton amplitude decays its width stays almost constant over the observed time interval. The error bars in all figures show the 1 s.d. interval of the mean values; where no error bars are visible the error is smaller than the plot markers.

breaking of the integrability of the Manakov model.

Additionally, scattering with perturbation potentials, like here in the form of the confining harmonic trap, is possible and has been studied for single-component dark solitons [22]. The acceleration of solitons leads to the emission of phonons [161], which, in a harmonic trap, may be re-absorbed [160]. In anharmonic potentials phonons may dephase which suppresses the re-capture and enhances the decay rate of the soliton. In multi-component solitons the dark component generates an effective potential for the bright components [100, 130]. Thus, a damping of the dark component may lead to radiating atoms out of the soliton to maintain the soliton solution. Additional to the scattering with an external potential, also interactions with the thermal part of the atomic cloud leads to dissipation [22]. The transverse extent of the dipole trap breaks the integrability of the Manakov model and allows scattering between thermal excitations and dark solitons, which leads to a decay of the darkness and an acceleration of the soliton [108]. For an initial darkness $\lesssim 0.4$ the amplitude decay can roughly be approximated by an exponential function, where the lifetime $t_0 \propto T$ depends on the temperature T.

This is in good agreement with the results observed in fig. 3.14. A more elaborate study of a 2-component dark-bright soliton in an harmonic trap suggests that the presence of the bright components reduces the damping in comparison to a single-component dark soliton [159]. This is conceivable because the increase of the soliton width due to the presence of the bright components places the soliton deeper in the 1d limit, where the transverse instability is less relevant [141]. Nevertheless, similar to scattering off a potential, both decay channels lead to a anti-damping of the osicllations. This occurs due to the coupling of soliton amplitude and velocity; a soliton of vanishing amplitude or energy has the largest velocity $v \approx c_\mathrm{d}$. Therefore,

in the harmonic trap the inversion points of the soliton motion, which is also the position at which the dark soliton component depletes the full background (becomes "black"), move outwards. This can nicely be observed in fig. 3.12.

Curiously, while the amplitude shows a significant decay we observe that the soliton width stays almost constant (see right plot of fig. 3.14). For atom loss from the soliton both a decrease in amplitude as well as a decrease of the width would reduce the atom number contributing to the soliton. For single-component dark solitons, in fact, the width would change together with the amplitude because the equivalent form of eq. (3.10) with an equal sign couples both quantities. For the vector soliton case, however, both quantities are independent and indeed, our experiment shows that the width of the vector solitons only weakly couples to the decay channel.

3.4.6. Effective Interactions

In the previous discussion of the BDB vector solitons we have seen that the interactions between dark and bright components significantly alter the soliton solution compared to single-component solitons. Nevertheless, many of the dynamical properties of its propagation the vector soliton inherits, at least analytically, from single-component dark solitons. Further, the dynamics of the bright soliton components during the collisions discussed in section 3.5.2 are very similar to the dynamics of 2-component bright solitons described in [23]. This suggests, that an effective description of the GPE (3.6) should be possible which decouples the dark and bright components $\tilde{\psi}_0$ and $\tilde{\psi}_\pm$ such that

$$\tilde{\psi}_0 = \left(-\frac{\hbar^2\nabla^2}{2m} + \tilde{V}_{\text{ext}} + \tilde{g}_{00}\left|\tilde{\psi}_0\right|^2\right)\tilde{\psi}_0, \tag{3.24}$$

$$\tilde{\psi}_\pm = \left(-\frac{\hbar^2\nabla^2}{2m} + \tilde{V}_{\text{ext}} + \tilde{g}_{\pm}\left|\tilde{\psi}_\pm\right|^2 + \tilde{g}_{+-}\left|\tilde{\psi}_\mp\right|^2\right)\tilde{\psi}_\pm. \tag{3.25}$$

with effective potential $\tilde{V}_{\text{ext}}$ and effective intra-species interaction constants $\tilde{g}_{00}$ and $\tilde{g}_\pm$ and inter-species interaction $\tilde{g}_{+-}$ between the bright components $\psi_\pm$ in $m_{\text{F}} = \pm 1$. These effective interactions are obtained by rewriting the density $|\psi_j|^2$ of the coupling term. Here, we also changed the notation from ψ_j to $\tilde{\psi}_j$ to indicate that this effective description only approximately describes the corresponding fields. Here, the effective interactions will be reduced in strength because of the repulsion provided by the respective other soliton components. Similarly, for the existence of bright components, effective attractive interactions $\tilde{g}_\pm < 0$ are required, although the underlying interactions of ^{87}Rb are purely repulsive.

The procedure for decoupling the GPEs of the bright and dark components is based on the scheme applied in [162] and also in [127, 163] for eliminating a highly occupied level in a two-component system. However, the procedure applied here will diverge at crucial points. For separating the GPEs two assumptions are applied: we assume that the total background density profile $n_0(x)$ (in analogy to the constant background in eq. (3.8)) of the system without the soliton[7] is

[7] Here, the excitation does not necessarily have to be a soliton but can also be a general excitation which fulfills the two relevant assumptions.

well-described by a TF profile (given by eq. (2.3)) and the density perturbations of the bright and dark components have the same functional form. Given that $|\psi_{-1}|^2 + |\psi_{+1}|^2 = af(x)$, the second condition implies that the dark component density is described by $|\psi_0|^2 = b(1 - f(x))$, with a and b being some real numbers. Thus, the densities can be expressed in terms of a perturbation $\delta n_0(x)$ of the total density as

$$|\psi_0|^2 + |\psi_{-1}|^2 + |\psi_{+1}|^2 = n_0 + \delta n_0. \tag{3.26}$$

Based on the assumption of the equal shape of the density profiles in all components this perturbation may be expressed in terms of the bright component densities as

$$\delta n_0 = \frac{D}{D_0 - D} \left(|\psi_{-1}|^2 + |\psi_{+1}|^2 \right). \tag{3.27}$$

Here, the explicit form of eq. (3.8) was assumed for $\psi_{\pm 1}$ to derive the prefactor in terms of the darkness D of the total density and darkness D_0 of the $m_\mathrm{F} = 0$ component of the BDB vector soliton. With these two relations the dark component density $|\psi_0|^2$ can be eliminated from the bright components in the GPE (3.6) to obtain eq. (3.25) with the effective couplings[8]

$$\tilde{g}_\pm = \left(1 - \frac{1}{\eta^2}\right) g_\pm, \tag{3.28}$$

$$\tilde{g}_{+-} = \left(\frac{g_{+-}}{g_\pm} - \frac{1}{\eta^2}\right) g_\pm. \tag{3.29}$$

Here, the real couplings $g_\pm$ and g_{+-} are associated to the intra- and interspecies scattering lengths of the bright components $m_\mathrm{F} = \pm 1$, respectively (cf. fig. 3.5). Note that the elimination simultaneously rescales the amplitude of an external potential such that $\tilde{V}_\mathrm{exp} = (1 - g_\pm/g_{00})V_\mathrm{exp}$. An analogous procedure may be applied to also decouple the dark component from the bright ones.

According to its definition the relative amplitude η of the bright vector soliton components is always < 1, which implies $\tilde{g}_\pm < 0$. Thus, the total density depletion induced by the vector soliton induces effective attractive interaction between the bright components. For the typical experimental soliton parameters given in section 3.4.4 $1/\eta^2 \sim 1.03$, such that $\tilde{g}_\pm < 0$ and $\tilde{g}_{+-} < 0$. Here, the effective scattering lengths are $\tilde{a}_\pm \approx -3.4 a_\mathrm{B}$ and $\tilde{a}_{+-} \approx -2.4 a_\mathrm{B}$. To verify the validity of this effective description we may approximate the bright components of eq. (3.25) as a single component bright soliton with interaction constant $g = \tilde{g}_\pm + \tilde{g}_{+-}$. When calculating the density amplitude of the bright soliton solution given by eq. (3.2) we arrive at a value of approx. 210 atoms/µm, which is in good agreement with the combined amplitude measured in fig. 3.11.

For small velocities and large soliton widths, when η becomes close to unity, $\tilde{g}_{+-}$ may also become attractive. Here, enforced by the strong interspecies repulsion between $m_\mathrm{F} = \pm 1$ and $m_\mathrm{F} = 0$, the approximations should still hold true but the difference of scattering lengths displaces the system far from the Manakov limit.

[8] Note that $1 + D/(D_0 - D) = 1/\eta^2$. Because away from the soliton the background is exclusively given by the $m_\mathrm{F} = 0$ population the corresponding density is expressed as $n_0(x) = (\mu - V_\mathrm{ext}(x))/g_{00}$ in terms of the $m_\mathrm{F} = 0$ interactions.

Therefore, different phenomena may be expected to emerge. It will be interesting to investigate whether the soliton interactions discussed in the next sections are still described by the Manakov predictions in this regime. Particularly, the soliton may transition to a state similar to a self-bound droplet [164]. However, for the collisions considered in the following, effects due to the presence of the dark component is expected [156].

3.5. Soliton Collisions

In the previous section we discussed the requirements for the generation of solitons in the experiment, the initial formation of these excitations. Further, we compared the measured density profiles with the predictions of the Manakov model and confirmed its applicability to the parameter regime of our experiment. Clearly, one of the most striking aspects of solitons is their non-dispersive propagation, shown in section 3.4.5. This may be viewed as particle-like behavior in the sense of classical objects. Actually, for solitons this analogy goes beyond their propagation but is also applicable to their interactions: they exhibit close-ranged interactions, which may change their state during collisions, and, after collision, retain this changed state.

Of course, the actually possible range of interactions phenomena between solitons are much richer than the simple case outlined above. Vector solitons combine the interaction effects of dark and bright components and therefore lead to a wider range of interactions and even bound states [131, 141]. Going beyond the mean-field approximation, also quantum effects influence correlations between phase and position or momentum of the soliton via their interactions [165]. While the latter effects require a tremendous experimental precision and stability, it is usually feasible to access these particle-like interaction effects outlined in the first paragraph .

3.5.1. Collisions in Single Component Systems

In general, for single-component Manakov solitons two types of interactions occur: "repulsive" and "attractive" collisions. These terms are related to the total density distributions describing the system at the time of closest approach. Here, "attractive" describes a singly peaked profile in which both solitons overlap while a "repulsive" interaction features a density minimum between the colliding solitons. For bright solitons these scenarios can be understood as interference between two patches of the coherent wavefunction, which depends on the phase offset of these patches [166]. In contrast, for dark solitons only repulsive collisions occur [167].

As an example, let us consider a pair of counter-propagating bright solitons with the same amplitude and velocity generated from the same coherent cloud. Then, only the position dependent phase evolution in eq. (3.11) will be different but of same absolute value and opposite sign. Therefore, the initial phase offset from the common coherent reference fully determines the interference of the solitons. Thus, a phase difference of π will lead to destructive interference ("repulsive" collision)

and a vanishing phase difference induces fully constructive interference ("attractive" scenario).

3.5.2. Vector Soliton Collisions

In comparison to the single-component scenario vector solitons allow for a much larger variety of collision dynamics by combining effects of the bright and dark constituents. As we have seen before, the motion of the solitons seems to be reminiscent of the dark soliton propagation. Here, we will further extend the conceptual separation between bright and dark components. Across collisions the dark components stay approximately invariant; i.e. they do not participate in collision dynamics. The bright components, on the other hand, constitute a coherent 2-component internal degree of freedom similar to a pseudo-spin 1/2 particle. We will see that soliton collisions change this internal polarization. In the following we will work out the experimental control required for the observation of this dynamics and discuss the properties and show an application of this behavior in the experiment.

3.5.2.1. Experimental Measurement

Starting from the procedure discussed in section 3.4.1 a pair of solitons can be generated in the experiment at arbitrary positions. Because the manipulation involved in this procedure is restricted to a spin rotation on a localized patch the remaining system is not perturbed. Thus, multiple local spin rotations can be combined to generate multiple soliton pairs as it shown in fig. 3.12. In principle, it is even possible to apply the rotations in parallel to simultaneously seed the desired number of solitons in the system. However, when combining multiple frequencies in an AWG signal undesired side-bands arise close to the required frequencies. Although the spectral power in these frequency ranges is small compared to the desired frequencies they still generate measurable perturbation on the background. To eliminate these effects we chose to generate the single pairs sequentially. Nevertheless, this happens "quasi-simultaneously" because the time scale of the local Rabi oscillation is small compared to the density interaction timescale and therefore also to the soliton movement in the system.

Applying this method we generate two pairs of solitons in our system and investigate the collision of the two inner solitons as shown on the right side of fig. 3.15. The local rotation generates vector solitons with equal populations occupying the bright components. Strikingly, as shown on the bottom of the left half of the figure, the bright components exchange population during the collision. This dynamics is associated to the soliton polarization $\boldsymbol{c} = (c_{+1}, c_{-1})^T$ in eq. (3.8). Note here, that for the observation of this effect it is crucial to cancel the magnetic field gradient to high precision as is discussed in section 3.5.3.

To investigate this phenomenon further it is necessary to control the phases between the bright components. Employing the pseudo-spin 1/2 description of the two levels $m_\mathrm{F} = \pm 1$ our method generates solitons without imbalance in the populations N_{m_F}, i.e. $S_z = (N_{+1} - N_{-1})/(N_{+1} + N_{-1}) = 0$. In the spin sphere picture this corresponds to expectation values on the equator. Analogous to the

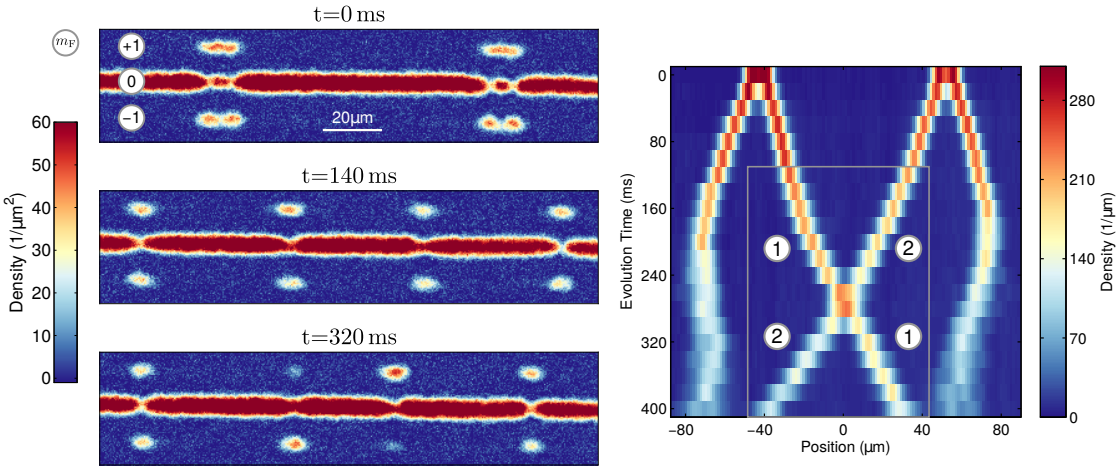

Figure 3.15.: Atomic Densities during collision of two vector solitons. The left plots show absorption pictures for the generation of two soliton pairs, after some free evolution and after collision. During the collision the bright components exchanged populations such that after collision the solitons have opposite atom number imbalances in the $m_F = \pm 1$ components. The plot on the right shows the propagation of the bright parts of the soltions as proxy for the soliton movement. Here, for each evolution time approx. 45 – 90 realizations have been averaged. The apparent decay of the bright component amplitude results from this averaging over realizations with fluctuating soliton positions. Pseudo-spin resolved data of the cutout marked by the rectangle are shown in fig. 3.16. The numbers (1) and (2) define the order of the solitons for the differences $\Delta\varphi_L$ (see text). The data on the left is shown for a phase difference of $\Delta\varphi_L^i \approx 215°$ while the data on the right is an average over all phases (cf. fig. 3.17 for the measured phases).

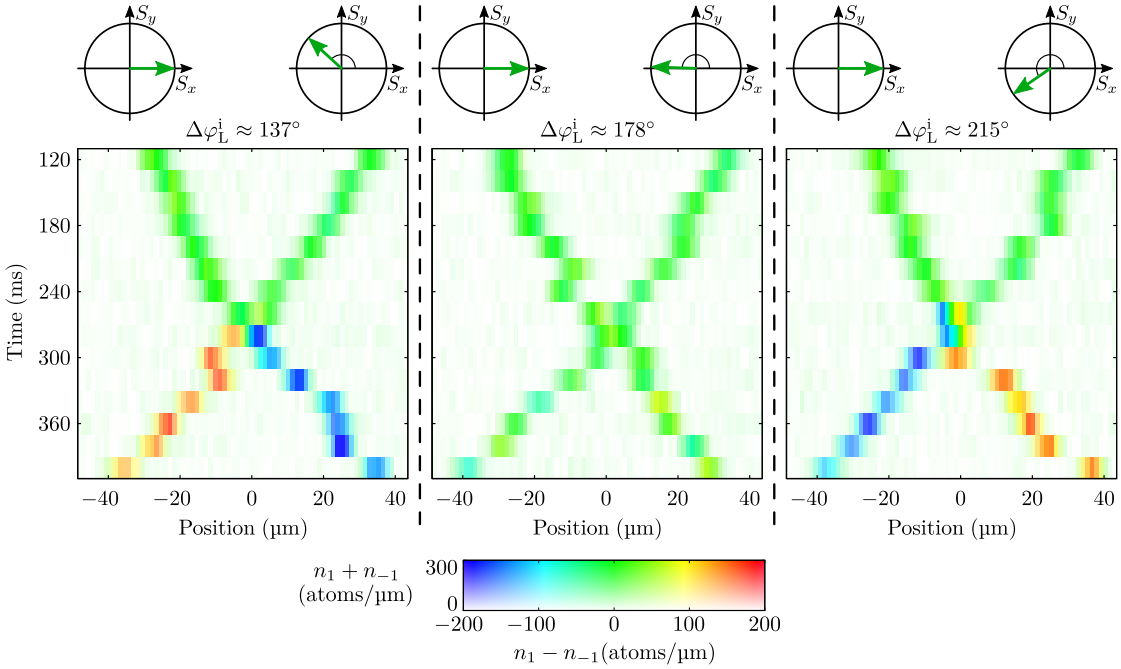

Figure 3.16.: Examples of vector soltion collisions for different initial Larmor phase differences $\Delta\varphi_{\mathrm{L}}^{\mathrm{i}} = \varphi_{\mathrm{L}}^{(1)} - \varphi_{\mathrm{L}}^{(2)}$. Here, the numbers refer to the ones marked on the right-hand side of fig. 3.15 and the cutout shown there is a zoom of the region marked by the rectangle of the same plot. The initial pseudo-spin 1/2 orientation in the x-y-plane is marked by the green arrows for each soliton. Below, the z-projection, indicated by the density difference $n_{+1} - n_{-1}$, is marked by the hue of the color. Simultaneously, the bright density $n_{+1} + n_{-1}$ is encoded in the saturation of the colormap. For each time a single realization is shown. The soliton polarization after collision shows a strong dependence on the initial phase difference $\Delta\varphi_{\mathrm{L}}^{\mathrm{i}}$. This figure is adapted from [83]

representation of 2-level states on the Bloch sphere, the rotation around the polar axis corresponds to a change of the relative phases, or, in spin language, the Larmor phase φ_{L}. This, in turn, is connected to the transverse spin projections S_x and S_y. Thus, to control and measure the full soliton polarization $\boldsymbol{c}$ we require access to all pseudo-spin projections of both colliding solitons.

Appropriately, the method of successive local rotations also enables the independent control of the local rotation. Analogous to spin-1/2 systems, its degree of freedom is given by the orientation of the rotation axis in the plane transverse to the homogeneous magnetic offset field. The angle of this axis can be adjusted by changing the phase of the amplitude modulation of the local control laser beam. The amplitude modulation generates the oscillation of the fictitious magnetic field required for the local coupling (see sections 2.4.3, 2.6.1 and 2.6.6). This changes the phase of the population which is transferred to $m_{\mathrm{F}} = \pm 1$ by the local coupling and thus adjusts the Larmor phase of the pseudo-spin system.

For the measurement of the pseudo-spin projections we apply two different readout schemes. The projection S_z along the magnetic offset field can be accessed directly from the populations obtained after the SG pulse. To obtain the transverse

projections we apply an appropriate spin rotation to map the quantity of interest to the z-axis for readout. However, fluctuations of the magnetic offset field lead to a 2π dephasing between the Larmor phase angle of the prepared spin and the readout axis over a time scale of less than 30 ms on the 1 s.d. level. Nevertheless, the field gradients along the cloud are experimentally well controlled, such that the relative Larmor phase fluctuations between solitons in the same realization are negligible. To obtain a precise measurement of the difference $\Delta\varphi_\mathrm{L}$ between the Larmor phases of the colliding solitons we measure both transverse pseudo-spin projections simultaneously as described in section 2.5.5. For this, the populations are split between the $F = 1$ an $F = 2$ hyperfine manifolds and in each system one of the spin projections is extracted. In the measurements we observe that the Larmor phase $\Delta\varphi_\mathrm{L}$ does not evolve significantly during free propagation when the magnetic field gradient is fully compensated (see section 3.5.3 for more details on the free phase evolution). This is also consistent with the Manakov solution (3.8) of the vector solitons, for which the complex polarization vector $\boldsymbol{c}$ is a constant parameter. Therefore, we define $\Delta\varphi_\mathrm{L}^\mathrm{i}$ and $\Delta\varphi_\mathrm{L}^\mathrm{f}$ as the initial and final Larmor phase differences between the central solitons, which only changes during their collision. More precisely, the differences $\Delta\varphi_\mathrm{L} = \varphi_\mathrm{L}^{(2)} - \varphi_\mathrm{L}^{(1)}$ between the two solitons are defined with respect to the numbers given on the right-hand side of fig. 3.15.

In fig. 3.16 we show the density and their imbalance in the bright components as measure for the pseudo-spin z-projection during the collision for different initial values of $\Delta\varphi_\mathrm{L}^\mathrm{i}$. The final pseudo-spin z-projection of the solitons after collisions show a strong dependence on this initial difference. In particular, we can tune the final polarizations of the solitons continuously and deterministically. For opposite initial polarizations with $\Delta\varphi_\mathrm{L}^\mathrm{i} = 180°$ obtain a vanishing S_z imbalance while for some other values we obtain large values of S_z. In the following we will investigate this effect more systematically.

3.5.2.2. Comparison with Mean Field Theory

To obtain a more thorough quantitative picture we extend the measurements of the final pseudo-spin projections also to the transverse plane to obtain also the final Larmor phase difference $\Delta\varphi_\mathrm{L}^\mathrm{f}$. The corresponding experimental measurements are shown in fig. 3.17. The measured data indicates vanishing S_z (i.e. no change in polarization) for $\Delta\varphi_\mathrm{L}^\mathrm{i} = 0°, 180°$ but the peak values for S_z seem to be reached not in the middle between these points (i.e. no sinusoidal behavior). Tagging the solitons with their Larmorphase, which does not evolve during free propagation, allows tracking them trough the collision. Comparing the final Larmor phase differences $\Delta\varphi_\mathrm{L}^\mathrm{f}$ with the initial values we obtain a curve which roughly tracks a line through the origin but shows interaction induced deviations from this unperturbed propagation. This suggests that the bright components of the solitons are transmitted through each other as compared to being reflected during collision. Further, by summing all measured spin projections to obtain the full pseudo-spin length $|\boldsymbol{S}| = \sqrt{S_x^2 + S_y^2 + S_z^2}$ we investigate the coherence of the bright components, each of which initially consist of approx. 1000 atoms. Overall, the initial state shows a large coherence $\gtrsim 0.8$ which is preserved during the collision.

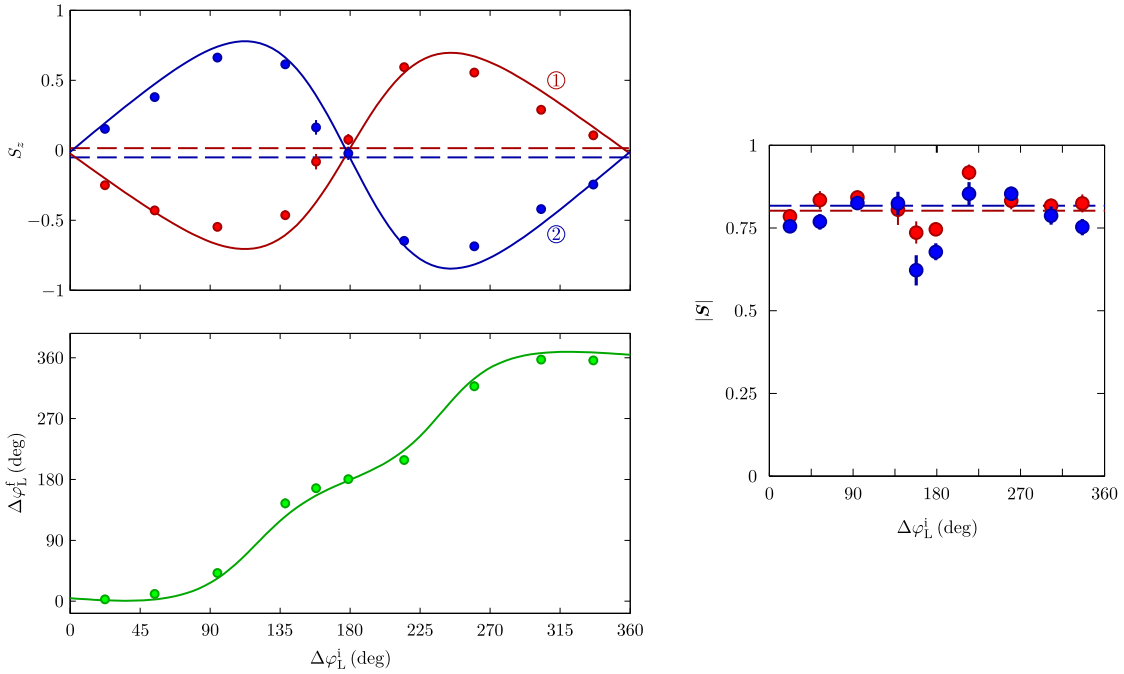

Figure 3.17.: Comparison of experimental data and model predictions of the polarization scattering of the vector soliton bright components. The data points and dashed lines show the measured experimental data for the different pseudo-spin projections after and prior to the collision, respectively. The total spin length $|\boldsymbol{S}| = \sqrt{S_x^2 + S_y^2 + S_z^2}$ is a measure for the coherence between the atoms contributing to the bright components. It shows a high value which is preserved during collision. The solid lines are predictions obtained from the Manakov model [143] for the soliton parameters given in the text. This mean-field model shows good agreement with our measurement results. The error bars mark statistical 1 s.d. intervals of the mean. This figure is adapted from [83]

For 2-component bright Manakov solitons the phenomenon of polarization scattering during their collisions has first been described analytically a long time ago [23]. In this work electromagnetic fields in a self-focusing medium (negative change of the refractive index with the power of the radiation) were considered, where the bright soliton components correspond to the two orthogonal orientations of the polarization. In this system soliton collisions lead to a redistribution of power between the two polarizations. Here, although qualitatively similar in form, the presence of the background and the dark component modify the analytical description. To obtain the polarization change during collisions in [143] soliton pair solutions of the GPE (3.7) are considered. Fixing the position of one of the solitons (i.e. in the moving frame of this soliton) its parameters in the asymptotic limit $t \to \pm\infty$ are calculated. From these the polarization change from initial vector $\boldsymbol{c}_j^{\mathrm{i}}$ to final value $\boldsymbol{c}_j^{\mathrm{f}}$ for soliton $j = 1, 2$ in accordance with the numbering scheme shown in fig. 3.15 can be obtained as

$$\begin{aligned} \boldsymbol{c}_1^{\mathrm{f}} &= \chi \left(\boldsymbol{c}_1^{\mathrm{i}} + A_{12} \left\langle \boldsymbol{c}_2^{\mathrm{i}} \middle| \boldsymbol{c}_1^{\mathrm{i}} \right\rangle \boldsymbol{c}_2^{\mathrm{i}} \right), \\ \boldsymbol{c}_2^{\mathrm{f}} &= \chi \left(\boldsymbol{c}_2^{\mathrm{i}} + A_{21}^{*} \left\langle \boldsymbol{c}_1^{\mathrm{i}} \middle| \boldsymbol{c}_2^{\mathrm{i}} \right\rangle \boldsymbol{c}_1^{\mathrm{i}} \right), \end{aligned} \tag{3.30}$$

with soliton parameter dependent coupling factors

$$A_{jk} = \frac{z_j^{*} \left(z_k^{*} - z_k \right) \left(q_0^2 - |z_k|^2 \right)}{z_k \left(z_j^{*} - z_k^{*} \right) \left(q_0^2 - z_j^{*} z_k^{*} \right)} \tag{3.31}$$

and normalization

$$\chi = \left(1 + \frac{\left(z_1^{*} - z_1 \right) \left(z_2 - z_2^{*} \right) \left(q_0^2 - |z_1|^2 \right) \left(q_0^2 - |z_2|^2 \right)}{|z_1 - z_2|^2 |q_0^2 - z_1 z_2|^2} \left| \left\langle \boldsymbol{c}_1^{\mathrm{i}} \middle| \boldsymbol{c}_2^{\mathrm{i}} \right\rangle \right|^2 \right)^{-1/2} . \tag{3.32}$$

The variable q_0 describes the chemical potential in dimensionless form and the eigenvalues $z_j = \xi_j + i\,\nu_j$ are associated with soliton j, where ξ_j and ν_j denote dimensionless measures of the velocity v_j and inverse width κ_j, respectively. The dimensionless quantities are related to physical units by

$$\begin{aligned} q_0^2 &= \frac{\mu}{n_0 c_0^{1\mathrm{d}}} , \\ \xi_j &= \sqrt{\frac{m}{n c_0^{1\mathrm{d}}}}\, v_j , \\ \nu_j &= \frac{\hbar}{\sqrt{m n c_0^{1\mathrm{d}}}}\, \kappa_j . \end{aligned} \tag{3.33}$$

Here, $c_0^{1\mathrm{d}}$ denotes the effective 1d coupling constants which we estimate in our system as $c_0^{1\mathrm{d}} = c_0/(2\pi a_\perp^2)$ with the transverse harmonic oscillator length $a_\perp = \sqrt{\hbar/(m\omega_\perp)}$. This is strictly valid only when no higher oscillator modes are excited in the transverse direction. With a transverse trapping frequency of $\omega_\perp = 2\pi \times 170\,\mathrm{Hz}$ our experiment however is in a crossover regime between this approximation and the TF approximation. Assuming a transverse TF profile one obtains values $\sim 20\,\%$ smaller than with the approximation given here. By extracting the soliton parameters in a similar fashion as presented in section 3.4.4 we obtain for the colliding solitons in

Quantity	Soliton 1	Soliton 2
v [µm/ms]	0.18	−0.21
κ [1/µm]	0.33	0.34
S_z	0.01	−0.05
n_0 [atoms/µm]	471	456
ξ_j	0.09	−0.09
ν_j	0.12	0.12

Table 3.1.: Experimentally extracted soliton parameters used for calculating the theoretical curves in fig. 3.17. The densities n_0 are the background values obtained for an evolution time $t = 220\,\mathrm{ms}$ before the collision. ξ_j and ν_j from these respective values while $q_0^2 \approx 0.64$ is obtained from the mean of both background densities, leading to $\mu \approx h \times 540\,\mathrm{Hz}$.

the current measurement the values given in table 3.1. By inserting these values into eq. (3.30) we calculate the Manakov predictions shown in fig. 3.17. Because the background density is not completely flat we use the background densities at the respective soliton positions to determine the dimensionless quantities for velocity ξ_j and width ν_j. Since the collision happens roughly in the middle between the positions where these densities are extracted, we calculate the chemical potential q_0 from the average of the two values of n_0.

The experimental system certainly is not a pure implementation of the Manakov model given by eq. (3.7). For the derivation of this equation we neglected the differences in the scattering length and the presence of SCCs (i.e. neglected the spin interactions) and dropped the magnetic filed contributions to the energy shifts. Nevertheless, we find that the solitons in our system (density profiles and interactions) are still well described by the Manakov model.

For such deviations, namely spin interactions and the presence of external magnetic fields, the properties of solitons in the spin-1 system have been studied analytically and numerically [153, 154]. In [153] the phase ground state diagram of solitons with dark component in $m_\mathrm{F} = 0$ has been mapped out. Its general features are reminiscent of the single-mode spin-1 groundstate phase diagram, where the second order Zeeman shift q influences the populations and relative phases between the $m_\mathrm{F} = \pm 1$ levels. For large $q > \mu/2$ the soliton groundstate corresponds to a single-component soliton which continuously transitions to a BDB soliton with equal populations in $m_\mathrm{F} = \pm 1$ for $\mu/4 \lesssim q < \mu/2$. At moderate shfits $q \lesssim \mu/4$ the groundstate develops a population imbalance in the bright components, corresponding to a growing z-polarization for $q \to 0$. In the experiment at $q \approx h \times 56\,\mathrm{Hz}$ we are thus in this latter regime where the energy of Manakov-like solitons is close to the actual minimal energy soliton in the system.

3.5.3. Application of Soliton Dynamics for the Measurement of Magnetic Field Gradients

In the previous chapters the properties of the soliton dynamics have been discussed. In particular, the internal pseudo-spin like degree of freedom in the bright components showed interesting dynamics, which critically depends on the Larmor phase of the colliding solitons. This chapter will discuss applying the coherent nature of the vector solitons to realize precise phase measurements for the determination of magnetic field gradients. This task is similar to a possible application of the concept of a soliton interferometer [24–26]. While in these references only attractive interactions are considered, a particular benefit of applying BDB vector solitons is the possibility to realize such interferometers also in repulsively interacting condensates.

In our experiment two scenarios are possible. As shown in the previous section, the S_z-projection after a soliton collision depends on the difference in Larmor phases of the colliding vector solitons. Therefore, S_z could directly be used as interferometric contrast. Instead, we want to focus on another approach which only utilizes the simultaneous readout to directly infer the differential Larmor phase evolution between a pair of solitons. This avoids the soliton collision and may potentially be more robust against technical fluctuations influencing the soliton parameters.

From the vector soliton solutions (3.8) we know that there is no relative phase evolution between the $m_\mathrm{F} = \pm 1$ components. Thus, the Larmor phase of the bright components only evolves due to the external fields. This behavior is a direct consequence of the self-consistent nature of the soliton solutions. The effective potential of the dark components which guides the bright components is adjusted precisely such that at all times there is no Larmor phase evolution. Even if the soliton travels through the curved background density of the harmonic trap, if the change if slow enough such that the soliton wavefunction can adjust adiabatically, there is no Larmor phase evolution. For this reason BDB solitons resemble a "probing particle" well suited to investigate the magnetic offset field.

In the experiment we apply a vertical magnetic offset field perpendicular to the long axis of the trap. By applying a current I to a coil oriented along the axial direction of the trap magnetic field gradients along the trap axis are canceled. For measuring and minimizing this gradient a Ramsey sequence is applied. It consists of two $\pi/2$ pulses applied to the $|F = 1, m_\mathrm{F} = -1\rangle \leftrightarrow |2, -2\rangle$ transition with an interrogation time of $t = 50\,\mathrm{ms}$ in between. We apply this Ramsey spectroscopy to the whole cloud and read out the resulting oscillation with spatial resolution. Due to the spatially changing magnetic field strength the detuning from the transition spatially varies. Thus, the final imbalance N_-/N_+ with $N_- = N_{F=2} - N_{F=1}$ and $N_+ = N_{F=2} + N_{F=1}$ obtained after the interrogation time varies with the spatial difference of the detuning. Assuming only a linear gradient, this detuning profile is given by the spatial variation of the Larmor frequency profile

$$\Delta\omega_\mathrm{L}(x) = \Delta m_F \, |g_F| \, \frac{\mu_B}{\hbar} \nabla B x \tag{3.34}$$

with Bohr magneton μ_B, Landé factor g_F, and magnetic field gradient ∇B along

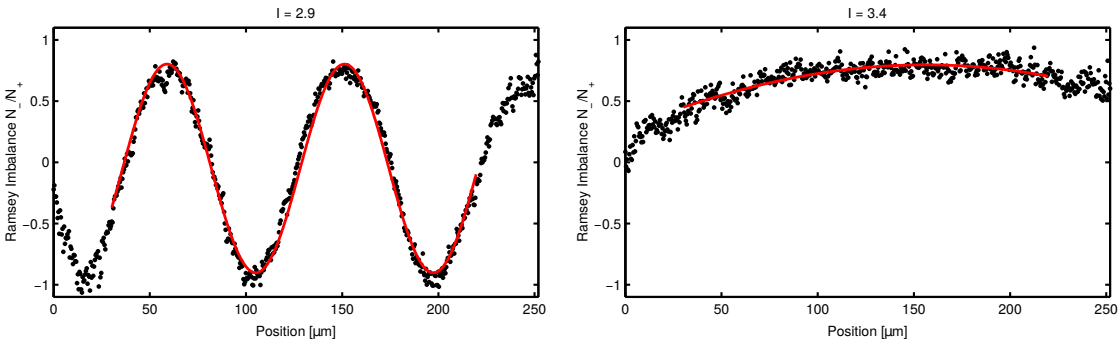

Figure 3.18.: Single experimental realizations of the magnetic field gradient along the condensate measured via spatially resolved Ramsey spectroscopy on the levels $|1,-1\rangle \leftrightarrow |2,-2\rangle$. The measured imbalance N_-/N_+ (black dots) varies spatially with the sine of the Larmor phase difference $\Delta\varphi_\mathrm{L}(x) = \omega_\mathrm{L}(x)t$ given by eq. (3.34) over the Ramsey interrogation time $t = 50\,\mathrm{ms}$. For a large gradient (left plot) the imbalance shows the expected modulation. For vanishing magnetic gradients (right plot; cf. fig. 3.19) the Ramsey imbalance has a residual curvature. This is most likely induced by mean field shifts of the curved background density in the harmonic trap or spatial dynamics during the interrogation time.

the condensate. Here, the factor Δm_F specifies the sensitivity of the transition to the Magnetic field. Because $g_F = -1/2$ in $F = 1$ and $g_F = +1/2$ in $F = 2$ this factor is $\Delta m_F = 3$ for the transition probed during the Ramsey sequence.

Two exemplary single realizations of the imbalance extracted from the Ramsey spectroscopy for different magnetic gradients are given in fig. 3.18. For large magnetic gradients (see left plot) this method leads to an oscillatory spatial modulation of the imbalance as expected. By linearly interpolating between large magnetic gradients the rough compensation coil current for a vanishing gradient can be estimated (cf. fig. 3.19). At this current, however the Ramsey imbalance (right plot of fig. 3.18) still shows a residual curvature. This most likely stems from spatially varying mean-field shifts due to the quadratic density profile in the harmonic trap or spatial dynamics during the interrogation time induced by the first $\pi/2$ pulse.

In contrast to this, solitons cancel all mean-field induced phase evolution as explained before. Thus, by tracking the magnetic field induced phase evolution over an extended period of time accurate measurements of the magnetic field gradient are obtained. Here, we generate two soliton pairs and simultaneously read out the transverse pseudo-pseudo spin projections S_x and S_y to gain access to the Larmor phase difference $\Delta\varphi_\mathrm{L} = \varphi_\mathrm{L}^{(2)} - \varphi_\mathrm{L}^{(1)}$ between the right and left soliton (see fig. 3.19). Here, one soliton serves as phase reference for the other, which effectively separates the fast Larmor precession time scale ($\omega_\mathrm{L} = 2\pi \times 618\,\mathrm{kHz}$) from the comparably long experimental evolution period $t \sim 200\,\mathrm{ms}$. This enables a tremendous enhancement of phase resolution. To make sure both solitons have the same initial Larmor phase orientation, i.e. $\Delta\varphi_\mathrm{L} = 0$ at $t = 0$, they are generated at the same time by simultaneously applying two local rotations via two spatially separated laser beams. The relative velocity $v = v^1 - v^{(2)} \approx 0.25\,\mu\mathrm{m/ms}$ of the

solitons is extracted from linear fits to their propagation. As shown before, the soliton propagation is sufficiently linear to assume the relative position to evolve according to $x(t) = x_0 - vt$, where the initial soliton separation, inferred from the linear fits to their propagation, is $x_0 \approx 75\,\mu\text{m}$. The values of x_0 and v are extracted for each magnetic field gradient setting separately. Thus, from eq. (3.34) we obtain the Larmor phase evolution

$$\Delta\varphi_{\text{L}}(t) = \int_0^t dt' \omega_{\text{L}}\left(x(t')\right) t' = \Delta m_F g_F \frac{\mu_B}{\hbar} \nabla B \left(x_0 t - \frac{1}{2} v t^2 \right) \tag{3.35}$$

with $g_F = -1/2$ in the $F = 1$ manifold and $\Delta m_F = 2$ for the Larmor phase evolution in the pseudo-spin system provided by the bright components in $m_{\text{F}} = \pm 1$. The upper right-hand plot in fig. 3.19 shows the measured phase evolution and fits according to eq. (3.35), where the only free parameter is ∇B. The resulting values for the magnetic field gradients from the Ramsey method and soliton propagation are shown in the lower plots of the same figure. The red line is a linear fit to the data obtained by the Ramsey spectroscopies. While gradients obtained from the Larmor phase method show a nice linear behaviour in the vicinity of $\nabla B = 0$ the Ramsey data displays an offset, as discussed before.

Effectively, the initial spin rotation and the readout of the transverse pseudo-spin projections constitute a Ramsey sequence. During its interrogation time the self-consistent canceling of mean-field shifts for the bright soliton components allows for an increase of the interrogation on the scale of the soliton lifetime os 1.4 s (see section 3.4.5). Thus, soliton-enhanced magnetic field gradient measurements allow for a significant increase of measurement precision over the usual Ramsey method. Here, technical fluctuations of the soliton velocity and initial positions will limit the achievable precision. At these long interrogation times also the small difference between the inter- and intraspecies scattering lengths (cf. fig. 3.5) may become important when the atom number in the bright components are not perfectly balanced.

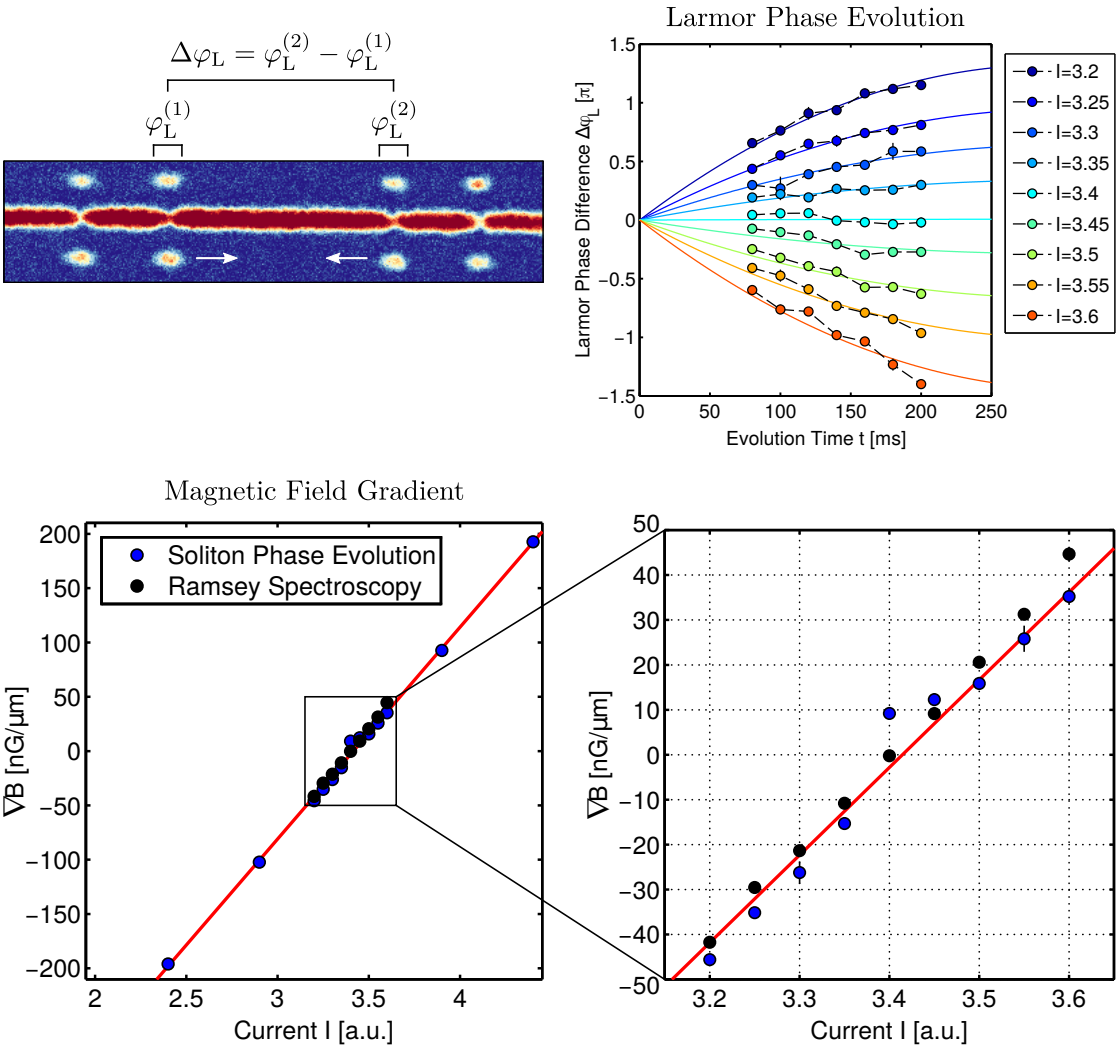

Figure 3.19.: Measurement of magnetic field gradients via soliton phase evolution. The relative phase evolution $\Delta\varphi_L$ of two approaching and (almost) identical solitons is measured. Depending on the current I applied to the magnetic field gradient compensation coil the gradient and therefore also the Larmor phase evolution of the solitons varies quadratically according to eq. (3.35). The data points are averages over 3 experimental realizations and the solid lines are fits with ∇B as only free parameter. The magnetic gradients, extracted from the soliton Larmor phase evolution and additionally also from Ramsey spectroscopies, are shown in the lower row. The red line is a linear fit to the data obtained from the Ramsey method. For $I < 3.4$ the sign of ∇B values extracted from Ramsey spectroscopies has manually been inverted. For small magnetic field gradients (around $I = 3.4$) the Ramsey method is probably limited by mean field shifts due to the curvature of the density or spatial dynamics during the interrogation time. Here, the differential Larmor phase evolution of the solions still allow for accurate results. All error bars show 1 s.d. intervals of the mean; where no error bars are visible they are smaller than the plot markers.

4. Spin Excitations in Quench Dynamics

Quenches, i.e. instantaneous changes of a microscopic control parameter, induce spontaneous excitations in the system. In case of many-body quantum systems, where potentially all particles are interacting with each other, the description of these highly excited states is, in general, intractable. Nevertheless, there are concepts which offer the prospect of a general classification far from equilibrium. While this aspect is discussed in chapter 5, here we will focus on the investigation of the general structure of excitations and the generation of local defects. In particular, this section will introduce the application of local spin rotations as an additional initial condition. During evolution this state develops strong persistent fluctuations in the system, which are distinct from previously studied initial conditions (ICs) in this system [32, 55]. After a short introduction of the experimental sequence and the initial conditions a characterization of typical spin excitations follows.

4.1. Layout of the Experiment

The experiments in this and the next chapter are performed in a quasi-1d box potential. This is generated by a red-detuned elongated dipole trap (WG) superimposed with two blue-detuned laser beams at a wavelength of 760 nm. These two beams are steered using the AOD setup and serve as sharp potential barriers[1] which confine the atoms in the central region of approx. 130 µm in size, where the longitudinal harmonic oscillator potential of the WG trap is approximately flat.[2] We choose this trap geometry because here we aim to study the dynamics subject to a large number of defects in the system. Here, the nearly constant density prevents an accumulation of defects at the low densities near the trap edges, which we usually observed for a harmonic confinement.

To initialize dynamics in the condensate the relative energy shift q between the $m_F = 0$ and $m_F = \pm 1$ components (cf. eq. (2.12)) is changed instantaneously. This quench is implemented via MW dressing (see section 2.4.2 for details) and tunes q from a value deep in the polar phase ($q \approx h \times 58\,\mathrm{Hz}$) to a value in the EP phase ($q \leq nc_1$). Here, spin-mixing processes driven by SCCs are tuned into resonance and allow the spontaneous redistribution of population between the hyperfine levels. The associated interaction time scale is $t_s \sim h/|nc_1| \sim 1\,\mathrm{s}$. For the observation of long-time non-equilibrium dynamics over the course of many t_s, this implies the

[1] The density drops from 90 % to 10 % of the bulk value over a range of approx. 6 µm for atom numbers between (40 – 150) k atoms. This corresponds roughly to the spin healing length $\xi_s = \hbar/\sqrt{2mn\,|c_1|} \sim (5-10)\,\mu\mathrm{m}$ for these densities.

[2] Within the box trap the density varies by approx. (10 – 20) % for atoms numbers of (150 – 40) k.

access to long experimental evolution times. Here, we observe the spin dynamics for up to $\sim 40\,\mathrm{s}$.

4.2. Initial conditions

Mainly, two initial conditions will be of interest here. The first one is the polar state, describing the scenario when all atoms are prepared in the level $|F = 1, m_\mathrm{F} = 0\rangle$. The second one is comprised of multiple local spin rotations with sufficient rotation amplitude to form soliton pairs in the system (see section 3.4.1). For shortness, these will be referred to as "polar IC" and "soliton IC" from here on. In the following their respective properties and dynamics after the quench are outlined.

Polar Initial Condition

In this scenario approx. 150 k atoms are prepared in the $m_\mathrm{F} = 0$ state After the quench, the polar state is unstable such that SCCs spontaneously build up population in $m_\mathrm{F} = \pm 1$, which leads to transverse spin $F_\perp$ (cf. sections 2.3.3 and 2.3.4). In accordance with the instabilities predicted by Bogoliubov theory, this process takes place at a characteristic momentum $\hbar k$ such that a large population builds up in the corresponding k-mode (see e.g. [55] for a measurement of this instability). In the following evolution this localized spectrum is redistributed in k-space.

In our experiments we observed that at large atom numbers of $\sim 150\,\mathrm{k}$ localized excitations, which are generated after the quench, decay. This provides a controlled reference of the non-equilibrium dynamics with a flat background spin length (see the next section for more details).

Soliton Initial Condition

While previously flat backgrounds (e.g. the polar state) or linear waves have been applied as initial condition [32, 55], here we introduce non-linear excitations in the initial state as seed for the dynamics. This presents a potentially fundamentally different IC because the longevity of these defects may affect the dynamics on much larger timescales than other ICs. For small atom numbers we observe a lower decay rate of these excitation, which is why we apply this IC in a system of $\sim 40\,\mathrm{k}$ atoms.

As shown in section 3.4.5 local spin rotations provide a versatile and well-controlled method to reproducibly excite independent pairs of coherent vector solitons. To initialize these in the system, a homogeneous condensate in the polar state is prepared, followed by multiple local rotations. These are performed consecutively within $< 1\,\mathrm{ms}$ and are roughly equally spaced across the system. Here we will usually investigate dynamics starting from up to 6 local spin rotations to ensure that the mean distance between the rotations is larger than their width (see fig. 4.1). Note, however, that due to this tight spacing the evolution of the emerging solitons is strongly dominated by their interactions and therefore is not captured by the free evolution usually assumed for the derivation of soliton solutions. Neither is it clear that over the course of the dynamics, especially in the presence of SCCs, the structure of the initially generated excitations persists.

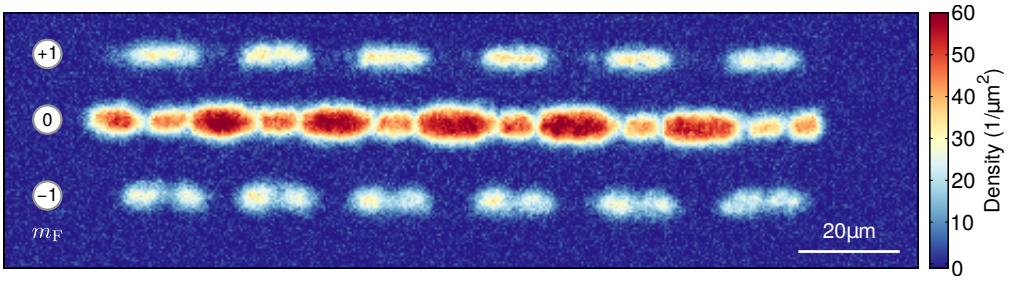

Figure 4.1.: Absorption picture with SG imaging of the soliton IC for the investigation of non-equilibirum dynamics. The atoms are confined in a box-like potential in the center of the harmonic trap with blue-detuned end caps. The atoms are initialized in $|1,0\rangle$ and at 6 positions spin rotations are performed sequentially. This particular realization is recorded for a total atom number of approx. 65 k.

Nevertheless, in the first ~ 300 ms of the evolution, where excitations due to the SCC instability are still small, the solitons start to propagate and collide with each other (see fig. 4.2 for an exemplary evolution without q quench in the harmonic trap).

In the first ~ 300 ms of the evolution, where excitations due to the SCC instability are still small, the solitons start to propagate and collide with each other (see fig. 4.2 for an exemplary evolution without q quench in the harmonic WG trap). Around the time of the third or fourth collision also SCC processes become relevant and the system begins to develop large local fluctuations between realizations. This is in contrast to the predictions of the integrable Manakov model which predicts that the solitons emerge from an arbitrary number of collisions without change in shape [168]. The differences of the scattering lengths between the hyperfine substates (cf. fig. 3.5) in the experiment and the associated SCCs, however, lead to a breaking of this integrability. Instead of recurrent soliton motion, we observe that the soliton interactions lead to a strongly fluctuating system. It is interesting to note, however, that even without the q quench such strong fluctuations build up.

4.3. Evolution of Spin Distributions

Over the course of the first ~ 10 s the initial excitations in the system are redistributed and a structure specific for the two initial conditions builds up. To illustrate their properties spin histograms of the full spin distribution will be presented in the following. These are obtained from a simultaneous readout of the 3 spin-1 projections F_x, F_y, and F_z as described in section 2.5.4. To obtain the histograms of the local spin observables the values measured at each position over all realization are evaluated equally. For an intuitive interpretation of the spin distributions, 2d projections of the histograms are shown for a view along z-direction (top line of plots) and along y-direction (bottom line) of the spin sphere. The relative frequency of the measured results is encoded in the color.

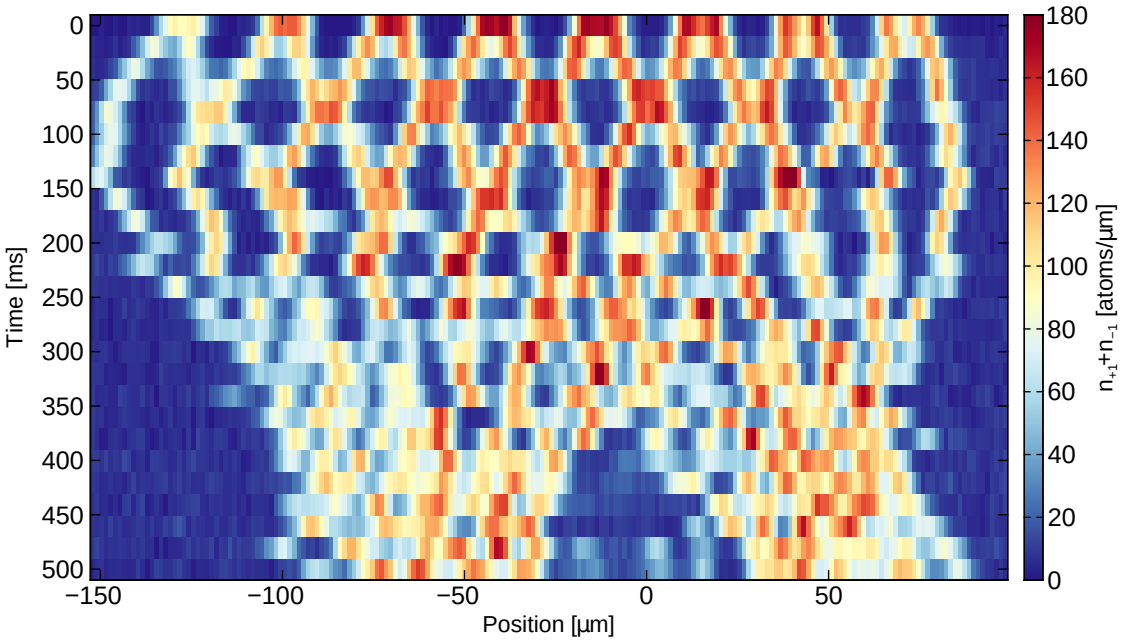

Figure 4.2.: Initial evolution after generation of the soliton IC. Averaged $m_\mathrm{F} = \pm 1$ densities (of up to 4 realizations) shown in the plot indicate the movement of the vector solitons. Note that this measurement, deviating from the remaining dynamics discussed here, is performed in the harmonic WG trap and without quench (i.e. in the Manakov limit applied in chapter 3). The trap center is indicated with zero and at the left and right edges the reversals of soliton propagation are visible. After approx. 300 ms the excitations start to bunch together, which indicates an attractive interaction. During the evolution the total density retains its approximately quadratic TF profile centered around zero.

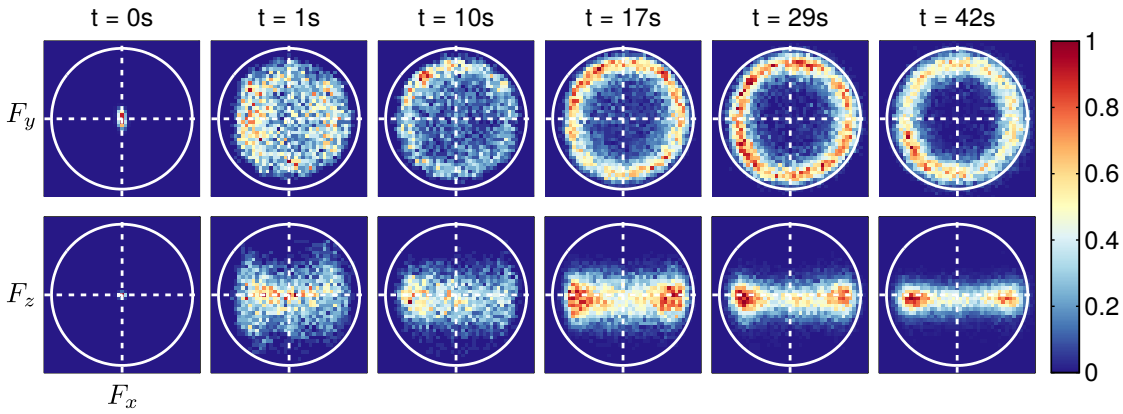

Figure 4.3.: Histograms of all 3 spin dipole operators for evolution from the polar initial condition (all atoms in $|1,0\rangle$) with $\sim 140\,\mathrm{k}$ atoms. The spin projections are measured simultaneously as discussed in section 2.5.4. All spatial points and realization contribute to the histograms. The upper row shows histograms in the F_x-F_y-plane measured after different evolution times t after the quench and in the lower row histograms of the F_x-F_z plane are displayed. Initially, the SCCs generate large fluctuations in all spin directions which dampen down over time. In the transverse directions the spin settles to a finite length and zero in z-direction. During the imaging sequence in this measurement the top of the reference picture is illuminated with higher intensity than the actual image. This leads to an underestimation of atom numbers in the topmost SG component. To compensate this, the atom numbers of the topmost component on the images (i.e $|1,+1\rangle$ and $|2,-2\rangle$) are scaled such that $\overline{F_x} = \overline{F_y} = 0$ for the initial condition at $t = 0$ (see section 2.5.4 for details on the calculation of the observables). This scaling factor is used for all t.

Polar Initial Condition

As shown in fig. 4.3 the initial instabilities quickly generate spin excitations in all directions. In the following dynamics these are redistributed such that after approx. 17 s a well-defined transverse spin length $|F_\perp|$ builds up while the F_z excitations become small. Here, at $t \geq 17\,\mathrm{s}$ the total spin length $|\boldsymbol{F}| = \sqrt{F_x^2 + F_y^2 + F_z^2}$ settles to a well-defined value of $\overline{|\boldsymbol{F}|} \geq 0.76$ which is mostly comprised of transverse spin length $\overline{|F_\perp|} \geq 0.73$. The quantity $\overline{O}$ denotes the average of the quantity O over all positions and realizations.

The corresponding ring-shaped histograms emerging in the in the x-y-plane for large evolution times are qualitatively in accordance with the Mexican-hat-shaped mean-field potential for $q > 0$ in the EP phase (cf. section 2.3.4).[3] In fact, in the experiment the parameter q is chosen by maximizing $|F_\perp|$ after 30 s. At this point the dynamics of the system is dominated by phase excitations. Their amplitude slowly decreases over time, which is associated to the scaling evolution (see chapter 5 for details) observed during this period. Here, the populations are transported

[3] Here ,the ring shape is mainly a result of a randomization of the orientation of the readout axes. At these large evolution times the histogram of a single realization does typically not cover the whole circle but only a fraction of it.

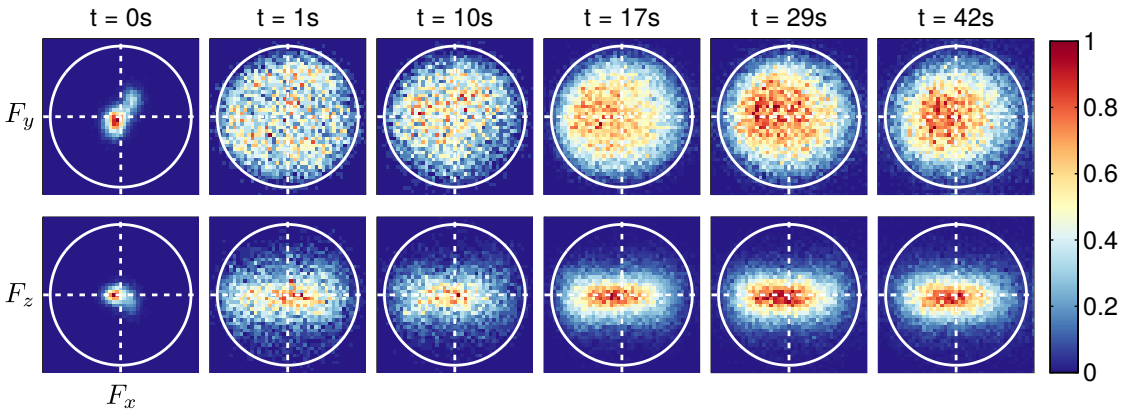

Figure 4.4.: Histograms of all spin dipole operators for evolution from the soliton initial condition with $\sim 30\,\mathrm{k}$ atoms. The data extraction, post-processing and display of the plots is equivalent to fig. 4.3. Throughout the evolution the fluctuations stay symmetric around zero.

towards lower momenta, leading to an increasing population of the $k = 0$ mode.

Soliton Initial Condition

Similarly to the polar IC, also for the soliton IC the excitations induce strong fluctuations in all spin projections. However, the crucial difference here is, that these fluctuations persist during the whole evolution. At 10 s the averaged spin lengths settle to $\overline{|\boldsymbol{F}|} \approx 0.61$ and $\overline{|F_\perp|} \approx 0.55$ in the transverse plane. Subsequently, only a small decay of these values and also no reduction of the fluctuations is observed. The initial generation of excitations in the system seemingly saturates the system at the length scale on the order of the spin healing length $\xi_s = \hbar/\sqrt{2mn\,|c_1|} \sim 5\,\mu\mathrm{m}$ (cf. spectra in fig. D.2, where the healing wavelength for the initial density corresponds to $1/\lambda_s = 1/(2\pi\xi_s) \sim 0.03\,\mu\mathrm{m}^{-1}$) such that only a slow redistribution is possible.

Comparison

Interestingly, the excitations emerging from the soliton IC are much more stable than the ones generated from the polar IC. This may be a result of the energy of the corresponding state. The local rotations introduce additional energy to the system which is not present for the polar IC. Furthermore, the lower atom number of the soliton IC leads to a shallower mean-field potential (cf. fig. 2.4), additionally inhibiting the build-up of the expected ring-structure. Nevertheless, the excess energy added by the local rotations corresponds to an energy well below 1 nK. Thus, this contribution is on the order of $\sim 0.01\,T_c$ of the critical temperature T_c of the condensate.[4] In thermal equilibrium this would not lead to a full suppression of the easy-plane spin expectation values as observed here [56]. Therefore, it can be concluded that the system initialized with the soliton IC does not reach thermal equilibrium during its whole evolution observed here.

[4] Estimating the order of the critical temperature [47] by applying the TF approximation in the WG potential with $N = 40\,\mathrm{k}$ atoms, we obtain $T_c \sim 60\,\mathrm{nK}$.

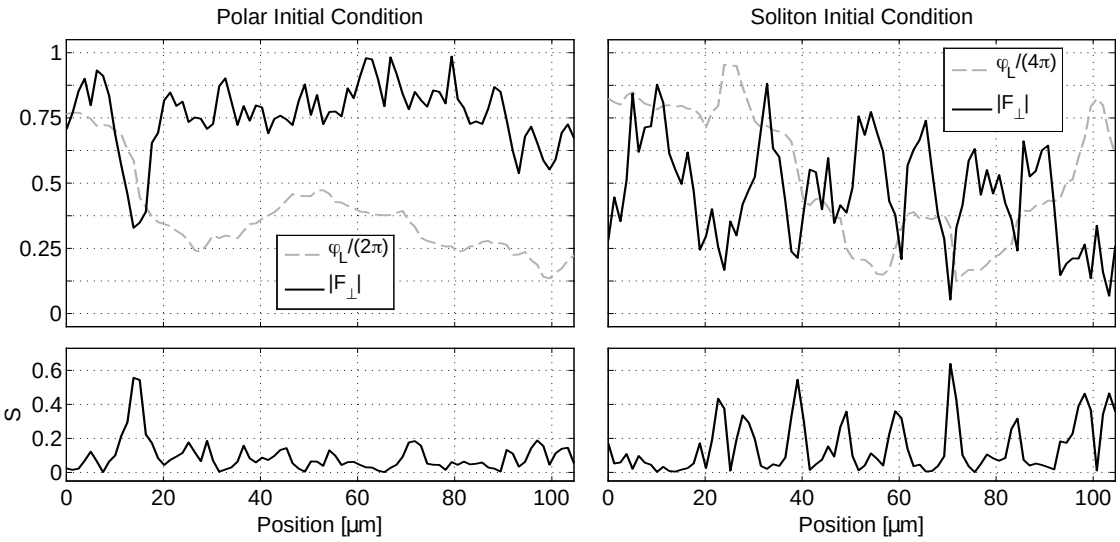

Figure 4.5.: Spatial profiles of $|F_\perp|$ and φ_L for single realizations at time $t = 29\,\mathrm{s}$ for the polar state and soliton ICs. Almost all transverse spin defects generated after the quench from the polar state decay over time. Their characteristic structure is a reduction in the spin length with simultaneous jump in the Larmor phase as shown in the left plot. The spin length $|F_\perp|$ and phase φ_L are qualitatively similar to the typical profiles of dark solitons of the NLSE (cf. fig. 3.2). To identify such excitations in the spin it is useful to evaluate the quantity $S(x) = \left(\overline{|F_\perp|} - |F_\perp|(x)\right) |\nabla\varphi_\mathrm{L}(x)|$ (see discussion of eq. (4.1) for the definition of the involved quantities). The corresponding profiles for the single realizations are shown in the lower plots. The evolved soliton IC shows strong fluctuations in both, the spin length and phase, leading to a strongly peaked signal of $\mathcal{S}(x)$. The average 1d density for the evolved polar IC (soliton IC) at $t = 29\,\mathrm{s}$ is approx. $510\,\mathrm{atoms/\mu m}$ ($170\,\mathrm{atoms/\mu m}$), which leads to $\xi_s \sim 7\,\mu\mathrm{m}$ ($\xi_s \sim 13\,\mu\mathrm{m}$) with the interaction constant extracted from fig. 2.5.

4.4. Generation and Spatial Structure of Spin Defects

Investigating the structure of spin excitations in the system reveals that often correlations between the spin length $|F_\perp|$ and jumps of the Larmor phase φ_L in the transverse plane arise (cf. fig. 4.5). Here, the properties of these excitations and possible mechanisms for their generation will be discussed.

To systematically investigate the amount of generated excitations and their stability over time we evaluate the two-point cross correlator between depletions in the spin length and phase gradient

$$\mathcal{S}(\Delta x, t) = \frac{1}{N_\Delta} \sum_x \left\langle \left(\overline{|F_\perp|}(t) - |F_\perp|(x,t)\right) |\nabla\varphi_\mathrm{L}(x+\Delta x, t)| \right\rangle . \tag{4.1}$$

Here, the quantity $\overline{|F_\perp|}(t) = \sum_x \langle |F_\perp|(x,t)\rangle / N_x$ denotes the mean transverse spin length averaged within the evaluation window consisting of N_x pixels, $\langle\cdot\rangle$ denotes the ensemble average, and $N_\Delta = N_x - \Delta x / s_\mathrm{px}$ is the number of pixels contributing

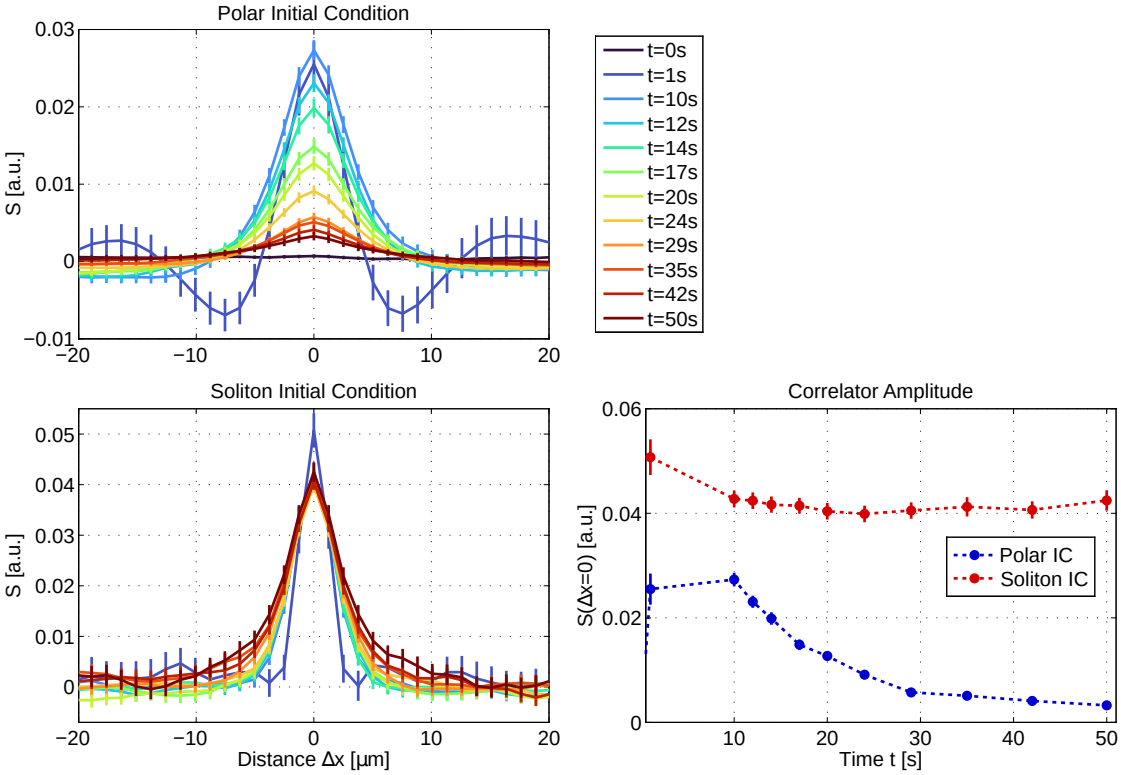

Figure 4.6.: Correlation between dips in the transverse spin length and Larmor phase gradient for polar and soliton (with 6 local rotations) initial conditions. The atom numbers at $t = 0$ are $\sim 150\,\mathrm{k}$ and $\sim 40\,\mathrm{k}$, respectively. In the left column the correlator profiles $\mathcal{S}(\Delta x, t)$ defined in eq. (4.1) shows a well-localized correlation as expected from the profiles shown in fig. 4.5. While for the polar initial condition only a small amount of these excitations are generated after the quench the correlator indicates a large amount of excitations for the soliton IC. The correlator amplitude $\mathcal{S}(\Delta x = 0, t)$ displayed in the right-hand plot shows the time evolution of the excitations in the system. In contrast to the quick decay for the polar IC the indicated amount of the excitations stays almost constant for the soliton IC.

to the sum in eq. (4.1). This value is the number of overlapping pixels when shifting the $|F_\perp|$ and $\nabla\varphi_\mathrm{L}$ arrays by the distance Δx, which corresponds to a shift of $\Delta x / s_\mathrm{px}$ pixels. The size of each pixel corresponds to the distance $s_\mathrm{px} \approx 3 \times 0.42\,\mu\mathrm{m}$ on the atomic cloud in the focal plane of the imaging setup.[5]

Polar Initial Condition

Although a well-defined spin length builds up for the quench from the polar state, the are some spin defects being generated after the quench. These usually exhibit the previously described correlation between spin length depletion and a

[5] Here, we are binning (i.e. averaging over non-overlapping intervals of) 3 adjacent pixels of the image to account for the optical resolution. The distance s_px therefore corresponds to the size of 3 camera pixels in the focal plane.

steep phase gradient as shown for an exemplary spin profile in the left-hand plot of fig. 4.5. This resembles the structure of dark solitons described in section 3.2. For previous quench experiments in a spinor gas solitons have already been discussed as excitations arising when imposing the F_z conservation of the spinor Hamiltonian also locally [169]. However, these soliton solutions have been associated to a full reversal of the transverse spin with a phase change of $\Delta\varphi_\mathrm{L} = \pi$.[6] In contrast to these full reversals, which are associated to a depletion to $|F_\perp| = 0$, we observe a rather continuous distribution of spin dips and Larmor phase changes. These may, however, correspond to similar solution of a more general type, which also allows for a more generalized change of the Larmor phase by arbitrary angles $\Delta\varphi_\mathrm{L}$.

Evaluating the correlator profiles given by eq. (4.1) for the polar IC plotted in the left-hand upper corner of fig. 4.6 show a clear localized correlation at the same position, as expected from the $F_\perp$ profile in fig. 4.5. Due to the construction of this correlator and the evaluation of the spatial spin profiles of fig. 4.5 the value of $\mathcal{S}(\Delta x, t)$ should indicate the strength of the perturbation to the system generated by these spin-soliton-like excitations. This strength depends on the number and amplitude (or "darkness") of the defects. To investigate the time evolution of the soliton excitations the amplitude $\mathcal{S}(\Delta x = 0, t)$ of the correlator is evaluated in the right-hand plot. For the polar initial condition the correlator indicates that for $t \leq 1\,\mathrm{s}$ (corresponds to $t \lesssim 2t_s$) some soliton excitations are generated after the quench which quickly decay again afterwards. Simultaneous to the build-up of the ring-shaped histograms with constant spin length $|F_\perp|$ between $(15-20)\,\mathrm{s}$ (cf. fig. 4.3), the amplitude approaches zero, indicating that almost all of these excitations decay.

Next, the possible origing of the spin excitations for the quench form the polar IC is investigated. The arguments provided here are in line with the discussion in [169]. For this investigation, it is instructive to measure the correlator consider $\mathcal{S}(\Delta x = 0, t)$ as a function of the quench parameter q. The lower left-hand plot in fig. 4.7 shows the correlator amplitude measured for an initial atom number of $\sim 120\,\mathrm{k}$ after a fixed evolution period of $t = 30\,\mathrm{s}$. For decreasing values of q the correlator amplitude indicates an increased number of soliton-like spin excitations in the system. Note, however, that in regions where the transverse spin length $|F_\perp|$ (see upper left-hand plot of fig. 4.7) is small, the correlator amplitude increases, simply because the phase gradients become large in this case. Therefore, only regions where also $|F_\perp| > 0$ should be considered here.

It is likely that the increased amount of excitations at lower q is connected to the k-dependence of the unstable Bogoliubov modes which grow after the quench. For $q < 2n\,|c_1|$ the corresponding dispersion relation of spin excitations in the transverse plane (see eq. (2.18)) features a k-range in which the frequency becomes imaginary. This leads to the instability in the form of exponentially growing populations $N(k) \sim \exp\left(-i\omega(k)t\right)$ in the respective observables. The wavefunctions related to these instabilities oscillate at a spatial frequency given by the wavenumber k. Thus, the wavelength of the generated transverse spin excitations will be around $\lambda \sim 2\pi\xi_s$. Therefore, the spin direction also reverses over an interval of comparable size. This

[6] Instead of a smooth $\tanh^2$ profile these spin solitons would therefore exhibit a sharp notch in the transverse spin length, which, however, would not be clearly resolvable in our experiment.

structure is similar to the soliton-like excitations observed in the system, which are also related to a rapid change of the spin direction. Thus it seems plausible that this instability induces the generation of the soliton-like spin defects we observe in $F_\perp$ after a quench from the polar state. For the arguments given above one would expect this process to become efficient when the distance, over which the spin orientation changes, is compatible with the soliton size.

In order to estimate the size of the spin structures generated by the Bogoliubov instability it is helpful to consider the most unstable momentum (see right-hand plot in fig. 4.7)

$$k_{\mathrm{mu}} = \pm\frac{1}{\hbar}\sqrt{-2m\left(q + nc_1\right)}. \tag{4.2}$$

In the instability region parameterized by $q < 2n\,|c_1|$ k_{mu} specifies the mode growing at the largest rate, which is given by the maximum of the imaginary part of $\omega(k)$. While for $q > n\,|c_1|$ the zero momentum modes grows fastest, at decreasing q the instability favors increasing momenta. At $q < 0$ its values become larger than the spin healing momentum $k_{\xi_s} = 2\pi/\lambda_s = 1/\xi_s$. Around this range of q the wavelength of these excitations becomes shorter than the spin healing length. For dark solitons the size of the localized density depletion $1/\kappa = \sqrt{2}\xi$ is given by the healing length (see section 3.4.4). Thus, for spin solitons it is conceivable that their size is given by the healing length $\xi_s = \hbar/\sqrt{2mn\,|c_1|}$ associated to the spin interaction strength c_1. This is roughly compatible with the excitations observed for the soliton IC, as shown in fig. 4.5.

Soliton Initial Condition

Seeding the dynamics with local rotations leads to a much larger density of spin defects, as already indicated by fig. 4.4. Interestingly, their structure, as shown in the $F_\perp$ profile in the right-hand plots of fig. 4.5, is very similar to the previously discussed defects appearing after the quench from the polar IC. However, the length scale of the excitations is notably shorter than the spin healing length ξ_s at the corresponding density. While the spin length $|F_\perp|$ is strongly fluctuating, most of the sharp dips are accompanied by a rapid change in the Larmor phase φ_{L}. This structure is also captured by the correlator $\mathcal{S}$ shown in the bottom left-hand corner of fig. 4.6. In accordance with the previous discussion of the spin excitations, the correlator profile only changes slightly and shows no significant decay of the amplitude after 10 s (cf. right-hand plot of fig. 4.6). The width of the correlator grows slightly over time, which may indicate the increase of the defect width. We experimentally confirmed that this is not connected to the change of the spin healing length due to a change of the density.

4.5. Characterization of the Soliton Initial Condition

To further characterize the behavior of the soliton IC at long times we systematically investigate the behavior of the system as function of different parameters. At first, the amount of excitations present after long times are investigated for different numbers of local rotations. The left plot in fig. 4.8 shows a strong increase of

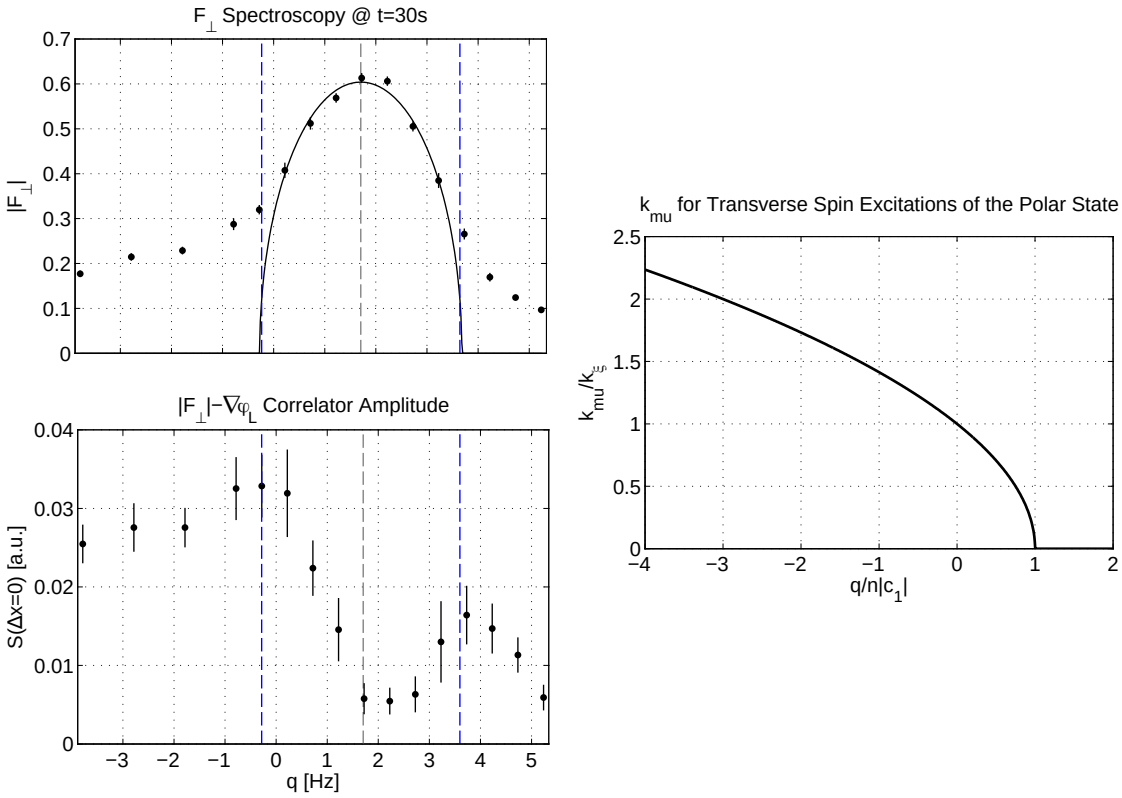

Figure 4.7.: Spin soliton correlations as a function of q after an evolution of $t = 30\,\mathrm{s}$ after a quench from the polar state initial condition. This measurement is carried out for an initial atom number of $\sim 120\,\mathrm{k}$ atoms. The upper left-hand plot shows a measurement of the transverse spin length $|F_\perp|$ averaged over the whole system. The point where $|F_\perp|$ is maximal is compatible with $q = 0$ in the single-mode mean-filed picture (black solid line; blue dashed lines indicate $\pm 2n\,|c_1|$ around $q = 0$) and is marked by a gray dashed line. For more information about the spectroscopy method and interpretation of the results see section 2.3.5. The lower plot shows the amplitude $\mathcal{S}(\Delta x = 0, t)$ of the spin soliton correlator given in eq. (4.1). Its value indicates the amount of excitations in the form of spin solitons in the system and shows a strong increase left to the center of the spectroscopy. For the q values inferred from the spectroscopy measurement this this range corresponds to $q < 0$. In contrast, for $0 < q < 2n\,|c_1| \approx h \times 3.7\,\mathrm{Hz}$ the correlator amplitude stays almost zero. At larger q the transverse spin length drops rapidly because the system looses its easy-plane ferromagnetic properties and enters the polar phase. The right-hand plot shows the most unstable momentum k_{mu} given by eq. (4.2) of the transverse spin Bogoliubov dispersion given in eq. (2.18).

the correlator amplitude $\mathcal{S}(\Delta x = 0, t)$ after a constant evolution of $t = 30\,\mathrm{s}$ for measurements starting from approx. 70 k atoms. This shows that a moderate number of local rotations leads to a significant amount of perturbations in the system. These excitations also show a sufficiently long lifetime to affect the dynamics over times scales of $\sim 40\,\mathrm{s}$ we are interested in. To further characterize the state of the system connected to the spin excitations, the right plot of fig. 4.8 shows the radial probability density $p_\perp(|F_\perp|)$ for the same measurement. Assuming rotational symmetry in the transverse plane, the probability to find $|F_\perp|$ in the interval $[a, b]$ is given by integrating the transverse spin plane in polar coordinates over the density $\tilde{p}_\perp$ as

$$P([a,b]) = 2\pi \int_a^b f\tilde{p}_\perp(f)df = \int_a^b f p_\perp(f)df. \tag{4.3}$$

Here, we absorb the contribution of the polar angle into the plotted density $p_\perp$. Thus, by assuming a slowly varying probability density profile, its value can be extracted from the transverse spin histogram by dividing by the centers of the histogram bins. For the polar initial state the system develops an almost constant spin length $\overline{|F_\perp|} \approx 0.75$ everywhere in the system which appears as sharp peak in the radial distribution. For an increasing number of rotations the probability density quickly transforms to an almost flat distribution up to this length. This behaviour is consistent with the histograms previously shown in figs. 4.3 and 4.4 for the polar and Soliton initial conditions with 6 local rotations.

For completeness we also checked the stability of the excitations generated from 6 local rotations to be stable against the other defining parameters of our system. Measurements after a fixed evolution of $t = 30\,\mathrm{s}$ show that an increase of he initial atom number from approx. 25 k to above 100 k leads to a decrease of about 30 % in the correlator amplitude (see left plot of fig. 4.9). This indicates that the stability of the spin excitations in the system is connected to the atom number. To further verify this systematic behavior a second set of measurements is performed in which no local rotations are used to initialize excitations in the system. However, just quenching the polar state only leads to a small correlator amplitude. Instead, to obtain a larger amount of excitations we prepared the coherent spin state with $F_x = 1$ followed by the application of a magnetic field gradient for a duration of 94 ms. This leads to a Larmor phase which is linearly increasing with the position along the cloud. The resulting spin wave in the transverse plane has a wavelength of approx. 14 µm. Afterwards, the experimental sequence proceeds with the quench of q as previously discussed. During the evolution this initial condition also leads to strong fluctuations in $F_\perp$ and a large signal in $\mathcal{S}$. Depending on the initial atom number however, the correlator amplitude $\mathcal{S}(\Delta x = 0, t)$ measured after $t = 29\,\mathrm{s}$ shows a strong dependence on the atom number in the system (see right plot in fig. 4.9). While for atom numbers around 60 k the correlator shows values similar to the usual soliton IC, for an increasing amount of atoms the correlator amplitude quickly drops towards zero.

However, because in our measurements a higher atom number is achieved by reducing the potential amplitude at the endpoint of the evaporation ramp in the optical trap the excitation lifetime may, to some degree, also be connected to the system temperature. An exact investigation of the temperature in our experiment

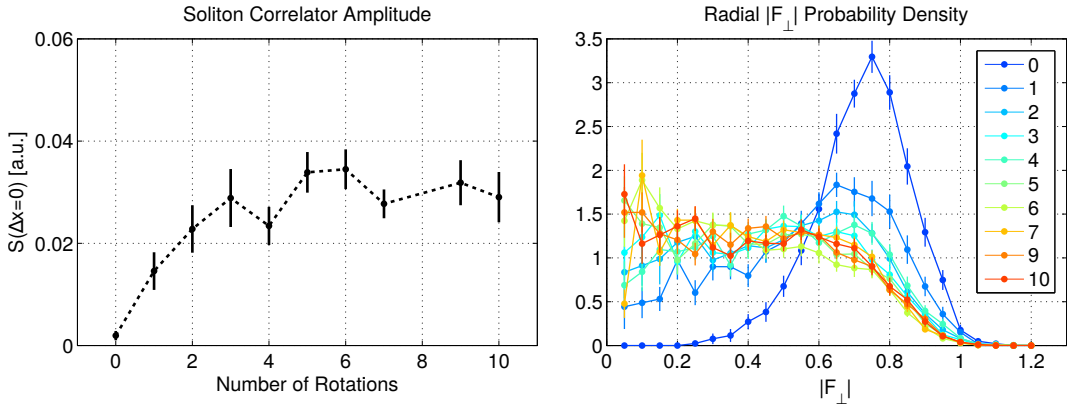

Figure 4.8.: Soliton correlator amplitude $\mathcal{S}(\Delta x = 0, t)$ and $|F_\perp|$ probability density after an evolution of $t = 30\,\mathrm{s}$ as function of the number of local spin rotations for generating vector solitons pairs. The measurement is performed at an initial atom number of approx. 70 k. The amount of excitations indicated by the correlator amplitude displayed in the left-had plot sharply increases with the number of local rotations in the system. Above 5 rotations its value becomes approximately constant value. Simultaneously, the right-hand plots shows how the the radial probability density of the transverse spin length $|F_\perp|$ changes its shape (numbers in the legend denote the number of local spin rotations). For the polar state initial condition (0 rotations) the transverse spin settles to approximately the same length at each position (cf. fig. 4.3), which corresponds to the sharp peak at $\overline{|F_\perp|} \approx 0.75$ displayed in the plot. For an increasing number of rotations the probability density transforms into an almost flat distribution up to around the spin length obtained from the polar initial condition. This is consistent with the 2d histograms shown in fig. 4.4. The errorbars in the plot on the left-hand side mark the 1 s.d. error interval of the mean. In the right-hand side plot the errors are obtained from jackknife resampling (see [170] or appendix D.2 for details on the error analysis).

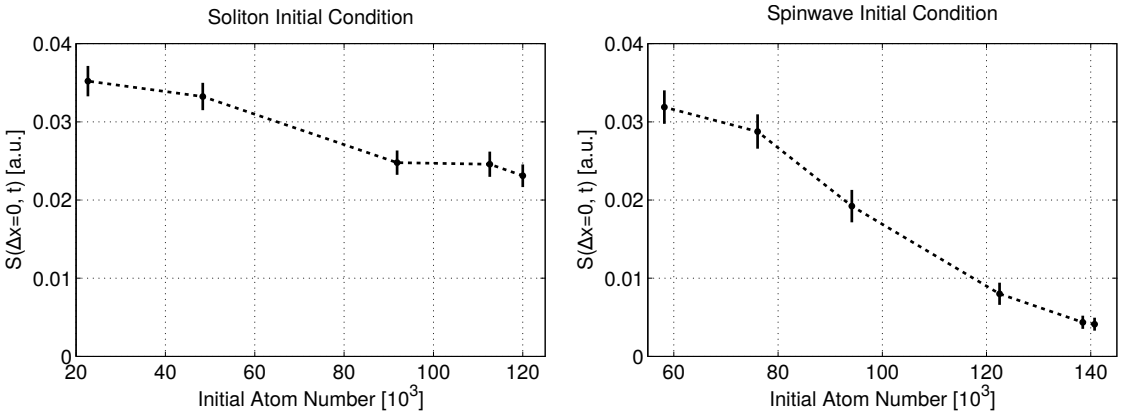

Figure 4.9.: Soliton correlator amplitude as function of initial atom number for different initial conditions. To induce perturbations in the system local spin rotations (left plot; measured after $t = 30\,\mathrm{s}$) and spinwaves in the Larmor phase (right plot; measured after $t = 29\,\mathrm{s}$) are used (see text for more details). Here, the size of the box trap is 130 µm for the soliton IC and 110 µm for spinwave IC. Here, the spin wave has a wavelength of approx. 14 µm. While low atom numbers show large correlator amplitudes for both initial conditions, at large atom numbers almost no excitations remain in the system with the spinwave initial condition as signified by the small correlator amplitude. In contrast, the excitations generated from local spin rotations show a strongly reduced sensitivity to the atom number.

is difficult because the setup does no permit standard time-of-flight measurements or $T/4$ imaging in a harmonic trap required to directly infer the temperature from a measurement of the momentum-space distribution. Nevertheless, both systematic measurements as well as as estimation of the temperature are possible in certain limits. Our findings in this respect are shortly summarized in the following.

In order to discuss the effects which may influence the temperature of the condensate we first want to quickly outline the relevant steps of the experimental sequence introduced in section 2.2. After loading the XDT from the magnetic trap, the optical power in the dipole beams is lowered to perform another step of evaporative cooling in the optical traps. After this, the crossed dipole beams is slowly ramped down to expand the atoms into the box trap consisting of the WG dipole beam and blue-detuned walls. Because the magnetic trap only confines low-filed seeking states all atoms are in the state $|1,-1\rangle$ at this point. Then, two consecutive MW π-pulses transfer all atoms into the state $|1,0\rangle$. This is the starting point for the local rotations for the soliton IC. To test whether the correlator amplitude exhibits a dependence on the strength of the dipole potential at the endpoint of the optical evaporation ramp we conduct a series of measurements with fixed evolution time $t = 30\,\mathrm{s}$. Between the measurements the final potential amplitude during evaporation is varied such that the atom number changes by almost a factor of 3. However, to exclude effects which stem from a change in the atom number it is quenched to a fixed value of approx. 60 k. This quench is performed by adjusting the MW pulses between $|1,-1\rangle \leftrightarrow |1,0\rangle$ such that only the desired population is transferred to $|1,0\rangle$. The atoms which remain in $|1,-1\rangle$ are then removed from the trap by a short SG pulse. For the lowest evaporation

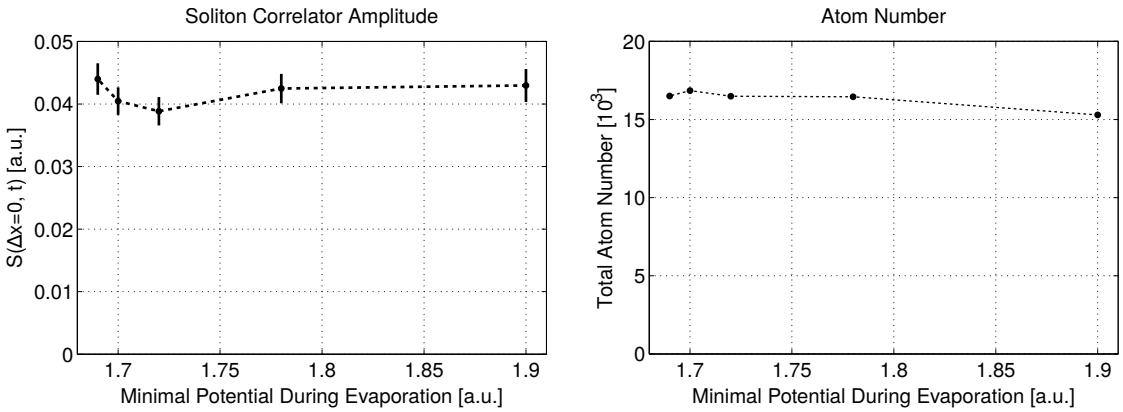

Figure 4.10.: Soliton correlator amplitude and corresponding atom number after an evolution of $t = 30\,\mathrm{s}$ for different potential amplitudes at the end of the evaporation ramp. After evaporation, atoms are removed from the trap in order to keep the initial number approximately constant (see text for details). The correlator amplitude stays constant for all evaporation ramp endpoints. For reference, the right plot shows the corresponding atom number after the evolution period.

potential no atoms are removed. Figure 4.10 shows that for all evaporation endpoints the correlator amplitude $\mathcal{S}(\Delta x = 0, t)$ stays constant within statistical errors. This result suggests that the temperature, controlled by the evaporation, does not influence. Although we cannot directly specify this temperature, the measurement nevertheless shows that the excitations are robust against changes in this experimental parameter. The removal of a toms via the SG pulse may additionally heat the system. However, assuming that the amount of potential heating induced by this step grows with the number of removed atoms, the atom number quench would add the same systematic temperature bias as the change in evaporation endpoint. That is, because for the largest final potential, which should also correspond to the largest temperature, also the largest amount of atoms needs to be removed to reach the desired atom number.

5. Universal Dynamics Far From Equilibrium

5.1. Introduction

In interacting many-body quantum systems, the microscopic description of highly excited states is, in general, intractable. In far-from equilibrium scenarios the excitation spectrum of the system is characterized by a strong deviation from the thermal scenario at a temperature compatible with the mean energy of the system. In this regime, usually many degrees of freedom, related to the large number of particles, are available to the system and therefore a microscopic description becomes exponentially hard in the system size. However, before eventual equilibration at large times, phenomena may emerge in these systems which allow a classification of the dynamics far from equilibrium [30]. Theoretical studies suggested that there exist regimes that feature universal dynamics, which is characterized by a scaling evolution of certain observables in time and space. This is associated to the existence of NTFPs [28, 31]. This offers the prospect of classifying non-equilibrium dynamics in universality classes [29, 30] in a similar way as equilibrium critical phenomena [171].

In the universal regime the dynamics in the infrared (i.e. low momenta $\hbar k$) fully governed by universal exponents α, β and scaling function f_s, which determine the time evolution of a dynamical observable f, via the scaling hypothesis [30]

$$f(k,t) = \left(\frac{t}{t_{\mathrm{ref}}}\right)^{\alpha} f_{\mathrm{s}}\left(\left(\frac{t}{t_{\mathrm{ref}}}\right)^{\beta} k\right). \tag{5.1}$$

Here, the observable f is determined by a universal function f_{s} by rescaling its amplitude and momentum axis in time, where t_{ref} is an arbitrarily chosen reference time for the scaling procedure. Close the a NTFP the scaling is tied to a transport of excitations towards the infrared. Here, the corresponding "particle" number, given by the integral over f, is conserved, which implies $\alpha = d\beta$, where d denotes the spatial dimension of the system; i.e. $d = 1$ for our experiment. In general, it is not clear which system observable is associated to f and this "relevant" quantity first has to be identified in the analysis of the dynamics.

Experimentally, non-equilibrium scaling has been observed in our spin-1 BEC [32]. Additionally, over the last years also other groups identified such universal dynamics with BECs prepared far from equilibrium by quenches. In a quasi-1d configuration a thermal cloud of single-component ^{87}Rb atoms has been quenched by rapidly reducing the trap depth to remove the large momentum population [33]. The following evolution shows a self-similar evolution of the density distribution in momentum space. Another experiment employed ^{39}K in a cylindrically symmetric

3d box, which quench-cooled the system by allowing the fast atoms to escape from the trapped region [34]. In the following evolution two distinct scaling evolutions at low and high momenta could explicitly be associated to the particle transport towards low k and the energy transport towards large k, respectively.

5.2. Previous Observation of Universal Dynamics in the Spin-1 BEC

For our first investigation of the occurrence of universal dynamics in the spin-1 BEC we start from the polar state as initial condition. By quenching q to a value in the easy-plane region strong spin excitations are generated via the SCC instability in the system. For measurements performed in the quasi-1d WG trap we have observed self-similar scaling in the Larmor phase spectra of the transverse spin $F_\perp$ [32] (see also [55] for a more detailed investigation of these non-equilibrium phenomena). To ensure that the scaling properties are independent of the initial condition we prepared additional initial states. These involve a homogeneous population of the $m_\mathrm{F} = \pm 1$ states via a short spin rotation, a spin wave with constant amplitude in the transverse plane, and an additional first quench to a different q value to generate excitations via SCCs over a short period of time, which are not commensurate to the final value of q. All these excitations show the same universal exponents and functional form of the rescaled spectra and are therefore robust against variations of the initial condition.

In accordance with these experimental findings, universal dynamics is expected to emerge for a certain set of initial conditions. Here, it may be expected that this set of states shares some feature which induces the approach to the same NTFP. However, which property governs this behavior is not yet clear. Therefore, it is possible that another set of initial conditions exists, which evolves towards another NTFP. Here, the question if this happens and what might be the relevant properties for this change in evolution poses an interesting question in the investigation of non-equilibirum dynamics.

To tackle this problem, we alter the experimental conditions with respect to the previously performed measurements on the spin-1 BEC. Here, a quasi-1d box trap is applied to confine the atoms. Further, the non-equilibrium behavior at long times is compared for the two different scenarios detailed in section 4.2.

5.3. Polar Initial Condition

As first we consider the polar IC, i.e. $\sim 150\,\mathrm{k}$ initialized in the polar state. Here, q is quenched to the value corresponding to the center of the spectroscopy feature shown in fig. 2.6. A short time after the quench the initially unstable modes excited by the SCCs are redistributed and a fixed transverse spin length starts to build up. This is nicely shown in fig. 4.3 and can be understood in terms of the mean-field Mexican-hat potential of the spin of the groundstate (see section 2.3.4 for details). At this point in time also a fixed functional form of the observable $f(k,t)$ develops and a self-similar evolution is observed by rescaling the spectra.

Here, the development of this fixed form is the feature defining the scaling regime in momentum k and t over which the rescaling is evaluated. In the previous measurements [32] the evolution of the Larmor phase, i.e. the Goldstone mode, towards lower k has been identified as relevant quantity for the scaling dynamics. Here, we will evaluate the structure factor of the transverse spin

$$f(k) = \mathcal{F}_{x\to k}\left\{\sum_{\tilde{x}} \langle F_\perp^*(\tilde{x}) F_\perp(x+\tilde{x})\rangle\right\} = \left\langle \left|\mathcal{F}_{x\to k}\left\{F_\perp(x)\right\}\right|^2\right\rangle, \tag{5.2}$$

which is related to the power spectrum of the spatial profile $F_\perp(x) = F_x(x) + iF_y(x)$[1] via the Wiener–Khinchin theorem (see e.g. [70]). We extract this quantity at each time t from the measured profiles by performing a spatial discrete Fourier transformation $\mathcal{F}_{x\to k}$. In the scaling regime, where the transverse spin length is approximately constant, the structure factor f captures the same physics as the Larmor phase observable applied in [32].

In fig. 5.1 bi-logarithmic plots of the strucutre factor $f(k,t)$ are shown in the scaling regime between $(17-42)$ s. Here, the range of momenta contributing to the scaling regime is marked by the gray shaded area, where the deviation from the power law behavior at large momenta defines the upper cutoff. This is motivated by the phase structure factor in [32], which shows a plateau region at low momenta and transitions to a power law at large momenta. This is well described by the function function $f_\mathrm{s} \propto 1/(1+(k/k_s)^\zeta)$, transitioning from a plateau region at small $k < k_s$ to a power law drop-off with exponent $-\zeta$ at large k [172]. In this measurement only the power law regime and the bending towards the plateau region is visible. We attribute this to a difference in system parameters as compared to [32], like the temperature and final q value.

To evaluate the scaling behavior a procedure similar to a least-squares optimization is applied to the scaling hypothesis given in eq. (5.1). A detailed explanation of the procedure is given in section 5.5. By choosing the last time $t_\mathrm{ref} = 42\,\mathrm{s}$ as reference the exponents[2]

$$\alpha = 0.46 \pm 0.38, \quad \beta = 0.49 \pm 0.18$$

are obtained, which collapse all times in the scaling regime to a single curve, i.e. the scaling function (see right-hand side of fig. 5.1). In a bi-logarithmic plot the rescaling with the exponent α leads to a shift upwards in time and the exponent β shifts the curves to the left of the plot.

The values of these exponents are similar to the ones obtained in [32] and thus suggest that the change in parameters (confinement in a box, change in temperature

[1] To account for the spatial resolution of the imaging setup the $F_\perp$ profiles are binned over a range of approx. 1.2 µm and normalized to the local atom number of the bins such that $|F_\perp| \leq 1$.

[2] The errors of the scaling exponents given here are estimated from jackknife resampling (for a short overview of this method see [170] and appendix D.2). The large error values for the polar IC stem from the closeness of the scaling function to a power law, which does not permit the determination of a unique set of (α, β) but instead allows a whole range of values. These correlations are visible in fig. 5.3 (and fig. D.3 for more details) but are not reflected in the errors given here.

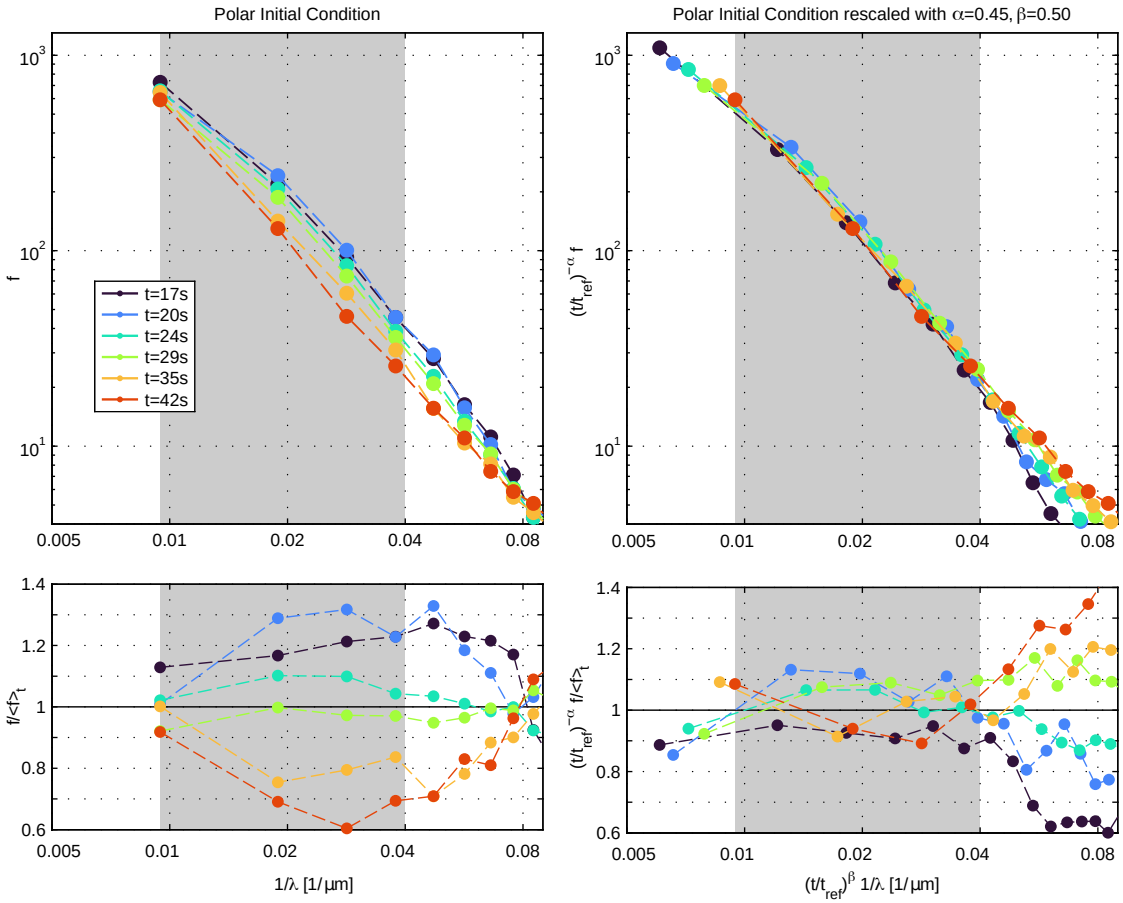

Figure 5.1.: Time evolution of structure factor $f(k,t)$ (left) and rescaled curves (right) for the polar IC. The optimal scaling exponents are extracted for a χ^2-like analysis (see section 5.5 for details) in the scaling regime where the functional from of the spectra stays constant (gray shaded area). Here, the momentum limits are defined by the lowest non-zero Fourier momentum and the upper bound is given by $k_{\mathrm{lim}} \approx 2\pi \times 0.04\,\mu\mathrm{m}^{-1}$. The rescaling procedure according to eq. (5.1) collapses the data to a common distribution (right-hand plots). To ease conversion to physical length scales, on the horizontal axis the reciprocal wavelength $1/\lambda$ is plotted instead of the wavenumber $k = 2\pi/\lambda$. Statistical 1 s.d. errors of the measured structure factor are smaller than the plot markers. The lower plots indicate the relative deviations of the spectra from the time-averaged strcuture factor $\langle f \rangle_t(k)$. For the rescaled data values for the time-averaged structure factor $\langle f \rangle_t(k)$ is obtained from piece-wise power law interpolation of the single spectra to common times.

and possibly also in q) noes not affect the non-equilibrium scaling significantly. For a proper interpretation of the error values given here, correlations between both values are important. More details about these are given in section 5.5.

5.4. Soliton Initial Condition

In contrast to the polar IC, the soliton IC leads to strong persistent fluctuations in the system. Therefore, it is interesting to see, whether also in this scenario a scaling evolution can be observed. For this, approx. 40 k atoms are prepared in the polar state and six pairs of local spin rotations generate vector solitons initially. As in the previously discussed measurement, q is quenched to approximately the same value. Over the same time scale of $(17-42)$ s as for the polar IC the structure factor $f(k,t)$ also shows a constant functional form (see fig. 5.2), as required for a scaling evolution. Here, a clear plateau region is present at low momenta, which is compatible with the smaller range of fluctuations compared to the polar IC (cf. fig. 4.5). At larger momenta it transitions to a smooth falloff. This functional form is compatible with the structure factor of a dilute soliton gas [173], consisting of a plateau region, which transitions to an exponential decay at large momenta. However, our system is not in the regime of dilute solitons but instead the size of the spin excitations in the system is comparable to their distance.

Applying the analysis described in section 5.5, a set of optimal rescaling exponents[3]

$$\alpha = 0.20 \pm 0.09, \quad \beta = 0.22 \pm 0.09$$

is extracted. These increase the overlap as is visible in the reduction of residuals especially at the right edge of the scaling regime (see right-hand side of fig. 5.2). Thus, also in the strongly fluctuating regime, where conceivably different excitations are relevant for the dynamics of the system, a scaling evolution is present.

5.5. Extraction Procedure for the Scaling Exponents

For faithfully extracting the scaling exponents we apply a method similar to a least-squares χ^2 optimization, which is adapted from [174]. Here, to avoid biasing the analysis by optimizing the data to a certain approximate scaling function the crucial difference of the analysis is to minimize the distance between the structure factors. For this we define the scaling residuum

$$\chi^2 = \sum_k \frac{\mathrm{Var}_t \left\{ f(k,t) \right\}}{\langle f(k,t) \rangle_t^2 \, k^2} \tag{5.3}$$

as distance measure on the measured structure factors, where time-subscripted quantities Var_t and $\langle \cdot \rangle_t$ specify averages with respect to time instead of ensemble averages. It evaluates the temporal deviations at each momentum k relative to the mean amplitude of the structure factor to weight all parts of the spectrum equally.

[3] The errors of the scaling exponents are estimated from jackknife resampling (see [170] and appendix D.2 for details).

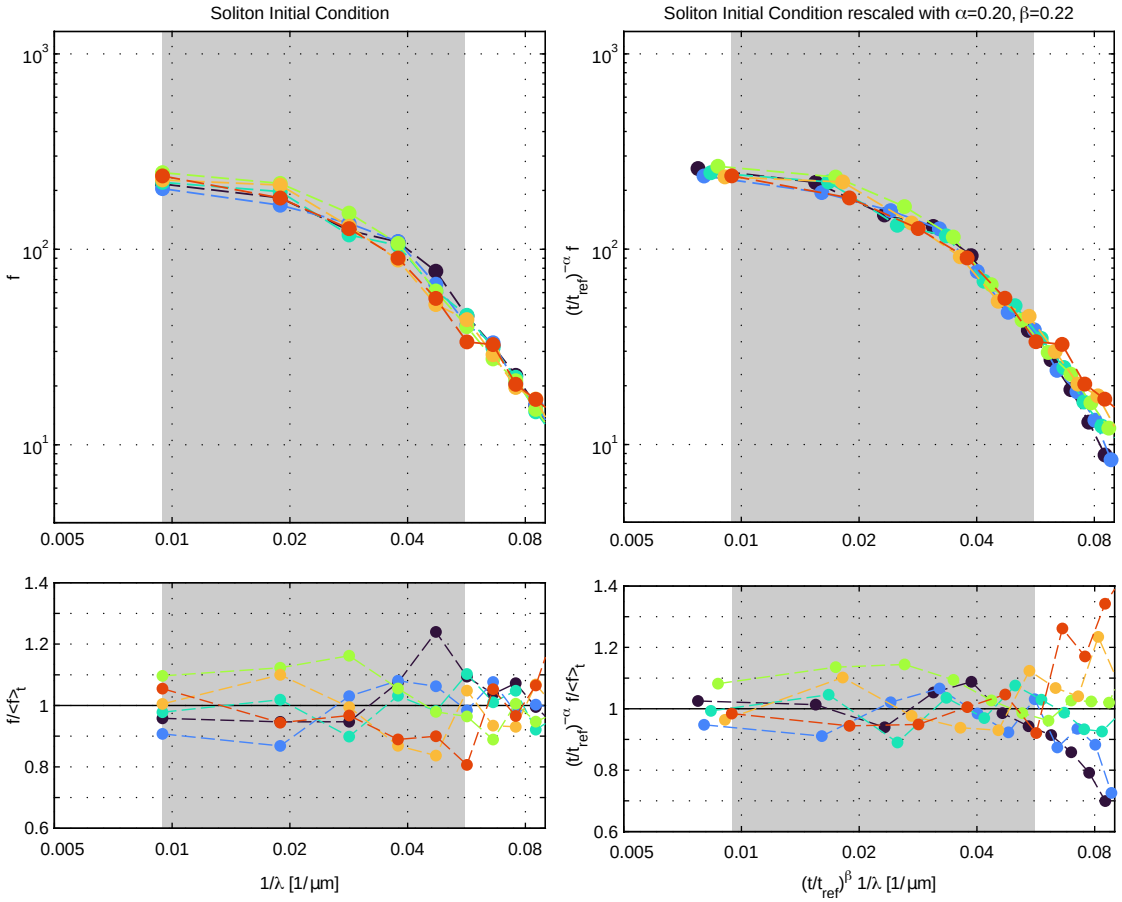

Figure 5.2.: Time evolution of structure factor $f(k,t)$ (left) and rescaled curves (right) for the soliton IC. See fig. 5.1 for more details on the structure of the figure. The gray shaded area marks the scaling regime in which the optimal scaling exponents are extracted. It is bounded by the lowest non-zero momentum and $k_{\mathrm{lim}} \approx 2\pi \times 0.056\,\mu\mathrm{m}^{-1}$. Note that on the horizontal axis the reciprocal wavelength $1/\lambda$ is plotted instead of the wavenumber $k = 2\pi/\lambda$. The lower plots indicate the relative deviations of the spectra from the time-averaged strcuture factor $\langle f \rangle_t(k)$.

Nevertheless, to approximately take the non-uniform distribution of the equally spaced Fourier momenta on the logarithmic axis into account, a heuristic factor of k^2 is introduced. Only momenta in the scaling regime (gray shaded area in figs. 5.1 and 5.2) are taken into account. The lower bound of these ranges is given by the lowest non-zero Fourier momentum and the upper limit k_{lim} is identified by a similar gradient of the structure factors $f(k,t)$. This upper cutoff k_{lim} is induced by the growth of $f(k,t)$ at large k (see the full structure factors provided in appendix D.1). χ^2 needs to be evaluated with respect to the rescaled spectra, i.e. in particular at rescaled momenta $(t/t_{\mathrm{ref}})^{\beta}k$. This results in differing momentum axes for the different times. We linearly interpolate the corresponding rescaled structure factors $(t/t_{\mathrm{ref}})^{\alpha}f$ to 20 equally distributed momenta in the bi-logarithmic plot (i.e. piece-wise power law interpolation[4]). This allows the evaluation of χ^2 at common momenta for all times, which is minimized to find the optimal scaling exponents α and β. To visualize the results of this analysis, in fig. 5.3 we plot the normalizable residual distribution

$$W = \frac{1}{\mathcal{N}} \exp\left(-\frac{\chi^2}{2\chi^2_{\mathrm{min}}}\right), \tag{5.4}$$

where χ^2_{min} denotes the smallest value obtained in the optimization and the normalization factor $\mathcal{N}$ is chosen such that $W = 1$ at this point. Here, χ^2_{min} takes the role of the systematic deviation of the measured structure factors from a perfect scaling behavior.[5] Its numeric value depends on the specific definition of χ^2 but it is useful to note that at the point where W dropped to ~ 0.6 the overlap of the spectra achieved by the rescaling procedure is separated by χ^2_{min} from the optimum.

For the polar IC the residual distribution has the shape of an ellipse, which is strongly extended along α. The reason for this is that the lack of a clear plateau in the strucutre factor (cf. fig. 5.1). Therefore, the exponents are not well constrained along the axis of the ellipse. The correlations in these uncertainties, which are connected to the orientation of the ellipse, are not captured by the error values given in section 5.3. Since the ellipse is not oriented along the diagonal this allows a better distinction of scaling exponents than one would naively expect from the error values. See also appendix D.2 for more details on the error extraction.

In contrast, the residual distribution for the soliton IC is more circular. Therefore, the error values resemble the actual uncertainties in the scaling exponents much better. This allows a distinction between the sets of exponents for the two different ICs.

5.6. Conclusions

For both the polar and soliton ICs, confined in a box potential, a non-equilibrium scaling evolution is observed in the structure factor f of the transverse spin $F_{\perp}$.

[4] This is most conveniently implemented by linearly interpolating the logarithms of the structure factor with respect to the logarithms of the momenta. After the interpolation the resulting spectrum needs to be transformed by the corresponding exponential function.

[5] The χ^2_{min} values extracted for the scaling analysis described here are $\chi^2_{\mathrm{min}} = (271 \pm 106)\,\mu\mathrm{m}^2$ for the polar IC and $\chi^2_{\mathrm{min}} = (185 \pm 75)\,\mu\mathrm{m}^2$ for the soliton IC. The errors are estimated, equivalently to the ones of the scaling exponents, from jackknife resampling.

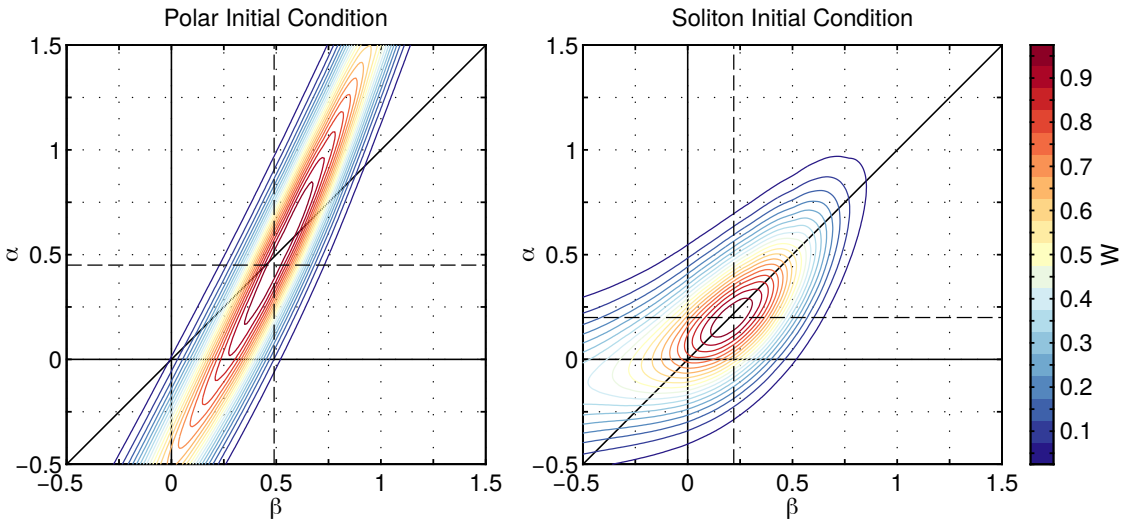

Figure 5.3.: Scaling residual distribution W (cf. eq. (5.4)) of the strcuture factors (see figs. 5.1 and 5.2) for time evolution from the polar and soliton ICs. The scaling residuals χ^2 (cf. eq. (5.3)) entering in the distribution are calculated from the structure factors summed over the gray area shown in the respective plots, rescaled with the exponents α and β in order to collapse the data to a common scaling function f_s according to eq. (5.1) (cf. axes in right-hand plots of the structure factor figures). W is normalized to 1 at the position where the minimal residuals are obtained. The corresponding optimal exponents are marked with dashed black lines. These values are clearly distinct for the two different scenarios.

Here, the equality $\alpha \approx \beta$ of the extracted exponents indicates particle number conservation in $d = 1$ dimension.[6] For the polar IC these values are compatible with the analytic prediction of $\beta = 1/2$ for $O(N)$ [30] and $U(N)$ [175] symmetric models for Bose gases.

However, for the soliton IC we find distinctly different set of scaling exponents with $\beta \approx 0.2$ and also a different scaling function, indicating the presence of a different NTFPs in this scenario. In a numerical study a reduction of the scaling exponents to $\beta \approx 0.2$ has been observed for the decay of non-elementary vortices with winding numbers > 1 in a 2d system, while the decay of elementary vortices with winding number 1 shows $\beta \approx 0.5$ [172]. Here, the clustering of like-sign (same direction of rotation) reduces the annihilation process between vortex and anti-vortex pairs and may play a role in the slowing of the scaling evolution. This whole process, however, is associated to phase-ordering kinetics [176]. There, the pairwise annihilation of defects (domain walls, vortices, etc.) leads to a growth of the length scales associated to the order parameter. While important for a wide variety of systems, in our system this description does not seem to be the driving mechanism because the defect density, as indicated by the correlator $\mathcal{S}$ does not decay for the soliton IC.

Nevertheless, not only the initial conditions, but also changed system parameters

[6] Although the system is not 1d for density excitations, here the relevant excitations are related to the spin d.o.f. Because the spin healing length ξ_s is larger than the transverse extent of the trap, for the spin dynamics the system should be 1d.

may be associated to the change in scaling behavior. The ICs clearly induce different excitations in the system but also the difference in density may affect the evolution. At the smaller density employed for the soliton IC the parameter $q/|nc_1|$ is effectively larger. Truncated-Wiegner simulations in a 1d system with homogeneous density and periodic boundary conditions have indicated an increase of the scaling exponents from $\alpha, \beta \sim 0.25$ at $q/|nc_1| = 1.1$ to $\alpha, \beta \sim 0.45$ at $q/|nc_1| = 0.1$ for both the polar and soliton IC[7] shows a similar behavior [177]. Experimentally, a sufficiently reliable investigation of the q-dependence has not been achieved, yet.

Additionally, the loss of atoms over the course of the $\sim 42\,\mathrm{s}$ required for the observation of the scaling dynamics may impact the measurement. The loss is roughly exponential[8] and leads to an also exponential decrease in the 1d density. As observed in fig. 2.5 the change in density is proportional to the spin interaction energy nc_1 and therefore induces a dynamical change of $q/|nc_1|$ over time. These have not yet been considered in the previously referenced simulations but given the q-dependence it would be conceivable that it reduces the scaling exponent. This, however, is not observed experimentally. To gauge the impact of the atom loss on the experimental dynamics we performed an experiment during which the left box wall was shifted inwards. This was implemented such that despite the continuous loss of atoms the density inside the box remained constant over time. This way we explicitly confirmed that changes in the width of the $\mathcal{S}$ correlator peak at $\Delta x = 0$ are not connected to the density-dependence of the healing length. However, a systematic study of the impact of the density change on the scaling exponents in still missing.

Nevertheless, the experiments discussed in this chapter show the realization of two distinct scaling phenomena, which indicates the presence of at least two NTFPs for the dynamics in a spin-1 BEC. This implies that, although the appearance of scaling seems to be robust against a wide range of initial conditions, there exist specific system parameters (initial condition, density or q) which constrain the non-equilibrium scaling. This sets the foundation for the precise determination of the relationship between universal dynamics and these parameters in future experimental or theoretical works.

[7] For both ICs the same density is used.

[8] However, during the initial period the decay is slightly faster. This is most likely connected to the density-dependence of three-body loss processes which are more relevant at larger densities at early times. Over the time range associated to the scaling regime $1/e$ lifetimes of 39 s and 53 s are observed for the polar and soliton IC, respectively.

6. Summary

In this thesis a method is introduced to generate coherent vector solitons in a spin-1 BECs. It is based on the application of the vector-Stark shift to generate local spin rotations with a steerable laser beam. In chapter 3 this method is applied to deterministically prepare three-component vector solitons. While also showing properties reminiscent of single-component solitons, the presence of population in multiple components gives rise to a richer parameter space and accompanying dynamics. Most prominently, the bright-dark-bright (BDB) vector solitons investigated here possess an internal degree of freedom associated to the two bright components, which may be described similar to a spin-1/2 particle. During collisions of two solitons this internal polarization state changes depending on the soliton parameters and the initial soliton polarization. This underlines the difference between linear waves and solitons: while the former only change amplitudes via interference while overlapping, solitons may alter their state in collisions and therefore act as a collective particle consisting of $\sim$ 2000 atoms. Both, the spatial motion and density profiles, as well as the collisional dynamics are consistent with analytical predictions for the three-component Manakov system. This model is also expected to give an accurate description of the microscopic Hamiltonian when the SCCs are switched off. However, dissipation and indications for a possible inelasticity of the collisions also show the presence of effects beyond the Manakov limit. Due to the self-consistent nature of the vector solitons the phase evolution of their polarization is not affected by mean-field shifts due to changes in the background density. This allows the application of these solitons as accurate sensors for magnetic field gradients.

In a separate set of experiments the impact of localized defects on non-equilibrium dynamics was investigated. In quench experiments starting from the homogenous polar state, instabilities highly excite the system. For small q these generate localized spin defects which bear a remarkable resemblance to dark solitons of the NLSE (i.e. Manakov solitons), although they appear in the transverse spin instead of the densities. At large densities these defects decay and appear to not significantly influence the long-time dynamics. In this limit the system shows a scaling evolution indicative for the presence of a NTFP. To investigate the dynamics with respect to the presence of a large number of defects, multiple local spin rotations of the type discussed in chapter 3 are applied to generate non-linear excitations as initial condition for the quench experiments. After some time, this system develops strong fluctuations in spin length and phase. At low densities, where these length-and-phase defects are stable, a scaling evolution is observed as well. However, due to the presence of the defects the structure factors show a different functional form and much slower shift than for the polar IC. This indicates the presence of two distinct NTFPs in the system.

7. Outlook

7.1. Improvement and Extension of the Local Control Setup

In section 2.6.6 we have shown that the vector-Stark shift of a focused laser beam can readily be used to drive local spin rotations. However, also shortcomings have been identified or general extensions to the experiments are possible and may yield interesting results. Some of these are presented in the following.

7.1.1. Differently Sized Rotations

Numerical simulations accompanying the investigation of the vector soliton dynamics suggested that spin rotations with a much larger beam diameter still lead to stable excitations in the system. These BDB structures additionally showed oscillations in the size as well as much more pronounced spatial dynamics during collisions.[1] Here, the usual repulsive interaction between colliding dark solitons [129] seems to be partly overcome by attractions in the bright components to permit multiple oscillations in the collision region, similar to numerically obtained oscillations of soliton bound states [131, 144]. This also promises access to bound states between these structures similar to dark-bright bound solitons observed in optics [129].

Experimentally, this increased size of the rotation region may be implemented using a frequency modulated AOD signal as demonstrated during the discussion of fluctuations in section 2.6.6. By sweeping the horizontal AOD frequency once during the pulse time of the local spin rotation, effectively a larger region is addressed by the spin rotation. The modulation waveform can be tuned to the desired spatial shape and may even be optimized for the generation of the solitons by minimizing the radiation of undesired wavepackets.

7.1.2. Cancellation of the Local Magnetic Offset Field

As shown in fig. 2.18 the application of circularly polarized light for the local rotation beam induces a magnetic offset field which scales with the spin rotation Rabi frequency Ω_{rot} (see appendix A). This leads to an, in general, undesired detuning and a phase evolution of the $m_{\mathrm{F}} = \pm 1$ atoms which perturbs the system and induces additional spatial dynamics. To cancel the offset field, it is imperative to remove the circular polarization. This is simply achieved by removing the $\lambda/4$

[1] These numerical simulations have been carried out by Christian-Marcel Schmied within the scope of [83].

waveplate in the optical setup after the AODs. To induce a vector Stark shift, however, the cross product between electric field components may not vanish. This is possible by using two separate beams with different polarization directions (see e.g. [80]). Here, both beams should be co-propagating to minimize the momentum transfer to the atoms induced by the coupling. The pairs of electric field components from both beams must also oscillate at distinct frequencies which are separated by the resonance frequency, i.e. the Larmor frequency ω_{L} in case of the spin rotations. This can be achieved by an appropriate modulation of the laser beams.

Because the diffraction of the AODs requires a fixed polarization direction of the incident light, only one of these linearly polarized beams may be deflected by the current AOD setup. However, a second beam with orthogonal polarization may be combined with the deflected beam with the help of a polarizing beam splitter after the AODs. Because the direction of this second beam cannot be adjusted during the experiments it should be focused to the back focal plane of the objective to obtain a collimated beam which illuminates the whole BEC. Because the wavelength of this laser is close to the tune-out wavelength of the scalar Stark shift and it is linearly polarized the atoms do not experience an energy shift due to this beam alone. Only in the region where the local control beam overlaps with this collimated beam are local spin rotations induced by the presence of the appropriate polarization and frequency components of the electric field.

7.1.3. Local Microwave Control

The local coupling via a steerable laser beam is not only limited to spin rotations within a hyperfine manifold. Instead, a two-photon Raman transition may be used to locally drive transitions between the hyperfine manifolds [127, 178]. Employing an electro-optic modulator for the appropriate modulation of the light at the hyperfine splitting frequency $\Delta E_{\mathrm{HFS}}/h \sim 6.8\,\mathrm{GHz}$ this scheme can be implemented similar to the current local control. Here, not only population transfers may be implemented but also local dressing can be achieved, similar to the global MW dressing already used in the experiment. This allows the spatially resolved control of q. This may allow for a Josephson-like contact in the transverse spin of the easy-plane phase without perturbing the total density.

Additionally, the phase control of different m_{F} levels, which may be implemented via two consecutive π-pulses with different phase or via dressing, allows for the full state control. Combined with the local spin rotations this may enable the full control of the vector soliton parameters. With the width of the local spin rotation the size of the solitons is adjusted while the control of the phase profile in $m_{\mathrm{F}} = 0$ should allow the access to the soliton velocity.

7.2. A Road Towards Soliton Entanglement

While soliton solutions in BECs are derived on the mean-field level they are still excitations which are inherently subject to quantum evolution. Therefore they also exhibit fluctuations constrained by the uncertainty relation and entanglement.

Quantity	Soliton 1	Soliton 2
Norm. velocity ξ_j	0.0452	−0.0563
Norm. inv. width ν_j	0.1794	0.1968
Chem. potential q_0^2	0.66	0.66

Table 7.1.: Soliton parameters applied for the simulation of polarization scattering. The values are given in the normalized form defined by eq. (3.33). These values are similar to the ones given in table 3.1.

These have been discussed in the context of the spatial and phase degrees of freedom for single-component solitons [165].

Here, we want to present an alternative approach to the extraction of entanglement based on the internal degree of freedom offered by multi-component vector solitons. The basic idea follows the concept of spin squeezing induced by the interaction of spins [179, 180]. Here, the role of the spin is assigned to the polarization $\boldsymbol{c}$ of the BDB solitons investigated in chapter 3 and the interactions are provided by the polarization scattering during the soliton collision. Instead of a single particle carrying spin we are therefore considering the combined spin of all atoms contributing to the soliton.

7.2.1. Polarization Squeezing and Entanglement

To exemplify the polarization squeezing we will consider the collision of two solitons (see table 7.1 for soliton parameters). Applying an approach similar to Truncated-Wigner simulations, 5000 complex polarization vectors $\boldsymbol{c}_{1,2}^{\mathrm{i}}$ are drawn from a Gaussian distribution with the same variance as the initial states for solitons 1 and 2. These are then inserted into the polarization scattering formula (3.30) to obtain the final polarization $\boldsymbol{c}_{1,2}^{\mathrm{f}}$ after a soliton collision. Here, we define the pseudo-spin-1/2 observable of the polarization (see section 3.5 or section 2.5.5 for the definition of the spin observables $\hat{S}_j$ with respect to the bright components of the soliton) as

$$\hat{S}(\phi) = \cos(\phi)\hat{S}_y + \sin(\phi)\hat{S}_z, \tag{7.1}$$

corresponding to a projection in the y-z-plane. In contrast to the previous use of the operators, here no implicit normalization with the atom number will be assumed (i.e. the maximal expectation value $\langle S(\phi)\rangle$ is given by the atom number N). As initial polarizations coherent states aligned with the x-axis, and occupied by $N = 50$ atoms, are used. The distribution of the Truncated-Wigner samples is shown on the left-hand side of fig. 7.1. For this choice of initial Larmor phases ($\varphi_{\mathrm{L}} = 0$ for soliton 1 and $\varphi_{\mathrm{L}} = \pi$ for soliton 2) the fluctuations of the spin observables are strongly enhanced by the collision. In fact, traces of this behavior may already be visible in the form of slightly increased error bars in fig. 3.17 for $\Delta\varphi_{\mathrm{L}}^{\mathrm{i}} \sim 180\,\mathrm{deg}$.

While spin interactions induce squeezing of a collective spin observable in spinor gases, in case of the solitons we will consider a combined observable

$$\hat{u}(\phi_1, \phi_2) = \hat{S}_1(\phi_1) + \hat{S}_2(\phi_2), \tag{7.2}$$

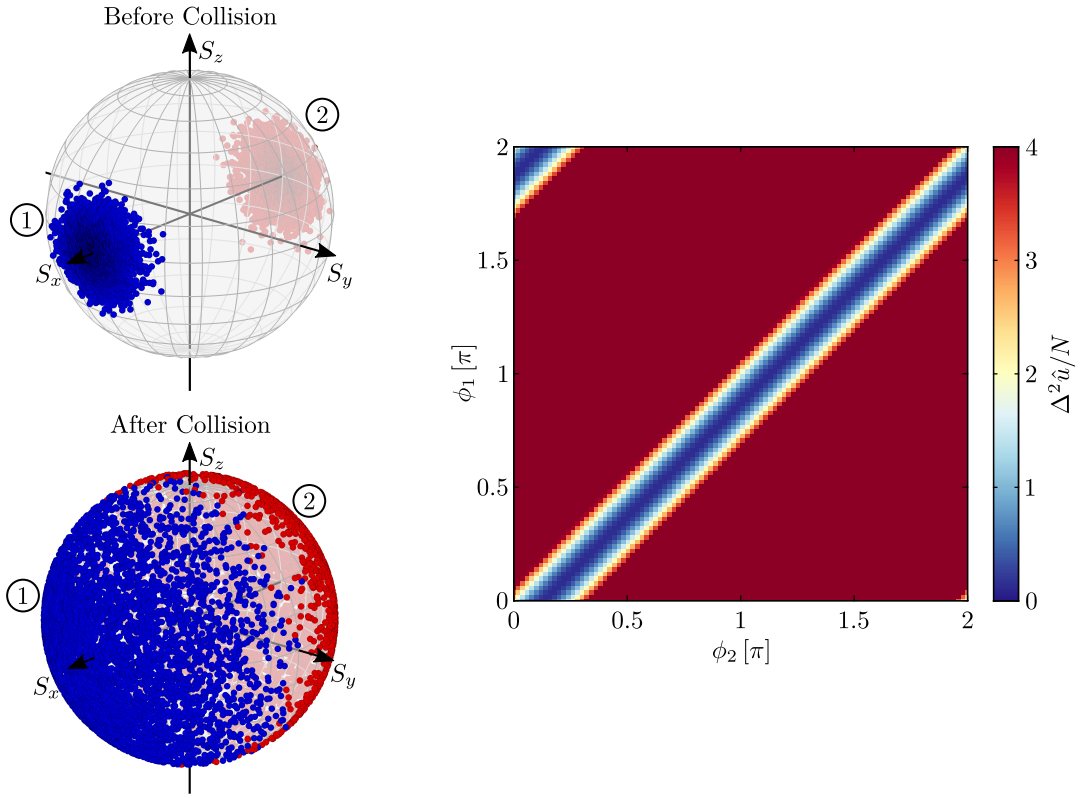

Figure 7.1.: Truncated-Wigner samples of the soliton polarizations before and after collision on the spin sphere (left) and squeezing variance $\Delta^2\hat{u}$ of the soliton polarizations after collision (right). On the left-hand side the observables are normalized by the atom number N to a maximal value of 1 while on the right-hand side no normalization is applied. This calculation uses an number of $N = 50$ atoms in the bright components $m_\mathrm{F} = \pm 1$ to properly visualize the distribution on the spin sphere (the usual atom numbers in the experiment are much larger cf. section 3.4.4). From Gaussian distributions with fluctuations corresponding to the initial coherent states of the soliton polarizations before collision 5000 samples are drawn and propagated with eq. (3.30) to obtain the polarizations after soliton collision. For certain angles $\phi_{1,2}$ the combined observable $\hat{u}(\phi_1, \phi_2)$ shows fluctuations which are smaller than the minimal uncertainty coherent states. Because $\hat{u}$ consists of a sum of observables from both solitons, the Heisenberg bound is 2 in this case. For the 5000 samples used here, the normalized variance $\Delta^2\hat{u}/N$ of the uncorrelated initial coherent states lies within a range of ± 0.15 around this value. Therefore, all variances significantly below 2 indicate squeezing below the standard quantum limit (blue part of the color map).

which is constructed by summing the spins of both solitons labeled by the numbers 1 and 2 (cf. fig. 3.15 for the definition of the soliton labels). For the initially uncorrelated coherent states the variance $\Delta^2\hat{u}(\phi_1,\phi_2) = \Delta^2\hat{S}_1(\phi_1)+\Delta^2\hat{S}_2(\phi_2) = 2N$ is equal to twice the coherent state variance orthogonal to its orientation on the spin sphere. Therefore, fluctuations smaller than 2 in the soliton polarizations after collisions show squeezing below the standard quantum limit and therefore signify the presence of entanglement. For angles $\Delta\phi = \phi_2 - \phi_1 \approx 0.12\,\pi$ the calculation shows the strongest squeezing to a value of $\Delta^2\hat{u}(\Delta\phi = 0.12\,\pi)/N \approx 0.13$ (see right-hand side of fig. 7.1). Here, the exact value of the offset $\Delta\phi$ is probably a result of the soliton interaction controlled by the exact soliton parameters used here.

To explicitly verify the presence of entanglement between the two solitons, the Duan inseparability criterion [181] may be applied. For separable states it bounds the sum of the variance of two observables from below. Here, we consider two observables $\hat{u}(\phi_{1,1},\phi_{1,2})$ and $\hat{u}(\phi_{2,1},\phi_{2,2})$, which differ in the respective projection angles. A similar calculation as performed in [181] leads to the following variance criterion fulfilled by all separable states:

$$\Delta^2\hat{u}(\phi_{1,1},\phi_{1,2}) + \Delta^2\hat{u}(\phi_{2,1},\phi_{2,2}) \geq 2\left(|\sin(\Delta\phi_1)|\left|\left\langle\hat{S}_{1,x}\right\rangle\right| + |\sin(\Delta\phi_2)|\left|\left\langle\hat{S}_{2,x}\right\rangle\right|\right), \tag{7.3}$$

where $\Delta\phi_j = \phi_{2,j} - \phi_{1,j}$ is the difference of the projection angles applied to soliton j and $\langle\hat{S}_{j,x}\rangle$ denotes the pseudo-spin S_x expectation value of soliton j. For the coherent state ICs $\langle\hat{S}_{j,x}\rangle/N = 1$, which leads to a a structure shown on the left-hand side of fig. 7.2. To obtain an entanglement witness $\mathcal{D}$, the left-hand side of eq. (7.3) may simply be divided by the right-hand side. This quantity signifies entanglement when $\mathcal{D} < 1$. This violation is strongest for a set of angles where the fluctuations are minimal (blue region in the squeezing plot of fig. 7.1), i.e. $\phi_{2,k} - \phi_{1,k} = 0.12\,\pi$, and the bound is maximal, i.e. $\Delta\phi_j = \pi/2$. This leads to a maximal violation of $\mathcal{D} \approx 0.09$ (see right-hand side plot of fig. 7.2).

This calculation suggests that collisions of BDB vector solitons may become entangled in their polarization degree of freedom during collisions. Further, the scheme of this discussion is almost equivalent to the method used in [66], implying that its extraction is experimentally feasible. However, magnetic field fluctuations in the experiment will lead to a scrambling of the Larmor phase before readout. This needs to be taken into account in the analysis. This may possibly also be overcome by another choice of initial polarization state. Therefore, the soliton polarization is a promising candidate to prove entanglement of solitons.

Here, not only soliton collisions may provide an interesting opportunity for the production of entanglement. In case of the generation from local spin rotation the formation process may, at least in the sense of the possibility for interactions, also be interpreted as a soliton collision. Therefore, also during formation entanglement may be generated between the two solitons emerging from a single rotation site.

7.2.2. Technical Limitations

For experimentally witnessing entanglement it is crucial that the technical fluctuations of the initial state preparation and readout are small enough to not scramble

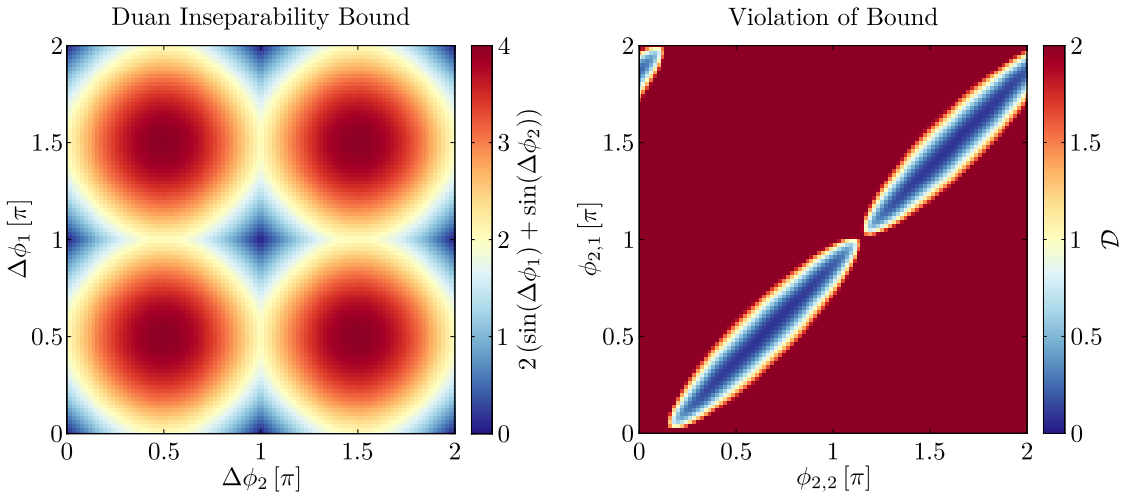

Figure 7.2.: Inseparability bound (left) and violation of the soliton polarization after collision (right) for the scenario shown in fig. 7.1. The inseparability bound corresponds to the right-hand side of eq. (7.3) for a coherent state with $\langle \hat{S}_{j,x}\rangle/N = 1$. However, the reduction the bound due to a change of $\langle S_x\rangle$ for the polarizations after collision needs to be taken into account. For a maximal violation fo the inseparability bound, for the first observable the angles $\phi_{1,1} = 0$ and $\phi_{1,2} = 0.12\pi$ are chosen to obtain minimal fluctuations (cf. right-hand plot in fig. 7.1). The entanglement witness $\mathcal{D}$ is the fraction between the left and right-hand side of eq. (7.3) and signifies entanglement when $\mathcal{D} < 1$ (blue part of the color map). This witness is shown as a function of the projection angles of the second observable in $\mathcal{D}$ and inherits its structure from the squeezing variance shown in fig. 7.1 and the bound on the left-hand side. As indicated by the bound, the largest violation of $\mathcal{D} \approx 0.09$ is obtained when $\Delta\phi_j = n\pi/2$ ($n \in \mathbb{N}$), i.e. $\phi_{2,1} = 0.5\,\pi$ and $\phi_{2,2} = 0.62\,\pi$.

the required signatures. In case of variance-based witnesses this is clear: if the technical fluctuations are larger than the Heisenberg bound of the coherent state no entanglement may be certified. As has been analyzed in section 2.6.6, the local spin rotation currently seems induce a critical level of noise, i.e. more than coherent state noise. Therefore, no entanglement certification is currently possible. Previous analysis of the local laser beam power and position suggest that position fluctuations contribute, but cannot fully explain the overall noise. Another possible source for fluctuations may be the polarization of the light, which also enters in the rotation amplitude. This may be analyzed with the Mako camera in the AOD setup shown in fig. 2.14 by inserting a $\lambda/4$ waveplate in combination with a polarizing beam splitter or polarization filter.

7.3. Non-Equilibrium Dynamics

The investigation of the non-equilibrium dynamics presented in chapter 5 clearly shows two different scaling scenarios with individual functions and exponents. However, due to the different densities applied in the initial condition and the inconclusive connection between q_{exp} and the actual value of q, different effects may be responsible for the observation of the two scaling phenomena. Here, a few ideas for measurements are given, which will allow the distinction of possible effects affecting the scaling dynamics.

The most likely origin of differences in the scaling behavior may be the exact value of $q/|nc_1|$, which defines the mean-field groundstate as discussed in section 2.3.4. As suggested by numerical simulations [177], this parameter may affect the scaling exponents. To test this experimentally, it would be sensible to systematically observe the dynamics for different final q values of the quench. Here, it would be sensible to enhance this measurement by ensuring a fixed $q/|nc_1|$ during the evolution (see section 7.3.2). Depending on the results, an impact of q on the scaling may already be excluded. On the other hand, if the q-dependence can be confirmed, this would imply a continuous dependence of the scaling behaviour on the parameters of the microscopic Hamiltonian. For NTFPs the microscopic details should not be relevant and therefore the experimental determination of the exponents for different q poses an interesting question.

Since a single measurement of the scaling dynamics (i.e. the measurement for a single q value) will require approx. 3 days of continuous measurements (for a single IC), this measurement will require at least 2 weeks of continuous measurements, over which the parameters need to be held constant. For this, special care must be taken to continuously calibrate q_{exp}. Also magnetic field gradients need to be monitored as they also affect the spin dynamics. Additionally, also a comparable temperature of the condensate must be ensured because large temperatures decrease the final spin length and therefore obviously impact the dynamics of the system.

7.3.1. Comparison of Polar and Soliton Initial Conditions

If only a change of $q/|nc_1|$ between the two settings presented in chapter 5 is supposed to be excluded, also a different approach is possible. When the exact

calibration of q_{exp} against q can be determined the same $q/|nc_1|$ value may directly be set in the experiment. For this, however, the calibration of q_{exp} has to be understood as a function of the density. The single-mode mean-field picture around the easy-plane phase suggests that the center of the resonance shown in fig. 2.6 corresponds to $q = 0$. However, it is not clear, how well this picture actually holds in the extended system, which is not at all in the single-mode limit. Deviating from this picture, for small densities the center of the resonance shifts to lower q_{exp}. To alleviate the uncertainty of applicability of the single-mode approximation in the calibration of the q_{exp} values it is therefore sensible to probe this resonance in a system with a spatial extension smaller than the spin healing length ξ_{s}. In this limit, even full quantum mechanical predictions are possible for ≥ 1000 atoms. Thus, the proper calibration can be performed in a small system and then be applied in the extended system for the measurement of the long-time dynamics.

Alternatively, measurements at an intermediate density can be performed to ensure the same system parameters. However, in this regime, both initial conditions show a similar decay of the soliton correlator amplitude, albeit with different initial offset. here, the initial excitations after a quench of the polar IC have an increased lifetime while the lifetime of the ones generated from the soliton IC decreases. This may again impact the properties of the scaling dynamics which may be observed in the system.

7.3.2. Suppression of q-Dependence

For comparison with theoretical predictions, which typically assume a constant value of $q/|nc_1|$ after the quench, it is desirable to keep this ratio fixed in the experiment. Experimentally, the atom loss over the large time scales involved in the dynamics is slowly increasing this ratio over time. Although the change of this quantity is slow, and therefore effectively adiabatic, it may still affect the exact properties of the evolution. To tackle this time dynamics there are currently two approaches available in the experiment which are shortly summarized in the following.

While a reduction of the atom loss is difficult, the density may be kept constant even though atoms are lost. This can be achieved by slowly reducing the box size during the evolution of the system by moving the box walls. Experimentally, this is readily implemented by a slow frequency modulation of the horizontal frequency of one box wall. Since this requires a non-periodic RF signal for the AOD, either another AWG must be used which supports a streaming mode[2] or frequency modulation[3] together with RF combiners may be applied. Either way, this approach changes the system size in time, which may also affect the dynamics.

[2]Here, the values sampled by the AWG are continuously supplied by the controlling computer. Given a sufficient computational throughput this allows either a calculation of the required "on the fly" or the signal may be pre-calculated and recalled from memory. A popular example for such an AWG is the 66xx-x8 series manufactured by Spectrum Instrumentation.

[3]The Keysight 33600 series of AWGs currently employed in the experiment already offer an integrated frequency modulation capability with an external drive. Therefore, a second AWG may be used to drive the slow modulation ramp and the appropriately modulated horizontal RF signals for each of the box walls required for the horizontal AOD.

Instead of changing the density, also the MW dressing may be adjusted dynamically to maintain a constant ratio of $q/|nc_1|$. Here, the newly implemented stabilization setup for the MW system [61] offers this capability. It regulates the power to a fixed value but the frequency of the radiation may dynamically be changed with an AWG (see section 2.4.2 for details on the setup). Here, a similar signal generation setup may be employed as discussed in the previous paragraph. This way the detuning of the dressing may be changed in order to adjust the dressing value q_{mw} to the change of the density induced by the atom loss.

The capability to dynamically vary q_{exp} also opens further possibilities. When adiabatically crossing the quantum phase transitions from the polar to the easy-axis phase entanglement is generated between $m_{\mathrm{F}} = \pm 1$ [182]. In addition to this, the spatial extension of our system offers the possibility to investigate the spatial distribution of entanglement, which may be directly accessed with the simultaneous readout [66]. For this, also novel entanglement witnesses based on entropies may be applied [183].

7.4. Towards Thermal Exquilibrium

Although not detailed in this work, we have further studied the structure of excitations in the quenched system in [184]. Starting from a homogeneous system which if fully spin-polarized transverse to the magnetic offset field (e.g. $F_x = 1$) we have found the system become approximately stationary and all measured spectra are consistent with curves obtained from Bogoliubov theory expanded around a thermal state. Using the steerable laser beam, the Landau criterion for superfluidity is probed with a blue-detuned optical potential as moving obstacle. This allows to certify superfluid behavior both in the density and transverse spin in the easy-plane phase of the spinor gas. Additionally, by applying local spin rotations, we performed linear response measurements in observables which are close to the Bogoliubov quasi-particle modes. The motion of the resulting wavepackets is in agreement with the structure of the relevant easy-plane Bogoliubov modes, supporting the validity of Bogoliubov theory in this scenario.

These measurements complement the study of non-equilibrium dynamics in the sense that the dynamical scaling associated to the presence of a NTFP in far-from-equilibrium many-body systems is expected to be only a transient phenomenon before the eventual equilibration of the system. Although the experimentally accessible timescales are still too short to observe the full evolution for the same initial state, the dynamical processes involved here seem to have the same structure, albeit at different energies.

The observation of a spin state compatible with thermal predictions may therefore allow a closer study of the equilibration of a far-from equilibrium state. This implies a detailed comparison of the time dynamics of the spin-polarized IC with that of the polar IC. Further, the equilibrated spin state represents a promising candidate for testing the fluctuation-dissipation theorem in ultracold gases [185].

A. Laser Modulation and Properties of the Local Spin Rotations

Here, a detailed description of the modulation applied to the 790 nm local control laser is given, which is required to drive the local spin rotations. Because for the effect of the vector-Stark shift the interference of the frequency components of the electric field are crucial, here the modulation spectrum of the light is derived. This allows a determination of the static and spin coupling contributions of the fictitious field. These are further used to analyze the local spin coupling Hamiltonian and the angle between of the magnetic fields.

A.1. Modulation Spectrum and Coupling Hamiltonian for Local Spin Rotations

To ensure a constant modulation amplitude the laser power is modulated with an AOM (cf. fig. 2.11) whose RF signal is modulated with an RF switch (ZASWA-2-50DR+ manufactured by Mini-Circuits; see fig. 2.12) that achieves a suppression of more than 75 dB. This leads to a square-wave amplitude modulation with a waveform shown on the left-hand side of fig. A.1. This modulation is performed at a frequency $\omega_{\mathrm{rf}} = 2\pi/T$, which is usually set to the Larmor frequency ω_{L} of the atomic spins and with a duty cycle $d = \tau/T = 0.5$. The corresponding modulation function can be expressed as Fourier series as

$$m(t) = Ad\left(1 + 2\sum_{n=1}^{\infty} \mathrm{sinc}(nd)\cos(n\omega_{\mathrm{rf}}t)\right), \tag{A.1}$$

where A specifies the modulation amplitude and $\mathrm{sinc}(x) = sin(\pi x)/(\pi x)$ denotes the normalized sinc function. This function is used to modulate the amplitude of the local spin rotation light described by the electric field amplitude $E(t) = E_0 e^{i\omega_{\mathrm{light}}t}$, where we drop the spatial dependence. The modulated signal is therefore given by

$$E_{\mathrm{mod}}(t) = E_0 m(t) e^{i\omega_{\mathrm{light}}t}. \tag{A.2}$$

To obtain the modulation spectrum we will employ the convolution theorem $\mathcal{F}\{gh\} = \mathcal{F}\{g\} * \mathcal{F}\{h\}$, which relates the Fourier transform $\mathcal{F}\{\cdot\}$ of a product of functions $g, h(t)$ to the convolution $(\tilde{f} * \tilde{g})(\omega) = \int d\tilde{\omega}\tilde{f}(\tilde{\omega})\tilde{g}(\omega - \tilde{\omega})$. Applying the definitions for the Fourier transform and its inverse

$$\begin{aligned} \mathcal{F}\{f\}(\omega) &= \int_{-\infty}^{\infty} dt f(t) e^{-i\omega t}, \\ \mathcal{F}^{-1}\{\tilde{f}\}(t) &= \frac{1}{2\pi}\int_{-\infty}^{\infty} d\omega \tilde{f}(\omega) e^{i\omega t}, \end{aligned} \tag{A.3}$$

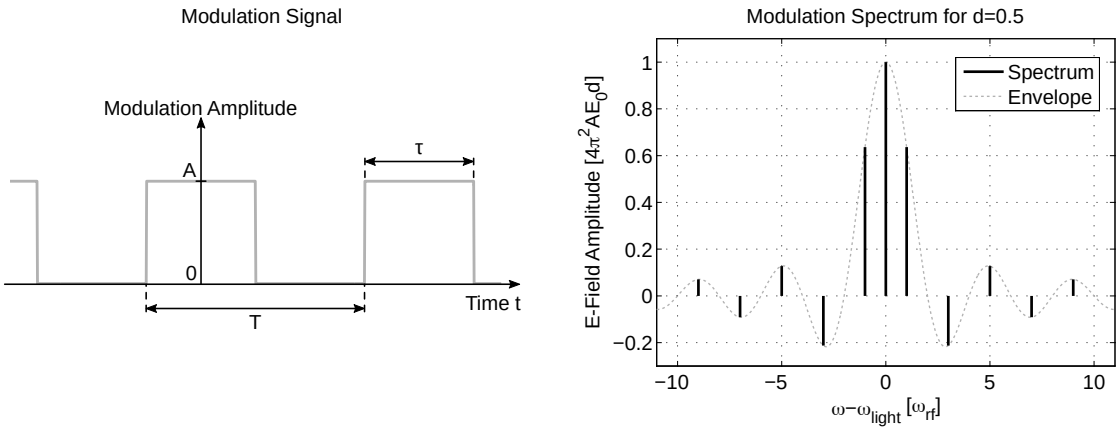

Figure A.1.: Amplitude modulation signal (left) and resulting $\boldsymbol{E}$-field spectrum of the 790 nm local control laser beam for the implementation of local rotations. The square-wave modulation is performed at frequency $\omega_{\mathrm{rf}} = 2\pi/T$ with a duty cycle of $d = \tau/T = 0.5$. This leads to a symmetric generation of discrete side-bands around the original laser frequency ω_{light} which are spaced by ω_{rf} and whose amplitude follows an envelope given by a sinc function. Because in the experiment the local rotation pulses are applied over a finite duration $\sim (20-100)\,\mu\mathrm{s}$ the frequency components acquire a finite width on the order of tens of kHz, which, however, is still $\ll \omega_{\mathrm{rf}}$.

we obtain $\mathcal{F}\{1\} = 2\pi\delta(\omega)$ and $\mathcal{F}\{e^{i\omega_0 t}\} = 2\pi\delta(\omega-\omega_0)$, where $\delta(\cdot)$ denotes the Dirac delta distribution. With this the spectrum of the modulation signal is obtained as

$$\mathcal{F}\{m\} = 2\pi A d \left(\delta(\omega) + \sum_n \mathrm{sinc}(nd)\left(\delta(\omega - n\omega_{\mathrm{rf}}) + \delta(\omega + n\omega_{\mathrm{rf}})\right)\right), \tag{A.4}$$

which allows the calculation of the full modulation spectrum:

$$\begin{aligned}\tilde{E}(\omega) &= \mathcal{F}\{E\} = E_0\mathcal{F}\{m\} * \mathcal{F}\{e^{i\omega_{\mathrm{light}}t}\} \\ &= 2\pi E_0 \int d\tilde{\omega}\mathcal{F}\{m\}(\tilde{\omega})\delta(\omega - \omega_{\mathrm{light}} - \tilde{\omega}) \\ &= 2\pi E_0 \mathcal{F}\{m\}(\omega - \omega_{\mathrm{light}})\end{aligned} \tag{A.5}$$

This leads to the discrete spectrum (black lines) shown in the right-hand plot of fig. A.1. Due to the finite duration of the local rotation pulses applied in the experiment the discrete frequencies are actually convoluted with a sinc function, which broadens them to a width of tens of kHz. This broadening is still much smaller than the separation of the frequencies given by ω_{rf}. This, however does not change the distribution of the amplitude between the peaks, which is why we will use this discrete approximation for further estimations.

According to eq. (2.41) the static field amplitude is given by the sum $B_0^{\mathrm{fict}} \propto \sum_n E_n^2$ of the amplitudes E_n of all frequency components while the oscillating part is generated by the cross-terms $B_{\mathrm{rf}}^{\mathrm{fict}} \propto 2\sum_n E_n E_{n+1}$ separated by ω_{rf} in frequency.[1]

[1] The factor of 2 in the amplitude of $B_{\mathrm{rf}}^{\mathrm{fict}}$ stems from the appearance of both cross terms $E_n E_{n+1}$ and $E_{n+1}E_n$ in the cross product between the electric fields in eq. (2.41).

The fraction of the static field is numerically calculated to be

$$\frac{B_0^{\text{fict}}}{B_{\text{rf}}^{\text{fict}}} \approx 0.785. \tag{A.6}$$

A.2. Spin Rotation Hamiltonian with Offset Field

For the description of the local spin rotations it is important to also take the static offset $\boldsymbol{B}_0^{\text{fict}}$ of the full fictitious field $\boldsymbol{B}^{\text{fict}} = \boldsymbol{B}_0^{\text{fict}} + \boldsymbol{B}_{\text{rf}}^{\text{fict}}$ into account. The static and oscillating field contributions $\boldsymbol{B}_0^{\text{fict}}$ and $\boldsymbol{B}_{\text{rf}}^{\text{fict}}$ give rise to the $\tilde{\Omega}_0$ and $\tilde{\Omega}_{\text{rot}}$ terms in eq. (A.7), respectively. Furthermore, the spin rotation coupling Hamiltonian (2.25) should be generalized to arbitrary angles of the coupling field in the y-z-plane. Assuming that the tilt of the total magnetic field due to the fictitious field is negligible[2] the coupling Hamiltonian may be written as

$$\hat{\mathcal{H}}_{\text{rf}} = \left(\hbar\tilde{\Omega}_0 + 2\hbar\tilde{\Omega}_{\text{rot}}\cos\left(\omega_{\text{rf}}t + \phi_{\text{rf}}\right)\right)\left(\sin(\gamma)\hat{F}_y + \cos(\gamma)\hat{F}_z\right). \tag{A.7}$$

Here, γ denotes the angle between the fictitious magnetic field $\boldsymbol{B}^{\text{fict}}$, given by the propagation direction of the local rotation beam, and the global magnetic offset field $\boldsymbol{B}_0$. These do not necessarily have to be orthogonal because the global field may be tilted slightly against the z-axis and the local rotation beam may be angled deflected in vertical direction by the objective if the AODs are not exactly on the same height as the BEC. Transforming this Hamiltonian to the rotating frame of the of the modulated fictitious field (cf. eq. (2.26)) leads to

$$\hat{\mathcal{H}}_{\text{rf}}^{\text{rot}} = \hbar\left(\delta_{\text{rf}} + \tilde{\Omega}_0\cos(\gamma)\right)\hat{F}_z + \hbar\tilde{\Omega}_{\text{rot}}\sin(\gamma)\left(\cos(\phi_{\text{rf}})\hat{F}_y + \sin(\phi_{\text{rf}})\hat{F}_x\right), \tag{A.8}$$

where all oscillating terms (at frequencies ω_{rf} and $2\omega_{\text{rf}}$) have been dropped and $\delta_{\text{rf}} = \omega_{\text{rf}} - \omega_{\text{L}}$ denotes the detuning between the coupling frequency and the Larmor precession with respect to the global offset field $\boldsymbol{B}_0$. Because the change of the total magnetic field amplitude is negligible[2] the amplitudes of the measurable amplitudes of the static and coupling contributions of the fictitious field are given by the projections relative to the quantization axis defined by the global offset field as

$$\Omega_0 \approx \tilde{\Omega}_0\cos(\gamma) = \frac{g_f\mu_{\text{B}}}{\hbar}B_0^{\text{fict}}\cos(\gamma), \tag{A.9}$$

$$\Omega_{\text{rot}} = \tilde{\Omega}_{\text{rot}}\sin(\gamma) = \frac{g_f\mu_{\text{B}}}{\hbar}B_{\text{rf}}^{\text{fict}}\sin(\gamma). \tag{A.10}$$

Therefore, the angle between fictitious field and global offset field can be determined to be

$$\gamma \approx \arctan\left(\frac{B_0^{\text{fict}}}{B_{\text{rf}}^{\text{fict}}}\frac{\Omega_{\text{rot}}}{\Omega_0}\right) \sim 63°. \tag{A.11}$$

[2] The modulation $\Delta B_0 = \left|\boldsymbol{B}_0 + \boldsymbol{B}_0^{\text{fict}}\right| - |\boldsymbol{B}_0|$ of the magnetic field amplitude becomes most relevant when the local rotation laser is orthogonal to the offset field, i.e. $\boldsymbol{B}_0^{\text{fict}} \perp \boldsymbol{B}_0$. In this case, the Rabi frequency amplitude of the local rotation directly determines the static fictitious field amplitude via eq. (A.6). In any realistic scenario the measured local rotation Rabi frequency Ω_{rot} will be on the order of the full coupling amplitude $\Omega_{\text{rot}} \sim \tilde{\Omega}_{\text{rot}}$. This allows the direct estimation of $\Delta B_0 \sim 0.1\,\text{mG} \ll B_0 \sim 0.9\,\text{G}$ for the largest observed local Rabi frequency of $\Omega_{\text{rot}} \approx 2\pi \times 12.6\,\text{kHz}$.

Here, the result $\Omega_0/\Omega_{\mathrm{rot}} \sim 0.4$ from fig. 2.18 is used. This leads to a realistic value of γ, which implies full fictitious field amplitudes of

$$\begin{aligned} \tilde{\Omega}_0 &\sim 2\pi \times 11.1\,\mathrm{kHz}, & B_0^{\mathrm{fict}} &\sim 16\,\mathrm{mG}, \\ \tilde{\Omega}_{\mathrm{rot}} &\sim 2\pi \times 14.1\,\mathrm{kHz}, & B_{\mathrm{rf}}^{\mathrm{fict}} &\sim 20\,\mathrm{mG}. \end{aligned} \tag{A.12}$$

for $\Omega_{\mathrm{rot}} \approx 2\pi \times 12.6\,\mathrm{kHz}$. The static fictitious field also induces a detuning

$$\delta_{\mathrm{fict}} = \Omega_0 \approx \cot(\gamma)\frac{B_0^{\mathrm{fict}}}{B_{\mathrm{rf}}^{\mathrm{fict}}}\Omega_{\mathrm{rot}} \sim 0.4\,\Omega_{\mathrm{rot}}, \tag{A.13}$$

which limits the maximal transfer fraction of the local spin rotation to $\Omega_{\mathrm{rot}}^2/(\delta_{\mathrm{fict}}^2 + \Omega_{\mathrm{rot}}^2) \sim 0.9$.

B. Retrieving Physical Units from Dimensionless Equations

In theoretical papers the equations are often presented in unitless form to simplify the expressions and simplify transformations. When comparing such models to experiments, however, it is crucial to reintroduce the proper physical units to all quantities. This section should serve as "recipe" for this process and as reference for the required transformation between physical and unitless quantities for the most important sources for this thesis.

As example for the transformation let us consider the GPE provided in [141]:

$$i\partial_{\bar{t}}\bar{\psi}_j = \left(-\frac{1}{2}\partial_{\bar{x}}^2 + \bar{V}_j + \left|\bar{\psi}_j\right|^2 + \delta g_{jk}\left|\bar{\psi}_k\right|^2 - \bar{\mu}_j\right)\bar{\psi}_j, \tag{B.1}$$

where the barred symbols (e.g. $\bar{x}$) denote dimensionless quantities. We want to translate this equation into the form of the Manakov GPE eq. (3.7) with physical units (associated to the plain variables; e.g. x)

$$i\hbar\partial_t\psi_j = \left(-\frac{\hbar^2\partial_x^2}{2m} + c_0\left|\psi_j\right|^2 + \delta g_{jk}c_0\left|\psi_k\right|^2 - \mu_j\right)\psi_j. \tag{B.2}$$

For this we first have to choose a normalization for the wavefunction for which we naturally use the background density n_0 (of the dark component $j = \mathrm{D}$), i.e. $\bar{\psi}_j = \psi_j/\sqrt{n_0}$. Inserting this identification into eq. (B.1) and comparing the resulting equation

$$i\partial_{\bar{t}}\psi_j = \left(-\frac{1}{2}\partial_{\bar{x}}^2 + \bar{V}_j + \frac{\left|\psi_j\right|^2}{n_0} + \delta g_{jk}\frac{\left|\psi_k\right|^2}{n_0} - \bar{\mu}_j\right)\psi_j \tag{B.3}$$

with eq. (B.2) we realize that we have to multiply the equation with n_0c_0 to obtain the $c_0\left|\psi_j\right|^2\psi_j$ term on the right-hand side. Identifying the result

$$in_0c_0\partial_{\bar{t}}\psi_j = \left(-\frac{n_0c_0}{2}\partial_{\bar{x}}^2 + n_0c_0\bar{V}_j + c_0\left|\psi_j\right|^2 + \delta g_{jk}c_0\left|\psi_k\right|^2 - n_0c_0\bar{\mu}_j\right)\psi_j \tag{B.4}$$

with eq. (B.2) we can extract the relations between dimensionless variables and

quantities in physical units:

$$\bar{t} = \frac{n_0 c_0}{\hbar} t \tag{B.5}$$

$$\bar{x} = \frac{\sqrt{m n_0 c_0}}{\hbar} x \tag{B.6}$$

$$\bar{\psi}_j = \frac{\psi_j}{n_0} \tag{B.7}$$

$$\bar{V}_j = \frac{V_j}{n_0 c_0} \tag{B.8}$$

$$\bar{\mu}_j = \frac{\mu_j}{n_0 c_0} \tag{B.9}$$

C. Derivation of all $F = 1$ Scattering Lengths g_{jk}

For the discussion of the 3-component vector solitons in the $F = 1$ hyperfine manifold of ^{87}Rb in chapter 3 it is helpful to consider the pair scattering lengths a_{jk} between all possible combinations of magnetic substates j and k. This form is usually applied in the discussion of Manakov solitons. In contrast, interactions in spinor gases are mainly discussed in terms of the pair spin scattering channels allowed for the s-wave collisions. Here, a conversion between these two representations is provided.

In full generality, the equation of motion for the BEC wavefunctions ψ_j for each of the magnetic substates j is given by the 3-component coupled GPE

$$i\hbar\partial_t\psi_j = \left(-\frac{\hbar^2\nabla^2}{2m} + V_{\text{ext}} + \sum_k g_{jk}\left|\psi_k\right|^2\right)\psi_j \tag{C.1}$$

with suitable external (magnetic and trapping) potentials V_{ext} and intra- and interspecies interaction constants $g_{jk} = 4\pi\hbar^2 a_{jk}/m$ (see fig. 3.5 for the scattering lengths in the $F = 1$ hyperfine manifold). Usually, the interactions in spinor gases are formulated in terms of spin operators and spin pair scattering lengths $a_{\mathcal{F}}$ [52, 53]. The scattering lengths $a_{\mathcal{F}}$ for the pair spin channels $\mathcal{F} = 0, 2$ fully specify all interactions. Employing a formulation in spin operators, the interactions are usually expressed by coupling constants c_0 and c_1 which depend on the sum and difference of the spin pair scattering lengths. Equivalently, the interaction Hamiltonian for $F = 1$ may be written in terms of the pair state projector $\hat{\mathcal{P}} = \sum_{\mathcal{M}=-\mathcal{F}}^{\mathcal{F}} |\mathcal{F},\mathcal{M}\rangle\langle\mathcal{F},\mathcal{M}|$ as follows [52, 58, 186]:

$$\begin{aligned}
\hat{\mathcal{H}}_{\text{int}} &= \sum_{\mathcal{F}=0}^{2F} g_{\mathcal{F}}\hat{\mathcal{P}}_{\mathcal{F}}\delta(\boldsymbol{r}) \\
&= \sum_{\mathcal{F},\mathcal{M}}\sum_{m_1,m_2}\sum_{m_3,m_4} g_{\mathcal{F}}\,|m_1;m_2\rangle\langle m_1;m_2|\mathcal{F},\mathcal{M}\rangle\langle\mathcal{F},\mathcal{M}|m_3;m_4\rangle\langle m_3;m_4|\,\delta(\boldsymbol{r}) \\
&= \sum_{m_1,m_2} g_{m_1m_2}\,|m_1;m_2\rangle\langle m_1;m_2|\,\delta(\boldsymbol{r}) \\
&\quad + c_1(|0;0\rangle\langle -1;1| + |-1;1\rangle\langle 0;0| + \dots)\delta(\boldsymbol{r})
\end{aligned} \tag{C.2}$$

Here, $\delta(\boldsymbol{r})$ constrains the interacting particles to the same position and we use the short-hand notation $|m_1;m_2\rangle = |F,m_1;F,m_2\rangle$ for the spin pair state in the basis of hyperfine sublevels. In the third line we split the sums running over the sublevels into two parts with equal and unequal initial and final states. Imposing conservation

of angular momentum for the unequal states therefore results in the SCC terms proportional to the spin interaction constant c_1. For equal spin states we can express the left part in terms of the interaction constants $g_{m_1 m_2} = 4\pi\hbar^2 a_{m_1 m_2}/m$ which couple the single magnetic sublevels. Here, the scattering lengths $a_{m_1 m_2}$ are connected to the pair scattering lengths $a_{\mathcal{F}}$ via

$$a_{m_1 m_2} = \sum_{\mathcal{F}=0}^{2F} \sum_{\mathcal{M}=-\mathcal{F}}^{\mathcal{F}} \langle F, m_1; F, m_2 | \mathcal{F}, \mathcal{M} \rangle^2 \, a_{\mathcal{F}} \tag{C.3}$$

with the Clebsch-Gordan coefficients $\langle F, m_1; F, m_2 | \mathcal{F}, \mathcal{M} \rangle$ for coupling the single spin states $|F, m_1\rangle$ and $|F, m_2\rangle$ to the pair spin state $|\mathcal{F}, \mathcal{M}\rangle$. Using the values $a_0 = 101.78\,\mathrm{a_B}$ and $a_2 = 100.4\,\mathrm{a_B}$ [53, 58] for the pair scattering lengths in units of the Bohr radius a_B leads to the scattering lengths displayed in fig. 3.5. The largest relative deviation of the scattering lengths is approx. 0.9 %.

D. Additional Strucutre Factor Data and Details on the Scaling Analysis

D.1. Full Time Evolution of Strucure Factors

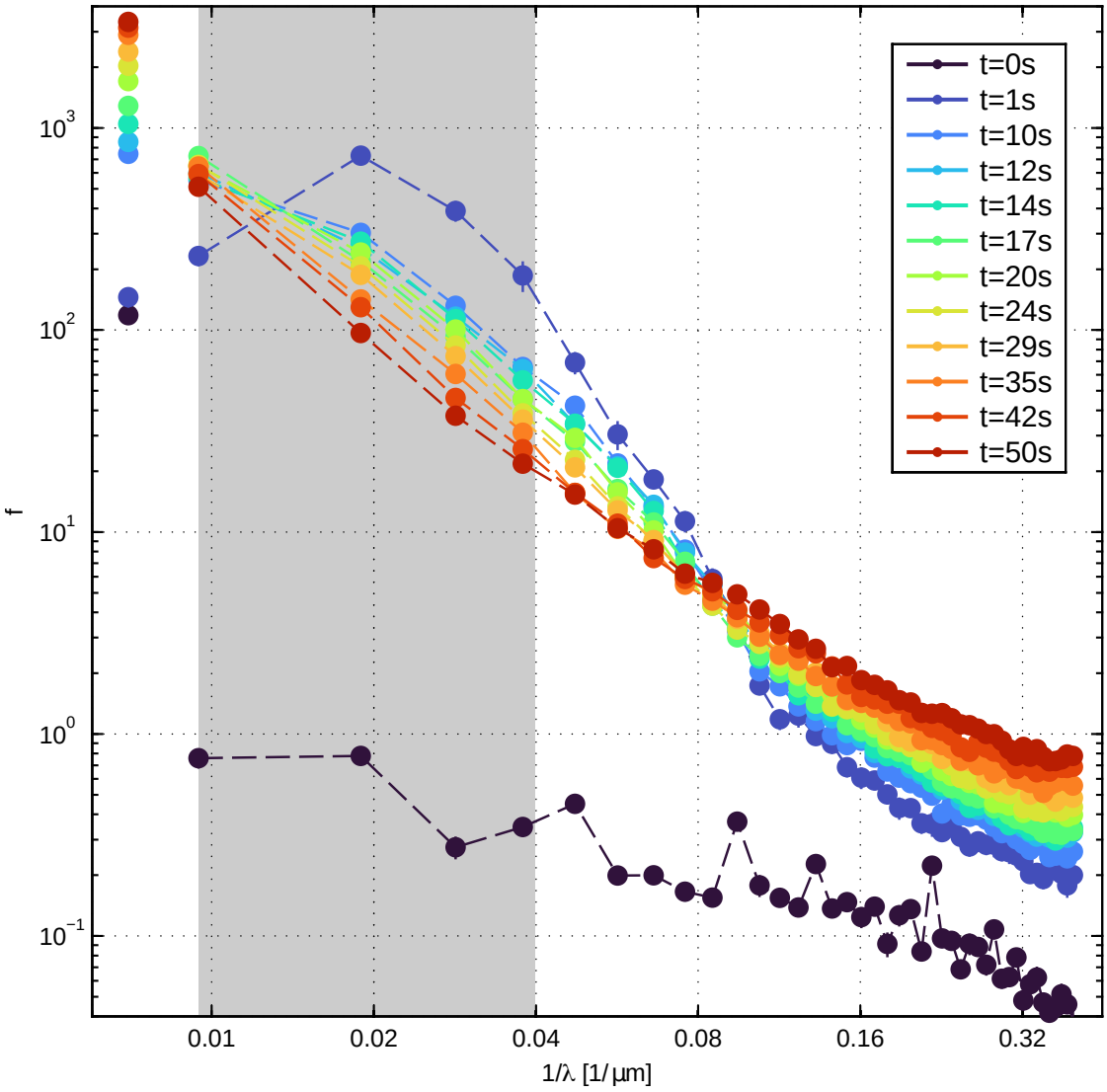

Figure D.1.: Full time evolution of the structure factor for the Polar IC. The leftmost points which are not connected with a dashed line indicate the value of $f(k = 0)$ for the corresponding times.

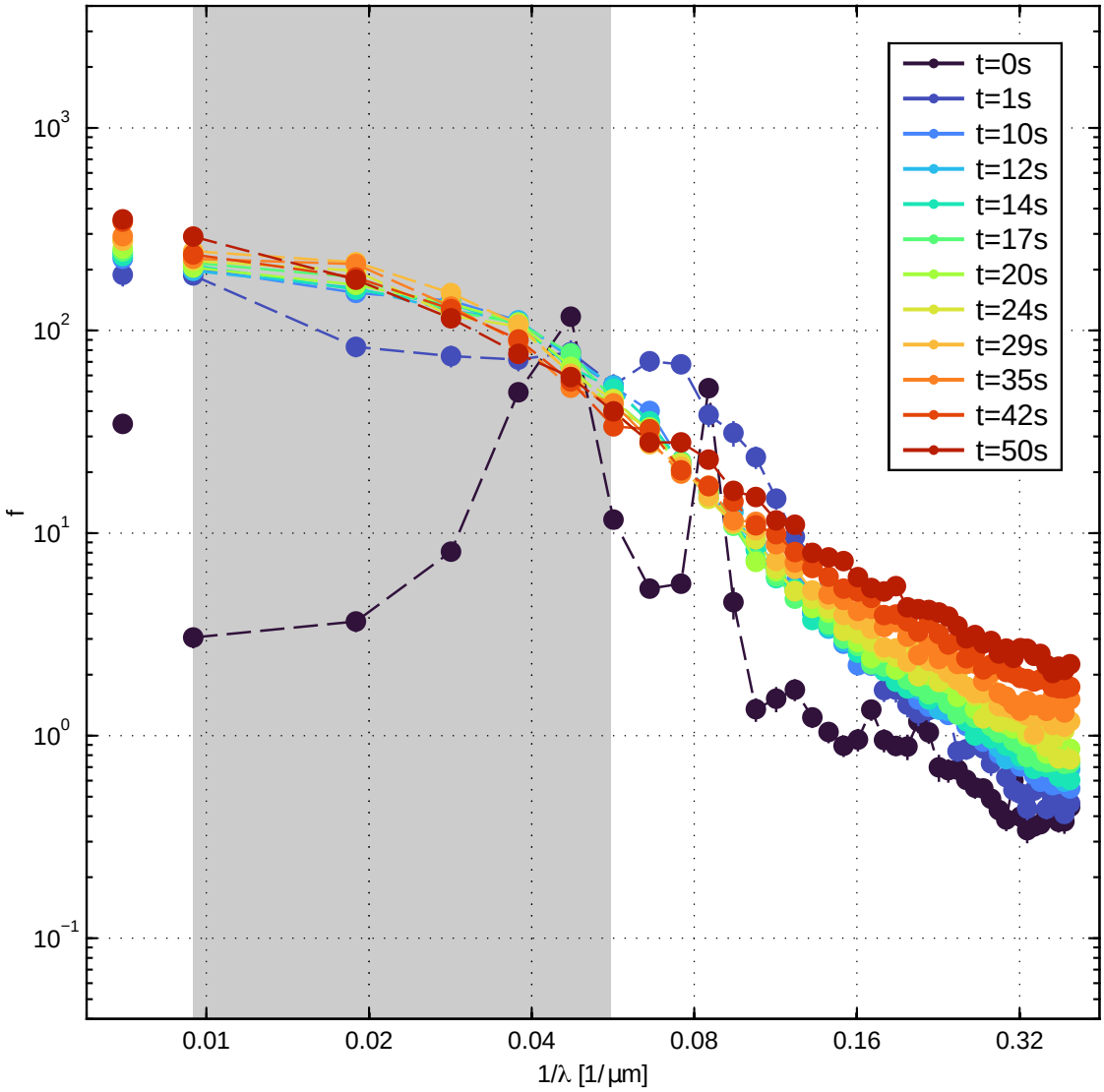

Figure D.2.: Full time evolution of the structure factor for the soliton IC. The leftmost points which are not connected with a dashed line indicate the value of $f(k = 0)$ for the corresponding times. The peaks in the initial condition correspond to the spin modulation of the six local rotations. Here, during the short time-of-flight before imaging small spin excitations are generated which appear as signal in the structure factor.

D.2. Additional Details on Errors of the Scaling Analysis

For the error analysis via jackknife resampling (see [170]) one single realization j is removed from the data (all realizations at all times in the scaling regime) contributing to the analysis. For this reduced data set the optimal scaling exponents α and β are calculated. This procedure is repeated for the removal of each of the N_s realizations. From this N_s values ν_j for each of the exponents is obtained and

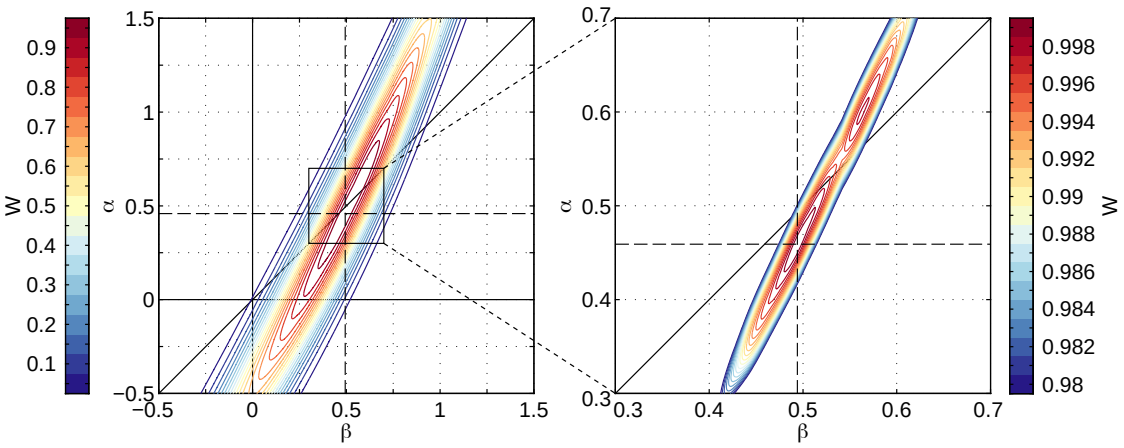

Figure D.3.: Scaling residual distribution W for the Polar IC with zoom to show the fine structure. The double-peaked structure around the minimal residual ($W = 1$) leads to the large jackknife error (see text).

the standard error of the best estimate ν of the actual exponent is calculated as

$$\Delta\nu = \sqrt{N_s - 1}\,\mathrm{Std}\{\nu_j\}, \tag{D.1}$$

where $\mathrm{Std}\{\cdot\}$ denotes the standard deviation.

For the Polar IC the distribution W of residuals χ^2 is rather unconstrained along one axis (see fig. D.3). However, this plateau region in W is not homogeneous with a single maximum but there is structure on the 10^{-3} level where even two maxima emerge. Most likely this is not a physical property of the spinor dynamics but rather a finite size effect which limits the number of available data points of the structure factor in the scaling region. For the removal of six individual realizations j instead of the lower maximum the upper one leads to a smaller χ^2_{min}. This results in an increased value of $\mathrm{Std}\{\nu_j\}$. When excluding these six jackknife samples from the analysis the resulting error estimation leads to $\Delta\alpha = 0.08$ and $\Delta\beta = 0.02$ for the Polar IC.

For each of the time steps between 200 and 300 realizations have been measured. This leads to a total number of realizations of $N_s = 1576$ for the Polar IC and $N_s = 1273$ for the soliton IC.

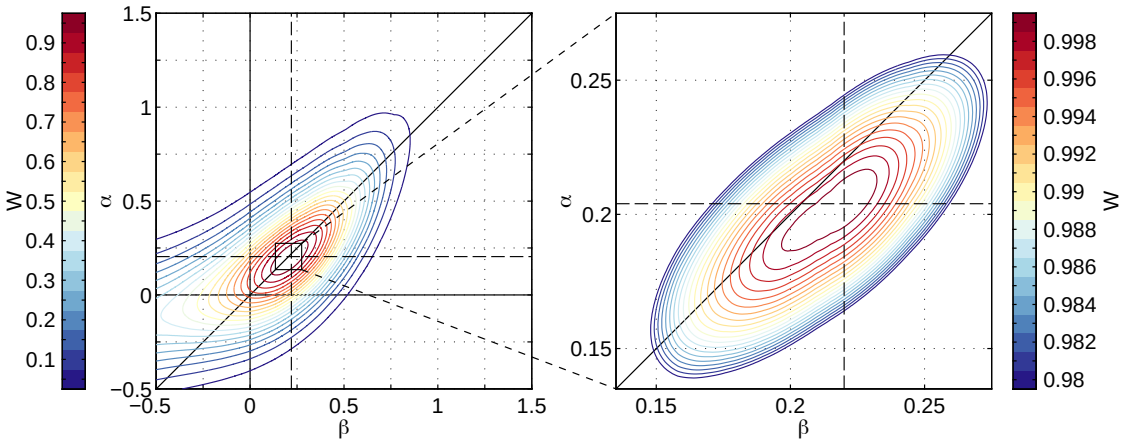

Figure D.4.: Scaling residual distribution W for the soliton IC. In constrast to the Polar IC (fig. D.3) the zoom shows only a single optimum.

List of Acronyms

MOT magneto-optical trap

TOP time-orbiting potential

XDT crossed dipole trap

WG waveguide

TF Thomas-Fermi

d.o.f. degree of freedom

AOD acousto-optic deflector

AOM acousto-optic modulator

RMS root mean square

SG Stern-Gerlach

IST inverse scattering transform

GPE Gross-Pitaevskii equation

NLSE non-linear Schrödinger equation

SCC spin-changing collision

s.d. standard deviation

AWG arbitrary waveform generator

BEC Bose-Einstein condensate

NTFP non-thermal fixed point

MW microwave

RF radio frequency

EP easy-plane

PBS polarizing beam splitter

PD photodiode

IC initial condition

BDB bright-dark-bright

Bibliography

[1] K. T. Alligood, T. D. Sauer, and J. A. Yorke. *Chaos*. Textbooks in Mathematical Sciences (Springer, 1996).

[2] U. Frisch. *Turbulence: The Legacy of A. N. Kolmogorov* (Cambridge University Press, 1995).

[3] J. Hald, J. L. Sørensen, C. Schori, and E. S. Polzik. *Spin Squeezed Atoms: A Macroscopic Entangled Ensemble Created by Light.* Phys. Rev. Lett. **83**, 1319–1322 (1999).

[4] W. Roedel and T. Wagner. *Physik unserer Umwelt: Die Atmosphäre*. 4th ed. (Springer, 2011).

[5] I. R. Epstein and K. Showalter. *Nonlinear Chemical Dynamics: Oscillations, Patterns, and Chaos.* The Journal of Physical Chemistry **100**, 13132–13147 (1996).

[6] A. Hastings. *Population Biology: Concepts and Models* (Springer, 1997).

[7] R. E. Slusher, L. W. Hollberg, B. Yurke, J. C. Mertz, and J. F. Valley. *Observation of Squeezed States Generated by Four-Wave Mixing in an Optical Cavity.* Phys. Rev. Lett. **55**, 2409–2412 (1985).

[8] D. F. Walls. *Squeezed states of light.* Nature **306**, 141–146 (1983).

[9] U. L. Andersen, T. Gehring, C. Marquardt, and G. Leuchs. *30 years of squeezed light generation.* Physica Scripta **91**, 053001 (2016).

[10] J. Abadie *et al.*. *A gravitational wave observatory operating beyond the quantum shot-noise limit.* Nature Physics **7**, 962–965 (2011).

[11] B. P. Abbott *et al.* (LIGO Scientific Collaboration and Virgo Collaboration). *Observation of Gravitational Waves from a Binary Black Hole Merger.* Phys. Rev. Lett. **116**, 061102 (2016).

[12] M. Tse *et al.*. *Quantum-Enhanced Advanced LIGO Detectors in the Era of Gravitational-Wave Astronomy.* Phys. Rev. Lett. **123**, 231107 (2019).

[13] F. Acernese *et al.* (Virgo Collaboration). *Increasing the Astrophysical Reach of the Advanced Virgo Detector via the Application of Squeezed Vacuum States of Light.* Phys. Rev. Lett. **123**, 231108 (2019).

[14] E. Fermi, P. Pasta, S. Ulam, and M. Tsingou. *Studies of the Nonlinear Problems.* Los Alamos National Lab, United States (1955).

[15] N. J. Zabusky and M. D. Kruskal. *Interaction of "Solitons" in a Collisionless Plasma and the Recurrence of Initial States.* Phys. Rev. Lett. **15**, 240–243 (1965).

[16] J. S. Russell. *Report on Waves.* Fourteenth meeting of the British Association for the Advancement of Science (1844).

[17] M. H. Jakubowski, K. Steiglitz, and R. Squier. *State transformations of colliding optical solitons and possible application to computation in bulk media.* Phys. Rev. E **58**, 6752–6758 (1998).

[18] K. Steiglitz. *Time-gated Manakov spatial solitons are computationally universal.* Phys. Rev. E **63**, 016608 (2000).

[19] A. Janutka. *Simulation of quantum logic via collisions of vector solitons.* Journal of Physics A: Mathematical and General **39**, 12505–12513 (2006).

[20] S. Burger, K. Bongs, S. Dettmer, W. Ertmer, K. Sengstock, A. Sanpera, G. V. Shlyapnikov, and M. Lewenstein. *Dark Solitons in Bose-Einstein Condensates.* Phys. Rev. Lett. **83**, 5198–5201 (1999).

[21] J. Denschlag, J. E. Simsarian, D. L. Feder, C. W. Clark, L. A. Collins, J. Cubizolles, L. Deng, E. W. Hagley, K. Helmerson, W. P. Reinhardt, S. L. Rolston, B. I. Schneider, and W. D. Phillips. *Generating Solitons by Phase Engineering of a Bose-Einstein Condensate.* Science **287**, 97–101 (2000).

[22] D. J. Frantzeskakis. *Dark solitons in atomic Bose–Einstein condensates: from theory to experiments.* J. Phys. A: Math. Theor. **43**, 213001 (2010).

[23] S. V. Manakov. *On the Theory of Two-Dimensional Stationary Self-Focusing of Electromagnetic Waves.* Sov. Phys. JETP **38**, 248 (1974).

[24] J. Polo and V. Ahufinger. *Soliton-based matter-wave interferometer.* Phys. Rev. A **88**, 053628 (2013).

[25] J. L. Helm, S. L. Cornish, and S. A. Gardiner. *Sagnac Interferometry Using Bright Matter-Wave Solitons.* Phys. Rev. Lett. **114**, 134101 (2015).

[26] O. J. Wales, A. Rakonjac, T. P. Billam, J. L. Helm, S. A. Gardiner, and S. L. Cornish. *Splitting and recombination of bright-solitary-matter waves.* Communications Physics **3**, 51 (2020).

[27] P. Calabrese and J. Cardy. *Quantum quenches in extended systems.* Journal of Statistical Mechanics: Theory and Experiment **2007**, P06008–P06008 (2007).

[28] J. Berges, A. Rothkopf, and J. Schmidt. *Nonthermal Fixed Points: Effective Weak Coupling for Strongly Correlated Systems Far from Equilibrium.* Phys. Rev. Lett. **101**, 041603 (2008).

[29] J. Berges, K. Boguslavski, S. Schlichting, and R. Venugopalan. *Universality Far from Equilibrium: From Superfluid Bose Gases to Heavy-Ion Collisions.* Phys. Rev. Lett. **114**, 061601 (2015).

[30] A. Piñeiro Orioli, K. Boguslavski, and J. Berges. *Universal self-similar dynamics of relativistic and nonrelativistic field theories near nonthermal fixed points.* Phys. Rev. D **92**, 025041 (2015).

[31] C.-M. Schmied, A. N. Mikheev, and T. Gasenzer. *Non-thermal fixed points: Universal dynamics far from equilibrium.* International Journal of Modern Physics A **34**, 1941006 (2019).

[32] M. Prüfer, P. Kunkel, H. Strobel, S. Lannig, D. Linnemann, C.-M. Schmied, J. Berges, T. Gasenzer, and M. K. Oberthaler. *Observation of universal dynamics in a spinor Bose gas far from equilibrium.* Nature **563**, 217–220 (2018).

[33] S. Erne, R. Bücker, T. Gasenzer, J. Berges, and J. Schmiedmayer. *Universal dynamics in an isolated one-dimensional Bose gas far from equilibrium.* Nature **563**, 225–229 (2018).

[34] J. A. P. Glidden, C. Eigen, L. H. Dogra, T. A. Hilker, R. P. Smith, and Z. Hadzibabic. *Bidirectional dynamic scaling in an isolated Bose gas far from equilibrium.* Nature Physics **17**, 457–461 (2021).

[35] B. Eiermann. *Kohärente nichtlineare Materiewellendynamik – Helle atomare Solitonen.* Ph.D. thesis. University of Konstanz (2004).

[36] T. Anker. *Ultracold quantum gases in one-dimensional optical lattice potentials – nonlinear matter wave dynamics.* Ph.D. thesis. University of Heidelberg (2005).

[37] A. Weller. *Dynamics and Interaction of Dark Solitons in Bose-Einstein Condensates.* Ph.D. thesis. University of Heidelberg (2009).

[38] T. Zibold. *Classical Bifurcation and Entanglement Generation in an Internal Bosonic Josephson Junction.* Ph.D. thesis. University of Heidelberg (2012).

[39] C. Groß. *Spin squeezing and non-linear atom interferometry with Bose-Einstein condensates.* Ph.D. thesis. University of Heidelberg (2010).

[40] W. Müssel. *Scalable Spin Squeezing for Quantum-Enhanced Magnetometry with Bose-Einstein Condensates.* Ph.D. thesis. University of Heidelberg (2014).

[41] H. Strobel. *Fisher Information and entanglement of non-Gaussian spin states.* Ph.D. thesis. University of Heidelberg (2016).

[42] C. Raman, M. Köhl, R. Onofrio, D. S. Durfee, C. E. Kuklewicz, Z. Hadzibabic, and W. Ketterle. *Evidence for a Critical Velocity in a Bose-Einstein Condensed Gas.* Phys. Rev. Lett. **83**, 2502–2505 (1999).

[43] A. J. Leggett. *Superfluidity.* Rev. Mod. Phys. **71**, S318–S323 (1999).

[44] L. Pitaevskii and S. Stringari. *Bose-Einstein Condensation* (Oxford University Press, 2003).

[45] M. R. Andrews, C. G. Townsend, H.-J. Miesner, D. S. Durfee, D. M. Kurn, and W. Ketterle. *Observation of Interference Between Two Bose Condensates.* Science **275**, 637–641 (1997).

[46] M. Olshanii. *Atomic Scattering in the Presence of an External Confinement and a Gas of Impenetrable Bosons.* Phys. Rev. Lett. **81**, 938–941 (1998).

[47] F. Dalfovo, S. Giorgini, L. P. Pitaevskii, and S. Stringari. *Theory of Bose-Einstein condensation in trapped gases.* Rev. Mod. Phys. **71**, 463–512 (1999).

[48] R. F. R.-M. Pimentel. *Probing Long-Time Spin Dynamics in a ^{87}Rb Bose-Einstein Condensate.* Master's thesis. University of Heidelberg (2018).

[49] P. Kunkel. *Splitting a Bose-Einstein condensate enables EPR steering and simultaneous readout of noncommuting observables.* Ph.D. thesis. University of Heidelberg (2019).

[50] C. Hamley. *Spin-Nematic Squeezing in a Spin-1 Bose-Einstein Condensate.* Ph.D. thesis. Georgia Institute of Technology (2012).

[51] T. Hoang. *Quantum Control of a Many-Body System in a Spin-1 Bose-Einstein Condensate.* Ph.D. thesis. Georgia Institute of Technology (2013).

[52] Y. Kawaguchi and M. Ueda. *Spinor Bose–Einstein condensates.* Physics Reports **520**, 253–381 (2012). spinor Bose–Einstein condensates.

[53] D. M. Stamper-Kurn and M. Ueda. *Spinor Bose gases: Symmetries, magnetism, and quantum dynamics.* Rev. Mod. Phys. **85**, 1191–1244 (2013).

[54] S. Uchino, M. Kobayashi, and M. Ueda. *Bogoliubov theory and Lee-Huang-Yang corrections in spin-1 and spin-2 Bose-Einstein condensates in the presence of the quadratic Zeeman effect.* Phys. Rev. A **81**, 063632 (2010).

[55] M. Prüfer. *Experimentally testing quantum field theory concepts with spinor Bose gases far from equilibrium.* Ph.D. thesis. University of Heidelberg (2020).

[56] N. T. Phuc, Y. Kawaguchi, and M. Ueda. *Effects of thermal and quantum fluctuations on the phase diagram of a spin-1 ^{87}Rb Bose-Einstein condensate.* Phys. Rev. A **84**, 043645 (2011).

[57] Y. Kawaguchi, N. T. Phuc, and P. B. Blakie. *Finite-temperature phase diagram of a spin-1 Bose gas.* Phys. Rev. A **85**, 053611 (2012).

[58] A. Widera, F. Gerbier, S. Fölling, T. Gericke, O. Mandel, and I. Bloch. *Precision measurement of spin-dependent interaction strengths for spin-1 and spin-2 ^{87}Rb atoms.* New Journal of Physics **8**, 152–152 (2006).

[59] S. Lannig. *Experimental Control of a Spin-1 Bose-Einstein Condensate*. Master's thesis. Universität Heidelberg (2018).

[60] D. A. Steck. *Rubidium 87 D Line Data*. (2021). available online at https://steck.us/alkalidata/.

[61] J. Dreher. *A Microwave Power Stabilization Setup for Controlling Spin Dynamics in a Bose-Einstein Condensate*. Master's thesis. University of Heidelberg (2022).

[62] F. Gerbier, A. Widera, S. Fölling, O. Mandel, and I. Bloch. *Resonant control of spin dynamics in ultracold quantum gases by microwave dressing*. Phys. Rev. A **73**, 041602 (2006).

[63] C. Cohen-Tannoudji, J. Dupont-Roc, and G. Grynberg. *Atom-Photon Interactions: Basic Process and Appilcations* (WILEY-VCH, 2004).

[64] P. Kunkel, M. Prüfer, H. Strobel, D. Linnemann, A. Frölian, T. Gasenzer, M. Gärttner, and M. K. Oberthaler. *Spatially distributed multipartite entanglement enables EPR steering of atomic clouds*. Science **360**, 413–416 (2018).

[65] M. Prüfer, T. V. Zache, P. Kunkel, S. Lannig, A. Bonnin, H. Strobel, J. Berges, and M. K. Oberthaler. *Experimental extraction of the quantum effective action for a non-equilibrium many-body system*. Nature Physics **16**, 1012–1016 (2020).

[66] P. Kunkel, M. Prüfer, S. Lannig, R. Strohmaier, M. Gärttner, H. Strobel, and M. K. Oberthaler. *Detecting Entanglement Structure in Continuous Many-Body Quantum Systems*. Phys. Rev. Lett. **128**, 020402 (2022).

[67] F. Le Kien, P. Schneeweiss, and A. Rauschenbeutel. *Dynamical polarizability of atoms in arbitrary light fields: general theory and application to cesium*. The European Physical Journal D **67**, 92 (2013).

[68] N. Goldman, G. Juzeliūnas, P. Öhberg, and I. B. Spielman. *Light-induced gauge fields for ultracold atoms*. Reports on Progress in Physics **77**, 126401 (2014).

[69] B. E. A. Saleh and M. C. Teich. *Fundamentals of Photonics*. 2nd ed. (Wiley, 2007).

[70] D. A. Steck. *Quantum and Atom Optics*. (2020). available online at https://steck.us/teaching.

[71] R. H. Leonard, A. J. Fallon, C. A. Sackett, and M. S. Safronova. *High-precision measurements of the ^{87}Rb D-line tune-out wavelength*. Phys. Rev. A **92**, 052501 (2015).

[72] R. H. Leonard, A. J. Fallon, C. A. Sackett, and M. S. Safronova. *Erratum: High-precision measurements of the ^{87}Rb D-line tune-out wavelength [Phys. Rev. A 92, 052501 (2015)].* Phys. Rev. A **95**, 059901 (2017).

[73] F. Schmidt, D. Mayer, M. Hohmann, T. Lausch, F. Kindermann, and A. Widera. *Precision measurement of the ^{87}Rb tune-out wavelength in the hyperfine ground state $F = 1$ at 790 nm.* Phys. Rev. A **93**, 022507 (2016).

[74] G. Lamporesi, J. Catani, G. Barontini, Y. Nishida, M. Inguscio, and F. Minardi. *Scattering in Mixed Dimensions with Ultracold Gases.* Phys. Rev. Lett. **104**, 153202 (2010).

[75] ComponentLibrary by Alexander Franzen, licensed under a Creative Commons Attribution-NonCommercial 3.0 Unported License.

[76] I. Chang. *I. Acoustooptic Devices and Applications.* IEEE Transactions on Sonics and Ultrasonics **23**, 2–21 (1976).

[77] A. Frölian. *Implementation of local addressability in a Bose-Einstein Condensate.* Master's thesis. Universität Heidelberg (2017).

[78] N. Navon, R. P. Smith, and Z. Hadzibabic. *Quantum gases in optical boxes.* Nature Physics **17**, 1334–1341 (2021).

[79] G. E. Marti, A. MacRae, R. Olf, S. Lourette, F. Fang, and D. M. Stamper-Kurn. *Coherent Magnon Optics in a Ferromagnetic Spinor Bose-Einstein Condensate.* Phys. Rev. Lett. **113**, 155302 (2014).

[80] Y.-J. Lin, R. L. Compton, A. R. Perry, W. D. Phillips, J. V. Porto, and I. B. Spielman. *Bose-Einstein Condensate in a Uniform Light-Induced Vector Potential.* Phys. Rev. Lett. **102**, 130401 (2009).

[81] Y.-J. Lin, R. L. Compton, K. Jiménez-García, J. V. Porto, and I. B. Spielman. *Synthetic magnetic fields for ultracold neutral atoms.* Nature **462**, 628–632 (2009).

[82] J. Steck. *Noise Characterization of Local Spin Rotations in a Spin-1 Bose-Einstein Condensate.* Bachelor's thesis. University of Heidelberg (2021).

[83] S. Lannig, C.-M. Schmied, M. Prüfer, P. Kunkel, R. Strohmaier, H. Strobel, T. Gasenzer, P. G. Kevrekidis, and M. K. Oberthaler. *Collisions of Three-Component Vector Solitons in Bose-Einstein Condensates.* Phys. Rev. Lett. **125**, 170401 (2020).

[84] J. S. Russell. *Experimental Researches into the Laws of Certain Hydrodynamical Phenomena that accompany the Motion of Floating Bodies, and have not previously been reduced into conformity with the known Laws of the Resistance of Fluids.* Transactions of the Royal Society of Edinburgh **XIV**, 47–109 (1837).

[85] L. F. Mollenauer, R. H. Stolen, and J. P. Gordon. *Experimental Observation of Picosecond Pulse Narrowing and Solitons in Optical Fibers.* Phys. Rev. Lett. **45**, 1095–1098 (1980).

[86] L. F. Mollenauer and J. P. Gordon. *Solitons in Optical Fibers* (Elsevier Inc., 2006).

[87] B. Denardo, B. Galvin, A. Greenfield, A. Larraza, S. Putterman, and W. Wright. *Observations of localized structures in nonlinear lattices: Domain walls and kinks.* Phys. Rev. Lett. **68**, 1730–1733 (1992).

[88] A. J. Heeger, S. Kivelson, J. R. Schrieffer, and W. P. Su. *Solitons in conducting polymers.* Rev. Mod. Phys. **60**, 781–850 (1988).

[89] J.-F. Paquerot and M. Remoissenet. *Dynamics of nonlinear blood pressure waves in large arteries.* Physics Letters A **194**, 77–82 (1994).

[90] L. hua Zhao, Y. yue Wang, and C. qing Dai. *Solitons and their interactions in a tapered aorta.* Physica Scripta **84**, 065401 (2011).

[91] A. Davydov. *The theory of contraction of proteins under their excitation.* Journal of Theoretical Biology **38**, 559–569 (1973).

[92] P. S. Lomdahl, S. P. Layne, and I. J. Bigio. *Solitons in Biology.* Los Alamos Science **10**, 1–22 (1984).

[93] A. Scott. *Davydov's soliton.* Physics Reports **217**, 1–67 (1992).

[94] P. S. Lomdahl. *What Is a Soliton?* Los Alamos Science **10**, 27–31 (1984).

[95] M. H. Anderson, J. R. Ensher, M. R. Matthews, C. E. Wieman, and E. A. Cornell. *Observation of Bose-Einstein Condensation in a Dilute Atomic Vapor.* Science **269**, 198–201 (1995).

[96] K. B. Davis, M. O. Mewes, M. R. Andrews, N. J. van Druten, D. S. Durfee, D. M. Kurn, and W. Ketterle. *Bose-Einstein Condensation in a Gas of Sodium Atoms.* Phys. Rev. Lett. **75**, 3969–3973 (1995).

[97] Z. Chen, M. Segev, and D. N. Christodoulides. *Optical spatial solitons: historical overview and recent advances.* Reports on Progress in Physics **75**, 086401 (2012).

[98] D. N. Christodoulides and R. I. Joseph. *Vector solitons in birefringent nonlinear dispersive media.* Opt. Lett. **13**, 53–55 (1988).

[99] C. Menyuk. *Nonlinear pulse propagation in birefringent optical fibers.* IEEE Journal of Quantum Electronics **23**, 174–176 (1987).

[100] P. Kevrekidis and D. Frantzeskakis. *Solitons in coupled nonlinear Schrödinger models: A survey of recent developments.* Reviews in Physics **1**, 140–153 (2016).

[101] M. Mitchell, Z. Chen, M.-f. Shih, and M. Segev. *Self-Trapping of Partially Spatially Incoherent Light.* Phys. Rev. Lett. **77**, 490–493 (1996).

[102] M. Segev and D. N. Christodoulides. *Incoherent Solitons.* Opt. Photon. News **13**, 70–76 (2002).

[103] P. G. Kevrekidis, D. J. Frantzeskakis, and R. Carretero-González. *Emergent Nonlinear Phenomena in Bose–Einstein Condensates.* Springer Series on Atomic, Optical, and Plasma Physics (Springer-Verlag, 2008).

[104] G. Arutyunov. *Elements of Classical and Quantum Integrable Systems* (Springer Nature Switzerland AG, 2019).

[105] V. E. Zakharov and A. B. Shabat. *Exact Theory of Two-Dimensional Self-Focusing and One-Dimensional Self-Modulation of Waves in Nonlinear Media.* Sov. Phys. JETP **34**, 62 (1972).

[106] V. E. Zakharov and A. B. Shabat. *Interaction between solitons in a stable medium.* Sov. Phys. JETP **37**, 823 (1973).

[107] M. A. Ablowitz and P. A. Clarkson. *Solitons, Nonlinear Evolution Equations and Inverse Scattering*. London Mathematical Society Lecture Note Series (Cambridge University Press, 1991).

[108] A. Muryshev, G. V. Shlyapnikov, W. Ertmer, K. Sengstock, and M. Lewenstein. *Dynamics of Dark Solitons in Elongated Bose-Einstein Condensates.* Phys. Rev. Lett. **89**, 110401 (2002).

[109] Z. Dutton, M. Budde, C. Slowe, and L. V. Hau. *Observation of Quantum Shock Waves Created with Ultra- Compressed Slow Light Pulses in a Bose-Einstein Condensate.* Science **293**, 663–668 (2001).

[110] S. Stellmer, C. Becker, P. Soltan-Panahi, E.-M. Richter, S. Dörscher, M. Baumert, J. Kronjäger, K. Bongs, and K. Sengstock. *Collisions of Dark Solitons in Elongated Bose-Einstein Condensates.* Phys. Rev. Lett. **101**, 120406 (2008).

[111] L. M. Aycock, H. M. Hurst, D. K. Efimkin, D. Genkina, H.-I. Lu, V. M. Galitski, and I. B. Spielman. *Brownian motion of solitons in a Bose-Einstein condensate.* Proceedings of the National Academy of Sciences **114**, 2503–2508 (2017).

[112] A. R. Fritsch, M. Lu, G. H. Reid, A. M. Piñeiro, and I. B. Spielman. *Creating solitons with controllable and near-zero velocity in Bose-Einstein condensates.* Phys. Rev. A **101**, 053629 (2020).

[113] A. Weller, J. P. Ronzheimer, C. Gross, J. Esteve, M. K. Oberthaler, D. J. Frantzeskakis, G. Theocharis, and P. G. Kevrekidis. *Experimental Observation of Oscillating and Interacting Matter Wave Dark Solitons.* Phys. Rev. Lett. **101**, 130401 (2008).

[114] I. Shomroni, E. Lahoud, S. Levy, and J. Steinhauer. *Evidence for an oscillating soliton/vortex ring by density engineering of a Bose–Einstein condensate.* Nature Physics **5**, 193–197 (2009).

[115] G. Theocharis, A. Weller, J. P. Ronzheimer, C. Gross, M. K. Oberthaler, P. G. Kevrekidis, and D. J. Frantzeskakis. *Multiple atomic dark solitons in cigar-shaped Bose-Einstein condensates.* Phys. Rev. A **81**, 063604 (2010).

[116] J. J. Chang, P. Engels, and M. A. Hoefer. *Formation of Dispersive Shock Waves by Merging and Splitting Bose-Einstein Condensates.* Phys. Rev. Lett. **101**, 170404 (2008).

[117] P. Engels and C. Atherton. *Stationary and Nonstationary Fluid Flow of a Bose-Einstein Condensate Through a Penetrable Barrier.* Phys. Rev. Lett. **99**, 160405 (2007).

[118] K. E. Strecker, G. B. Partridge, A. G. Truscott, and R. G. Hulet. *Formation and propagation of matter-wave soliton trains.* Nature **417**, 150–153 (2002).

[119] L. Khaykovich, F. Schreck, G. Ferrari, T. Bourdel, J. Cubizolles, L. D. Carr, Y. Castin, and C. Salomon. *Formation of a Matter-Wave Bright Soliton.* Science **296**, 1290–1293 (2002).

[120] S. L. Cornish, S. T. Thompson, and C. E. Wieman. *Formation of Bright Matter-Wave Solitons during the Collapse of Attractive Bose-Einstein Condensates.* Phys. Rev. Lett. **96**, 170401 (2006).

[121] A. L. Marchant, T. P. Billam, T. P. Wiles, M. M. H. Yu, S. A. Gardiner, and S. L. Cornish. *Controlled formation and reflection of a bright solitary matter-wave.* Nature Communications **4**, 1865 (2013).

[122] J. H. V. Nguyen, P. Dyke, D. Luo, B. A. Malomed, and R. G. Hulet. *Collisions of matter-wave solitons.* Nature Physics **10**, 918–922 (2014).

[123] P. J. Everitt, M. A. Sooriyabandara, M. Guasoni, P. B. Wigley, C. H. Wei, G. D. McDonald, K. S. Hardman, P. Manju, J. D. Close, C. C. N. Kuhn, S. S. Szigeti, Y. S. Kivshar, and N. P. Robins. *Observation of a modulational instability in Bose-Einstein condensates.* Phys. Rev. A **96**, 041601 (2017).

[124] P. Medley, M. A. Minar, N. C. Cizek, D. Berryrieser, and M. A. Kasevich. *Evaporative Production of Bright Atomic Solitons.* Phys. Rev. Lett. **112**, 060401 (2014).

[125] B. Eiermann, T. Anker, M. Albiez, M. Taglieber, P. Treutlein, K.-P. Marzlin, and M. K. Oberthaler. *Bright Bose-Einstein Gap Solitons of Atoms with Repulsive Interaction.* Phys. Rev. Lett. **92**, 230401 (2004).

[126] C.-A. Chen and C.-L. Hung. *Observation of Universal Quench Dynamics and Townes Soliton Formation from Modulational Instability in Two-Dimensional Bose Gases.* Phys. Rev. Lett. **125**, 250401 (2020).

[127] B. Bakkali-Hassani, C. Maury, Y.-Q. Zou, E. Le Cerf, R. Saint-Jalm, P. C. M. Castilho, S. Nascimbene, J. Dalibard, and J. Beugnon. *Realization of a Townes Soliton in a Two-Component Planar Bose Gas.* Phys. Rev. Lett. **127**, 023603 (2021).

[128] Z. Chen, M. Segev, T. H. Coskun, D. N. Christodoulides, Y. S. Kivshar, and V. V. Afanasjev. *Incoherently coupled dark–bright photorefractive solitons.* Opt. Lett. **21**, 1821–1823 (1996).

[129] E. A. Ostrovskaya, Y. S. Kivshar, Z. Chen, and M. Segev. *Interaction between vector solitons and solitonic gluons.* Opt. Lett. **24**, 327–329 (1999).

[130] E. T. Karamatskos, J. Stockhofe, P. G. Kevrekidis, and P. Schmelcher. *Stability and tunneling dynamics of a dark-bright soliton pair in a harmonic trap.* Phys. Rev. A **91**, 043637 (2015).

[131] A. P. Sheppard and Y. S. Kivshar. *Polarized dark solitons in isotropic Kerr media.* Phys. Rev. E **55**, 4773–4782 (1997).

[132] B. P. Anderson, P. C. Haljan, C. A. Regal, D. L. Feder, L. A. Collins, C. W. Clark, and E. A. Cornell. *Watching Dark Solitons Decay into Vortex Rings in a Bose-Einstein Condensate.* Phys. Rev. Lett. **86**, 2926–2929 (2001).

[133] C. Becker, S. Stellmer, P. Soltan-Panahi, S. Dörscher, M. Baumert, E.-M. Richter, J. Kronjäger, K. Bongs, and K. Sengstock. *Oscillations and interactions of dark and dark–bright solitons in Bose–Einstein condensates.* Nature Physics **4**, 496–501 (2008).

[134] S. Middelkamp, J. Chang, C. Hamner, R. Carretero-González, P. Kevrekidis, V. Achilleos, D. Frantzeskakis, P. Schmelcher, and P. Engels. *Dynamics of dark–bright solitons in cigar-shaped Bose–Einstein condensates.* Physics Letters A **375**, 642–646 (2011).

[135] C. Hamner, J. J. Chang, P. Engels, and M. A. Hoefer. *Generation of Dark-Bright Soliton Trains in Superfluid-Superfluid Counterflow.* Phys. Rev. Lett. **106**, 065302 (2011).

[136] M. A. Hoefer, J. J. Chang, C. Hamner, and P. Engels. *Dark-dark solitons and modulational instability in miscible two-component Bose-Einstein condensates.* Phys. Rev. A **84**, 041605 (2011).

[137] D. Yan, J. J. Chang, C. Hamner, P. G. Kevrekidis, P. Engels, V. Achilleos, D. J. Frantzeskakis, R. Carretero-González, and P. Schmelcher. *Multiple dark-bright solitons in atomic Bose-Einstein condensates.* Phys. Rev. A **84**, 053630 (2011).

[138] D. Yan, J. J. Chang, C. Hamner, M. Hoefer, P. G. Kevrekidis, P. Engels, V. Achilleos, D. J. Frantzeskakis, and J. Cuevas. *Beating dark–dark solitons in Bose–Einstein condensates.* Journal of Physics B: Atomic, Molecular and Optical Physics **45**, 115301 (2012).

[139] A. Álvarez, J. Cuevas, F. R. Romero, C. Hamner, J. J. Chang, P. Engels, P. G. Kevrekidis, and D. J. Frantzeskakis. *Scattering of atomic dark–bright solitons from narrow impurities.* Journal of Physics B: Atomic, Molecular and Optical Physics **46**, 065302 (2013).

[140] I. Danaila, M. A. Khamehchi, V. Gokhroo, P. Engels, and P. G. Kevrekidis. *Vector dark-antidark solitary waves in multicomponent Bose-Einstein condensates.* Phys. Rev. A **94**, 053617 (2016).

[141] T. Busch and J. R. Anglin. *Dark-Bright Solitons in Inhomogeneous Bose-Einstein Condensates.* Phys. Rev. Lett. **87**, 010401 (2001).

[142] T. M. Bersano, V. Gokhroo, M. A. Khamehchi, J. D'Ambroise, D. J. Frantzeskakis, P. Engels, and P. G. Kevrekidis. *Three-Component Soliton States in Spinor $F = 1$ Bose-Einstein Condensates.* Phys. Rev. Lett. **120**, 063202 (2018).

[143] B. Prinari, F. Vitale, and G. Biondini. *Dark-bright soliton solutions with nontrivial polarization interactions for the three-component defocusing nonlinear Schrödinger equation with nonzero boundary conditions.* J. Math. Phys. **56**, 071505 (2015).

[144] R. Radhakrishnan, N. Manikandan, and K. Aravinthan. *Energy-exchange collisions of dark-bright-bright vector solitons.* Phys. Rev. E **92**, 062913 (2015).

[145] C. Qu, L. P. Pitaevskii, and S. Stringari. *Magnetic Solitons in a Binary Bose-Einstein Condensate.* Phys. Rev. Lett. **116**, 160402 (2016).

[146] K. Fujimoto, R. Hamazaki, and M. Ueda. *Flemish Strings of Magnetic Solitons and a Nonthermal Fixed Point in a One-Dimensional Antiferromagnetic Spin-1 Bose Gas.* Phys. Rev. Lett. **122**, 173001 (2019).

[147] X. Chai, D. Lao, K. Fujimoto, and C. Raman. *Magnetic soliton: From two to three components with SO(3) symmetry.* Phys. Rev. Research **3**, L012003 (2021).

[148] L.-Z. Meng, Y.-H. Qin, and L.-C. Zhao. *Spin solitons in spin-1 Bose–Einstein condensates.* Communications in Nonlinear Science and Numerical Simulation **109**, 106286 (2022).

[149] A. Farolfi, D. Trypogeorgos, C. Mordini, G. Lamporesi, and G. Ferrari. *Observation of Magnetic Solitons in Two-Component Bose-Einstein Condensates.* Phys. Rev. Lett. **125**, 030401 (2020).

[150] X. Chai, D. Lao, K. Fujimoto, R. Hamazaki, M. Ueda, and C. Raman. *Magnetic Solitons in a Spin-1 Bose-Einstein Condensate.* Phys. Rev. Lett. **125**, 030402 (2020).

[151] J. Ieda, T. Miyakawa, and M. Wadati. *Matter-Wave Solitons in an F=1 Spinor Bose–Einstein Condensate.* Journal of the Physical Society of Japan **73**, 2996–3007 (2004).

[152] H. E. Nistazakis, D. J. Frantzeskakis, P. G. Kevrekidis, B. A. Malomed, and R. Carretero-González. *Bright-dark soliton complexes in spinor Bose-Einstein condensates.* Phys. Rev. A **77**, 033612 (2008).

[153] I.-K. Liu, S.-C. Gou, and H. Takeuchi. *Phase diagram of solitons in the polar phase of a spin-1 Bose-Einstein condensate.* Phys. Rev. Research **2**, 033506 (2020).

[154] G. C. Katsimiga, S. I. Mistakidis, P. Schmelcher, and P. G. Kevrekidis. *Phase diagram, stability and magnetic properties of nonlinear excitations in spinor Bose–Einstein condensates.* New Journal of Physics **23**, 013015 (2021).

[155] K. Geier. *Dynamics of Vector Solitons in Spinor Bose-Einstein Condensates.* Master's thesis. Universität Heidelberg (2017).

[156] M. Vijayajayanthi, T. Kanna, and M. Lakshmanan. *Bright-dark solitons and their collisions in mixed N-coupled nonlinear Schrödinger equations.* Phys. Rev. A **77**, 013820 (2008).

[157] C. F. Ockeloen, A. F. Tauschinsky, R. J. C. Spreeuw, and S. Whitlock. *Detection of small atom numbers through image processing.* Phys. Rev. A **82**, 061606 (2010).

[158] T. Busch and J. R. Anglin. *Motion of Dark Solitons in Trapped Bose-Einstein Condensates.* Phys. Rev. Lett. **84**, 2298–2301 (2000).

[159] V. Achilleos, D. Yan, P. G. Kevrekidis, and D. J. Frantzeskakis. *Dark-bright solitons in Bose–Einstein condensates at finite temperatures.* New Journal of Physics **14**, 055006 (2012).

[160] B. Jackson, N. P. Proukakis, and C. F. Barenghi. *Dark-soliton dynamics in Bose-Einstein condensates at finite temperature.* Phys. Rev. A **75**, 051601 (2007).

[161] N. G. Parker, N. P. Proukakis, M. Leadbeater, and C. S. Adams. *Soliton-Sound Interactions in Quasi-One-Dimensional Bose-Einstein Condensates.* Phys. Rev. Lett. **90**, 220401 (2003).

[162] Z. Dutton and C. W. Clark. *Effective one-component description of two-component Bose-Einstein condensate dynamics.* Phys. Rev. A **71**, 063618 (2005).

[163] A. Romero-Ros, G. C. Katsimiga, S. I. Mistakidis, B. Prinari, G. Biondini, P. Schmelcher, and P. G. Kevrekidis. *Realization of the Peregrine soliton in repulsive two-component Bose-Einstein condensates.* (2021).

[164] C. R. Cabrera, L. Tanzi, J. Sanz, B. Naylor, P. Thomas, P. Cheiney, and L. Tarruell. *Quantum liquid droplets in a mixture of Bose-Einstein condensates.* Science **359**, 301–304 (2018).

[165] M. Lewenstein and B. A. Malomed. *Entanglement generation by collisions of quantum solitons in the Born approximation.* New Journal of Physics **11**, 113014 (2009).

[166] G. I. Stegeman and M. Segev. *Optical Spatial Solitons and Their Interactions: Universality and Diversity.* Science **286**, 1518–1523 (1999).

[167] Y. S. Kivshar and B. Luther-Davies. *Dark optical solitons: physics and applications.* Physics Reports **298**, 81–197 (1998).

[168] T. Tsuchida. *N-Soliton Collision in the Manakov Model.* Progress of Theoretical Physics **111**, 151–182 (2004).

[169] H. Saito, Y. Kawaguchi, and M. Ueda. *Topological defect formation in a quenched ferromagnetic Bose-Einstein condensates.* Phys. Rev. A **75**, 013621 (2007).

[170] A. McIntosh. *The Jackknife Estimation Method.* arXiv:1606.00497.

[171] P. C. Hohenberg and B. I. Halperin. *Theory of dynamic critical phenomena.* Rev. Mod. Phys. **49**, 435–479 (1977).

[172] M. Karl and T. Gasenzer. *Strongly anomalous non-thermal fixed point in a quenched two-dimensional Bose gas.* New Journal of Physics **19**, 093014 (2017).

[173] M. Schmidt, S. Erne, B. Nowak, D. Sexty, and T. Gasenzer. *Non-thermal fixed points and solitons in a one-dimensional Bose gas.* New Journal of Physics **14**, 075005 (2012).

[174] J. Berges, K. Boguslavski, S. Schlichting, and R. Venugopalan. *Universal attractor in a highly occupied non-Abelian plasma.* Phys. Rev. D **89**, 114007 (2014).

[175] A. N. Mikheev, C.-M. Schmied, and T. Gasenzer. *Low-energy effective theory of nonthermal fixed points in a multicomponent Bose gas.* Phys. Rev. A **99**, 063622 (2019).

[176] A. Bray. *Theory of phase-ordering kinetics.* Advances in Physics **43**, 357–459 (1994).

[177] I. Siovitz. *Topological Excitations and Universal Scaling of the One-Dimensional Spin-1 Bose-Einstein Condensate Far from Equilibrium.* Master's thesis. University of Heidelberg (2022).

[178] Y.-Q. Zou, É. L. Cerf, B. Bakkali-Hassani, C. Maury, G. Chauveau, P. C. M. Castilho, R. Saint-Jalm, S. Nascimbene, J. Dalibard, and J. Beugnon. *Optical control of the density and spin spatial profiles of a planar Bose gas.* Journal of Physics B: Atomic, Molecular and Optical Physics **54**, 08LT01 (2021).

[179] J. Estève, C. Gross, A. Weller, S. Giovanazzi, and M. K. Oberthaler. *Squeezing and entanglement in a Bose–Einstein condensate.* Nature **455**, 1216–1219 (2008).

[180] C. D. Hamley, C. S. Gerving, T. M. Hoang, E. M. Bookjans, and M. S. Chapman. *Spin-nematic squeezed vacuum in a quantum gas.* Nature Physics **8**, 305–308 (2012).

[181] L.-M. Duan, G. Giedke, J. I. Cirac, and P. Zoller. *Inseparability Criterion for Continuous Variable Systems.* Phys. Rev. Lett. **84**, 2722–2725 (2000).

[182] X.-Y. Luo, Y.-Q. Zou, L.-N. Wu, Q. Liu, M.-F. Han, M. K. Tey, and L. You. *Deterministic entanglement generation from driving through quantum phase transitions.* Science **355**, 620–623 (2017).

[183] S. Floerchinger, M. Gärttner, T. Haas, and O. R. Stockdale. *Entropic entanglement criteria in phase space.* Phys. Rev. A **105**, 012409 (2022).

[184] M. Prüfer, D. Spitz, S. Lannig, H. Strobel, J. Berges, and M. K. Oberthaler. *Condensation and thermalization of an easy-plane ferromagnet in a spinor Bose gas.* arXiv:2205.06188.

[185] R. Kubo. *The fluctuation-dissipation theorem.* Reports on Progress in Physics **29**, 255–284 (1966).

[186] A. Widera. *Constructing Correlated Spin States with Neutral Atoms in Optical Lattices.* Ph.D. thesis. Johannes Gutenberg-Universität Mainz (2007).

Acknowledgements

Finally, I would like to thank all the people who accompanied me throughout this project and without many of whom this work would not have turned out like this.

First of all I want to thank Markus for not only the opportunity to work on a PhD project in his group but also allowing for the freedom of pursuing own ideas. I especially value the detailed discussions allowing for everyone's arguments to be considered and be taken into account. I am deeply grateful for all the suggestions and continuing support during the whole time. Finally, I want to express my gratitude for promoting an open and trusting atmosphere, which allows the work here to be a joyful experience.

I also want to thank Panos Kevrekidis for sharing his profound knowledge about any type of non-linear excitation and the help in finding a theoretical description for the vector solitons.

Many thanks also to thank Selim Jochim, for agreeing to referee my thesis and also for lectures and conversations which have been a part of my motivation to enter this fascinating field of ultracold atoms.

Most importantly, I wish to extend a particularly heartfelt thanks to my colleagues and friends of the BEC team, who shared the challenges and sometimes also the frustration, but above all the joy during the countless hours in the lab and one or the other after-work beer. Thanks to Max, Philip, Helmut, Rodrigo, Alexis, Robin, Benedikt, Jakob, David, Yannick and Alex for the many discussions, support, jokes, musical interludes, and opportunities to learn so many new things over this whole time! Also many thanks to our theoretical colleagues Christian, Thomas, Martin and Ido, who are so close to the experiment to also be considered part of the experimental team. Thank your for the many discussions, new perspectives and joint sporting activities.

My sincerest thanks goes also to all the members of the whole Matterwave and SynQs group for an unforgettable time and continued social events during such wild and unusual times. I especially enjoyed the many lunches, dinners and grilling events with many of the members of the BECK, ATTA, NaLi and SoPa experiments. Especially in dark times the company of these people brightened the mood considerably.

Ganz herzlich möchte ich mich auch bei Dagmar und Christiane bedanken, deren unschätzbar wertvolle Organisation das alltägliche Leben ungemein erleichtern und uns zahlreiche Probleme ersparen. Vielen Dank auch an Frau Müller für die zügige und bürokratiearme Abarbeitung der unzähligen Bestellungen und insbesondere die geduldige Lösung von so manchnen zähen Problemen. Herzlichen Dank auch an die Mitarbeiterinnen und Mitarbeiter der EDV, Elektro- und Mechanikwerkstatt, die bei der Behebung der vielen kleinen Probleme des Laboralltags eine Zentrale Rolle einnehmen und uns immer wieder mit vielen spontanen Lösungen unterstützen.

Zu guter Letzt möchte ich noch meiner Familie danken. All die schöne Zeit und auch die bauliche Vergnügungen über die letzten Jahre haben mein Leben doch ganz schön erheitert. Besonders gilt der Dank natürlich meinen Eltern, für die bedingungslose und anhaltende Unterstützung in allen Lebenslagen.